MAGNETIC FIELDS OF F-TYPE STARS

A thesis submitted by

John M Seach

BSc, MoA

for the award of

Doctor of Philosophy

2022

ABSTRACT

Magnetic fields are an observable feature of many stars, with warm, F-type stars of interest in searching for the transition from the fossil fields in hot stars to dynamos in cool stars driven by convection zones. Thus, this thesis presents an observational survey of F-type stars close to the expected transition between fossil and dynamo magnetic fields. A magnetic snapshot survey of 55 targets resulted in 14 magnetic field detections, across every spectral class from F3V-F9V ranging in strength from 0.3±0.1G (36 UMa, F8V) to 8.3±0.9 G (h Dra, F8V). These results are followed up with detailed mapping using Zeeman Doppler Imaging (ZDI) of the large-scale surface magnetic fields for four of these stars, β CrB, σ Boo, θ Dra, and β Vir. On the hot side of the suspected transition zone, β CrB (A9) shows a relatively complex, but stable topology which is not common for a fossil field and is more complex than a dipole. On the cool side of the suspected transition zone, the surface magnetic field of σ Boo (F3V) shows a relatively simple field topology with a dominant dipole structure. This is the first magnetic map for an F3 star and provides an opportunity to study magnetism in a star with an outer convection zone thickness less than three per cent of the stellar radius. ZDI maps are also presented for two late F-stars, θ Dra (F8IV) and β Vir (F9V). These two late F-stars are contrasted with σ Boo, and show a more complex magnetic topology. There are differences in complexity of the magnetic field between θ Dra and β Vir, which is possibly related to an increased rotation rate for θ Dra which shows more detail due to a greater surface resolution. The ZDI maps are also used in modelling the stellar winds. While definitive evidence of the transition from fossil to dynamo field is not clear from the single-epoch magnetic map results obtained, this work suggests additional future maps obtained across different epochs will provide empirical evidence for how stellar mass, rotation and age drive the emergence of dynamo fields in stars with shallow convection zones.

CERTIFICATION OF THESIS

I John Seach declare that the PhD Thesis entitled "Magnetic Fields of F-Type Stars" is not more than 100,000 words in length including quotes and exclusive of tables, figures, appendices, bibliography, references, and footnotes. This Thesis is the work of John Seach except where otherwise acknowledged, with the majority of the contribution to the papers presented as a Thesis by Publication undertaken by the Student. The work is original and has not previously been submitted for any other award, except where acknowledged.

Student: John M. Seach, (11 March 2022)

Principal Supervisor: Associate Professor Stephen C. Marsden

Associate Supervisor: Professor Bradley D. Carter

Associate Supervisor: Doctor Leigh Brookshaw

Student and supervisors' signatures of endorsement are held at the University.

STATEMENT OF CONTRIBUTION

This section details contributions by the various authors for each of the papers presented in this thesis by publication.

Chapter 2, Seach et al. (2020):

Seach, J. M., Marsden, S. C., Carter, B. D., Neiner, C., Folsom, C. P., Mengel, M. W., Oksala, M. E., Buysschaert, B. (2020), A Magnetic Snapshot Survey of F-type Stars.

Author	Percent Contribution	Tasks performed
J. M. Seach	85	Performed analysis, interpretation, wrote all drafts of paper.
S. C. Marsden B. D. Carter C. Neiner C. P. Folsom M. W. Mengel M. E. Oksala M. E. Buysschaert	15	Conception of project, provision of codes, suggested edits to manuscript.

Chapter 3, Seach et al. (2022a):

Seach, J. M., Marsden, S. C., Carter, B. D., Evensberget, D., Folsom, C. P., Neiner, C., Mengel, M. W. (2022). The magnetic fields and stellar winds of the mature late F-stars: β Virginis and θ Draconis.

Author	Percent Contribution	Tasks performed
J. M. Seach	80	Performed analysis, interpretation, wrote all drafts of paper.
S. C. Marsden B. D. Carter D. Evensberget C. P. Folsom C. Neiner M. W. Mengel	20	Conception of project, provision of codes, wind modelling section, suggested edits to manuscript.

Chapter 4, Seach et al. (2022b):

Seach, J. M., Marsden, S. C., Carter, B. D., Neiner, C., Folsom, C. P. (2022). The Magnetic Field of β Coronae Borealis and Early F-star σ Bootis. In preparation.

Author	Percent Contribution	Tasks performed
J. M. Seach	85	Performed analysis, interpretation, wrote all drafts of paper.
S. C. Marsden B. D. Carter C. Neiner C. P. Folsom	15	Conception of project, provision of codes, suggested edits to manuscript.

ACKNOWLEDGEMENTS

I would like to offer my sincere thanks and acknowledgements to many people and organizations for allowing me to complete this thesis. Firstly, I would like to acknowledge this research was supported by an Australian Government Research Training Program (RTP). Data for the project was provided by the BCool and BRITEpol collaborations. This data was collected using the HARPS South instrument at the European Southern Observatory, La Silla, Chile; the NARVAL instrument located at the Telescope Bernard Lyot (TBL) at the Observatoire Midi-Pyrenees, France; and the ESPaDOnS instrument at the Canada-France-Hawaii Telescope (CFHT) located at the Mauna Kea Observatory in Hawaii. TBL/NARVAL are operated by the Institut National des Sciences de l'Univers of the Centre National de la Recherche Scientifique of France. CFHT/ESPaDOnS is operated by the National Research Council of Canada, the Institut National des Sciences de l'Univers of the Centre National de la Recherche Scientifique of France, and the Univervity of Hawaii.

Thanks to the co-authors and colleagues on my papers who provided comments, feedback, access to computer code: Dr. Coralie Neiner, Dr Colin Folsom, Dr Matthew Mengel, and fellow student Dag Evensberget. Special thanks, of course to my supervisors, mentors and co-authors, Associate Professor Stephen Marsden, and Professor Brad Carter. Stephen and Brad always generously made their time available, and I could not have completed this research without their guidance and support.

Finally, my enduring thanks to my partner Elicia who always believed in my goal of obtaining my PhD, and provided unwavering support throughout the years, and to my two cats, who kept me company throughout the many late nights working at the computer. Thank you to everyone for making this possible.

TABLE OF CONTENTS

LIST OF FIGURES

Excluding publications in Chapters 2-4

LIST OF TABLES

Excluding publications in Chapters 2-4

CHAPTER 1

INTRODUCTION

The transition from fossil to dynamo magnetic fields in stars is an important area of astrophysics study. In this thesis two research questions are addressed. Firstly, what changes occur, if any, in the strength and detectability of the magnetic fields of F-type stars across spectral types from F0-F9? Secondly, how does the surface magnetic topology differ between early and late F-stars?

1.1 Astrophysical Magnetic Fields

Magnetic fields are everywhere in the Universe and have been in existence since the first seed magnetic fields were created (Rees, 1987), possibly during the inflation period (Turner & Widrow, 1988; Ratra, 1992), or more likely during the phase transitions which followed (Sigl et al., 1997; Widrow et al., 2012). Theoretical calculations have shown that a primordial field strength of 10^{-10} G with a wavelength of 10 kpc possibly formed during the electroweak phase transition (first 10^{-12} s of the Universe) (Field & Carroll, 2000). Astrophysical magnetic fields have been described as an 'organism' (Parker, 1979) which feeds on the

energy flow from stars and galaxies, where a small magnetic field diverts energy, which then creates a larger field, and contributes to restlessness (Born, 1935) in the Universe. Partly due to the presence of magnetic fields, the increase in entropy and disorder of the Universe can be locally modified to produce regions of order (Parker, 1979), which allows for the development of stars, planets and ultimately the development of advanced life forms (Dubrov, 2013).

An understanding of magnetism has its basis in Maxwell's laws of electrodynamics (Maxwell, 1865; Jackson, 1962). The form of Maxwell's second law as given by Fleisch (2008) is,

$$\oint_S \vec{B}\hat{n}da = 0 \tag{1.1}$$

where $\oint_S$ is the surface integral over a closed surface, $\vec{B}$ is the vector magnetic field in Teslas, $\hat{n}$ is the unit vector normal to the surface, and da is an increment of surface area in m^2. The zero magnetic flux through a closed surface allows solutions involving complex surfaces especially if the flux through a portion of a surface can be found by integration (Fleisch, 2008). A consequence of Maxwell's second law is that magnetic monopoles do not exist in the nature (Dirac, 1931; Shnir, 2006), and all magnetic fields form loops, and are able to extend over long distances (Kuijpers et al., 2015). Once formed, astrophysical magnetic fields can remain for a long time, in contrast to electric fields which are short circuited relatively fast (Charbonneau, 2013). The properties of astrophysical magnetic fields are very different from that seen in the laboratory or everyday experience (Parker, 1979). The simplest form of magnetic field is a dipole which is equivalent to a current loop (Huang, 2007) where the field is commonly represented visually by lines of force (see Fig. 1.1), although Blackman & Hubbard (2014) suggest that ribbons may characterize magnetohydrodynamic magnetic fields better because

they are able to include magnetic helicity.

Stars are one of the building blocks of the Universe, and have been in existence since the end of the cosmic dark age (Bromm et al., 1999; Bromm & Larson, 2004; Bromm, 2013) about 10^6 to 10^9 years after the beginning of the Universe. Stellar magnetic fields are created from either amplification of primordial magnetic fields during the collapse of molecular clouds (Borra et al., 1982; Koh et al., 2021), or re-generated in the turbulent convection zones of stars by dynamo processes (Charbonneau, 2013). The range of stellar magnetic field strengths ranges from sub Gauss levels in some cool main-sequence stars (Marsden et al., 2014; Seach et al., 2020), to 10^{17} G on the surface of magnetars (Kaspi & Beloborodov, 2017). The first suggestion the Sun was magnetic came from Bigelow (1890) who observed the shape of coronal streamers on photos from the 1878 and 1889 solar eclipses, and attributed this to the effect of a magnetic field. Pioneering work by Hale (1908) linked sunspots to magnetic fields in a study of the solar spectrum. The initial observations were made with a 60-foot tower telescope and a 30-foot spectrograph. Later, using a 150-foot telescope Hale was able to observe important features of the solar magnetic field (Hale, 1912, 1913; Hale et al., 1918) which included the longitudinal magnetic field having a maximum strength about +45 deg and -45 deg. Additionally Hale identified the solar magnetic field had opposite polarities in the northern and southern hemisphere, with the polarity reversing at the equator. Hale's work opened an era of solar magnetic studies which was followed 40 years by the first detection of the magnetic field in a star other than the Sun by Babcock (1947) who used circular polarisation to measure a magnetic field in (78 Vir, A2p). A hundred years ago Larmor asked, "How could a rotating body such as the Sun become a magnet?" (Lamor, 1919). Studying stellar magnetic activity in stars is important for many areas of astrophysics, including stellar evolution, stellar winds, space weather, and the habitability of

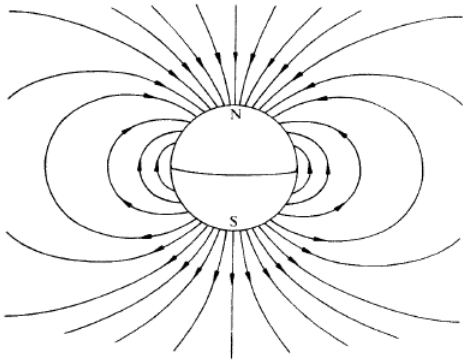

Figure 1.1: Example of a dipole magnetic field, showing lines of force. Figure from Parker (1979).

exoplanets.

1.2 Hot and Cool Stars

In studies of stellar magnetism it is useful to make a distinction between hot and cool stars because of the important implications for the type of magnetism present. Besides the difference in temperature, another distinction between hot and cool stars relates to the absence or presence of a convection zone in the outer atmosphere. The conditions for convective instability were introduced by Schwarzschild (1906) and convection is present in stellar atmospheres when the actual temperature gradient becomes steeper than the adiabatic temperature gradient (De Loore & Doom, 1992). This classical description of convective instability can be understood in terms of a small vertical displacement of a fluid element from its equilibrium position in a local density, and according to Stothers & Chin (1992),

$$-\frac{d\rho}{dr} > -\left(\frac{d\rho}{dr}\right)_{ad} \tag{1.2}$$

where $(d\rho/dr)_{ad}$ is the adiabatic density gradient and r is the distance from the origin. If a fluid element has a lower density compared with that of the surrounding medium the element will continue to rise upward due to buoyancy. Conversely if the fluid element has a higher density compared with that of the surrounding medium the element will continue to descend. Both these scenarios result in convective instability. In the case of a stellar atmosphere this gradient may be caused by partially ionised hydrogen (Fricke & Teleki, 1982) which occurs in cool stars. Qualitatively the lower boundary of a stellar outer convection zone occurs at a layer where the ionization of the most abundant elements are nearly complete (Böhm-Vitense, 1992), and this degree of ionisation is given by the Saha equation:

$$\frac{N^+}{N} = \frac{2u^+}{u}\frac{(x_k 2\pi m_e kT)}{h^3} exp - (x_{ion}/kT)\frac{1}{n_e} \tag{1.3}$$

where N^+ indicates the number of ionized particles and N the number of neutral particles, u^+ and u are the so-called partition functions for the ion and the atom respectively, which describe the distribution of the electrons over the different energy levels of the ion or atom. From the Saha equation it can be seen that larger temperatures result in a greater ratio of N^+/N which means a greater degree of ionization.

In hot stars (spectral types O,B,A, and early F) hydrogen is fully ionised in the outer atmosphere due to high temperatures, therefore convection does not occur, resulting in an outer radiative zone. Fossil magnetic fields, which are stable over long periods of time are associated with hot stars (see Section 1.3). In contrast, cool stars (spectral type mid-F,G,K,M) contain partially ionised hydrogen which causes a superadiabatic temperature gradient (Fricke & Teleki, 1982) resulting in convection in the outer atmospheric layers. Dynamo magnetic

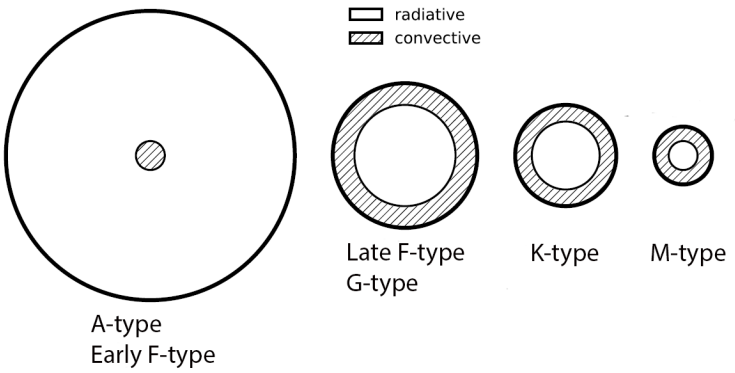

Figure 1.2: Schematic diagram of several representative main-sequence stars labelled by spectral type. Radiative and convective regions are displayed. Early F-type stars are grouped with the hotter A-type stars and late F-type stars are grouped with the cooler G-type stars. Figure adapted from Bars & Lecoanet (2019).

fields are associated with cool stars which contain an outer convection zone where the combined effects of convection and differential rotation create the conditions for magnetic field regeneration (see Section 1.4). The cores of hot stars are thought to be convective, however the magnetic field likely to be trapped and cannot reach the surface (Charbonneau, 2013).

The effective temperature of stars is a good diagnostic of the depth of the stellar outer convection zone (Pinsonneault et al., 2001) and as temperatures increase towards early F-type stars there comes a point when the outer convection zone becomes too thin for dynamo magnetic fields to operate. Fig. 1.2 shows a schematic diagram of a hot A-type star and cool stars of spectral types G,K, and M. The transition between hot and cool stars, which also spans the transition between fossil and dynamo magnetic fields is believed to occur in F-stars, although the exact spectral type is not known exactly (see Section 1.6). This makes F-type stars important targets for understanding stellar magnetism and the dynamics of the outer atmosphere.

1.3 Fossil Magnetic Fields

The fossil field hypothesis was introduced by Cowling (1945) who determined that some magnetic fields would exist for a long time, and decay over the order of the lifetime of the Universe. These fossil fields remain as a relic of a past time in the Universe unless they are disrupted by turbulent motion or electromotive forces. The term fossil field relates to a magnetic field that is not currently being generated and sustained by dynamo action (Oranje et al., 1982). According to Cowling (1953) the decay time t_c of a purely toroidal magnetic field is given by:

$$t_c = 4\pi\sigma L^2 \tag{1.4}$$

where σ is the electrical conductivity, L is the characteristic scale length. Cowling calculated the decay time for a magnetic field in the stable radiative interior of the Sun using estimated values of $\sigma = 10^{-4}$ emu and $L = 2$ x 10^{10} cm (a third the diameter of the Sun), and found $t_c = 1.5$ x 10^{10} yr. The long lifetime of fossil fields in stable interiors of stars is due to both the high electrical conductivity of the ionized gas, and the large size of stars, which protects the field from Ohmic decay (Neiner et al., 2009). Fossil fields in hot main-sequence stars are thought to be left over from star formation (Borra et al., 1982), formed by pre-main sequence dynamos (Kitchatinov et al., 2001), or stellar mergers (Shultz et al., 2019).

The oblique rotator model introduced by Babcock (1949) and developed by Stibbs (1950), is a description of a dipole fossil field in a rotating star. The geometry of the oblique rotator model is shown in Fig. 1.3. The geometry and strength of the dipole fossil field is derived using the parameters: inclination of the rotational axis with respect to the observer (i), obliquity of the dipole axis with respect to the rotational axis (β) counted from the positive rotational pole

towards the positive magnetic pole, and the polar strength of the surface magnetic field ($B_{\rm d}$) calculated at the positive magnetic pole. Following the oblique rotator model of Preston (1967a):

$$\beta = arctan\left[\left(\frac{1-r}{1+r}\right) - \cot i\right] \tag{1.5}$$

where

$$r = \frac{B_l(min)}{B_l(max)} = \frac{\cos\beta\cos i - \sin\beta\sin i}{\cos\beta\cos i + \sin\beta\sin i} \tag{1.6}$$

The polar field strength ($B_{\rm d}$) (Blazère et al., 2016) is,

$$B_{\rm d} = B_{\rm max}\left(\frac{15+u}{20(3-u)}\left(\cos\beta\cos i + \sin\beta\sin i\right)\right)^{-1} \tag{1.7}$$

where u is the limb-darkening coefficient. From Eq.1.7, if $\beta \neq 0$ there is a sinusoidal variation of magnetic field with the stellar rotation.

The oblique rotator model is a simplification of a hot star magnetic field, however it is useful for a first order analysis of a fossil field. It has been known for some time that the field cannot be represented completely by a simple dipole (Preston, 1967b). Developments in the fossil field model were made by Landstreet (1970) who introduced the decentered dipole, and Landstreet & Mathys (2000) characterized the field by a co-linear dipole, quadrupole, and octupole geometry, while Bagnulo et al. (2002b) modeled the field by a superposition of an arbitrarily oriented dipole and a quadrupole field. Fossil fields are usually distinguished from dynamo generated fields by their simple dipolar topography, and stable structure, in contrast to dynamo magnetic fields in cooler stars of around spectral class F5, and later, which are complex and dynamic, due to turbulent convection and differential rotation. Recent observations have shown this distinction between fossil

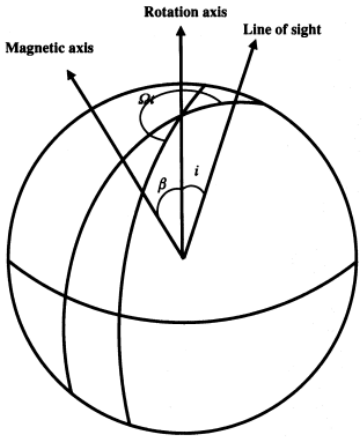

Figure 1.3: Geometry of the oblique rotator model. β is the angle between the magnetic axis and the stellar rotation axis, i is the angle between the line if sight and the rotation axis, and Ω is the rigid rotation angular frequency. The equations for the oblique rotator model are described in (Section 1.3). Figure from Shibahashi & Takata (1993).

and dynamo magnetic fields is not so clear, with the discovery of complex fossil fields in magnetic Am stars (Blazère et al., 2016; Neiner et al., 2017), and potentially simple dynamo fields in late F-type stars (Seach et al., 2022a). Therefore, mapping the topology of surface magnetic fields at multiple epochs is important for the determination of the type of magnetic field present in stars.

1.4 Dynamo Magnetic Fields

Dynamo theory has its beginnings in the first half on the 20th century, and describes the mechanism by which the Sun and solar-type stars amplify and regenerate magnetic fields. There is a large literature on dynamo theory, see for example reviews by Moffatt (1978); Parker (1979); Krause & Rädler (1980); Zeldovich et al. (1983); Roberts & Soward (1992); Brandenburg & Subramanian (2005); Childress & Gilbert (1995); Dormy & Soward (2007); Charbonneau (2013); Mof-

fatt & Dormy (2019). Dynamos work by converting kinetic energy of plasma motion into magnetic energy. The dynamo problem can be stated as finding a flow field that can sustain a magnetic field against Ohmic dissipation (Charbonneau, 2013). The first mathematical description of a self-excited dynamo was by Elsasser (1946) who showed that differential rotation alone can never maintain a dynamo. This was followed by Batchelor (1950) who recognised turbulence as an additional ingredient for dynamo action.

The classic paper by Parker (1955) began the investigation of steady-state amplification of magnetic fields in a fluid, and extended the work of Elsasser (1950) who indicated that various fluid motions were capable of regenerating magnetic field configurations. It is important to distinguish between a dynamo, and a transient amplification of magnetic field (Cattaneo et al., 1991). Differential rotation may cause a transient amplification of magnetic field by sheared transient flow, but this is not a dynamo (Thompson et al., 2009). This transient small-scale dynamo action is caused by turbulent convection, and produces disordered magnetic fields of opposite polarity, which cancel out leaving a zero net field (Cattaneo et al., 1991; Vögler & Schüssler, 2007). Two main dynamo models have been developed to describe solar-type dynamos; the Babcock-Leighton flux transport dynamo (BLFT) and the Interface dynamo.

The Babcock-Leighton flux transport dynamo model (Babcock, 1961; Leighton, 1969; Dikpati & Charbonneau, 1999) (Fig. 1.4) produces toroidal magnetic flux in the tachocline via the Ω-effect. In a thin zone at the base of the convection zone, rotational shear causes an amplification of magnetic flux, and then magnetic buoyancy causes the flux tubes to rise towards the surface. If a magnetic field is strong enough it will survive the rise through the convection zone and emerge at the photosphere as a pair of bipolar active regions which manifests itself as cool spots. During its rise through the convection zone the magnetic flux tube is sub-

jected to twisting by the Coriolis force and results in the trailing bipolar region being displaced poleward according to Joy's Law (Miesch & Toomre, 2009). Once the magnetic flux tubes reach the surface they become disconnected from their roots within a few days (Schüssler & Rempel, 2005). Meridional circulation then transports the flux polewards on the surface, followed by a downward transport towards the tachocline where the cycle continues. The toroidal magnetic field is transformed to a poloidal field via the α-effect in the near surface layer.

The Interface dynamo model (Parker, 1993) involves the generation of a toroidal field in the tachocline via the Ω-effect which is the same as BLFT model. However, the poloidal magnetic field is generated throughout the convection zone by turbulent motions of the plasma rather than a shear layer in BLFT model. The two regions are coupled by convective transport with magnetic buoyancy and meridional circulation not being an essential component (Miesch & Toomre, 2009). The magnetic cycle is determined by meridional circulation in the BLFT dynamo, while dynamo waves determine the cycle in Interface models. Both BLFT and Interface dynamos may operate together in stars and there may even be a blurring between the two models (Miesch & Toomre, 2009). A variation on the distributed dynamo model was introduced by Brandenburg (2005) who describe a distributed dynamo which is shaped by near-surface shear. This model model potentially solved some long-standing issues like the large number of toroidal flux belts produced by interface dynamos (Donati & Landstreet, 2009).

The stellar dynamo is expected to change as the outer convection becomes thin, although how this happens is still to be determined (Schrijver, 1993; Augustson et al., 2012). It is hypothesised that a shrinking convection zone will affect thin shell and distributed dynamos in different ways. Thin shell dynamos depend strongly on the properties of the tachocline, while distributed dynamos are strongly influenced by turbulent convection. The tachocline will possibly re-

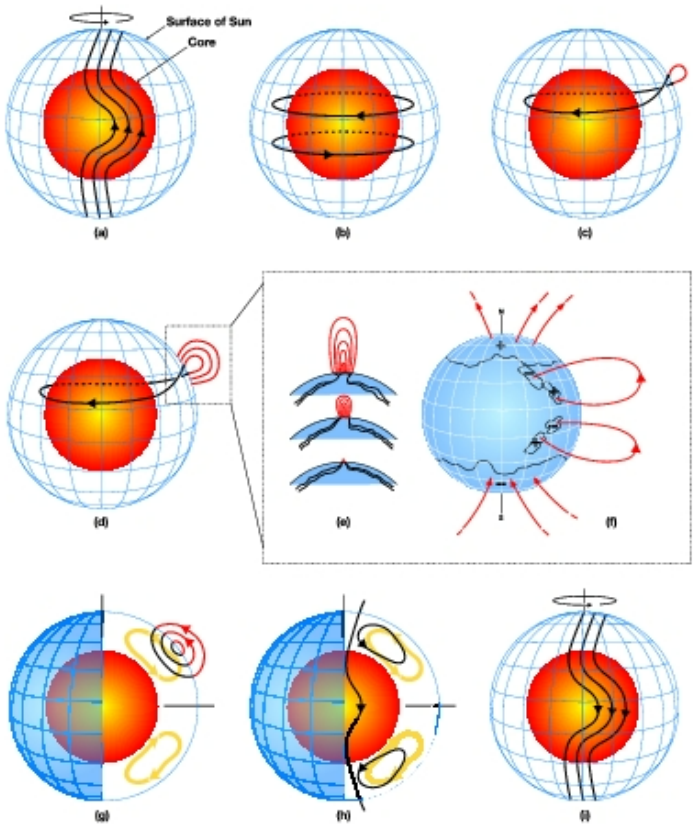

Figure 1.4: Representation of solar flux-transport dynamo. A poloidal magnetic field (vertical black lines) is sheared by differential rotation to produce a toroidal field (horizontal black lines). A strong toroidal field rises to the surface to produce magnetic loops which may be associated with sunspots (insert). Meridional flow (yellow lines) then re-creates the poloidal fields to complete the cycle. Figure from Gargaud & Irvine (2011).

main intact in thin convection zones, while distributed dynamos will be affected by changes in the convection zone properties where the time and length scales of the convective motions become shorter (Küker & Rüdiger, 2007). Walter (1983) suggests there are two possible reasons for a sharp onset of magnetic activity in late F-type stars. Firstly, there may be a "critical convection zone thickness" below which the amplification of the field is not strong enough to produce observable magnetic activity. Secondly, differential rotation may change at the onset of convection. However the distinction between rigid rotation occurring in hot stars and differential rotation in solar-type stars is less clear with studies showing rapid differential rotation is present in some A-type stars (Reiners & Royer, 2004; Balona & Abedigamba, 2016).

The finding of surface shear in A-type stars compliments the discovery of a weak magnetic field on the surface of the hot star Vega (A0) (Lignières et al., 2009) and the presence of starspots (Böhm et al., 2015). These findings indicate the distinctions between hot and cool stars are less clear than previously believed. An abrupt spindown of stars later than spectral type F5 due to angular momentum loss via the stellar wind, suggests the onset of dynamo-generated magnetic fields. On the other hand, an absence of rotation-activity relationship in these stars argues against solar-like dynamo. Which dynamo is operating in stars with thin convection zones has not been resolved.

1.5 Transition from Fossil to Dynamo Fields

The spectral type at which the transition from fossil to dynamo magnetic magnetic fields occurs has not been exactly defined, but is believed to occur somewhere from early-to-mid F-stars. The first suggestion of the location of the transition was made by Schatzman (1959, 1962) who pointed out the change from stars

with outer radiative zones to those with outer convection zones occurred in early F-stars. The transition was considered sharp around mid F-type by Kraft (1965) in a study of rotational velocities of stars in the Hyades and Coma clusters.

Theoretical considerations using mixing-length theory by Demarque & Roeder (1967), appeared to confirm Kraft's conclusion that the transition occurred around F4. In contrast to the suggestion that the transition is well-defined, Copeland et al. (1970) concluded that the transition varies according to the efficiency of convection in the outer atmosphere, where inefficient convection drives the transition towards later types. A magnetic basis for determining the transition was based on the appearance of hot chromospheres around spectral type G0 (Vaughan Jr & Zirin, 1968), however this appears to place to the spectral type much later than other methods.

A method for determining the transition from fossil to dynamo magnetic fields is to map the surface magnetic fields on a range of F-stars on either side of the suspected transition using tomographic techniques like Zeeman Doppler Imaging (ZDI) (see Section 1.8.2), and view the magnetic geometry at at least two epochs to see if there is any change in the field structure, which would indicate a dynamo field. No change in field structure between several epochs, potentially indicating a fossil field.

1.6 F-Type Stars

F-type stars are characterised by strong Ca II (H and K lines), which become stronger than the hydrogen lines of the Balmer series (Jaschek & Jaschek, 1990). There are $\approx$ 1300 F-type stars with V mag $\lesssim$ 6.5, listed in the Bright Star Catalog (Hoffleit, 1991) with 2 per cent chemically peculiar, 49 per cent dwarfs, and 49 per cent non-dwarfs (Jaschek & Jaschek, 1990). The number of binary

F-stars appears to be similar to other solar-type stars with approximately two thirds found in higher order systems (Fuhrmann & Chini, 2012, 2015). F-stars are slightly more massive than the Sun (1.23-1.73 $M_{\odot}$), have effective temperatures from 6040-7200 K, and luminosity varying from 1.6-7.2 $L_{\odot}$ (Table 1.6).

An interesting feature about F-type stars is they represent the hot limit for stars with significant potential for forming a habitable zone (Sato et al., 2014), and have stellar lifetimes of about 2-4 billion years, which is thought to be the minimum time required for advanced life to develop (Augustson et al., 2012). The estimated climatological habitable zone for F5 stars is located at 3 AU and for F8 stars at 2.5 AU (Sato et al., 2014). Two important criteria are necessary for a habitable planet; the planet should be located in a habitable zone, which provides Earth-like surface temperatures, and it should contain a magnetosphere large enough to shield the exoplanet from stellar winds (See et al., 2014). For planets with a strong magnetosphere, the stellar wind may be deflected away from the planet, however, a weak planetary magnetic field may allow increased atmospheric escape Egan et al. (2019).

Both thermal and non-thermal processes are involved with planetary atmospheric escape (Gronoff et al., 2020). Thermal escape Chassefière & Leblanc (2004); Selsis (2006); Linsky (2019) is one of the most important processes and is dependent on the upper atmospheric temperature, which in turn is affected by the host star's extreme ultraviolet and X ultraviolet flux. Non-thermal processes (Lammer et al., 2003a; Dong et al., 2018; Konatham et al., 2020) are thought to be more complicated and are affected by plasma interactions. Photochemical escape is the main non-thermal process (Gronoff et al., 2020) along with other processes which include ion loss and ionospheric outflow. The stripping of a non-magnetised planetary atmosphere has been investigated for by several authors; see for example the interaction between an exoplanet and young solar-type stars

(Lammer et al., 2003b), and M-type stars (Cohen et al., 2015). The wind Ram pressure is the dominant pressure in the habitable zone of solar-type stars (See et al., 2014) and this may be calculated using stellar wind models (Nicholson et al., 2016). See Section 1.9 for more on stellar wind modelling.

Early studies of F-type stars discovered important features which are related to the presence of magnetic fields. For example, a survey of rotational broadening of 112 F-stars concluded that appreciable rotation seems to disappear suddenly between F2 and F5 (Westgate, 1934), and that the early F-stars have a rotational frequency similar to the faster rotating A and B-stars. An early paper using mixing-length theory by Böhm-Vitense (1958) indicated that the onset of convection in the outer convection zone appears abruptly in F-type stars. The abrupt slow down in stellar rotation and the onset of convection has subsequently been shown to be associated with the presence of dynamo magnetic fields (see Section 1.4).

1.7 Detecting Stellar Magnetic Fields

"*Only a handful of freak stars have fields so strong as to produce a detectable signal. For all other stars there is no direct indication of magnetic fields,*" (Parker, 1979).

It was not long ago that the direct detection of stellar magnetic fields was rare, and the ability to measure relatively weak fields was beyond the reach of the available instruments. Since the first successful magnetic field detected in star other than the Sun (78 Vir, A2p) by Babcock (1947), increasingly sensitive techniques have been developed to study stellar magnetism. The following sections describe the physics of stellar magnetic field detection, and a brief summary of relevant papers which detected fields.

Table 1.1: Stellar parameters for F-type stars compared with the Sun. [1]Pecaut & Mamajek (2013). [2]Gray et al. (2003, 2006). [3]Calculated using mass-luminosity relationships from Eker et al. (2015),

Spectral Type	$T_{\rm eff}$ (K)[1]	Radius ($R_\odot$)[2]	Lum ($L_\odot$)[3]	Mass ($M_\odot$)[1]	B-V[1]
F0V	7200	1.73	7.2	1.61	0.294
F1V	7030	1.67	6.2	1.50	0.334
F2V	6810	1.59	5.1	1.46	0.374
F3V	6720	1.57	4.7	1.44	0.389
F4V	6640	1.52	4.2	1.38	0.412
F5V	6510	1.44	3.6	1.33	0.438
F6V	6340	1.39	2.7	1.25	0.484
F7V	6240	1.33	2.5	1.21	0.510
F8V	6150	1.28	2.0	1.18	0.530
F9V	6040	1.23	1.6	1.13	0.552
G2V (Sun)	5770	1.00	1.0	1.00	0.650

1.7.1 Zeeman Effect in Spectral Lines

The detection of magnetic fields in stellar atmospheres relies on the Zeeman effect (Zeeman, 1897), whereby spectral lines are split in the presence of a magnetic field (Fig. 1.5). The classical interpretation of the Zeeman effect (Condon & Shortley, 1951; Degl'Innocenti & Landolfi, 2004) follows the action of a magnetic field on a vibrating electron moving according to classical mechanics. In the classical approach, absorbing and emitting electrons can be considered linear oscillators (Lorentz, 1892; Unno, 1956) which can be resolved into three component oscillators (Haken et al., 2005). These consist of a linear oscillator which oscillates parallel to the direction of the magnetic field, and two oscillators which oscillate in opposite circular directions in a plane perpendicular to the magnetic field which produce the π-component and the σ-components, respectively (see Fig. 1.6).

A quantum mechanical description of the Zeeman effect (Herzberg & Spinks, 1944; Condon & Shortley, 1951; Schiff, 1955) describes an atom having a net magnetic moment which is the result of spin and orbital magnetic moments of optically active electrons. In an external magnetic field the magnetic moment has an orientational potential energy which is given by the following expression from (Eisberg, 1961).

$$\triangle E = \mu_H H \tag{1.8}$$

where μ_H is the component of μ in the direction of H. There are several possible values of μ_H which correspond to split energy levels. In the presence of an external magnetic field with a strength, energy levels are split into several components, where the magnitude of splitting for different levels is determined by the magnetic sensitivity (Landé factor g).

When viewed along the line of sight of the magnetic field, the spectral lines are split into two components, and when viewed transverse to the field a triplet of components are observed (Sobel'man et al., 1972). The magnitude of Zeeman splitting in a magnetic field is given by Stenflo (1971),

$$\triangle \lambda_h = 4.67 \times 10^{-13} \lambda^2 g H \tag{1.9}$$

where λ is the wavelength in Å, g is the Landé factor, and H is the magnetic field strength in G. The Landé factor is a measure of the wavelength separation of the centre of gravity of the split σ components of the line (Degl'Innocenti, 1982) with typical g values of about 1.2, but may vary from 0.0 to 3.0 (Landstreet, 1992). The magnetic splitting of spectral lines in a magnetic field depends upon the structure of the energy levels which corresponds to the line (Böhm-Vitense,

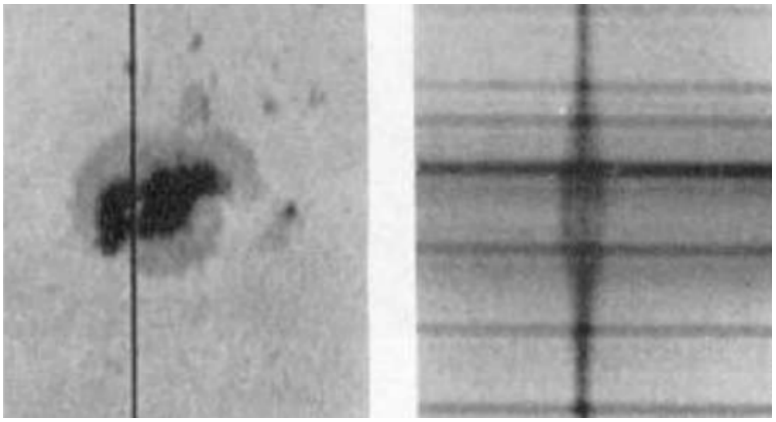

Figure 1.5: Example of the Zeeman effect in sunspots. The figure at left shows a sunspot with the location of a spectrograph slit marked with the vertical line. The figure at right shows splitting of the spectral line by the solar magnetic field, which consists of the undisplaced linearly polarised component in the direction of the field, and satellites which are oppositely circularly polarised perpendicular to the field. Figure from Stenflo (2017).

1989). Some lines will split more than given by Eq. 1.9, and some lines will not split at all. Examples of magnetically sensitive lines are Fe II 492.393 nm, Fe II 501.844 nm, Ca I 616.217 nm (Wade et al., 2000a) (see also Chapter 4).

A consequence of the Zeeman effect is that the resulting radiation is polarised, and this polarisation carries important information on the vectorial nature of the electromagnetic field (Clarke, 2010). The analysis of polarised radiation allows information about the geometry of a stellar magnetic field to be obtained which would not otherwise be able to be determined. Polarised radiation may be used to reconstruct surface magnetic maps of stars through inversion techniques like ZDI.

1.7.2 Stokes Parameters

A useful way to fully describe the polarisation state of radiation is by using Stokes parameters (Stokes, 1851) which are essentially intensities measured by

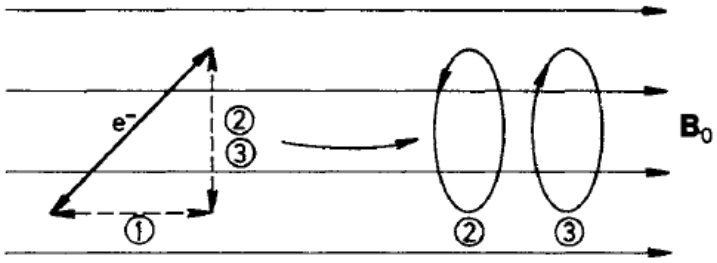

Figure 1.6: Classical explanation of the Zeeman effect. The radiating electron can be resolved into three component oscillators, a linear component (1) plus two components (2,3) which rotate in opposite circular directions in a plane perpendicular to the magnetic field, producing the π-component and the σ-components, respectively. Figure from Haken et al. (2005).

specific devices (Landi Degl'Innocenti & Landi Degl'Innocenti, 1981). The Stokes parameters form a four-dimensional mathematical vector which is represented by a 4x4 matrix. The advantage of a matrix representation is that a beam of polarised light that transverses a series of devices can be analysed by reducing the problem to a matrix calculation (Walker, 1954). Even though the Stokes parameters are represented in four dimensions, they have a physical reality, and are able to be observed.

Stokes parameters were first used to describe partially polarised light by Soleillet (1929) in a formulation of the radiative transfer equation, however it was not until a series of papers by Chandrasekhar (1946a,b, 1947) that the Stokes parameters were introduced to astrophysics. The Stokes parameters are designated by a variety of symbols in the literature but the widely used designations of I, V, U, Q were introduced by Chandrasekhar (1947) are used in this thesis.

The definition of the Stokes parameters as given in Shurcliff (1962) are as follows; Stokes I is the intensity of the unpolarised radiation, Stokes V is the intensity of right circularly polarized radiation minus intensity of left circularly polarized radiation. Right circularly polarized radiation is defined as the vector

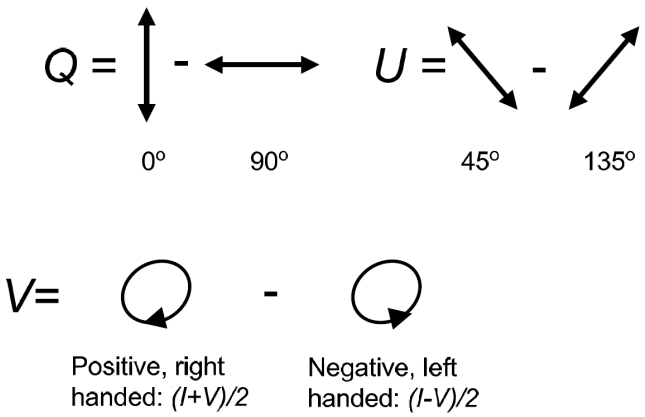

Figure 1.7: Geometrical visualization of the Stokes parameters. I is the radiation intensity, Q and U are linear polarisation, and V is circular polarisation. The observer is looking toward the source. Figure from Landi Degl'Innocenti et al. (2007).

associated with the radiation beam which is rotating clockwise by an observer looking toward the source, and left circularly polarised radiation rotates in an anticlockwise direction (Bagnulo et al., 2009). Stokes Q is the intensity of radiation with the vector oscillating towards the observer minus the intensity with electric field oscillating perpendicular to the line of sight. Stokes U is the intensity of radiation with the vector oscillating at 45 degrees with respect to the line of sight minus the intensity with the electric field oscillating at 135 degrees. A visualisation of the geometry of the Stokes parameters are shown in Fig. 1.7.

1.7.3 Magnetic Zeeman Signatures

Magnetic fields in stellar photospheres may produce circular and linear polarisation signals which are known as Zeeman signatures (Donati, 2001). Classic Zeeman signatures show a double peaked shape (see for example Fig. 1.8). For F-type stars with expected weak surface fields (Marsden et al., 2014), individual

profiles need to be added together to further increase the SNR so the signature becomes visible above the noisy individual profiles (see Section 1.7.5). Useful information about a stellar magnetic field may be obtained from the Zeeman signature. For example, a polarised signal which shows a complex shape with many zero crossings aligned with the line profile, indicates there are many areas of opposite polarity on the stellar surface (Donati, 2001).

Analysis of Stokes V profiles (Stenflo, 1985) may provide important information about the stellar magnetic field. The amplitudes of the Stokes V profile contains information on the magnetic flux, with stronger magnetic fields containing larger amplitudes. The amplitude is measured on one wing normalised on the Stokes V intensity of the continuum. The Stokes V width contains information on the intrinsic field strengths and non-thermal Doppler broadening. The Stokes V width is measured at the full width half maximum.

Asymmetry in the Stokes V profiles occurs when the amplitude or area of the blue and red wings differ. This asymmetry is caused by mass flows inside flux tubes where there is a shift in the Stokes V zero crossing position relative to the Stokes I which is mainly determined by the surrounding non-magnetic atmosphere Stenflo (1985). When a magnetic field is present on the stellar surface, many individual spectral lines may produce an associated Zeeman signature, resulting in a complexity in the profile, however when no magnetic signal is present the Stokes V profile remains relatively featureless (Silvester et al., 2009).

1.7.4 Longitudinal Magnetic Field

The longitudinal magnetic field (B_l) is a widely used measure of magnetic field strength in stellar astrophysics and has been in use for over 100 years (Seares, 1913). It is defined as the line of sight line-of-sight component of the magnetic

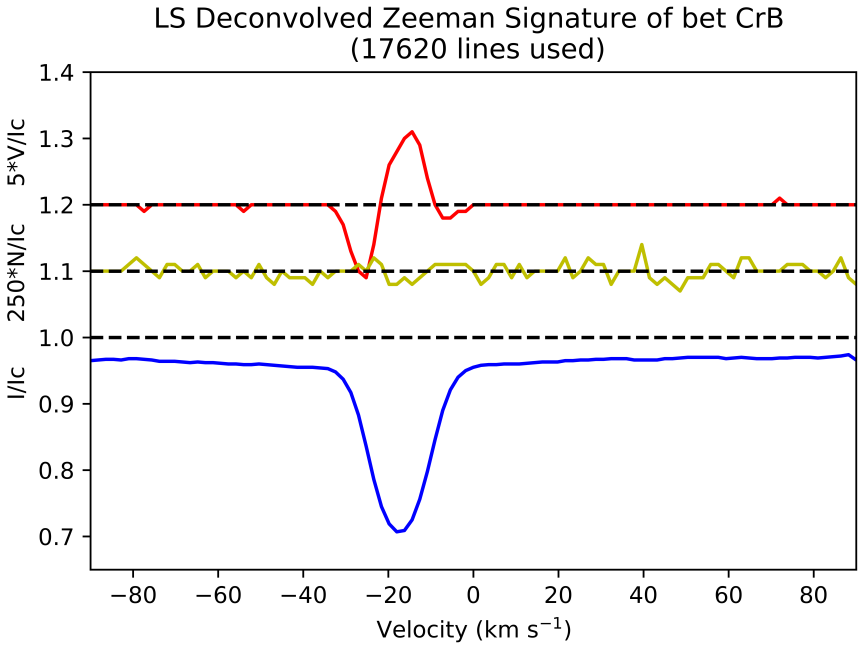

Figure 1.8: Example of an LSD profile (single spectra) for β CrB on 2017 April 13. The upper plot (red) shows the Stokes V profile (y-axis expanded and shifted up by 0.2 to allow better visibility). The magnetic Zeeman signature is visible in the Stokes V profile as a strong amplitude signal above and below the continuum line. The middle plot (yellow) shows the null profile (expanded and shifted up by 0.1). The lower plot (blue) shows the Stokes I profile. Figure from Seach et al. (2020).

field averaged over the visible hemisphere (Babcock, 1947; Schwarzschild, 1950; Mathys, 1989). According to Donati et al. (1997),

$$B_l = -2.14 \times 10^{11} \frac{\int vV(v)dv}{\lambda gc \int [I_c - I(v)]dv} \tag{1.10}$$

where B_l is the longitudinal magnetic field in gauss, λ is the mean wavelength of LSD profile in nm, g is the mean value of the Landé factors of all lines used to construct the LSD profile, c is the speed of light (in the same units as v) and I_c is the continuum level of the intensity profile. B_l is measured from the first-order moment of the Stokes V profile (Donati et al., 1997; Wade et al., 2000b), and as

a first approximation is proportional to the shift in wavelength between left and right circular polarization lines (Mathys, 1995).

The use of B_l is subject to several limitations (Gregory et al., 2010). Since B_l is averaged over the visible stellar hemisphere and therefore, the entire width of the line profile, it may suffer from cancellation effects where areas of opposite polarity cancel out resulting in a reduced magnetic field strength. This cancellation in B_l has its origin in the Stokes V signal where left and right circularly polarised components may suffer from cancellation effects. Since B_l is only sensitive to the components of the magnetic field which are not cancelled, a large part of the surface flux may be missed (Reiners & Basri, 2009). B_l is only measured at one particular point of the rotational phase therefore, it may vary as different magnetic features rotate into view.

1.7.5 Least Squares Deconvolution

The Zeeman signatures and B_l of F-type stars are expected to be weak, therefore using a mathematical technique called Least Squares Deconvolution (LSD) (Donati et al., 1997; Kochukhov et al., 2010) is useful to enhance the SNR of the spectral lines. LSD adds many line profiles together to give a single line with mean parameters. The technique was developed from earlier multiline techniques pioneered by Borra et al. (1981); Semel (1989); Carter et al. (1996); Semel & Li (1996).

There are four assumptions in LSD (Barnes et al., 2001); the shapes of lines are similar, the continuum and limb-darkening are constant with wavelength, line profiles are additive, and the magnetic fields are weak, i.e. the Zeeman splitting is small compared to intrinsic line width. The overall shape of the lines are considered to be similar and only differ in the amplitude of the line, called the

scaling factor (Mathys, 1999). These basic assumptions of LSD are considered robust for Stokes I and Stokes V analysis but are more questionable for Stokes U and Stokes Q (Kochukhov et al., 2010).

A reason LSD is valuable is the Zeeman signature of many stars are weak and may be lost in the noise, where the relative amplitudes may be about 0.1 per cent (Donati et al., 1992). For example, the magnetic field strengths of F-type stars in many cases are present at sub Gauss levels (Marsden et al., 2014; Seach et al., 2020), and therefore would not be able to be detected without the use of LSD to enhance the SNR of spectra. Another important benefit of LSD is its efficiency at all stellar rotation rates (Donati et al., 1997), therefore avoiding the problem of rotational broadening of spectral lines (Shapley & Nicholson, 1919; Westgate, 1934; Collins & Truax, 1995) which was previously an issue for tomographic mapping techniques. High stellar rotational velocities, which produce a broadening of spectral lines is more common in stars earlier than about mid F-type, due to the lack of wind braking effects which are present in stars with dynamo generated magnetic fields (Schatzman, 1962; Skumanich, 1972).

1.7.6 Chromospheric Emission

In addition to the direct measurement of stellar magnetic fields using B_l, there are a number of indirect measures which are useful in studies of cool star magnetism. The most widely used indirect measure of stellar magnetism is emission from the core of the Ca II H&K resonance lines formed in the chromosphere. The stellar chromosphere is an intermediate region of the outer atmosphere located between the photosphere and the corona (Hall, 2008).

Early work on stellar Ca II H&K line emission (Eberhard & Schwarzschild, 1913; Wilson & Bappu, 1957; Wilson, 1963, 1968) identified that Ca emission

occurrs in the middle of the absorption line, and proposed these emission lines could be used an indicator of magnetic activity. An early catalog of Ca emission from 445 stars by Joy & Wilson (1949) identified G, K, and M stars were more commonly found to show emission, compared to F-type and earlier stars.

Chromospheric emission is the result of two processes, a basal component that depends only on effective temperature and gravity, and a magnetically related component which depends on convection zone properties and rotation rates (Schrijver, 1987). In early F-stars, basal chromospheric flux may dominate, which makes chromospheric emission a less reliable indicator of magnetic activity. A second challenge for using the Ca emission in F-type stars, is that chromospheric emission may be less visible since the continuum flux can dominate the weak Ca emissions (Knutson et al., 2010). Despite these challenges, the measurement of chromospheric emission remains a valuable tool for cool star magnetic studies.

Work on stellar chromospheric emission was advanced with the publication of seminal papers on the S-index (Wilson, 1978; Vaughan et al., 1978; Duncan et al., 1991; Baliunas et al., 1995, 1998). The S-index is a dimensionless, stellar colour dependent quantity, which measures the ratio of flux in the Ca II H&K lines compared to two nearby continuum lines, as defined by Duncan et al. (1991),

$$S - \text{index} = \frac{\mathrm{aF_H} + \mathrm{bF_K}}{\mathrm{cF_{R_{HK}}} + \mathrm{dF_{V_{HK}}}} + \mathrm{e} \tag{1.11}$$

where F_H and F_K are the fluxes in the resonance lines from 20 Å-wide channels (with triangular profiles) centered at wavelengths, 396.8492 nm and 393.3682 nm respectively, compared to the flux at two bands in the continuum on the red and blue side of the H&K line. The coefficients (a,b,c,d,e) specific to ESPaDOnS and NARVAL spectropolarimeters used in this thesis are tabulated in Marsden et al. (2014). A benefit of using the S-index, is the values are independent of

the cancellation effects which are present in B_l measurements, and it provides a complimentary way to measure magnetic activity. Another benefit of S-index measurements are they can be used to determine activity cycles in solar-type stars, which are analogous to the 11 year Solar cycle. Further details on activity cycles are presented in the Section 1.7.7.

Besides the flux from Ca II H&K lines, the Hα spectral line (656.28 nm) is another indirect measure of stellar magnetic activity (Zarro, 1983b,a; Zarro & Rodgers, 1983; Herbig, 1985). The Hα-index is not as widely used as the S-index, and although it has been claimed that a strong correlation between these two indices exists, it is not clear if that is the case for all spectral types or levels of activity (Da Silva et al., 2011).

1.7.7 Stellar Activity Cycles

The large-scale magnetic field of the Sun and cool stars is known to be variable over time, and in many cases the variation is cyclic (Baliunas & Vaughan, 1985). Analysis of magnetic cycles may provide useful information on the nature of the stellar dynamo (Kleeorin et al., 1983) and dynamics of the outer atmosphere of stars. Chromospheric cycles refer to values determined from analysis of S-index measurements, while magnetic cycles are twice and long and are determined from analysis of magnetic field strengths.

As a consequence of the solar-stellar connection, a study of magnetism across a range of stars may provide information which helps to understand the variable nature of the Sun and it's affect on the Earth's environment. Knowledge of the cyclic variation in radiation output from a host star is increasingly important in exoplanet research (Perryman, 2018), where the star's magnetic field affects the space weather environment (Bothmer & Daglis, 2007), and exoplanet atmospheric

conditions (Hanslmeier, 2018; Linsky, 2019).

Chromospheric activity cycles in solar-type stars were first discovered by Wilson (1978) in the pioneering study on chromospheric emission in 91 main-sequence stars from spectral types F5-M2. Follow up observations of the Mt Wilson survey extended the observation period to 25 years (Baliunas et al., 1995) and showed magnetic activity cycles in a third of the stars (Baliunas et al., 1996). A large variety of stellar magnetic activity was observed, with young solar-type stars showing high activity with no maunder minimums, intermediate age stars (1-2 Gyr) having moderate activity and some smooth activity periods, and stars of similar age to the Sun showing the lowest activity levels and occasional Maunder minimums. The Mt Wilson survey found it difficult to determine chromospheric variability in F-type stars due to the weakness of emission and low contrast relative to the photospheric flux.

More recently, two large-scale chromospheric activity surveys of solar-type stars have been conducted. Boro Saikia et al. (2018a) compiled a catalogue of 4454 cool stars using the Mt Wilson survey, HARPS survey and VizieR catalogue sources. The survey identified 53 stars with well-defined chromospheric periods. The authors excluded cycle periods less than 2 yr since it was argued it becomes difficult to distinguish between the rotation period and the activity-cycle period. The only exception was HD 115043, (G1V) with a cycle of 1.6 yr which was considered to have a high probability of cycle detection.

Activity cycles in ι Horologii (G0V) have been discovered by several studies including a 1.6 year chromospheric cycle (Metcalfe et al., 2010), a 1.6 year cycle confirmed in both X-rays and chromospheric emission (Sanz-Forcada et al., 2013, 2019), and a discovery of two out-of-phase, periodic signals with chromospheric cycle periods of 1.97 yr and 1.41 yr (Alvarado-Gómez et al., 2018).

A survey of chromospheric activity by Da Silva et al. (2021) aimed to characterise chromospheric activity of 1674 FGK stars from the HARPS archive from 2013-2019. The survey found the proportion of active F dwarfs was 24 per cent, G-dwarfs 20 per cent, and K dwarfs 52 per cent. Only the Mount Wilson and HARPS surveys have multi-epoch observations suitable for a period search in large numbers of solar-type stars.

Using ZDI to measure magnetic fields over several epochs is a direct way to search for activity cycles in solar-type stars. Unlike the large-scale surveys of chromospheric emission, magnetic cycles using ZDI have been studied in smaller number of stars due to the time-intensive nature of the observations. Magnetic cycles have been identified in several F-type stars; including τ Bootis (Donati et al., 2008; Fares et al., 2009; Mengel et al., 2016; Jeffers et al., 2018); HD 49933. (García et al., 2010); HD 181420 (Barban et al., 2009), HD 17051 (Metcalfe et al., 2010), and HD 75332 (Brown et al., 2021). τ Bootis is the best studied example of an F-type star with magnetic cycles. It has been observed periodically since 2007 and shows a chromospheric cycle of 120 d and a magnetic cycle of 240 d (Jeffers et al., 2018). F-type stars are considered good targets for stellar dynamo studies because they are expected to show short cycles, and a larger frequency of variations compared to the Sun (Metcalfe et al., 2007; García et al., 2010; Salabert et al., 2011; Mathur et al., 2014). Some of the earlier studies of chromospheric emission in solar-type stars may have suffered from an observational bias, since only longer cycles similar to the Sun were expected, therefore shorter cycles may have been missed (Seach et al., 2022a).

1.7.8 Magnetic Fields in Solar-Type Stars

Prior to the 1980's hundreds of papers were written on stellar magnetism but magnetic fields in solar-type stars had not been directly measured. The presence of magnetic fields was inferred through indirect effects of magnetism which included; starspots (Kron, 1950; Chugainov, 1966, 1971; Hall, 1972), flares (Kunkel, 1970), chromospheres (Linsky, 1980), activity cycles (Wilson, 1978), and coronae (Warner, 1976; Vaiana & Rosner, 1978; Mewe, 1979).

The first detection of magnetic fields in solar-type stars was achieved by Robinson (1980) who extended a method based on Zeeman broadening of spectral lines first used by Preston (1971). The technique relies on the broadening of magnetically sensitive line profiles compared to less sensitive lines, and is able to determine both the field strength and coverage on the surface of the star (filling factor). The Zeeman broadening technique uses two lines with similar equivalent widths, central intensities, heights of formation, and temperature sensitivities, but having different magnetic sensitivities. Robinson detected magnetic fields in two stars, ξ Boo A (G8V) and 70 Oph A (K0V).

Using Zeeman broadening techniques on a sample of 18 F, G, and K dwarfs, Gray (1984) found magnetic detection in all stars from G6 and cooler, however failed to detect fields in any of the F-type stars ranging from F2V-F9V. Three of the F-stars which were not identified as magnetic, have subsequently been found to contain magnetic fields, σ Boo (F3V), χ Dra (F7V), β Vir (F9V), and are included in this thesis. Gray (1985) found a larger number of non detections in F and early G stars compared to later types. This was explained by the authors as being due to both the larger rotation and macroturbulence in the earlier stars, which increase the deterction threshold for Zeeman broadening.

Several limitations of the Robinson method have been discussed in reviews,

see for example Hartmann (1987); Linsky (1989); Saar (1990). These limitations include an incomplete treatment of radiative transfer (Gray, 1984), a lack of correction for line blends (Giampapa, 1984), and the method does not work in fast rotators where rotational broadening of spectral lines causes interference. Due to the problems with using Zeeman broadening to detect stellar magnetic fields, the Robinson method has largely been superseded by measurements using net circular polarisation which measures the longitudinal magnetic field (Section 1.7.4) and ZDI (Section 1.8.2).

A survey of cool star magnetism has been conducted by the BCool project (Marsden et al., 2014), which is an international collaboration, aiming to observe bright ($\lesssim$ mag 9.0) stars to further understand magnetic activity in solar-type stars. A BCool survey of 170 F-, G-, and K solar-type stars between 2006 and 2013 detected magnetic activity in 6/19 (32 per cent) F-type stars, 49/130 (38 per cent) G-type stars, and 12/21 (57 per cent) K-type stars (Marsden et al., 2014). The lower detection rate of magnetic activity in F-type stars compared to G and K-stars is consistent with the relationship that shows large-scale magnetic fields are inversely associated with stellar mass.

The BCool project has shown that with good to signal to noise ratio almost 100 per cent detection rate was achieved for F, G, and K-type stars having mean surface field strength of 5 G or greater. One of the aims of the BCool project is to produce surface magnetic maps of solar-type stars, which can be used to provide constraints for stellar dynamo models, and inputs into stellar wind models.

1.8 Mapping Stellar Surfaces

"*How far away from Earth are those remotest of the stars: they are beyond the reach of eye, or man's devices, or man's thought - William Gilbert, English physician 1600*" (Kragh, 2007).

The idea that stars could be resolved beyond points of light, and have their surfaces mapped, or their chemical composition analysed, was not considered possible until recently. The first map of a stellar surface, other than the Sun, was achieved by Deutsch (1958) who developed a method based on Fourier analysis of spectral line profiles, and radial velocity variations, to plot abundance irregularities and magnitude of the magnetic field on the surface of the AP star HD 125248. Further use of the Deutsch method were made by Pyper (1969) mapping the variable star α^2 CVn, Preston (1969) mapping 21 Persei (A2V), Rice (1970) mapping the α^2 CVn-type star HD 173650 (A1V), Falk & Wehlau (1974) refining the map of α^2 CVn, and Megessier (1975) producing a chemical abundance and magnetic map of the Ap star 108 Aqr (A0V).

A breakthrough in mapping stellar surfaces was achieved by Goncharskii et al. (1977) who suggested using a regularisation function to ensure uniqueness of the imaging solution. The paper proposed a mathematical solution to the inverse method of reconstructing a map from the inversion of spectral line profiles using a regularisation function (Tikhonov et al., 1977; Piskunov & Kochukhov, 2002). Other regularisation methods available for inversion of spectral lines include the Landweber iteration (Carroll et al., 2012) and the maximum entropy method which is used in this research (see Section 1.8.1). The Deutsch method produced some useful maps, however was limited by not using the full information in the spectral line (Rice et al., 1989), and has been superseded by the improved methods of Doppler Imaging (Section 1.8.1) and Zeeman Doppler Imaging (Section 1.8.2).

1.8.1 Doppler Imaging

The term Doppler Imaging (DI) was introduced by Vogt & Penrod (1983a,b) who improved the technique for mapping the stellar surface, in a study of starspots on the subgiant component of HR 1099 (K1 IV + G5V). The principle of DI operates by dividing the stellar surface into a series of surface elements, each with a limb-darkened, and Doppler shifted local intensity profile. The strips have a constant radial velocity and are parallel to the stellar axis of rotation. Conversely, a bright patch on the stellar surface will produces a bump in the local line profile. Importantly, there is a direct correlation between the position of a feature on the spectral line, and its corresponding position on the stellar surface.

When a cool (dark) spot, or a local enhancement of the concentration of a chemical element is present on the stellar surface, the local intensity spectrum shows a depression. As the bright or dark feature rotates across the stellar surface the depression or bump propagates across the spectral line (see Fig. 1.9). The disk-integrated line profile will show a bump for cool spots, or an absorption feature for an enhanced concentration of elements. The correlation between the location of a feature on the one-dimensional line profile and its position on the stellar surface allows a two-dimensional map of the stellar surface to be produced.

The inversion process of DI is an ill-posed problem (Kabanikhin, 2012), which means an infinite number of solutions are possible. However, by applying a regularisation function, like Tikhonov regularization (Tichonov et al., 1977), or maximum entropy method (MEM) (Hobson & Lasenby, 1998), additional constraints are imposed in order to find a unique solution. Regularization places additional constraints on the inverse operator. Mathematically this is achieved by finding a solution that minimises the sum of χ^2 of the data fit to observations and

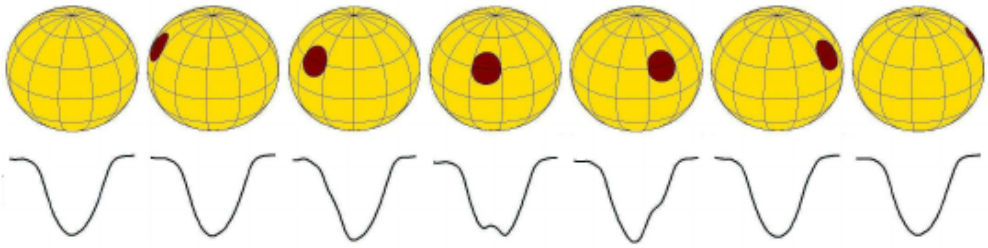

Figure 1.9: The principle of Doppler Imaging (DI) of a stellar surface from Kõvári & Weber (2004). An unspotted line profile produces a summed intensity profile which is equivalent to the rotationally broadened line. As a spot rotates into view it produces a bump on the depressed disc-integrated spectral line intensity profile. According to Vogt & Penrod (1983a) the bump does not represent a true emission, but rather a lack of line absorption. Using a time-series of intensity profiles DI is able to reconstruct a brightness map of the stellar surface.

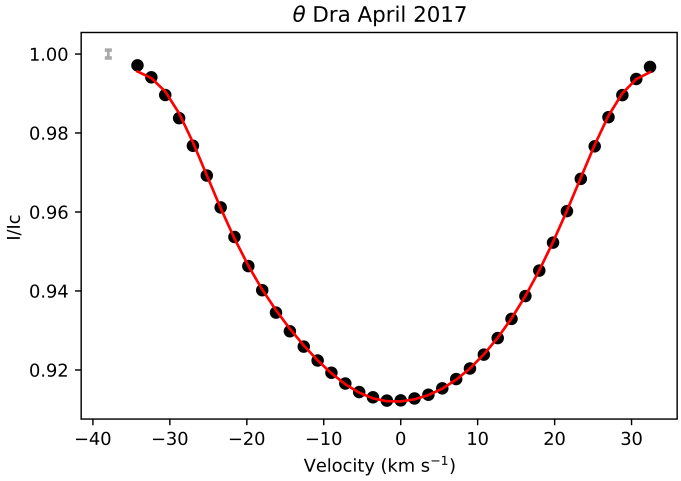

Figure 1.10: Example of a Doppler Imaging maximum entropy fit for θ Dra from a single observation in April 2017. The black circles represent the observed Stokes I signatures, while the red line represents the modelled lines. The 1-σ error bar is shown at left. The figure shows a close agreement between the model and observations, which indicates a reliable brightness map reconstruction. Figure adapted from Seach et al. (2022a)

.

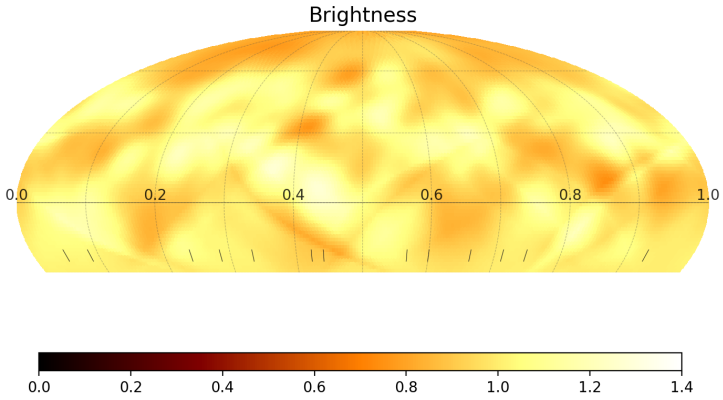

Figure 1.11: Example of a stellar brightness map for θ Dra in April 2017 produced using Doppler Imaging. The colour bar at bottom indicates the pixel brightness on a linear scale where a value of 1.0 represents the quiet photosphere, values less than one are cool spots and values greater than one are bright spots. Figure from Seach et al. (2022a)

regularization function (Kochukhov, 2016).

The maximum entropy method of regularization when applied to an ill-posed problem says that we should choose the solution with the maximum entropy. Introducing this criteria enables the "smoothest" or "simplest" image to be chosen which enables a unique solution to be achieved (Wu, 2012). The algorithm is a consistent way of selecting an image from many possible images, and a constraint is set up using a comparison of observations with a model of the data. The procedure is an iterative process due to the non-linear nature of the problem.

A important development in DI technique was achieved by Vogt et al. (1987) who combined DI with the maximum entropy regularisation method of Skilling & Bryan (1984). The technique involves finding the image with the greatest entropy (S) given by the expression from Vogt et al. (1987),

$$S = \sum_j p_j log(p_j) \tag{1.12}$$

where p_j is the surface brightness in this case of the jth pixel summed over all n pixels.

The process of DI proceeds by creating a theoretical intensity profile for the star, and iteratively adjusting stellar parameters and comparing the result with the observed profile. The parameters used to perform DI include inclination of the stellar rotational axis relative to the line of sight, the projected rotational velocity ($v\sin i$), stellar rotation period, and radial velocity. The closeness of fit between theoretical and observed profiles is quantified by both χ^2 statistics and the regularisation function. An example of the comparison of the modelled vs observed Stokes I is shown in Fig. 1.10, and an example of a brightness map produced by DI is shown in Fig. 1.11. In this research, DI is used to create a brightness map of a relatively fast rotator θ Dra, and to use the map as an input into the process for creating a magnetic map (see Section 1.8.2).

An early brightness map of a F-type star was produced for σ^2 CrB (F9V) by Strassmeier & Rice (2003) who showed the star contained a high latitude cool spot and an equatorial warm spot. The F8V star AF Lep was studied using DI by Marsden et al. (2006) who found a relatively small polar spot covering about 2 per cent of the stellar surface. DI of the F7V star HD 199143 was conducted by Garcia-Alvarez et al. (2011) using both maximum entropy and Tikhonov regularisation. The brightness maps using both regularisations produced similar results, and a remarkable increase in spot coverage was seen over a three week period. Similar to other fast rotating solar-type stars, the spot is located in a high latitude position.

The F8V star AF Lep was investigated by Järvinen et al. (2015) using DI. Similar to other solar-type stars, a cool spot was located near the pole, which showed a small evolution over four epochs between 2005-2010. Brightness maps for V1358 Ori (F9V) were produced in several papers using data from 2013 and

2017. There was no dark polar spot in data from 2013 by Hackman et al. (2016), however the 2013 data showed a polar spot when analysed by Kriskovics et al. (2019), and a polar spot also showed in 2017 data by Willamo et al. (2021).

HD 35296 (F8V) was imaged using DI by Willamo et al. (2021), and the brightness map from 2017 is unusual because it is a fast rotator which does not contain a cool polar spot, however there is a large spot at lower latitudes. The authors suggested one possibility for the lack of polar spot may be the low $v\sin i$ of 15.9 km s^{-1} which is close to the lower limit which will produce a reliable brightness map.

The literature is sparse with papers showing DI maps of F-type stars, and there are almost no other examples found in the literature in recent years. While DI maps of F-type stars are rare, magnetic maps using ZDI are more common (see Section 1.8.2). It might be concluded from the lack of papers, that F-type stars have been unfairly neglected in brightness and magnetic mapping studies.

1.8.2 Zeeman Doppler Imaging

Zeeman Doppler Imaging is the technique of Doppler Imaging which has been adapted for use with circular polarisation (Semel, 1989; Donati et al., 1989; Donati & Semel, 1990; Brown et al., 1991). The original use of ZDI by Semel (1989) relates to the detection of a magnetic signal using polarised spectra and the Doppler effect. The modern use of ZDI is for producing magnetic maps of the stellar surface, based on the inversion of Stokes profiles, ideally sampled over at least a full rotation period. ZDI is able to measure intensity, orientation and surface distribution of the magnetic field (Donati et al., 1989; Semel, 1989; Donati & Semel, 1990). ZDI also allows the energy of different field components to be calculated e.g. axisymmetric/non-axisymmetric, dipole/quadrupole/higher

multipoles, poloidal/toroidal, by expressing the field as a spherical harmonic expansion (see section 1.8.3). The technique of ZDI avoids the disadvantage of integrating over the whole disk (Donati et al., 1992) and mostly prevents regions of opposite polarity cancelling, however some ZDI cancellation may still occur in slower rotating stars (Lehmann et al., 2019). Rotational modulation of the Stokes V profiles is able to provide information on the orientation of the surface magnetic field. Fig. 1.12 shows the effects of a magnetic spot on the surface of a star, and the Stokes V profile corresponding to the radial, meridional and azimuthal magnetic field. An example of a ZDI map which is reconstructed from a series of Stokes V profiles is shown in Fig. 1.13.

An advantage of using ZDI as a stellar mapping technique is that it can distinguish between radial and azimuthal magnetic components, and for high latitude regions it can recover radial and meridional field subcomponents (Donati & Brown, 1997). Another benefit of ZDI is that knowledge of stellar atmospheric parameters is not as critical to the result as in conventional Doppler Imaging. Reconstruction of the spatial structure of the stellar magnetic field allows the type of dynamo to be determined, and can distinguish between interface dynamos (Deluca & Gilman, 1986, 1988; Parker, 1993; MacGregor & Charbonneau, 1997; Charbonneau & MacGregor, 1997) like the Sun, and distributed dynamos (Parker, 1955; Brandenburg et al., 1991; Moss et al., 1995; Lanza et al., 1998; Donati et al., 1999; Brandenburg, 2005) operating throughout the whole convection zone in some cool stars. For example, persistent large-scale azimuthal fields at high latitude, may indicate a non-solar type dynamo (Rüdiger & Elstner, 1994; Donati et al., 1999; Carter et al., 2014).

There are several limitations of ZDI (Gregory et al., 2010; Johnstone et al., 2010) which include some missing information in maps which is the result of stellar inclination, where part of a hemisphere is hidden from the observer. While stellar

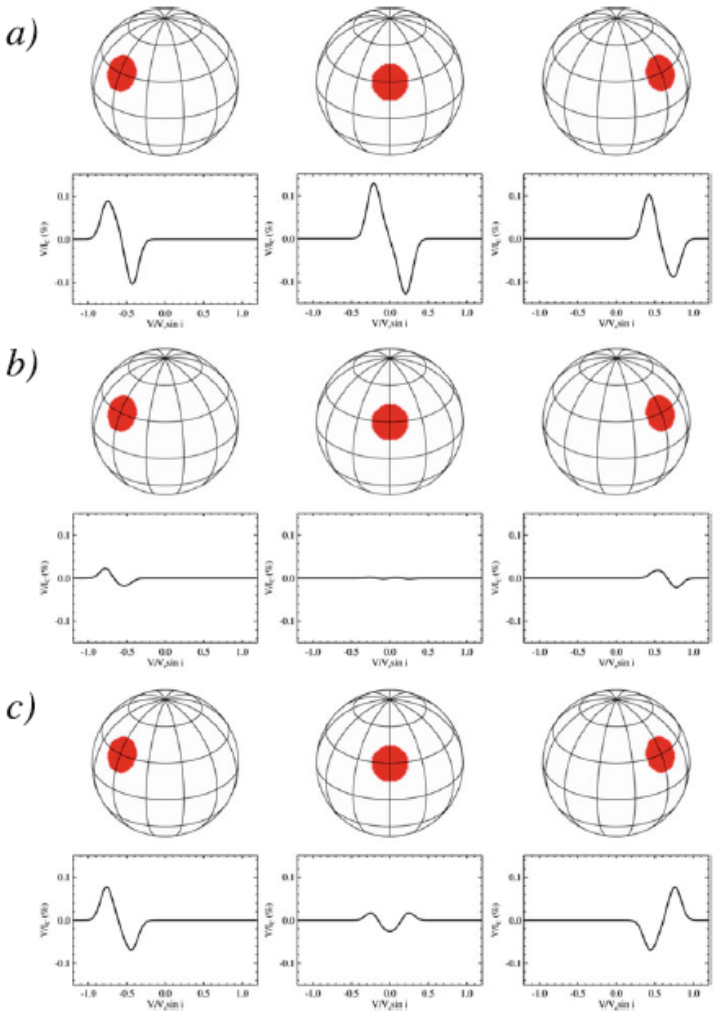

Figure 1.12: Zeeman signatures of magnetic spot on the surface of a star. (a) Stokes V profile corresponding to the radial magnetic field. (b) Stokes V profile corresponding to the meridional magnetic field. (c) Stokes V profile corresponding to the azimuthal magnetic field. The star is shown at three rotational phases separated by 0.125. Figure from Kochukhov (2016).

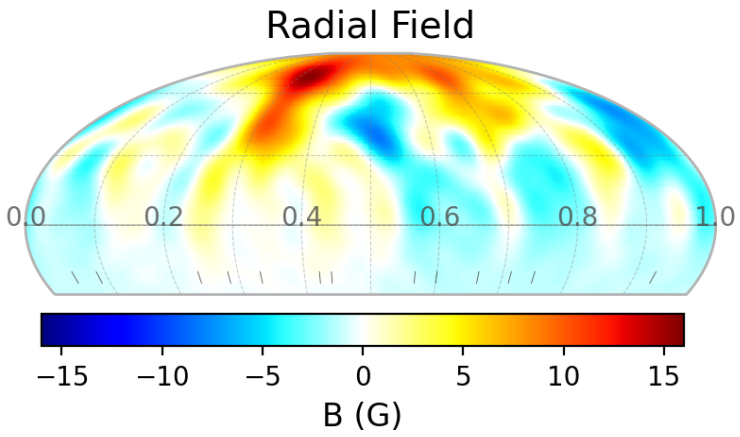

Figure 1.13: An example of a ZDI map showing the large-scale radial surface magnetic field for θ Dra (F8IV) from observation between 06-24 April 2017. Tick marks at bottom of figure represent phase of individual observations. The colour bar at bottom indicates the magnetic field strength in Gauss. Figure from (Seach et al., 2022a).

spectropolarimetric measurements are able to reconstruct the large-scale magnetic field, they do not map the small scale field regions, since small magnetic areas of opposite polarity cancel out. The Zeeman signal is suppressed in dark spots, however this problem can be partly overcome in fast rotators when a brightness image can be used an an input in the the ZDI code to adjust for the location of dark spots on the stellar surface. Despite some limitations, ZDI remains a powerful technique for reconstructing the surface magnetic field in both cool and hot stars (Kochukhov, 2016).

The study of F-type stars using ZDI began with the analysis of AF Lep (F8V) by Budding et al. (2002) with a magnetic analysis showing complex Zeeman signals which indicated a dynamo magnetic field was present on the star. The first surface magnetic map of AF Lep was made by (Marsden et al., 2006) who reconstructed the field at two epochs December 2001/January 2002, and September 2004. The dominant magnetic feature was a ring of positive azimuthal field at

the north pole with a mean magnetic field of $\sim$ 13 G. An azimuthal was not expected to be dominant at the surface of a dynamo field in a solar-type star, which is expected to be located at the tachocline at the base of the convection zone. The authors concluded this was possible evidence for a distributed dynamo which operates throughout the entire convection zone. AF Lep was further imaged by Marsden et al. (2009) with the surface map showing a polar ring of azimuthal field at three epochs.

Magnetic maps produced using ZDI were obtained for AF Lep (F8V) by Marsden et al. (2006), which showed the dominant azimuthal-field feature appearing as a ring of positive field around the pole. The presence of the azumuthal field was again interpreted as identifying a distributed dynamo operating throughout the entire convection zone, unlike the solar-type dynamo which is believed to be confined to a shear layer at the base of the convection zone.

The F7V star τ Boo has been the subject of several ZDI studies over the past 15 years. The first reconstructed surface magnetic field τ Boo was achieved by Catala et al. (2007) who found a weak surface magnetic field of about 2 G in June 2006. The surface magnetic topology was more complex than the Sun, although a limited phase coverage provided an incomplete magnetic map. A more in-depth study of τ Boo was conducted by Donati et al. (2008) with a magnetic map reconstructed using ZDI confirming a relatively complex magnetic field with a strength of up to 10 G from June 2007. The authors found a reversal of the magnetic field since 2006 which was the first magnetic polarity switch observed for a star other than the Sun. It was speculated that the magnetic polarity reversal may be shorter than the 11 year cycle of the Sun.

A second magnetic polarity reversal in two years for τ Boo was found by Fares et al. (2009) in a reconstruction of three magnetic maps for three epochs in 2008. Three new epochs of magnetic maps were produced from observations in

2009, 2010, and 2011 by Fares et al. (2013). The magnetic field strength for the three epochs ranged from 2.7 to 3.8 G, which was similar to previous reported values. An additional magnetic polarity reversal was observed in the star between January 2010 and January 2011. The topology of the surface magnetic field showed changes from 2009 and 2010 with an increase in the azimuthal field and a decrease in the radial field. Using data obtained for τ Boo between 2006-2008, Vidotto et al. (2012) presented magnetic maps which confirmed a radial field changing polarity between 2006-2007 and reverting back in 2008.

A continued evolution of τ Boo magnetic field was studied by Mengel et al. (2016) with observations at six epochs between 2011 and 2015. The analysis indicated a coupling between the magnetic and chromospheric cycles with reversals appearing to occur at or near the peak of every third chromospheric cycle. Using magnetograms from May 2009 to January 2015, Nicholson et al. (2016) modelled the stellar wind for τ Boo in an extensive monitoring of the wind behaviour. The results showed there was variability in the wind over six years, and that variations in the magnetic field created changes in the space weather environment, although the planetary magnetosphere can remain stable in size for all observed stellar cycle epochs. Jeffers et al. (2018) mapped the large-scale magnetic field geometry of τ Boo using ZDI at four epochs in 2016, and observed a significant evolution of the radial magnetic field, including a polarity reversal. An increased in magnetic field complexity was observed over a four month time-frame with magnetic energy from orders $\ell > 2$ increasing from 23 to 55 per cent.

Further ZDI maps for F-type stars have been obtained for HIP 71933 (F8V) (Waite et al., 2011), HD 179949 (F8V) (Fares et al., 2012), HD 35296 (F8V) (Waite et al., 2015; Willamo et al., 2021), and V1358 Ori (F8V) (Willamo et al., 2021). A larger number of magnetic maps for F-type stars need to be obtained to provide better constraints for dynamo and wind models. F-type stars are prime

targets for understanding how stellar magnetic activity begins at the onset of convection, and what type of dynamo operates in stars with a thin convection zone.

1.8.3 Spherical Harmonics

We describe the surface magnetic field in terms of vector spherical harmonics (Hansen, 1935; Hill, 1954; Jackson, 1962) and use the spherical harmonics decomposition outlined in Donati et al. (2006) to describe radial B_r, meridional B_θ, and azimuthal B_ϕ components as functions of colatitude θ and longitude ϕ,

$$B_r(\theta,\phi) = \sum_{\ell,m} \alpha_{\ell,m} Y_{\ell,m}(\theta,\phi) \tag{1.13}$$

$$B_\theta(\theta,\phi) = \sum_{\ell,m} \left[\beta_{\ell,m} Z_{\ell,m}(\theta,\phi) + \gamma_{\ell,m} X_{\ell,m}(\theta,\phi)\right] \tag{1.14}$$

$$B_\phi(\theta,\phi) = -\sum_{\ell,m} \left[\beta_{\ell,m} X_{\ell,m}(\theta,\phi) - \gamma_{\ell,m} Z_{\ell,m}(\theta,\phi)\right] \tag{1.15}$$

where,

$$Y_{\ell,m}(\theta,\phi) = c_{\ell,m} P_{\ell,m}(cos\,\theta)\, e^{im\phi} \tag{1.16}$$

$$Z_{\ell,m}(\theta,\phi) = \frac{c_{\ell,m}}{\ell+1} \frac{\partial P_{\ell,m}(cos\,\theta)}{\partial\theta} e^{im\phi} \tag{1.17}$$

$$X_{\ell,m}(\theta,\phi) = \frac{c_{\ell,m}}{\ell+1} \frac{P_{\ell,m}(cos\,\theta)}{sin\theta} im\, e^{im\phi} \tag{1.18}$$

$$c_{\ell,m} = \sqrt{\frac{2\ell+1}{4\pi}\frac{(\ell-m)!}{(\ell+m)!}} \tag{1.19}$$

where $\alpha_{\ell,m}, \beta_{\ell,m}, \gamma_{\ell,m}$ are the spherical harmonic coefficients, $c_{\ell,m}$ is a normalization constant, and $c_{\ell,m}P_{\ell,m}(cos\ \theta)$ is the associated Legendre polynomial of degree ℓ and order m. We use the convention where the radial field B_r points outward, the meridional field B_θ increases with colatitude from north to south, and azimuthal field B_ϕ increases with the direction of rotation with longitude.

The spherical harmonic coefficients represent the best model fit for the spectropolarimetric data. Using spherical harmonics to describe the surface magnetic field has the advantage of being able to represent a variety of spatial scales of magnetic topology (Kochukhov et al., 2014). The spherical harmonics expansion is paramaterised by the degree ℓ, which ranges from 1 to ℓ_{max}, with higher degrees allowing smaller scale magnetic features to be recovered. Limiting the maximum values of ℓ recovers only the large-scale magnetic field (Vidotto et al., 2018). The maximum spherical harmonic expansion is influenced by the stellar rotation period. Faster rotators enable a higher resolution map to be created and subsequently a higher degree of spherical harmonic decomposition may be used (i.e. $\ell = 15$). For solar-type stars with slower rotation, only large-scale magnetic features may be recovered, therefore a smaller degree decomposition is used (i.e. $\ell = 5$). The highest degree available for magnetic field reconstruction is given according to Morin et al. (2010),

$$\ell_{max} \simeq \max\left(\frac{2\pi\nu\sin i}{W}; \ell_{min}\right) \tag{1.20}$$

where W is the unpolarized local profile width in km s^{-1}, $v\sin i$ refers to the limit when the line broadening is mostly due to rotation, and ℓ_{min} is the minimum

resolution at the low $v\sin i$ limit, with ℓ_{min} ranging from about 4-8.

The advantage of using a spherical-harmonic expansion of the stellar surface magnetic field is that it can reconstruct both simple and complex magnetic geometries unlike previous methods, which could not reconstruct simple geometries like dipoles (Donati et al., 2006). This method also allows splitting of the field into poloidal field and toroidal components, which is useful for study of the stellar dynamo. Magnetic maps are produced to show the radial, azimuthal, and meridional field components of the large-scale photospheric field at each observing epoch. When multiple epochs are imaged the results can display the dynamic nature of the surface magnetic field.

1.8.4 Stellar Differential Rotation

Stars with an outer convection zone may show differential rotation (Gilman, 1980) which is present as a difference in rotation rate between the equator and the pole, or radial shear between the interior and the surface. For example on the Sun, the equator rotates 20 per cent faster than the higher latitude regions (Lang, 1992) and this differential rotation varies over time (Lamb, 2017). In stars other than the Sun, surface differential rotation ($d\Omega$) may also be present, and can be measured by several methods which includes, Fourier transform method (Huang, 1961; Bruning, 1981; Reiners & Schmitt, 2002; Reiners, 2007), time-series photometry (Hall, 1991), time-series chromospheric Ca II emission (Donahue et al., 1996), starspot tracking (Collier Cameron et al., 2002), and ZDI analysis using χ^2 minimisation (Petit et al., 2002). The amplitude of $d\Omega$ may be defined by a simplified solar-type law (Donati et al., 2000; Waite et al., 2015) where equatorial

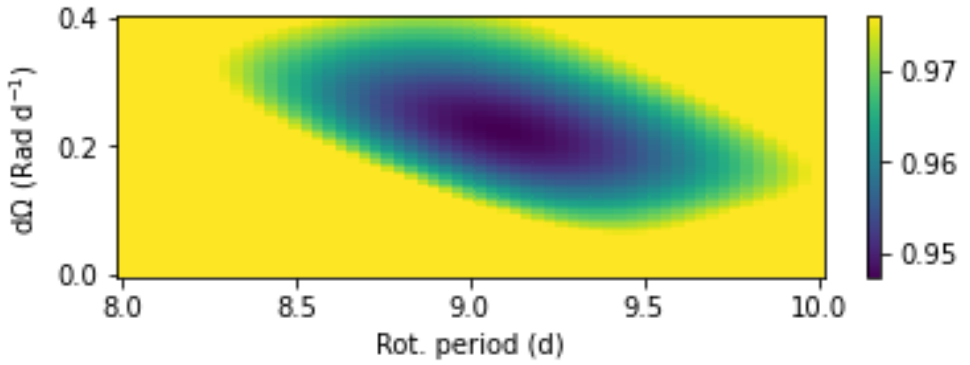

Figure 1.14: Example of determination of surface differential rotation (dΩ) and rotation period for β Vir from ZDI grid analysis using spectra from 3-24 April 2017. The bar at right shows the χ^2 values represented as a colour. The optimal parameters correspond to the minimum χ^2 of 0.95, which gives values in this epoch of dΩ =0.23 ± 0.09 rad d^{-1} and rotation period = 9.1 ± 0.4 d. Figure from current work by the author. Further details in Seach et al. (2022a).

regions have larger angular velocity than polar regions:

$$\Omega(l) = \Omega_{\rm eq} - {\rm d}\Omega \sin^2 l \tag{1.21}$$

where l denotes the latitude, $\Omega_{\rm eq}$ is the rotation rate at the equator, and dΩ is the rotational shear between the equator and the pole, the differential rotation, which we express in rad d^{-1}. An example of the determination of stellar dΩ is shown in Fig. 1.14.

Studying stellar dΩ is important because it is one of the key ingredients, for maintaining a magnetic field against ohmic dissipation (Bullard & Gellman, 1954; Parker, 1955). In mean-field dynamo theory (Steenbeck et al., 1966; Krause & Rädler, 1980; Rädler, 1980) the shearing of a magnetic field by differential rotation is assumed to occur either in the body of the convection zone (Stix, 1976, 1981; Parker, 1979; Cowling, 1981), in a layer at the base of the convection zone (Spiegel & Weiss, 1980; Galloway & Weiss, 1981), or at the top of the radiative zone

(Parker, 1975; Van Ballegooijen, 1982). Modelling dΩ in stars with a shallow outer convection zone by Gilman (1980) indicated that F-type stars may have different patterns of surface differential rotation compared with later spectral types, and Walter (1983) suggested there may be an abrupt change in differential rotation around spectral type F5, based on abrupt rotational spindown which occurs in F-stars.

Reiners & Schmitt (2003) searched for dΩ in a larger number of F and G-type stars and concluded that fast surface differential rotation (> 0.1 rad d^{-1}) was common in slow rotators ($v\sin i \lesssim 50$ km s^{-1}), and less common in faster rotators. Consistent with this trend, Waite et al. (2015) showed the young moderately rotating F8V star (HD 35296) contained high level of dΩ of 0.22 rad d^{-1}. A change in dΩ with spectral type was observed by Barnes et al. (2005) in a study of 10 stars from spectral type G2-M2. A trend was observed of increasing dΩ with increasing effective temperature. Models developed to recreate stellar dynamos using dΩ as an ingredient in G2 and K5 stars found faster rotation in the earlier type star (Kitchatinov & Rüdiger, 1999), and this trend of decreasing differential rotation with decreasing effective temperature was confirmed in several recent papers, see for example Reinhold et al. (2013); McQuillan et al. (2014); Reinhold & Gizon (2015). A study of τ Boo (F7V) by Mengel et al. (2016) revealed a range of surface differential rotation values ranging from 0.1-0.42 rad d^{-1} and the authors suggested an actual variation could not be ruled out. The F7V star HD 75332 was studied by Brown et al. (2021) who found a dΩ rate of 0.25 rad d^{-1} but a large uncertainty in the value was attributed to the low $v\sin i$ of 9.5 km s^{-1}.

Large-scale stellar surveys with high-cadence precision photometry by satellite missions, CoRoT (Auvergne et al., 2009), Kepler (Gilliland et al., 2010), and TESS (Ricker et al., 2014) have allowed constraints to be placed on stellar dΩ. Individual differential rotation values are harder to obtain from large-scale surveys

compared to higher precision techniques on individual stars as described above, however good statistical conclusions can be made from the data. The Kepler data (Reinhold & Gizon, 2015) showed $d\Omega$ was present in 12,300 out of a sample of 24,124 stars, with the magnitude of $d\Omega$ increasing with increasing effective temperature as previously predicted by Küker & Rüdiger (2011), and $d\Omega$ rate is almost independent of rotation period over a wide period range, but increases over shorter periods. This is in contrast to the findings of Hall (1991) who found increasing $d\Omega$ with decreasing rotation periods.

1.9 Winds of Solar-Type Stars

Stellar magnetic activity not only affects processes on the star's surface, it also has far-reaching effects into surrounding space via the stellar wind. The term solar and stellar wind was first introduced by Parker (1958, 1960), although their existence was known from earlier studies of Wolf-Rayet stars, which exhibit nova like wind properties in their spectrum (Wolf & Rayet, 1867). Stellar winds originate from open field lines of hot coronae (Wood et al., 2015), which are heated by the release of magnetic energy generated by dynamo action in the star's interior. Stellar winds are the emission of ionised particles flowing away in all directions at supersonic speeds from stars, and occur in continuous way rather than a catastrophic way like supernova explosions (Maciel, 2014). The wind particles consist of protons, electrons, and a few percent of alpha particles and heavy ions (Petrosyan et al., 2010), and have the properties of a turbulent, nearly incompressible, magnetofluid.

An understanding of stellar winds is important for several reasons. At a theoretical level, stellar winds are an ideal laboratory to study collisionless plasma phenomena, and hydromagnetic turbulence (Bruno & Carbone, 2016). Stellar

winds also provide a means for understanding the heliosphere, the hot bubble of plasma which surrounding stars, which is able to interact with planetary atmospheres, by compressing a planet's magnetosphere, leading to erosion of the upper atmosphere via non-thermal escape of hydrogen ions (Johnstone et al., 2015), In this way, stellar winds are an important ingredient in the developing field of space weather and the habitability of exoplanets.

Early observations of the space weather hazard to Earth began with the discovery of the Van Allen belts (Van Allen et al., 1958) which is a zone of solar energetic particles captured by the Earth's magnetosphere. Measurements from the Luna spacecraft and Mariner 2 led to the confirmation of the existence of the solar wind (Hundhausen, 1968; Parker, 2001).

Numerical simulation of the solar corona as the source of the solar wind was investigated by the pioneering work of Pneuman & Kopp (1971). Early models used empirical source terms (Usmanov, 1993; McKenzie et al., 1997; Mikić et al., 1999; Suess et al., 1999; Wu et al., 1999; Groth et al., 2000), while in more realistic models solar wind heating and acceleration was caused by an interaction between Alfvén turbulence and solar plasma (Jacques, 1977; Barnes, 1992; Usmanov et al., 2000; Usmanov & Goldstein, 2003). A revised model for the solar wind was developed by Cohen et al. (2006) who managed to succeed in reproducing the mass flux from Sun to Earth.

The first 3-dimensional magnetohydrodynamic models of the solar wind were developed in the 1980's (Leboeuf et al., 1981; Wu et al., 1981; Brecht et al., 1981, 1982). Since then many global MHD models of the magnetosphere have been developed (Ogino & Walker, 1984; Lyon et al., 1986; Watanabe & Sato, 1990; Winglee, 1994; Tanaka, 1995; Raeder et al., 1995; White et al., 1998).

A widely used solar and stellar wind modelling framework is the Block-

Adaptive-Tree-Solarwind-Roe-Upwind-Scheme (BATS-R-US) code (Powell et al., 1999; Tóth et al., 2012) developed by Centre for Space Environment Modeling (CSEM) at University of Michigan, which has developed into a useful space physics modeling tool. The code aims to provide a complete single numerical solution of the solar wind from subsonic to supersonic regions, by solving eight magnetohydrodynamic equations in a finite volume. The BATS-R-US code provides a self-consistent magnetohydrodynamic model which aims to produce a single solar wind solution. This contrasts with other models which look at transonic and supersonic plasma flow regions separately. Using the BATS-R-US magnetohydrodynamic regime, two approaches have been developed; a thermally-driven polytropic wind (Cohen et al., 2011; Vidotto et al., 2012, 2015) and Alfvén wave turbulence dissipation (Cohen et al., 2014). This latter approach has been further developed using realistic stellar parameters from the stars HD 1237 (G8), HD 147513 (G5) and HD 22049 (K2) were developed (Alvarado-Gómez et al., 2016a,b).

Early wind models of solar-type stars focused on winds driven by the high gas pressure in the corona (Mestel, 1968; Mestel & Spruit, 1987; Tout & Pringle, 1992), with the coronal heating believed to originate from convective motions of the outer atmosphere. Further developments involved magnetohydrodynamic modelling which included the region from the photosphere to the corona (Suzuki & Inutsuka, 2005, 2006; Matsumoto & Suzuki, 2012). The advantage of this method is that it includes the photosphere which is the source of much observational information (Fujimura & Tsuneta, 2009; Matsumoto & Kitai, 2010). Using ZDI as an input to wind models early attempts to were made to constrain the stellar winds of young active solar type stars and T-tauri stars Johnstone et al. (2013); Vidotto (2014).

Wind monitoring of τ Boötis (F7IV-V) between 2009 and 2015 was carried

out by Nicholson et al. (2016), using an input of the surface radial magnetic field obtained from ZDI. The use of observed radial magnetic fields was used as an input to the wind modelling (see for example; Jiang et al. (2011); Schüssler & Baumann (2006)) since non-potential field components have a negligible effect on wind solutions (Jardine et al., 2013). The surface magnetic flux of τ Bootis was observed to vary between epochs and this was reflected in changes in stellar wind. The mass loss rate showed a small variation of 4 per cent over the eight epochs, which averaged 100 times the solar mass rate. There was a variation of 140 per cent in the angular momentum loss rate and a calculated spin-down time-scale, which agreed with predictions (Gallet & Bouvier, 2013).

Stellar wind models of solar-type stars by Cohen & Drake (2014) indicated that mass loss rates depended on magnetic field strength, where the magnetic field affects the wind density, which can be considered the pressure required to overcome the confining magnetic field. For solar-type stars the models were consistent with the stellar spin down law of Skumanich (1972) although the authors noted applicability to the solar case required more complex models.

Recent stellar wind models for five young solar-type stars in the Hyades cluster were determined by Evensberget et al. (2021) who determined mass-loss rates, angular momentum loss and wind pressure over a range of magnetic field strength values for young solar-type stars. For the open magnetic flux and the mass-loss values were attributed to shape and complexity of the magnetic field. The authors suggested that wind mass-loss of young solar-type stars may be dominated by transient phenomena like coronal mass ejections rather than more steady wind loss. Further wind-modelling of a sample of ten young solar-type stars by Evensberget et al. (2022) found the dipolar magnetic field component obtained from ZDI dominates the wind angular momentum loss, as long as the wind mass-loss does not exceed a certain threshold value.

The properties of stellar winds of F-type stars and their link with magnetic activity is poorly understood. The study of F-star winds is important for providing constraints on the exoplanet environment at the hot end of habitability. F-stars are the hottest stars which can reasonably be expected to provide conditions for exobiology to develop, due to their relatively short lifetimes as small as one billion years (Maeder & Meynet, 1988; Sato et al., 2014).

1.10 Research Questions

F-type stars are chosen for this research because magnetic studies have been lacking compared to other spectral types, and magnetic features in stars with shallow outer convection zones requires further investigation. In this thesis two questions are addressed:

QUESTION 1. WHAT CHANGES OCCUR, IF ANY IN THE STRENGTH AND DETECTABILITY OF THE MAGNETIC FIELDS OF F-TYPE STARS ACROSS SPECTRAL TYPES FROM F0-F9?

This question is addressed in Chapter 2 of this thesis and is covered in the publication Seach et al. (2020) which is a magnetic snapshot survey of 53 F-type stars ranging from spectral types F0 to F9 plus 2 chemically peculiar stars β CrB, and δ Cap. The longitudinal magnetic field is measured for the stars at a single epoch and compared with stellar parameters. Additionally we provide some constraints on the location of the transition between fossil and dynamo magnetic fields.

QUESTION 2. HOW DOES THE SURFACE MAGNETIC TOPOLOGY DIFFER BETWEEN EARLY AND LATE F-TYPE STARS?

This question is addressed in chapters 3 and 4 of this thesis. In Chapter 3 and Seach et al. (2022a) surface magnetic maps for θ Dra (F8IV) and β Vir (F9V) are compared and contrasted at multiple epochs. In Chapter 4 and Seach et al. (2022b) surface magnetic fields are mapped for the chemically peculiar hot star β CrB, and the early star σ Boo (F3V) which contains a very thin outer convection zone thickness less than 3 per cent of the stellar radius. The two stars are compared and contrasted, and discussed in the context of the two late F-stars which are discussed in Chapter 2.

CHAPTER 2

PAPER 1: A MAGNETIC SNAPSHOT SURVEY OF F-TYPE STARS

Published in the Monthly Notices of the Royal Astronomical Society, 2020, Volume 494, pp. 5682–5703 (Seach et al., 2020).

2.1 Introduction to Paper

The study of magnetic fields in F-type stars begins with a survey of 55 stars which span a range of temperatures where the transition from fossil to dynamo magnetic fields is expected to occur. The aim of the first paper is to search for the presence of a magnetic field in the sample by measuring the longitudinal magnetic field (B_l) and to look for correlations with stellar parameters.

Target stars for the paper are studied as part of the BCool project, which is an international collaboration of scientists studying the magnetic activity of

low-mass stars. The 55 stellar targets consist of 25 stars chosen as part of the transition project ranging from spectral type F2-F9, and 30 stars from the BRITEpol project (Neiner & Lèbre, 2014) with 28 stars ranging from spectral type F0-F9, plus the chemically peculiar stars β CrB and δ Cap. Targets are chosen to be bright enough ($\leq$ mag 5) to enable a high signal-to-noise ratio (SNR) to be achieved with a reasonable exposure time.

Photospheric magnetic fields are detected in 14 stars (12 definite detections, 2 marginal detections) covering all spectral classes from F3V-F9V. There are two binary stars with a detection, but since we couldn't separate the magnetic detection, it was not able to be determined if the magnetic field was located on the F-star component. There is no evidence of magnetic fields in 13 stars with spectral types F0 to F2. The hottest F-star with a definite magnetic detection is σ Boo (F3V), with an outer convection zone thickness less than few per cent of the stellar radius. The surface magnetic fields of many of the F-stars are weak, as was expected, with 6 of 14 stars having $B_l < 1.0$ G. There is a positive correlation between Stokes V amplitude and B_l, while no correlation is found between B_l and $T_{\rm eff}$, B_l and $v\sin i$, or B_l and age.

2.2 Published Paper

The published paper Seach et al. (2020), "A Magnetic Snapshot Survey of F-type Stars" follows.

Monthly Notices of the ROYAL ASTRONOMICAL SOCIETY

MNRAS **494,** 5682–5703 (2020) doi:10.1093/mnras/staa1107
Advance Access publication 2020 April 24

A magnetic snapshot survey of F-type stars

J. M. Seach,[1]★ S. C. Marsden,[1] B. D. Carter,[1] C. Neiner,[2] C. P. Folsom,[3] M. W. Mengel,[1] M. E. Oksala[2,4] and B. Buysschaert[2,5]

[1]*University of Southern Queensland, Centre for Astrophysics, Toowoomba 4350, Australia*
[2]*LESIA, Paris Observatory, PSL University, CNRS, Sorbonne University, Université de Paris, 5 place Jules Janssen, F-92195 Meudon, France*
[3]*IRAP, Université Toulouse, CNRS, CNES, UPS, F-31400 Toulouse, France*
[4]*Department of Physics, California Lutheran University, 60 West Olsen Road # 3700, Thousand Oaks, CA 91360, USA*
[5]*Instituut voor Sterrenkunde, KU Leuven, Celestijnenlaan 200D, B-3001 Leuven, Belgium*

Accepted 2020 April 20. Received 2020 April 18; in original form 2019 November 20

ABSTRACT

We present a spectropolarimetric magnetic snapshot survey of 55 stars which includes 53 F-type stars ranging from spectral types F0 to F9 plus 2 chemically peculiar stars β CrB, and δ Cap. We look for magnetic fields in stars spanning a range of effective temperatures where the transition from fossil to dynamo magnetic fields is believed to occur. High-resolution spectropolarimetry using circularly polarized spectra is used to look for a magnetic detection in the Stokes V profile, determine the mean longitudinal magnetic field (B_l), and to look for correlations with stellar parameters. Surface magnetic fields are detected on 14 F-stars, and present in every spectral class from F3V-F9V ranging in strength from 0.3 ± 0.1 G (36 UMa, F8V) to 8.3 ± 0.9 G (h Dra, F8V). Thus we find photospheric magnetic fields are present in stars as early as spectral type F3V with an outer convection zone thickness less than a few per cent of the stellar radius.

Key words: stars: early-type – stars: late-type – stars: magnetic field.

1 INTRODUCTION

Magnetic fields are present almost everywhere in the Universe and span 26 orders of magnitude from the extragalactic medium 10^{-9} G (Dolag et al. 2010) to the interior of magnetars 10^{17} G (Beskin et al. 2016). The Sun was first shown to be magnetic by Hale (1908) who identified the existence of a strong magnetic field in sunspots. The second magnetic star (78 Vir, A2p) was not discovered for another 40 yr, with the pioneering paper by Babcock (1947) who developed a technique for measuring stellar magnetic fields using circular polarization. Recent advances in spectropolarimetry enabled by the high resolution instruments ESPaDOnS (CFHT, Hawaii) (Donati 2003; Donati et al. 2006a), and NARVAL (Pic du Midi Observatory, France) (Aurière 2003) have enabled sub-Gauss stellar magnetic fields to be detected for the first time (Lignières et al. 2009). This has opened up new opportunities for understanding the nature of stellar magnetic fields across a range of masses, as shown for example by the MiMeS survey of hot stars (Wade et al. 2016) and the BCool survey of solar-type stars (Marsden et al. 2014).

F-type stars occupy an interesting region on the Hertzsprung-Russell diagram where important changes occur in the stellar atmosphere. They occupy a 'sweet spot' (Mizusawa et al. 2012) spanning a region where warm stars with negligible outer convection zones and fossil magnetic fields, transition to cool stars with deepening outer convection zones and dynamo magnetic fields. Fossil magnetic fields (Cowling 1945; Spitzer 1958; Mestel 1967; Neiner et al. 2015; Braithwaite & Spruit 2017) may originate from several different sources including primordial fields retained from the molecular cloud from which the stars were formed (Mestel & Spitzer 1956; Mestel 1966), from pre-main sequence dynamos (Moss 2001), or stellar mergers (Shultz et al. 2019). These fossil fields decay over a time-scale of the order of the lifetime of the star (Cowling 1945) and are frozen (Schussler 1975) into the atmosphere. Fossil magnetic fields are only detected in up to 10 per cent of hot stars (Grunhut et al. 2017; Sikora et al. 2018), and their strengths peak at 34 kG (Babcock 1960). In contrast, cool stars host dynamo generated magnetic fields (Moffatt 1978; Parker 1979; Krause & Radler 1980; Zeldovich, Ruzmaikin & Sokolov 1983; Roberts & Soward 1992; Brandenburg & Subramanian 2005; Mestel 2012) which show complex and dynamic structures.

The location of the transition between fossil and dynamo magnetic fields is believed to occur somewhere from early-to-mid F-stars, based on activity-rotation relationships (Wilson 1966), stellar wind breaking (Schatzman 1962; Kraft 1967; Skumanich 1972; Böhm-Vitense & Dettmann 1980), coronal X-ray emission (Schmitt et al. 1985), and mixing-length theory (Demarque & Roeder 1967; Baschek & Reimers 1969). Studying the transition from fossil to dynamo magnetic fields in F-stars is important for understanding the nature of the stellar dynamo, and dynamics of the outer atmospheres

★ E-mail: john.seach@usq.edu.au

of stars. The photospheric magnetic field is also an important input parameter for models of stellar winds surrounding F-stars, which affects the heliospheric magnetic field (Owens & Forsyth 2013) in the environment at the hot end of habitability for exoplanets (Sato et al. 2014).

The aim of this paper is to use high-resolution spectropolarimetry of a sample ranging from early-to-late F-type stars to determine the strength of the longitudinal magnetic field (B_l), and look for correlations with stellar parameters. This provides an insight into the nature of magnetism in stars with thin outer convection zones.

2 OBSERVATIONS

2.1 Target selection

Our 55 targets (Table 1) consist of 25 stars chosen as part of our transition project ranging from spectral type F2-F9, and 30 stars from the BRITEpol project (Neiner et al. 2017a) with 28 stars ranging from spectral type F0-F9, plus the chemically peculiar stars β CrB (Han et al. 2018) and δ Cap (Gray et al. 2006). δ Cap is classified as an Am star (Trilling et al. 2007) and these stars are expected to show only weak or non-existent magnetic fields (Conti 1970; Trust et al. 2020). The BRITEpol stars helped expand our sample mainly for early F-stars. Targets are chosen to be bright enough ($\leq$ mag 5) to enable a high signal-to-noise ratio (SNR) to be achieved with a reasonable exposure time. The sample was also limited by time allocated at the telescope and weather conditions. Table 2 shows our sample of 53 F-stars (excluding two chemically peculiar stars β CrB and δ Cap) consists of 27 per cent of the F-stars $\leq$ mag 5 from the Bright Star Catalogue (Hoffleit 1991). The proportion of our F-stars stars in each spectral type ranges from 12 to 56 per cent, indicating good coverage from each spectral class. A journal of observations for our stars are shown in Table 3. Further details for the individual transition project stars are found in Appendix A. Background information on the 30 BRITEpol stars used in this paper can be found in Marsden et al. (in preparation).

2.2 Spectropolarimetry

Observations of our 55 stars were obtained with both Stokes *I* (unpolarized) and Stokes *V* (circular polarized) light using the 3.6 m Canada-France-Hawaii Telescope (CFHT; Mauna Kea, Hawaii, with ESPaDOnS spectropolarimeter), the 2.0 m Télescope Bernard Lyot, (TBL, Observatoire du Pic du Midi, France, with NARVAL spectropolarimeter), and 3.6 m European Southern Observatory telescope (La Silla Observatory, Chile, using HARPSpol polarimetric mode of the HARPS spectrograph).

The ESPaDOnS (Aurière 2003) and NARVAL (Donati et al. 2006a) spectropolarimeters are almost identical instruments. They consist of a cross-dispersed, bench mounted, echelle spectrograph and a Cassegrain unit. Both NARVAL and ESPaDOnS have a spectrograph wavelength coverage in a single exposure from 370–1050 nm with small gaps at 922.4–923.4 nm, 960.8–963.6 nm, and 1002.6–1007.4 nm. The full spectrum spans 40 grating orders from #22 in the red to #61 in the blue, with a resolving power of $\approx$ 68 000 when using the spectropolarimetric mode. The Cassegrain module consists of the polarimeter, calibration unit and guiding camera, and has a 1.6 arcsec aperture.

The HARPSpol spectropolarimeter (Snik et al. 2008; Piskunov et al. 2011) is a bench-mounted spectrograph, fibre fed from the Cassegrain unit which contains the polarimetric optics. The wavelength coverage is from 380–690 nm with gaps between 526 and 534 nm, and a resolving power of $\approx$ 110 000. The spectra are recorded on two 2k $\times$ 4k EEV CCD's, with the full spectrum spanning 71 orders with 45 on the blue CCD and 26 on the red CCD.

2.3 Extraction of spectra

The extraction and calibration of polarized spectra from ESPaDOnS and NARVAL were completed automatically using the libre-ESpRIT software package based on an algorithm by Donati et al. (1997). The HARPSpol data were reduced using the REDUCE package (Piskunov & Valenti 2002; Makaganiuk et al. 2011). The output of libre-ESpRIT and REDUCE are intensity spectra (Stokes *I*), circular polarization (Stokes *V*), and null (*N*) polarization spectra. One stellar observation consists of four sub-exposures which are combined to produce the Stokes *I*, combined constructively to produce the Stokes *V* spectrum, and combined destructively to give the null spectrum where the Zeeman signature cancels out, leaving only non-magnetic effects in the profile (Semel, Donati & Rees 1993; Donati et al. 1997; Bagnulo et al. 2012). This acts as a check to ensure spurious signatures have not contaminated the circular polarization spectra.

3 DATA ANALYSIS

3.1 Least-Squares Deconvolution (LSD)

The magnetic fields of F-stars are expected to be weak (Marsden et al. 2014), and difficult to detect above background noise. Our data analysis involves combining the contribution of many spectral lines to give a mean line with higher SNR which improves the sensitivity of magnetic field detection (Semel 1989; Semel & Li 1996). We use the line addition technique of Least Squares Deconvolution (LSD) (Donati et al. 1997, 2006b) to improve the ability to detect a magnetic signal. LSD combines thousands of spectral lines into a single line with mean parameters. The method is based on the assumption that the circular polarization line profiles across different wavelengths correspond to a common basic Zeeman signature (Semel et al. 2009). The LSD profiles are generated from line masks which are created using the Vienna Atomic Line Database (VALD3) (Ryabchikova et al. 2015). Effective temperature, surface gravity, and metallicity are used as inputs and lines are chosen with a depth greater than or equal to 10 per cent of the continuum. The line mask which best matches each star are from Marsden et al. (2014). The sampling size for LSD output velocity bins are chosen as 1.8 km s^{-1}.

The number of lines used in the LSD calculation varies from 6192 to 18879 (Table 4). A larger number of lines are used for spectra obtained with NARVAL, which accounts for most of our hotter stars. This may have been due to overlap with the orders on NARVAL, with many lines being counted twice. The weighting of spectral lines are adjusted as in Marsden et al. (2014) to produce a mean weight of the Stokes *I* and *V* LSD profiles close to unity. The normalization parameters from Marsden et al. (2014) are used, varying every 250 K up to a maximum of 6500 K and extrapolated for temperatures above this. Extrapolation of the normalization parameters for our hotter stars is considered reasonable since the values only changed a small amount with increasing effective temperature. In addition to combining multiple lines to produce a LSD profile, we also co-added individual LSD profiles from a single night to give a mean value with even higher sensitivity. The SNR of our mean LSD profiles shown in (Table 4) are generally higher (by a factor of 2–3 times)

Table 1. Stellar parameters for our 55 stars.

Target	HIP	Spectral Type	$T_{\rm eff}$ (K)	Age (Gyr)	$v\sin i$ (km s^{-1})	Refs[2] (s,t,a,v)
F-star definite detections						
β CrB	75695	*	7980 ± 180	0.6 ± 0.3	13.7 ± 6.1	*, 5, 5, 3
σ Boo	71284	F3V	6720 ± 144	1.6 ± 0.3	9.7 ± 2.3	16, 1, 2, 3
ϵ Lib	75379	F4V+K5-M2	6405 ± 187	2.0 ± 0.1	9.5 ± 0.7	17, 1, 2, 3
ϵ Cet	12390	F5V+F6V	6537 ± 129[1]	2.4 ± 0.5	10.8 ± 5.5[1]	17, 1, 2, 3
α Com	64241	F5V+F6V	6433 ± 325[1]	2.9 ± 0.1	20.0 ± 6.1[1]	17, 5, 2, 3
χ Dra	89937	F7V+K1V	6150 ± 57	5.2 ± 0.6	5.1 ± 2.9	17, 9, 2, 3
h Dra	82860	F8V+M1V	6271 ± 80	2.3 ± 0.9	10.0 ± 0.5	17, 1, 2, 3
36 UMa	51459	F8V+K7	6183 ± 118	0.5 ± 1.4	6.0 ± 4.0	17, 1, 2, 3
17 Crt	56280	F8V+F8V	6157 ± 42[1]	2.8 ± 0.2	8.7 ± 0.5[1]	17, 1, 2, 3
γ CrA B	93825	F8V	6188 ± 80[1]	3.2 ± 1.1	8.4 ± 4.0[1]	17, 2, 2, 3
ω Dra B	86201	F8V	5900	2.1 ± 0.4	12.8 ± 2.8[1]	15, 15, 2, 3
θ Dra	78527	F8IV+M2	6105 ± 271	2.1 ± 0.2	28.1 ± 0.9	18, 1, 2, 3
β Vir	57757	F9V	6083 ± 58	3.1 ± 0.8	6.1 ± 2.6	17, 10, 2, 3
F-star marginal detections						
τ PsA	109422	F6V	6352 ± 36	0.6 ± 0.3	12.8 ± 0.8	17, 1, 2, 3
γ Ser	78072	F6V	6291 ± 50	3.1 ± 0.4	10.0 ± 0.7	17, 6, 2, 3
F-star non-detections						
δ Cap	107556	kA5hF0mF2III	7395 ± 251	2.8 ± 0.0	90.0 ± 2.4	22, 5, 12, 3
α Hyi	9236	F0IV	7377 ± 251	0.8 ± 0.4	135.3 ± 19.8	17, 5, 5, 3
h UMa	46733	F0IV+K5	7101 ± 241	1.5 ± 0.1	144.0 ± 2.9	17, 5, 2, 3
γ Cap	106985	F0III	7167 ± 206	1.5 ± 0.0	31.0 ± 10.0	19, 7, 11, 3
δ Ser	76276	F0IV+F0IV	6954 ± 371[1]	1.0 ± 0.0	88.0 ± 10.0[1]	16, 1, 11, 3
α Crv	59199	F1V	6722 ± 440	0.2 ± 0.6	24.9 ± 0.9	17, 1, 2, 3
β TrA	77952	F1V	7458 ± 254	0.9 ± 0.5	82.3 ± 6.1	17, 5, 5, 3
δ Aql	95501	F1IV-V	7216 ± 245	1.5 ± 0.0	85.1 ± 5.4	17, 5, 11, 3
ω Dra A	86201	F2V	6500	2.1 ± 0.4	12.8 ± 2.8[1]	15, 15, 2, 3
υ UMa	48319	F2IV+M	6738 ± 306	1.3 ± 0.0	105.7 ± 4.2	16, 1, 11, 3
δ Gem	35550	F2IV-V+K3	6300 ± 248	1.9 ± 0.1	121.7 ± 6.2	3, 1, 2, 3
τ Cyg	104887	F2IV+G0V	6772 ± 230	1.8 ± 0.0	88.4 ± 13.5	17, 5, 13, 3
η Lep	28103	F2V	6560 ± 311	1.8 ± 0.2	16.2 ± 1.1	17, 1, 2, 3
ι Leo	55642	F3V+G3V	6536 ± 415	1.5 ± 0.1	14.5 ± 2.1	17, 1, 2, 3
10 UMa	44248	F3V+G5V	6538 ± 222[1]	1.7 ± 0.5	21.4 ± 1.3[1]	17, 5, 2, 3
ψ Vel	46651	F3V+F0IV	7122 ± 242[1]	1.5 ± 0.1	260.0[1]	17, 5, 2, 3
γ Tuc	114996	F3IV/V	6561 ± 148	1.8 ± 0.2	84.8 ± 6.2	20, 1, 2, 3
γ Cet	12706	F4V+A2Vn	6982 ± 329[1]	0.6 ± 0.1	10.0[1]	17, 1, 8, 3
σ Cet	11783	F4IV+K5	6393 ± 53	2.5 ± 0.1	8.4 ± 5.5	3, 1, 2, 3
58 Oph	86736	F5V+G5	6351 ± 81	2.1 ± 0.6	12.8 ± 1.3	17, 1, 2, 3
β Del	101769	F5IV+F5IV	6485 ± 67[1]	1.5 ± 0.0	47.0 ± 4.8[1]	17, 1, 13, 3
ψ Gem	32362	F5IV-V	6510 ± 221	1.6 ± 0.1	68.3 ± 6.2	17, 5, 2, 3
α CMi	37279	F5IV-V+DQZ	6652 ± 226	1.7 ± 0.4	5.2 ± 2.1	17, 5, 2, 3
ι Peg	109176	F5V+G8V	6265 ± 380	1.7 ± 0.5	7.9 ± 2.5	17, 1, 2, 3
ψ Peg	112447	F6V+M1	6282 ± 238	3.2 ± 0.4	8.1 ± 1.0	17, 1, 2, 3
μ Cyg	107310	F6V+G2V	6406 ± 138	2.7 ± 0.3	7.3 ± 3.3	17, 1, 2, 3
α For	14879	F6V+G7V	6208 ± 248	3.2 ± 1.2	7.8 ± 4.3	17, 1, 2, 3
γ Lep	27072	F6V+K2	6333 ± 28	1.0 ± 1.1	9.9 ± 3.0	17, 2, 2, 3
θ UMa	46853	F6IV+M	6374 ± 50	2.3 ± 0.2	7.8 ± 1.6	3, 6, 2, 3
ι Psc	116771	F7V+M5	6186 ± 174	3.2 ± 0.2	6.6 ± 1.4	17, 1, 2, 3
σ02 UMa	45038	F7IV-V+K6	6315 ± 103	2.6 ± 0.3	7.3 ± 1.9	21, 1, 2, 3
δ Equ	104858	F7V+G0V	6283 ± 395[1]	3.0 ± 0.2	6.1 ± 1.1[1]	17, 1, 2, 3
γ Del	102531	F7V+K1 IV	6450 ± 91	2.1 ± 0.2	8.7 ± 4.5	3, 6, 2, 3
6 Cet	910	F8V	6258 ± 90	3.9 ± 1.1	5.8 ± 2.3	17, 1, 2, 3
ζ Cnc	40167	F8V+G0V	6191 ± 85[1]	2.6 ± 0.2	2.8 ± 0.5[1]	17, 2, 2, 3
γ CrA A	93825	F8V	6188 ± 80[1]	3.2 ± 1.1	8.4 ± 4.0[1]	17, 2, 2, 3
HD 84117	47592	F9V	6168 ± 283	2.6 ± 0.7	5.7 ± 0.5	17, 1, 2, 3
η Cas	3821	F9V+K5-M0	5801 ± 132	2.9 ± 7.2	3.9 ± 2.6	17, 14, 2, 3
Definite detections, but uncertain which component						
κ Peg	107354	F5IV+G0V	6581 ± 224[1]	1.3 ± 0.1	19.9 ± 9.3[1]	3, 5, 2, 3
20 Oph	82369	F6IV+>G2	6295 ± 66[1]	1.6 ± 0.3	10.3 ± 1.4[1]	22, 1, 2, 3

Notes. Parameters refer to the F-star component, unless marked with superscript[1] where the value is a combined value from binary components.

References: 1: Gaia collaboration (2018), 2: Casagrande et al. (2011), 3: Glebocki & Gnacinski (2005), 4: Anderson & Francis (2012), 5: David & Hillenbrand (2015), 6: Aguilera-Gómez, Ramírez & Chanamé (2018), 7: McDonald, Zijlstra & Watson (2017), 8: Gullikson, Kraus & Dodson-Robinson (2016), 9: Torres, Andersen & Giménez (2010), 10: Jofre et al. (2018), 11: Gontcharov (2012), 12: Vican (2012), 13: Marsakov & Shevelev (1995), 14: Prieto & Lambert (1999), 15: Konacki et al. (2010), 16: Samus et al. (2017), 17: Wenger et al. (2000), 18: Slovak & Barnes (2002), 19: Chen, Liu & Shan (2017), 20: Wright et al. (2003), 21: Edwards (1976), 22: Gray et al. (2006).

[2]The order of references in column 7 corresponds to spectral type (s), $T_{\rm eff}$ (t), age (a) and $v\sin i$ (v).

*No spectral type assigned to β CrB.

Table 2. Comparison of the 53 F-stars in our sample with the ≤ mag 5 F-stars from Bright Star Catalogue (Hoffleit 1991). Table does not include β CrB and δ Cap with no assigned spectral type.

Spectral Type	No. of F-stars in our sample	No. F-stars in BSC ≤ mag 5	Per cent sampled
F0	4	33	12
F1	3	6	50
F2	5	32	16
F3	5	14	36
F4	3	10	30
F5	8	29	28
F6	8	28	29
F7	5	13	38
F8	9	16	56
F9	3	12	25
Total	53	193	27

for the 25 transition project stars observed with CFHT compared to the 30 BRITEpol stars. The SNR of the mean Stokes V profiles are determined by propagating the formal error bars associated with each spectral pixel through the deconvolution (Wade et al. 2000). The time between the first and last exposure on each night typically covers less than 5 per cent of the star's estimated rotation period, thus minimising smearing of the magnetic field. The stellar rotation period is estimated using literature values of projected rotational velocity ($v \sin i$), stellar radius, and assuming an inclination of 60 degrees. LSD profiles for 15 stars with a magnetic detection are shown in Appendix B.

3.2 Longitudinal magnetic field (B_l)

The mean longitudinal magnetic field (B_l) is defined as the line of sight component of the magnetic field, averaged over the visible stellar disc (Babcock 1947; Schwarzschild 1950). According to Donati et al. (1997),

$$B_l = -2.14 \times 10^{11} \frac{\int v V(v) \mathrm{d}v}{\lambda g c \int [I_c - I(v)] \mathrm{d}v}, \quad (1)$$

where B_l is the longitudinal magnetic field in gauss, λ is the mean wavelength of LSD profile in nm, g is the mean value of the Landé factors of all lines used to construct the LSD profile, c is the speed of light (in the same units as v), and I_c is the continuum level of the intensity profile. B_l is measured from the first-order moment of the Stokes V LSD profile (Donati et al. 1997; Wade et al. 2000), and as a first approximation is proportional to the shift in wavelength between left and right circular polarization lines (Mathys 1995). The mean wavelength and Landé factors are the same as normalization parameters discussed in 3.1. The error in B_l is calculated by propagating the uncertainties in the reduction pipeline through equation (1).

B_l is a widely used measure of stellar magnetic fields in both hot (Wade et al. 2016) and cool stars (Marsden et al. 2014), although its use is subject to several limitations. Since B_l is averaged over the visible stellar hemisphere and therefore, the entire width of the line profile, it may give a null result due to cancellation effects where areas of opposite polarity cancel out, even if a magnetic field is present in individual LSD velocity bins. B_l is a measure of the large-scale magnetic field and therefore not sensitive to small-scale fields, which means that a large part of the surface flux may be missed (Reiners & Basri 2009). Our snapshot survey determines B_l at one particular point of the rotational phase. Therefore, our determined B_l is the maximum field strength at the time of observation, and may be different if measured at another rotational phase.

3.3 Magnetic field detection

A second method for determining the presence of a magnetic field on the surface of stars is the False Alarm Probability (FAP), which is a statistical criteria used to determine if a star has either a magnetic signature in the Stokes V or a spurious signal in the Null profile (Donati, Semel & Rees 1992; Donati et al. 1997). The technique uses chi-square (χ^2) statistics which are computed inside and outside the spectral line using the probability function of Abramowitz & Stegun (1964), which is then converted into a detection probability. χ^2 statistics are used outside stellar lines to check any magnetic detection is stellar in origin, and not from spurious sources which may show as a detection outside the lines. The χ^2 probability function according to Donati et al. (1992) is used to give the probability of the circularly polarized data deviating from a zero magnetic field. A magnetic signal is considered unambiguously detected if the FAP is smaller than 10^{-5}, a marginal detection if FAP between 10^{-3} and 10^{-5}, and no detection if FAP is greater than 10^{-3}. A magnetic detection requires no detection of signal outside the spectral line nor in the null profile.

Integration limits for determination of the FAP were estimated visually from the LSD Stokes I profile, centred on the line core and covering the full profile up to the continuum on the red and blue wings. The integration limits were chosen to be wide enough to include information in the Stokes V profile, but narrow enough to minimize noise from outside the profile. An analysis by Wade et al. (2000) showed that even though integration limits are somewhat subjective, the FAP is relatively insensitive to small variations. Determination of FAP was done for both the Stokes V and null profiles.

A detection of signal in the Stokes V can be the result of true polarization caused by a photospheric magnetic field, or a spurious signal caused by instrumental or other effects. The stellar origin of the polarization signal is confirmed by checking the signal is located only in the Stokes V profile and not located in the Null profile, and that the signal is located within the line velocity range (Donati et al. 1997). FAP for our stars are listed in Table 4.

3.4 Spectral line analysis

3.4.1 Radial velocity

The stellar radial velocity (Lindegren & Dravins 2003) is the line of sight component of a star's motion and is a basic stellar parameter. The radial velocity of our stars (Table 5) are computed by using the centre of gravity (COG) method (Uitenbroek 2003). The radial velocities derived in this work are compared to literature values of Buccino & Mauas (2008), Anderson & Francis (2012), and are used as an input into the S-index calculation (Section 3.5), and as a reference for analysing line asymmetries in the Stokes I profiles (Section 3.4.2). Radial velocities for our stars are calculated from the mean and standard deviation from individual measurements on the night of maximum B_l determination. The radial velocity precision of ESPaDOnS is about 15 m s^{-1} within a single run and 30 m s^{-1} from run to run (Moutou et al. 2007), where a run comprises observations over several consecutive nights. The radial velocity precision of NARVAL is 18 m s^{-1} and HARPS 0.7 m s^{-1} (Soubiran et al. 2018).

Table 3. Journal of observations for our 55 stars showing dates corresponding to maximum B_l determination.

Target Star	Instrument	HJD Range 2450000+	Date YMD	UT HMS	T_{exp} (s)	SNR Range (Stokes *I*)
F-star definite detections						
β CrB	NARVAL	7867.579	2017-04-23	01:42:18	4 × 150	968
σ Boo	ESPaDOnS	7768.051–7768.158	2017-01-14	13:15:45–15:50:15	4 × 139	648–727
ϵ Lib	ESPaDOnS	7826.005–7826.149	2017-03-13	12:02:24–15:29:10	4 × 113	666–706
ϵ Cet	ESPaDOnS	7652.916–7653.174	2016-09-21	09:53:06–16:05:07	4 × 199	629–737
α Com	ESPaDOnS	7800.910–7801.083	2017-02-16	09:45:45–13:55:44	4 × 120	757–849
χ Dra	NARVAL	7136.582	2015-04-24	01:54:01	4 × 120	780
h Dra	ESPaDOnS	7882.876–7883.028	2017-05-09	08:59:56–12:39:36	4 × 194	645–716
36 UMa	ESPaDOnS	7767.055–7767.166	2017-01-13	13:16:37–15:57:38	4 × 180	690–704
17 Crt	ESPaDOnS	7817.859–7818.043	2017-03-05	08:28:37–12:52:52	4 × 209	600–680
γ CrA B	ESPaDOnS	7910.958–7911.022	2017-06-06	10:54:23–12:25:43	4 × 101	553–617
ω Dra B	ESPaDOnS	7878.921–7879.070	2017-05-05	10: 05:44–13:40:13	4 × 189	761–785
θ Dra	NARVAL	7889.433–7889.504	2017-05-15	22:09:39–23:51:32	4 × 320	726–1018
β Vir	NARVAL	7855.453–7855.466	2017-04-11	22:39:39, 22:54:36	4 × 223	894–1024
F-star marginal detections						
τ PsA	ESPaDOnS	7676.742–7676.925	2016-10-15	05:46:08–10:08:44	4 × 204	740–849
γ Ser	NARVAL	6893.329–6893.344	2014-08-23	19:43:51–20:06:05	4 × 269	488–491
F-star non-detections						
δ Cap	NARVAL	6950.367–6950.396	2014-10-19	20:40:22–21:21:21	4 × 103	348–420
α Hyi	HARPSpol	6969.641–6969.677	2014-11-08	03:16:44–04:07:51	4 × 120	885–891
h UMa	NARVAL	6643.622	2013-12-17	02:41:11	4 × 234	378
γ Cap	NARVAL	6912.404	2014-09-11	21:30:08	4 × 95	338
δ Ser	NARVAL	6764.633–6764.661	2014-04-17	02:54:42–03:35:05	4 × 239	353–357
α Crv	ESPaDOnS	6694.089–6694.132	2014-02-05	14:00:41–15:03:43	4 × 50	513–524
β TrA	HARPSpol	7481.744–7481.7573	2016-04-03	05:44:21–06:02:53	4 × 106	944–955
δ Aql	NARVAL	6811.623–6811.635	2014-06-03	02:43:02–03:00:12	4 × 194	353–358
ω Dra A	ESPaDOnS	7878.921–7879.070	2017-05-05	10: 05:44–13:40:13	4 × 189	761–785
υ UMa	NARVAL	6764.376–6764.406	2014-04-16	20:50:24–21:33:35	4 × 260	352–361
δ Gem	NARVAL	7134.325–7134.372	2015-04-21	19:41:44–20:49:56	4 × 190	347–361
τ Cyg	NARVAL	6816.586–6816.615	2014-06-08	01:53:00–02:34:52	4 × 250	392–396
η Lep	NARVAL	7327.718	2015-11-01	05:00:03	4 × 95	330
ι Leo	NARVAL	7800.534–7800.598	2017-02-16	00:29:31–02:02:09	4 × 286	498–506
10 UMa	ESPaDOnS	7745.011–7745.144	2016-12-22	12:11:25–15:23:12	4 × 105	797–827
ψ Vel	ESPaDOnS	6699.918–6699.954	2014-02-11	09:54:15–10:46:28	4 × 60	629–653
γ Tuc	HARPSpol	7235.793–7235.817	2015-08-01	06:48:46–07:23:02	4 × 224	1313–1317
γ Cet	NARVAL	6947.567–6947.642	2014-10-17	01:19:27–03:08:24	4 × 208	314–316
σ Cet	ESPaDOnS	7651.995–7652.055	2016-09-20	11:47:04–13:13:55	4 × 179	734–747
58 Oph	ESPaDOnS	7885.916–7886.040	2017-05-12	09:51:35–12:51:03	4 × 200	693–742
β Del	NARVAL	6786.650	2014-05-09	03:31:36	4 × 103	483
ψ Gem	NARVAL	6744.324–6744.345	2014-03-27	19:38:06–20:08:54	4 × 167	497–509
α CMi	NARVAL	7339.723	2015-11-13	05:16:21	4 × 10	1031
ι Peg	NARVAL	7623.528	2016-08-23	00:24:14	4 × 258	864
ψ Peg	ESPaDOnS	7615.860–7615.920	2016-08-15	08:30:08–09:55:56	4 × 105	715–732
μ Cyg	ESPaDOnS	7612.920–7613.035	2016-08-12	09:56:24–12:42:44	4 × 139	700–722
α For	ESPaDOnS	6703.707–6703.718	2014-02-15	04:58:05–05:13:23	4 × 50	51–411
γ Lep	ESPaDOnS	6698.811–6698.835	2014-02-10	07:22:17–07:55:58	4 × 53	683–704
θ UMa	NARVAL	7718.690–7718.745	2016-11-26	04:24:41–05:44:15	4 × 150	502–520
ι Psc	ESPaDOnS	7617.076–7617.156	2018-08-16	13:41:49–15:37:51	4 × 95	706–723
σ02 UMa	ESPaDOnS	7744.090–7745.172	2016-12-21	14:07:31–16:05:55	4 × 179	700–720
δ Equ	ESPaDOnS	7911.029–7911.125	2017-06-06	12:38:26–14:57:14	4 × 144	608–765
γ Del	NARVAL	6902.463–6902.479	2014-09-01	22:49:17–23:12:36	4 × 286	385–387
6 Cet	ESPaDOnS	7975.977–7976.017	2017-08-10	11:21:15–12:18:44	4 × 192	735–765
ζ Cnc	ESPaDOnS	7799.947–7799.964	2017-02-15	10:37:30–11:01:44	4 × 159	635–651
γ CrA A	ESPaDOnS	7911.967–7912.042	2017-06-07	11:06:00–12:54:50	4 × 101	564–620
HD 84117	ESPaDOnS	7823.910–7823.952	2017-03-11	9:42:01–10:42:42	4 × 201	691–705
η Cas	NARVAL	6902.580–6902.591	2014-09-02	01:45:18–02:01:24	4 × 177	481–482
Definite detections, but uncertain which component						
κ Peg	ESPaDOnS	7616.849–7617.068	2019-08-16	08:14:11–13:29:20	4 × 104	696–777
20 Oph	ESPaDOnS	7608.735–7608.862	2016-08-08	05:36:03–08:38:40	4 × 155	690–719

Table 4. Results from Stokes *V* LSD analysis our 55 stars.

Target Star	Obs. Date UT	T_{exp} (s)	No. Spectra[1]	SNR Stokes *V* mean LSD	No. lines used	FAP inside line	Vel range (km s^{-1})	B_l (G)	N_l (G)
F-star definite detections									
β CrB	23apr17	150.0	1	2766	17620	$<10^{-16}$	−31, −4	+735.8 ± 6.2	+0.1 ± 0.5
σ Boo	14jan17	139.0	14	105 071	6304	3.465×10^{-6}	−14, +16	− 1.4 ± 0.4	+0.5 ± 0.4
ϵ Lib	13mar17	213.0	14	114 485	6829	1.666×10^{-7}	−35, +10	− 0.5 ± 0.1	+0.1 ± 0.1
ϵ Cet	21sep16	199.0	16	124 397	6693	1.456×10^{-11}	−5, +40	+0.6 ± 0.1	0.0 ± 0.1
α Com	16feb17	120.0	27	154 986	7628	$<10^{-16}$	−50, +20	+3.1 ± 0.3	+0.2 ± 0.4
χ Dra	24apr15	120.0	1	27 693	6838	$<10^{-16}$	+27, +61	− 6.3 ± 1.2	− 0.0 ± 1.2
h Dra	09may17	194.0	16	109 211	7186	$<10^{-16}$	−50, −15	+8.3 ± 0.9	+0.6 ± 0.9
36 UMa	13jan17	180.0	12	120 020	7058	$<10^{-16}$	−5, +25	− 0.3 ± 0.1	0.0 ± 0.1
17 Crt	5mar17	209.0	18	108 986	8309	4.441×10^{-16}	−10, +22	+0.4 ± 0.1	+0.2 ± 0.1
γ CrA B	06jun17	101.0	12	67 072	7608	$<10^{-16}$	−65, −40	+5.6 ± 0.8	− 0.2 ± 0.8
ω Dra B	05may17	189.0	16	135 380	9099	$<10^{-16}$	+15, +45	− 2.9 ± 1.2	− 1.0 ± 1.2
θ Dra	15may17	320.0	4	44 295	9552	8.203×10^{-13}	−50, +20	+7.4 ± 2.9	− 0.6 ± 2.9
β Vir	11apr17	223.0	2	48 830	10621	$<10^{-16}$	−14, +23	+1.7 ± 0.5	− 0.4 ± 0.5
F-star marginal detections									
τ PsA	15oct16	204.0	14	134 948	8637	2.233×10^{-5}	−40, +5	− 0.6 ± 0.2	+0.3 ± 0.2
γ Ser	23aug14	269.0	2	57 763	7265	6.800×10^{-3}	−10, +25	+0.9 ± 0.4	− 0.5 ± 0.4
F-star non-detections[2]									
δ Cap	19oct14	103.0	5	33 776	15411	4.896×10^{-1}	−120, +60	− 2.9 ± 5.9	1.4 ± 5.9
α Hyi	08nov14	120.0	6	32 272	15846	$1.000 \times 10^{+00}$	−150, +200	+24.8 ± 11.3	− 6.7 ± 11.3
h UMa	17dec13	234.0	1	22 999	16569	9.265×10^{-1}	−158, +151	− 3.8 ± 17.6	+21.3 ± 17.6
γ Cap	11sep14	95.0	1	14 394	16578	5.142×10^{-1}	−80, +10	+4.0 ± 3.6	+3.2 ± 3.6
δ Ser	17apr14	239.0	3	43 993	18879	9.863×10^{-1}	−160, +60	− 1.6 ± 4.8	+2.3 ± 4.9
α Crv	05feb14	50.0	8	42 414	16310	6.433×10^{-1}	−30, +40	− 0.8 ± 1.0	1.4 ± 1.0
β TrA	03apr16	106.0	3	27 157	14537	9.452×10^{-1}	−80, +80	− 17.3 ± 7.4	− 6.0 ± 7.4
δ Aql	03jun14	194.0	2	45 176	15389	7.127×10^{-1}	−120, +80	+3.3 ± 4.0	− 1.7 ± 4.1
ω Dra A	05may17	189.0	16	136 494	9096	3.358×10^{-1}	−65, −30	+0.2 ± 0.1	− 0.1 ± 0.1
υ UMa	16apr14	260.0	3	48 900	15291	9.831×10^{-1}	−90, +160	+2.6 ± 6.1	− 0.8 ± 6.4
δ Gem	21apr15	190.0	5	43 796	15241	9.056×10^{-1}	−140, +120	+20.8 ± 9.9	− 18.5 ± 9.9
τ Cyg	08jun14	250.0	3	45 303	16891	7.501×10^{-1}	−40, −10	− 3.6 ± 4.9	− 3.1 ± 4.9
η Lep	01nov15	95.0	1	13 989	15037	1.775×10^{-1}	−30, +30	− 6.6 ± 3.4	− 2.3 ± 3.4
ι Leo	16feb17	286.0	5	67 120	7507	7.171×10^{-1}	−40, +20	− 0.8 ± 0.4	0.0 ± 0.4
10 UMa	22dec16	105.0	21	189 946	8930	[3] $< 10^{-16}$	0, +60	[3] − 4.8 ± 1.1	+0.3 ± 1.1
ψ Vel	11feb14	60.0	9	47 467	16064	7.119×10^{-1}	−20, +30	− 3.3 ± 3.0	+1.8 ± 3.0
γ Tuc	01aug15	224.0	3	37 707	6192	6.996×10^{-1}	−100, +90	− 6.3 ± 6.2	− 2.1 ± 6.2
γ Cet	17oct14	208.0	7	59 547	16047	8.546×10^{-1}	−25, +5	− 45.2 ± 23.9	− 4.5 ± 23.9
σ Cet	20sep16	179.0	7	87 618	7482	5.724×10^{-1}	−50, −15	0.0 ± 0.2	0.0 ± 0.2
58 Oph	12may17	200.0	13	96 046	6833	9.002×10^{-1}	−15, +30	+0.4 ± 0.2	− 0.6 ± 0.2
β Del	09may14	103.0	1	28 969	8030	2.959×10^{-1}	−80, −20	− 3.1 ± 3.9	− 0.6 ± 4.0
ψ Gem	27mar14	167.0	3	64 315	7456	2.318×10^{-1}	−40, +100	− 5.1 ± 2.4	+2.9 ± 2.4
α CMi	13nov15	10.0	1	26 419	7468	7.746×10^{-1}	−20, +9	− 0.7 ± 0.3	− 0.3 ± 0.3
ι Peg	23aug16	258.0	1	28 229	6463	5.910×10^{-1}	−36, −18	− 3.6 ± 1.3	− 0.8 ± 1.3
ψ Peg	15aug16	105.0	10	109 945	7499	8.099×10^{-1}	−25, +15	+0.1 ± 0.1	0.0 ± 0.1
μ Cyg	12aug16	139.0	15	118 196	7043	2.649×10^{-1}	−2, +25	− 0.4 ± 0.1	0.0 ± 0.1
α For	15feb14	50.0	3	17 152	7152	8.189×10^{-1}	−30, +0	+3.1 ± 1.3	+0.3 ± 1.3
γ Lep	10feb14	63.0	6	75 580	8161	8.943×10^{-1}	−20, +10	− 0.2 ± 0.2	+0.2 ± 0.2
θ UMa	26nov16	150.0	7	66 879	7268	1.943×10^{-1}	0.0, +30	− 0.1 ± 0.2	+0.2 ± 0.2
ι Psc	16aug16	95.0	14	122 548	7502	4.510×10^{-3}	−15, +25	− 0.2 ± 0.1	+0.1 ± 0.1
σ02 UMa	21dec16	179.0	4	94 164	8648	9.598×10^{-1}	−20, +15	+0.1 ± 0.1	0.0 ± 0.1
δ Equ	06jun17	144.0	12	98 789	7182	2.012×10^{-2}	−40, +5	+0.7 ± 0.2	− 0.3 ± 0.2
γ Del	01sep14	286.0	2	64 651	10137	7.083×10^{-1}	−10, +5	− 0.1 ± 0.1	0.0 ± 0.1
6 Cet	10aug17	192.0	5	72 919	7659	4.349×10^{-1}	−2, +28	0.0 ± 0.1	+0.1 ± 0.1
ζ Cnc	15feb17	159.0	3	35 867	8813	6.533×10^{-1}	−20, +10	− 0.7 ± 0.4	− 0.1 ± 0.4
γ CrA A	07jun17	101.0	14	57 601	7613	6.317×10^{-1}	−70, −35	− 0.1 ± 0.1	− 0.1 ± 0.1
HD 84117	11mar17	201.0	5	69 158	8804	3.329×10^{-1}	+15, +50	+0.2 ± 0.1	+0.2 ± 0.1
η Cas	02sep14	177.0	2	58 444	7579	4.934×10^{-1}	−10, +10	0.0 ± 0.1	+0.1 ± 0.1
Definite detections, but uncertain which component									
κ Peg	16aug16	104.0	34	183 631	6684	3.757×10^{-13}	−50, −5	+0.9 ± 0.3	0.0 ± 0.3
20 Oph	08aug16	155.0	15	128 114	8378	2.612×10^{-6}	−20, +20	+0.7 ± 0.2	0.0 ± 0.2

Notes. [1]Spectra are constructed from four sub-exposures as described in Section 2.3. For example, the 14 spectra for σ Boo were produced from 56 sub-exposures. SNR for the Stokes *I* profiles are shown in Table 3.
[2]For stars with non-detections we have taken the maximum B_l measurement, and B_l values refer to an upper limit.
[3]Detection is most likely from the G-star component of the blended spectra.

Table 5. Radial Velocity (RV), S-index, bisector analysis, and Stokes *V* for our stars.

Target	RV this work (km s^{-1})	RV literature (km s^{-1})	S-index this work	S-index literature	Bisector slope	Bisector span (m s^{-1})	Stokes *V* Amplitude (*V*/*Ic*)
F-star definite detections							
β CrB	− 17.32 ± 0.07	− 26.90 ± 0.20	NA	NA	\	231 ± 13	–
σ Boo	+0.28 ± 0.01	+0.37 ± 0.09	0.240 ± 0.004	0.156–0.253	/	211 ± 35	0.059
ϵ Lib	− 13.98 ± 0.01	− 9.8 ± 0.70	0.180 ± 0.012	NA	\	13 ± 13	0.057
ϵ Cet	+15.81 ± 0.26	+15.49 ± 0.19	0.186 ± 0.003	0.219	NA	NA	NA
α Com	− 18.02 ± 0.27	− 16.05 ± 0.21	0.272 ± 0.008	0.308	NA	NA	NA
χ Dra	+43.70	+31.90 ± 0.14	0.175 ± 0.002	0.152–0.161	/	211 ± 56	0.198
h Dra	− 32.95 ± 0.03	− 21.00 ± 0.80	0.251 ± 0.036	0.195–0.219	\	71 ± 13	0.257
36 UMa	+8.71 ± 0.01	+8.69 ± 0.09	0.193 ± 0.011	0.173	/	107 ± 14	0.120
17 Crt	+5.85 ± 0.01	+5.80 ± 0.40	0.157 ± 0.013	0.158–0.167	|	12 ± 18	0.069
γ CrA B	− 50.40 ± 0.10	− 51.60 ± 0.30	0.139 ± 0.015	0.165	|	8 ± 80	0.080
ω Dra B	+28.42 ± 0.89	− 13.98 ± 0.02	0.307 ± 0.008	0.174–0.191	/	102 ± 16	0.134
θ Dra	+11.99 ± 0.70	− 8.23 ± 0.20	0.206 ± 0.004	0.164	NA	NA	NA
β Vir	+4.60 ± 0.01	+4.71 ± 0.08	0.162 ± 0.002	0.138–0.186	/	114 ± 3	0.077
F-star marginal detections							
τ PsA	− 16.11 ± 0.01	− 16.23 ± 0.09	0.156 ± 0.011	0.144–0.173	|	12 ± 75	0.047
γ Ser	+6.82 ± 0.03	+6.78 ± 0.09	0.153 ± 0.001	0.131–0.193	\	356 ± 14	0.075
F-star non-detections							
α Hyi	+20.31 ± 0.12	+8.70 ± 3.10	NA	NA	∗	∗	–
h UMa	−2.54	− 10.40 ± 0.70	0.240	NA	∗	∗	–
γ Cap	−33.75	− 31.20 ± 0.50	0.171	NA	/	107	–
δ Ser A	− 40.95 ± 0.21	− 41.50 ± 2.70	0.186 ± 0.001	NA	∗	∗	–
α Crv	+3.21 ± 0.02	+2.80 ± 0.30	0.279 ± 0.001	0.170–0.231	NA	NA	–
β TrA	+0.72 ± 0.08	+0.40 ± 0.60	NA	NA	∗	∗	–
δ Aql	− 31.70 ± 0.15	− 34.00 ± 0.20	0.241 ± 0.001	0.155–0.234	∗	∗	–
ω Dra A	− 47.74 ± 0.71	− 13.98 ± 0.02	0.240 ± 0.007	0.174–0.191	/	178 ± 16	–
δ Cap	− 21.73 ± 4.55	− 3.40 ± 0.80	0.298 ± 0.001	NA	∗	∗	–
υ UMa	+32.49 ± 0.58	+27.30 ± 4.10	0.210 ± 0.002	0.135	∗	∗	–
δ Gem	+3.37 ± 0.12	+4.10 ± 7.40	0.272 ± 0.001	0.174–0.182	∗	∗	–
τ Cyg	− 21.73 ± 0.03	− 20.90 ± 0.80	0.253 ± 0.001	0.176–0.243	NA	NA	–
η Lep	−1.33	− 2.14 ± 0.17	0.245	[1]0.141–0.184	\	83	–
ι Leo	− 10.62 ± 0.01	− 11.80 ± 0.20	0.230 ± 0.001	0.231–0.270	/	190 ± 21	–
10 UMa	+27.68 ± 0.04	+27.80 ± 2.80	0.216 ± 0.007	0.206–0.233	NA	NA	–
ψ Vel	+3.24 ± 0.01	+8.80 ± 1.80	0.365 ± 0.002	0.277	NA	NA	–
γ Cet	− 5.94 ± 1.33	− 4.90 ± 0.90	0.432 ± 0.002	NA	∗	∗	–
γ Tuc	− 2.31 ± 0.12	+18.40 ± 0.70	NA	NA	∗	∗	–
σ Cet	− 29.80 ± 0.01	− 27.50 ± 0.90	0.160 ± 0.001	0.157–0.197	|	0 ± 27	–
58 Oph	+10.34 ± 0.01	+10.20 ± 0.30	0.164 ± 0.018	0.197	|	8 ± 18	–
β Del	−28.36	− 33.90 ± 1.50	0.231	0.197–0.221	NA	NA	–
ψ Gem	+28.50 ± 0.12	+27.20 ± 0.70	0.217 ± 0.001	0.209–0.239	∗	∗	–
α CMi	− 5.36 ± 0.01	− 2.70 ± 1.01	0.165 ± 0.001	[1]0.137–0.174	/	201 ± 31	–
ι Peg	−26.66	− 5.50 ± 0.70	0.164 ± 0.003	0.150	/	131	–
ψ Peg	− 5.73 ± 0.01	− 5.37 ± 0.08	0.148 ± 0.001	0.121–0.176	/	71 ± 3	–
μ Cyg	+16.97 ± 0.02	+16.95 ± 0.16	0.178 ± 0.001	0.181	|	18 ± 14	–
α For	− 16.67 ± 0.05	− 17.14 ± 0.20	0.147 ± 0.054	0.162	/	127 ± 13	–
γ Lep	− 8.83 ± 0.01	− 9.29 ± 0.15	0.168 ± 0.001	0.143–0.183	\	441 ± 7	–
θ UMa	+14.47 ± 0.02	14.40 ± 0.20	0.141 ± 0.001	0.148–0.204	/	113 ± 14	–
ι Psc	+5.77 ± 0.01	+5.95 ± 0.08	0.161 ± 0.001	0.149–0.170	/	71 ± 26	–
σ02 UMa	− 3.13 ± 0.01	− 2.98 ± 0.09	0.135 ± 0.014	0.138–0.171	|	30 ± 32	–
δ Equ	− 15.76 ± 0.05	− 15.85 ± 0.07	0.166 ± 0.016	0.160	NA	NA	–
γ Del	− 6.00 ± 0.01	− 7.70 ± 0.30	0.110 ± 0.001	0.194	|	0 ± 18	–
6 Cet	+15.14 ± 0.01	+14.81 ± 0.09	0.174 ± 0.001	0.136–0.180	/	59 ± 23	–
ζ Cnc	− 5.24 ± 0.01	− 7.93 ± 0.08	0.143 ± 0.002	0.160–0.169	NA	NA	–
γ CrA A	− 52.82 ± 0.06	− 51.60 ± 0.30	0.128 ± 0.030	0.165	\	100 ± 45	–
HD 84117	+34.80 ± 0.01	+35.30 ± 0.44	0.151 ± 0.006	0.147–0.186	/	77 ± 41	–
η Cas	+8.68 ± 0.01	+8.44 ± 0.09	0.161 ± 0.001	0.138–0.172	/	38 ± 9	–
Definite detections, but uncertain which component							
κ Peg	− 21.45 ± 2.62	− 0.80 ± 0.20	0.237 ± 0.001	0.170	NA	NA	–
20 Oph	− 0.30 ± 0.01	− 1.60 ± 0.60	0.227 ± 0.001	NA	NA	NA	–

Notes. RV literature values from Anderson & Francis (2012) and [1]Buccino & Mauas (2008). Bisector velocity span based on points at 40 and 80 per cent *I*/*Ic*. Positive bisector slope with top leaning towards right is solar-type. ∗Bisectors are increasingly difficult to determine for stars with vsini > 20 km s^{-1} due to rotational broadening of spectral lines. NA = data not available. Bisectors not determined for unresolved spectroscopic binaries. α Crv not used for bisector analysis due to unusual line shape.

3.4.2 *Stokes I asymmetry*

Asymmetry in photospheric absorption lines provide information on the dynamics of gas flows in the stellar atmosphere (Dravins 1982), along the line of sight in the region where the lines are formed (Buonaura & Caccin 1982). The method of using bisectors to study stellar line asymmetry was pioneered by Gray (1981) and provides more information on conditions in the atmosphere than the alternative method of using a mirror image of an intensity line profile (Gray 1980). We calculated bisectors using the midpoint of horizontal lines connecting adjacent equal intensity points on the Stokes *I* profile as defined by Kulander & Jefferies (1966). Using a mean LSD profile to calculate the bisector was considered reasonable under the assumption that all spectral lines are affected in a similar way in the velocity field. The use of bisector analysis using Stokes *I* LSD profiles has been previously used for the G8 star ξ Bootis (Petit et al. 2005; Morgenthaler et al. 2012). An additional advantage of using mean bisectors is that it averages photometric noise in the data, and according to Gray (1982), it was not necessary to study intrinsic differences between lines for a first approximation study of bisectors. A limitation of using mean bisectors is that spectral lines of different depths can have different widths and shapes (Dravins 2008), which was also shown in a study of bisectors in A-Type stars by Landstreet et al. (2009) where a line shape difference was observed between weak and strong lines.

Two measures are used to characterize the Stokes *I* bisector; slope and velocity span. The slope of the bisector (Gray & Hatzes 1997) is the spectral line velocity at a point near the top, minus a point at the bottom, with a positive slope having the part of the line closest to the continuum leaning redwards. The exact depth of intensity points used in the measurement of bisector slope is not critical, but should be far enough from continuum and core to avoid measurement errors (Gray 1983). It is usually sufficient to estimate the slope visually from a bisector plot, while being careful to discount spurious points which are occasionally present. The second measurement of asymmetry, the velocity span, defined by Toner & Gray (1988) as the difference in velocity between two bisector points, which we take as $I/I_c = 0.8$ and 0.4 measured from the core to the continuum, similar to Hatzes et al. (2003). The bisector velocity span is considered a measure of the strength of convection in cool stars (Gray 1992), and is a useful measurement in stars where rotational broadening has not introduced errors due to a shallow line profile (Gray 1983). The bisector errors are determined by taking the standard deviation of bisector measurements from individual spectra. The Stokes *I* bisector slope and velocity span for our stars are shown in Table 5.

3.4.3 ***Stokes V amplitude***

The Stokes *V* profile contains important information on the stellar magnetic field (Grossmann-Doerth, Schussler & Solanki 1989), with the amplitudes of Stokes *V* signal providing information on the magnetic flux (Stenflo 1985). For unresolved weak solar magnetic fields (Solanki 1993), and stellar fields (Stenflo 1989), the amplitude of the Stokes *V* signal is proportional to B_l. We measured the amplitude (V/Ic) by taking the maximum height of the Stokes *V* signal above or below the continuum line. The Stokes *V* amplitudes of our stars are shown in Table 5.

3.5 Chromospheric emission (S-index)

Various methods have been used by researchers as indicators of stellar magnetism including, photometric variability (Hall 1991), asteroseismology (García et al. 2010), interferometry (Roettenbacher et al. 2016; Kochukhov et al. 2017), and non-thermal emission from chromospheric line cores including Ca II H&K (Wilson 1978; Duncan et al. 1991; Baliunas et al. 1995), Mg II (Howard & Stenflo 1972), Hα (Cincunegui, Díaz & Mauas 2007), and Ca II infrared triplet (Dempsey et al. 1993). The most widely used indirect indicator of stellar activity is the S-index introduced by Vaughan, Preston & Wilson (1978) as part of the decades long Mt Wilson survey of chromospheric activity in solar-type stars. The S-index is defined as,

$$S-\text{index} = \frac{aF_H + bF_K}{cF_{R_{HK}} + dF_{V_{HK}}} + e, \quad (2)$$

where F_H and F_K are the fluxes in the resonance lines from 20 Å-wide channels (with triangular profiles) centred at wavelengths, 396.8492 and 393.3682 nm, respectively (Duncan et al. 1991), compared to the flux at two bands in the continuum on the red and blue side of the H&K line. The coefficients determined for the ESPaDOnS and NARVAL spectropolarimeters (a,b,c,d,e) are taken from Marsden et al. (2014). The S-index is not calculated for 3 HARPSpol stars (α Hyi, β TrA, γ Tuc) with no coefficients available for use. We determined the S-index for our stars by calculating the mean and standard deviation from the individual spectra.

4 RESULTS

4.1 Stellar parameters

Table 1 lists the parameters for our 55 stars obtained from literature sources. The parameters which are significantly affected from a blend of binary components are identified in the table.

4.2 Magnetic detections

The rates of surface magnetic field detection for 51 of our stars are shown in Fig. 1. The figure does not include κ Peg and 20 Oph because we cannot determine if the detection comes from the F-star component. β CrB and δ Cap are not included because they could not be assigned a spectral type. The overall detection rate for our F-stars was 27 per cent (14 of 51). This detection rate is similar to that found in Marsden et al. (2014) who found magnetic detection rate of 32 per cent (6 of 19) for a sample of stars from F5-F9. A fossil field is present in β CrB, which shows a strong B_l of 735.8 ± 6.2 G. Magnetic fields are detected in every spectral type from F3V to F9V with a B_l ranging from 0.3 ± 0.1 G (36 UMa, F8V) to 8.3 ± 0.9 G (h Dra, F8V). We obtained no detections in F0 to F2 stars. ϵ Cet (F5V+F6V) and α Com (F5V+F6V) have definite detections which we assume comes from at least one of the F-star components. κ Peg and 20 Oph have definite detections, but we are not able to determine if the detection comes from the F-star component.

4.3 $|B_l|$ versus effective temperature ($T_{\rm eff}$)

Fig. 2 shows a plot of $|B_l|$ versus $T_{\rm eff}$ for all our 55 stars. The lack of magnetic detection for stars hotter than $T_{\rm eff} = 6720$ K (σ Boo, F3V)

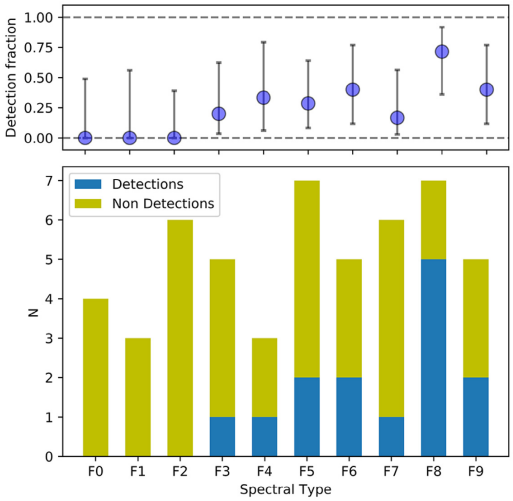

Figure 1. Histogram of detections/non-detections of surface magnetic fields for 51 of our stars from spectral type F0-F9. The detections include both marginal and definite detections. κ Peg and 20 Oph are omitted because we cannot determine if the detection came from the F-star component. β CrB and δ Cap are omitted because they are not assigned a spectral type. Overall detection rate is 27 per cent (14/51) and a 95 per cent confidence interval of 17–41 per cent. The upper panel shows the detection fraction along with 2σ error bars calculated using the original Wilson interval (Wilson 1927).

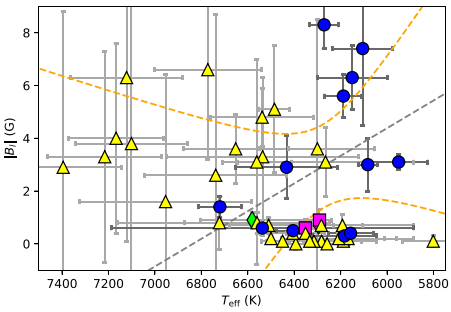

Figure 2. $|B_l|$ versus $T_{\rm eff}$ for 50 of our stars (excluding β CrB with a fossil field, and excluding 4 non-detections, α Hyi, α Crv, η Lep, and γ Cet, with large B_l and large uncertainties). The blue circles indicate definite magnetic detection on an F-star, yellow triangle indicates no detection, a magenta square is a marginal detection, while a green diamond is a definite detection but uncertain if detection is from the F-star or a companion. The dashed grey trend line and orange 95 per cent confidence intervals are shown for our 14 stars with magnetic detection, excluding β CrB. No significant trend observed between $T_{\rm eff}$ versus $|B_l|$.

is obvious. The only exception is β CrB ($T_{\rm eff}$ = 7980 K), shown in Fig. B1 with a fossil magnetic field. We find no significant trend between $|B_l|$ and $T_{\rm eff}$ for 14 stars with magnetic detections from F3 to F9 (Fig. 2). F-stars undergo a rapid increase in the depth of the outer convection zone when moving towards later spectral types, where $T_{\rm eff}$ can be considered a useful proxy for the convection zone depth (Pinsonneault, DePoy & Coffee 2001). In σ Boo, we find a definite magnetic field in a convection zone which is estimated

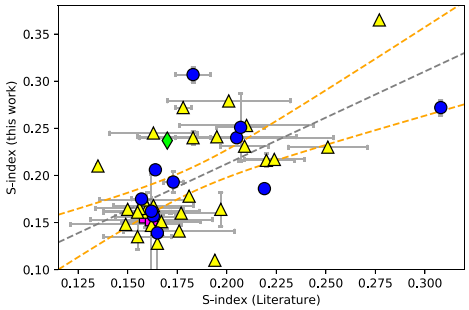

Figure 3. Chromospheric emission (S-index) found in this work versus the range of S-index from Pace (2013) and Buccino & Mauas (2008). The graph includes 44 stars which have both our S-index calculation and literature values. The dashed grey trend line and orange 95 per cent confidence intervals are shown. The error bars on the x-axis represent the range of values from the literature. The error bars on the y-axis represent the standard deviation for our determination. The symbols are the same as Fig. 2.

to be as thin as a few per cent of the stellar radius (Gilman 1980; Kuker & Rudiger 2007). The median $|B_l|$ of our 14 F-stars with a magnetic detection (excluding β CrB with a fossil field) is 2.2 G (mean 3.0 $\pm$ 2.7 G), which is similar to the mean of 3.3 G found in Marsden et al. (2014). While there is no linear increase in B_l strength with decreasing $T_{\rm eff}$, our results indicate the three hottest stars with detections (excluding β CrB) have among the weakest B_l. For stars cooler than $T_{\rm eff}$ 6400 K with magnetic detections there is no clear trend between $|B_l|$ and $T_{\rm eff}$.

4.4 Chromospheric emission (S-index)

The chromospheric emission (S-index) of our F-stars compared to the literature value of Pace (2013) and Buccino & Mauas (2008) are shown in Fig. 3. There is a correlation between our S-index values and the mid point of the range from Pace (2013), however the scatter for our F-stars, compared to literature values, is larger than Marsden et al. (2014, Fig. 4). In F-stars, as well as later spectral types, chromospheric emission is known to vary over time (Baliunas et al. 1995; Wright et al. 2004; Saikia et al. 2018), while our measurements are snapshots at a specific time. We cannot determine stellar magnetic activity cycles from our data, but can provide an indication of the strength of chromospheric emission compared to literature values, and see if this relates to a high or low point of a possible magnetic cycle. One explanation for the lack of magnetic detection of some of our stars is that we obtained spectra during low periods of the magnetic activity cycle. For 10 of 28 (36 per cent) of our stars with a non-magnetic detection, we measured the star at what is possibly a low point of the S-index range when comparing to literature values, therefore providing one possible explanation for the lack of magnetic detections.

Theoretical calculations using mixing-length theory indicate dynamo periods are short for F-stars, and increase towards later spectral types (Belvedere, Paterno & Stix 1980; Stix 1982). For an F5 star, the model by Belvedere et al. (1980) predicts a dynamo period of 0.88 yr, increasing by an order of magnitude to 9.5 yr for a G5 star. Olspert et al. (2017) estimated magnetic cycles for 10 F-type stars using a probabilistic analysis of Mt Wilson CaII H&K data, and determined cycle lengths ranging from 3.6 to 16.6 yr. The potentially short dynamo periods make early F-stars good targets for studies

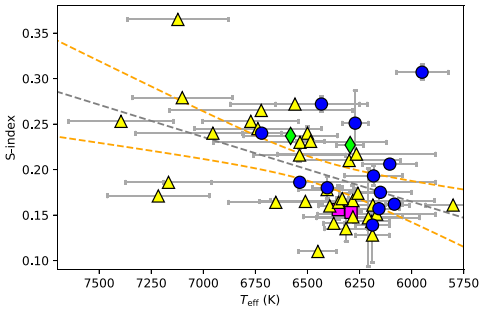

Figure 4. S-index versus $T_{\rm eff}$ for our 50 stars (excludes γ Cet which is a blend of F4V+A2Vn components and has a large S-index of 0.432). Three HARPSpol stars with no S-index calculation are excluded. β CrB with a fossil field is not included. The dashed grey trend line and orange 95 per cent confidence intervals shown. The symbols are the same as Fig. 2.

on stellar activity cycles, because the time required to measure a magnetic cycle may be as short as a few months, compared to years for later-type stars. See Mengel et al. (2016) for evidence for a very rapid ∼120 d magnetic cycle in τ Boo, an F7V star.

4.5 S-index versus $T_{\rm eff}$

Our plot of S-index versus $T_{\rm eff}$ (Fig. 4) shows an increase in S-index with increasing $T_{\rm eff}$ which is consistent with that found for F6 and later stars in Strassmeier et al. (1990). This contrasts with the lack of trend seen in our plot of $|B_l|$ versus $T_{\rm eff}$ (Fig. 2). While both S-index and B_l are indicators of stellar magnetic fields, they measure different parts of the stellar atmosphere and are not directly comparable. B_l is a measure of the large-scale photospheric magnetic field, and the S-index is a measure of chromospheric emission, caused by magnetic activity. The S-index is influenced by small scale magnetic fields which do not suffer from cancellation effects like B_l.

The S-index may also measure a basal chromospheric component unrelated to magnetic activity (Schrijver, Dobson & Radick 1989) which is caused by acoustic heating (Schrijver 1987; Ulmschneider, Priest & Rosner 1991). The S-index depends on both photospheric and chromospheric radiation, with photospheric line strength changing as a function of spectral type due to flux in the continuum windows (Cincunegui et al. 2007). Hotter stars have weaker photospheric absorption lines which leads to a larger S-index. S-index is a poor indicator of chromospheric activity in F-stars (Wolff, Heasley & Varsik 1985) due to the weakness in chromospheric emission and low contrast relative to the photospheric flux (Baliunas et al. 1995). The correlation between S-index and $T_{\rm eff}$ in our F-stars is possibly due to the changing strength of photospheric absorption lines rather than magnetic activity or basal chromospheric component.

It is interesting that γ Cet (F4V+A2Vn) has a very high S-index of 0.432 ± 0.24. Neither of the components from the blended spectra would be expected to create such a high S-index. The A2 component of γ Cet may be showing a high level of acoustic heating of the outer atmosphere, which is consistent with acoustic flux peaking in A-type stars (Walter, Matthews & Linsky 1995). Alternatively, A-type stars may have a different shape and strength to their Ca H&K lines, and potentially some Balmer lines blending into the continuum bands of the S-index. Therefore, the high S-index in γ Cet may not be due to chromospheric emission.

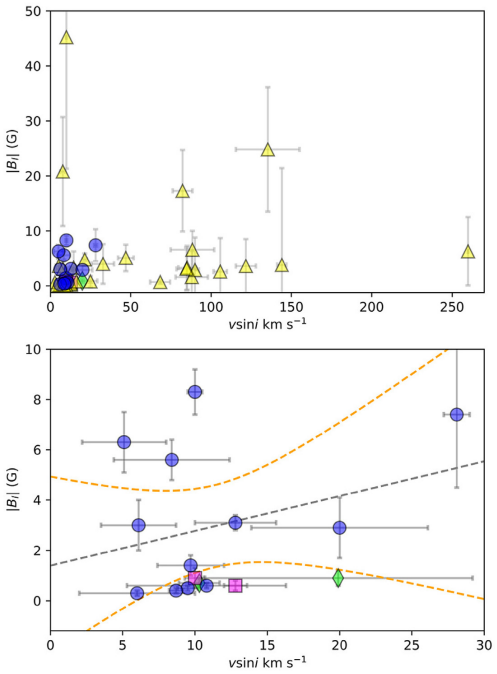

Figure 5. Top Figure. $|B_l|$ versus $v\sin i$ for 54 of our stars (excluding β CrB with a fossil field). Bottom figure. $v\sin i$ versus $|B_l|$ for 14 of our stars with a magnetic detection except β CrB. The dashed grey trend line and orange 95 per cent confidence intervals shown. No significant trend observed. The symbols are the same as Fig. 2.

4.6 $|B_l|$ versus stellar rotation

Stellar rotation is one of the major dynamo ingredients (Roberts & Soward 1992; Charbonneau & Steiner 2012) and the strength of the dynamo depends on the rate a star rotates (Noyes 1984; Simon & Fekel Jr 1987) along with other parameters such as differential rotation (Bullard & Gellman 1954; Spruit 2002) and the strength of convection (Parker 1955; Childress & Soward 1972). A plot of $|B_l|$ versus $v\sin i$ for our F-stars is shown in Fig. 5. We found no significant trend between $|B_l|$ and $v\sin i$ which differs from the positive correlation found for F-stars in Marsden et al. (2014, Fig. 13).

4.7 $|B_l|$ versus stellar age

The stars in our sample show a range of ages from 0.2 ± 0.6 to 5.2 ± 0.6 Gyr (Table 1). Our results in Fig. 6 show no correlation between $|B_l|$ and stellar age, which is different to the expected trend of a decrease in magnetic activity with increasing age shown in G,K,M stars by Saar (1991). When plotted into bins of 1.0 Gyr (Fig. 7) we find the highest rate of magnetic detection is in stars aged 2–3 Gyr (with the exception of the single 5.2 Gyr star), which is broadly comparable to that found in Marsden et al. (2014, Fig. 6).

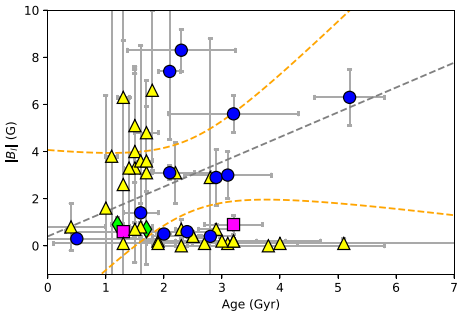

Figure 6. $|B_l|$ versus stellar age for 50 of our stars, excluding β CrB (fossil field) and excluding 4 stars (α Hyi, β TrA, θ UMa, and γ Cet) with no detection and large B_l with large uncertainties. The dashed grey trend line and orange 95 per cent confidence intervals shown for our 14 stars with a magnetic detection excluding β CrB. No significant trend observed. The symbols are the same as Fig. 2.

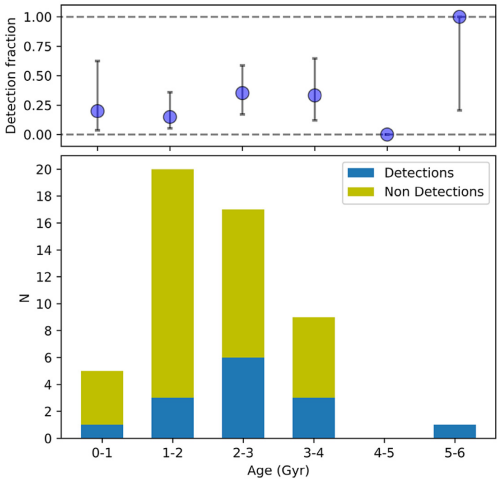

Figure 7. Histogram magnetic detection rate versus age for our 52 F-stars grouped into 1.0 Gyr bins. The detections include both definite and marginal detections. κ Peg and 20 Oph were omitted because we cannot determine if the detection came from the F-star component. β CrB with a fossil field was omitted. The upper panel shows the detection fraction along with 2σ error bars calculated using the original Wilson interval (Wilson 1927).

4.8 Bisector span versus $T_{\rm eff}$

Stokes *I* bisector velocity span (proxy for strength of convection) for our F-stars ranges from 0 to 441 m s^{-1} (Table 5). Our bisector velocity span for α CMi was 201 m s^{-1} compares with a value of 500 m s^{-1} in Gray (2010). Our results are consistent with the higher velocity spans found in F-stars compared to later spectral types (Gray 2010). Similarly, Kuker & Rudiger (2005, 2007) found F-type stars have higher convection velocities and shorter convective turnover times compared to solar-type stars, with an order of magnitude increase in convection velocity for a 1.4 $M_\odot$ star compared to the Sun. We do not find an increase in bisector

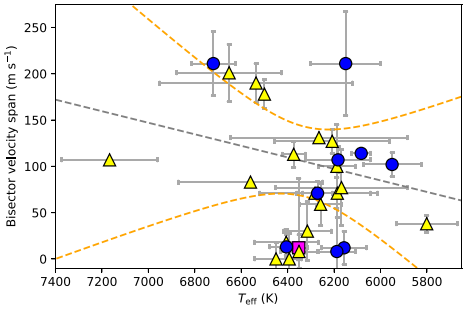

Figure 8. Bisector velocity span versus $T_{\rm eff}$ for our 31 stars with a calculated bisector span. β CrB with a fossil field is not included. The dashed grey trend line and orange 95 per cent confidence intervals shown. No significant trend observed. The symbols are the same as Fig. 2.

velocity span with increasing $T_{\rm eff}$ across the range of stars from F9 to F0 (Fig. 8).

We find that 7 of 12 (58 per cent) of our stars with a magnetic detection have a bisector span $\geq$ 100 m s^{-1}, compared to 7 of 20 (35 per cent) of stars without a magnetic detection with measured bisectors. This result is consistent with the expectation that stars with stronger convection are more likely to show a magnetic field. An analysis of the slope of the Stokes *I* bisector (Table 5) shows 53 per cent (17 of 32) of stellar components have solar-type bisectors (positive slope), 25 per cent (8 of 32) have no slope (velocity span not significantly different from zero), and 22 per cent (7 of 32) have reversed bisectors. We do not see a trend of reversing bisectors towards the hotter stars. The phenomenon of reversed bisectors (Gray & Toner 1986; Gray 1989; Gray & Nagel 1989) has been associated with the granulation boundary (Gray 1982) a location on the HR-diagram where a lack of outer convection zone results in a net upward velocities in the stellar atmosphere.

4.9 $v\sin i$ versus $T_{\rm eff}$

Due to rotational braking (Schatzman 1962; Weber & Davis Jr 1967; Skumanich 1972) which is known to occur around mid F-stars (Kraft 1967), we expect to see a large decrease in $v\sin i$ with decreasing $T_{\rm eff}$ corresponding to the onset of dynamo magnetic fields. Our plot in Fig. 9 shows a large decrease in $v\sin i$ occurring at $T_{\rm eff} \approx 6400$ K, which is consistent with an onset of dynamo magnetic fields which causes magnetic braking. All our stars with magnetic detections appear to have spun down, which is consistent with expectations due to rotational breaking. Fig. 9 also shows the strength of $|B_l|$ does not appear to correlate with either $T_{\rm eff}$ (see Section 4.3) or $v\sin i$.

4.10 SNR versus $T_{\rm eff}$

In Fig. 10 we plot SNR versus $T_{\rm eff}$ (Stokes *V* LSD) for all our 55 stars to see if there is a difference between the early and late F-stars which may explain the lack of magnetic detections in F0-F2 stars. The SNR is taken from values listed in Table 4. The mean SNR for our F0-F2 stars is 41515 $\pm$ 30085 compared to F3-F9 stars 84394 $\pm$ 42229. The lower SNR in the F0-F2 stars made it more difficult to detect the expected weak dynamo fields if they were present, however we detected magnetic fields in four later F-stars

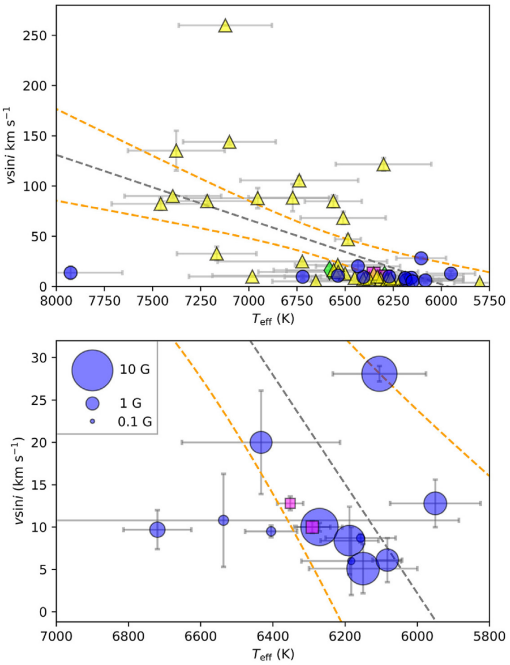

Figure 9. Figure at top shows $v \sin i$ versus $T_{\rm eff}$ for all our 55 stars. The dashed grey trend line and orange 95 per cent confidence intervals shown. The symbols are the same as Fig. 2. The bottom figure shows the expanded region comprising 14 stars with a magnetic detection, except β CrB. Circle radius and square width is proportional to B_l.

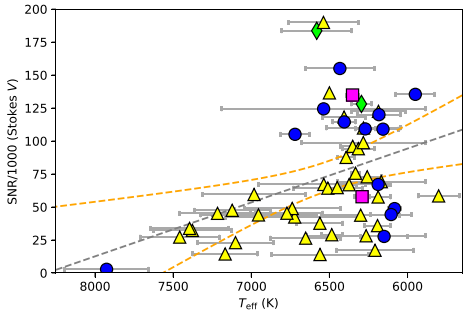

Figure 10. SNR (LSD Stokes V) versus $T_{\rm eff}$ for all our 55 stars. The dashed grey trend line and orange 95 per cent confidence intervals shown. The smbols are the same as Fig. 2.

from the BRITEpol sample with SNR comparable to the F0-F2 stars.

4.11 Stokes V amplitude versus $|B_l|$

In Fig. 11 we plot the Stokes V amplitude versus $|B_l|$ for 11 stars with a magnetic detection, excluding 3 stars which are unresolved spectroscopic binaries, and β CrB with a fossil field. We found a significant positive correlation for our 11 F-stars, which is in

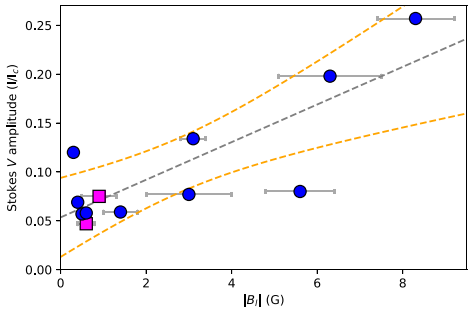

Figure 11. LSD Stokes V amplitude versus $|B_l|$ for 11 stars with a magnetic detection. Excluded is β CrB with a fossil field and 3 unresolved spectroscopic binaries. The dashed grey trend line and orange 95 per cent confidence intervals shown. Significant trend observed. The symbols are the same as Fig. 2.

agreement with the trend discussed by Stenflo (1989) where an increase in B_l results in a larger Stokes V amplitude.

5 DISCUSSION

Early F-type stars have superficial outer convection zones which at some effective temperature become too thin to sustain a magnetic dynamo. Our snapshot survey includes 53 F-type stars from spectral types F0-F9 plus 2 chemically peculiar stars β CrB and δ Cap. Our sample covers 27 per cent of the F-stars brighter than magnitude 5 listed in the Bright Star Catalogue (Table 2). The number of stars in our survey allows a study of the high temperature boundary for dynamo magnetic fields with an expected detection rate similar to Marsden et al. (2014) who found photospheric magnetic fields in 32 per cent of F-stars (6 of 19). We found a similar result with magnetic fields detected in 27 per cent (14 of 51) of our F-stars. Since fossil fields have an incidence of only about 10 per cent in higher mass stars and fall to about 1 per cent in stars with lower masses (Sikora et al. 2018) we would need a larger sample of early F-stars to explore more fully the low temperature boundary for fossil fields.

The hottest star in our sample β CrB is a well known chemically peculiar star with a fossil field and many published magnetic curves (Preston & Sturch 1967; Wolff & Wolff 1970; Borra & Landstreet 1980; Kurtz 1989; Han et al. 2018). The magnetic curve of β CrB has been modelled to represent a superposition of a dipole and a quadrupole field (Bagnulo et al. 2000) and shows a sinusoidal shape (Han et al. 2018) with a maximum $|B_l|$ of 653 G (Borra & Landstreet 1980), 754 G (Borra, Fletcher & Poeckert 1981), and 762 G (Wade et al. 2000). Our maximum measured $|B_l|$ of 735.8 $\pm$ 6.2 G is consistent with these published measurements.

Fossil magnetic fields have been detected in stars as cool as 6400 K. See for example HD 213637, $T_{\rm eff}$ = 6400 K (Kochukhov 2003), HD 101065, $T_{\rm eff}$ = 6400 K (Shulyak, Ryabchikova & Kochukhov 2013), ρ Pup $T_{\rm eff}$ = 6500–6850 K (Neiner, Wade & Sikora 2017b), HD 24712, $T_{\rm eff}$ = 7250 K (Shulyak et al. 2013), HD 188774 $T_{\rm eff}$ = 7600 K (Neiner & Lampens 2015), and HD 115226, $T_{\rm eff}$ = 7640 K (Kochukhov et al. 2008). These low temperature fossil fields may have large B_l, similar to β CrB, or weak B_l as shown by recently discovered Ap and Fp stars with sub-Gauss magnetic fields. Ultra-weak fossil fields were first detected in Vega (A0V) by Lignières et al. (2009) with B_l strength of 0.6 $\pm$ 0.3 G (Stokes

V SNR of 1500 per 1.8 km s^{-1}) and have been detected in stars as cool as F2 (Neiner et al. 2017b).

We detect photospheric magnetic fields in all spectral classes from F3V-F9V (Figs B2–B15), and no evidence of magnetic fields in 13 stars with spectral types F0 to F2. The hottest F-star with a definite magnetic detection is σ Boo (F3V), with an outer convection zone thickness less than few per cent of the stellar radius. The $|B_l|$ strengths for stars from F3-F9 ranges from 0.3 ± 0.1 G to 8.3 ± 0.9 G (median 2.2 G). χ Dra (F7V) is an interesting star which shows a relatively stable Stokes *V* magnetic signature with some characteristics of a fossil field. These multiple observations are not included here, but are being presented in a future paper using Zeeman Doppler imaging to map the magnetic field of χ Dra (Seach et al. in preparation).

From our magnetic snapshot survey with most stars having observations from only a single night, it is not possible to say definitely whether magnetic fields in our F-stars are dynamo or weak fossil fields. With $|B_l|$ ranging from 0.3 to 8.0 G, and sub-Gauss fossil fields existing in stars as cool as F2, the strength of magnetic field cannot be used solely to distinguish between fossil and dynamo fields. Another possible distinction with fossil fields having simple and stable Stokes *V* signatures and dynamo fields having complex Stokes *V* signatures does not always apply. For example, the Stokes *V* signatures of our 14 F-stars with a magnetic detection (with the exception of α Com) are not much more complex than that of β CrB with a fossil field (Appendix B). Stars with fossil fields can also show complex Stokes *V* signatures similar to those expected in dynamo fields. Examples of complex Stokes *V* signatures in stars with a fossil field include γ Gem, an Am star with a weak fossil field (Blazère, Neiner & Petit 2016), and ρ Pup, a δ Scuti F2m star (Neiner et al. 2017b), and several fast rotating stars with fossil fields (Silvester et al. 2012).

A possible reason we did not detect magnetic fields in stars earlier than spectral type F3V is due to the lower sensitivity of the spectra obtained for the early F-stars. However, even though the SNR of our F0-F2 stars is mostly lower than the F3-F9 stars, it is still possible to detect magnetic fields in the early F-star sample. We detected four late F-stars with an SNR comparable to the F0-F2 sample (Fig. 10), therefore, the lower SNR of the F0-F2 spectra was unlikely to be the sole reason for lack of magnetic field detection in our early F-stars. Another possibility for a lack of magnetic field detection in our early F-stars is the presence of cancellation effects. B_l is an average of the line of sight component of the magnetic field vector over the visible hemisphere, therefore regions of opposite polarity may cancel out, resulting in a field too weak to detect. With the suggestion by Giampapa & Rosner (1984) that spots on early F-type stars are small and evenly distributed over the stellar surface, this may indicate there are small areas of opposite polarity which may cause cancellation effects to be more pronounced in early F-stars compared with late F-stars.

We find a positive correlation between $T_{\rm eff}$ and S-index (Fig. 4) from spectral types F0V-F9V. In cool stars from spectral types G and later, the S-index is an indicator of chromospheric emission related to areas of magnetic activity on the star's surface. The higher levels of chromospheric emission for our early F-stars may be an indication of a basal chromospheric component which is unrelated to magnetic activity. Therefore the S-index may not be a good indicator of magnetic activity in early F-stars (Schrijver et al. 1989). The S-index is also dependent on the spectral type of the star, and our results may indicate the well known temperature dependence on chromospheric activity (Middelkoop 1982; Noyes 1984). We find no correlation between $|B_l|$ and stellar age (Fig. 6). This is different from the trend expected where stellar activity declines with age as shown by Marsden et al. (2013) and studies on stellar activity proxies using on Mg II, Ca IV, Hα, and X-ray emission (Hartmann & Noyes 1987). We have shown for our F-stars there is a positive correlation between the Stokes *V* amplitude and $|B_l|$ which was consistent with expectations for stars with weak magnetic fields. We do not find a correlation between $|B_l|$ and $T_{\rm eff}$ or $v \sin i$. Magnetic mapping of the surface of early F-type stars with Zeeman Doppler imaging (Kochukhov 2016) will be valuable in providing further details about the nature of stellar magnetism.

6 CONCLUSIONS

We detect photospheric magnetic fields in 14 out of 51 F-stars from a survey of spectral types from F0V to F9V. There are 12 definite detections, 2 marginal detections, and 2 binary stars with a detection but we were unable to determine if it came from the F-star component. As expected, surface magnetic fields of many of our F-stars are weak, with 6 of 14 stars having $|B_l| < 1.0$ G. There is a positive correlation between Stokes *V* amplitude and $|B_l|$. We found no correlation between $|B_l|$ and $T_{\rm eff}$, $|B_l|$ and $v \sin i$, or $|B_l|$ and age. Further work on magnetic mapping of interesting targets from this work is planned in the future, in order to gain more insights into stellar magnetism in stars with shallow convection zones.

ACKNOWLEDGEMENTS

This research was based on observations obtained at the Canada-France-Hawaii Telescope (CFHT) which is operated by the National Research Council of Canada, the Institut National des Sciences de l'Univers of the Centre National de la Recherche Scientifique of France, and the University of Hawaii. This work is based on observations obtained at the Bernard Lyot Telescope (TBL, Pic du Midi, France) of the Midi-Pyrénées Observatory, which is operated by the Institut National des Sciences de l'Univers of the Centre National de la Recherche Scientifique of France. Observations were collected at the European Organisation for Astronomical Research in the Southern Hemisphere under ESO programmes 094.D–0274(A), 097.D–0156(A), 095.D–0155(B). This research was supported by an Australian Government Research Training Program (RTP) Scholarship. This research has made use of the SIMBAD data base, operated at CDS, Strasbourg, France. This research has made use of the VizieR catalogue access tool, CDS, Strasbourg, France. This work has made use of data from the European Space Agency (ESA) mission *Gaia* (https://www.cosmos.esa.int/gaia), processed by the *Gaia* Data Processing and Analysis Consortium (DPAC, https://www.cosmos.esa.int/web/gaia/dpac/consortium). Funding for the DPAC has been provided by national institutions, in particular the institutions participating in the *Gaia* Multilateral Agreement.

REFERENCES

Abramowitz M., Stegun A., 1964, Handbook of Mathematical Functions, 9th edn. Dover Publications, USA
Abt H. A., 2009, ApJS, 180, 117
Abt H., Levy S., 1976, ApJS, 30, 273
Adelman S. J., Bolcal C., Hill G., Koçer D., 1991, MNRAS, 252, 329
Aguilera-Gómez C., Ramírez I., Chanamé J., 2018, A&A, 614, A55
Anderson E., Francis C., 2012, Astron. Lett., 38, 331
Aurière M., 2003, EAS Pub. Ser., 9, 105
Babcock H., 1947, ApJ, 105, 105

Babcock H. W., 1960, ApJ, 132, 521
Bagnulo S., Landolfi M., Mathys G., Landi Degl'Innocenti M., 2000, A&A, 358, 929
Bagnulo S., Landstreet J., Fossati L., Kochukhov O., 2012, A&A, 538, A129
Baliunas S. et al., 1995, ApJ, 438, 269
Barlow D. J., Scarfe C. D., 1977, PASP, 89, 857
Baschek B., Reimers D., 1969, A&A, 2, 240
Behr B. B., Hajian A. R., Cenko A. T., Murison M., McMillan R. S., Hindsley R., Meade J., 2009, ApJ, 705, 543
Behr B. B., Cenko A. T., Hajian A. R., McMillan R. S., Murison M., Meade J., Hindsley R., 2011, AJ, 142, 6
Belvedere G., Paterno L., Stix M., 1980, A&A, 91, 328
Beskin V., Balogh A., Falanga M., Lyutikov M., Mereghetti S., Piran T., Treumann R., eds, 2016, The Strongest Magnetic Fields in the Universe. Springer-Verlag, New York, p. 583
Blazère A., Neiner C., Petit P., 2016, MNRAS, 459, L81
Böhm-Vitense E., Dettmann T., 1980, ApJ, 236, 560
Borra E., Landstreet J., 1980, ApJS, 42, 421
Borra E. F., Fletcher J., Poeckert R., 1981, ApJ, 247, 569
Braithwaite J., Spruit H. C., 2017, Royal Soc. Open Sci., 4, 160271
Brandenburg A., Subramanian K., 2005, Phys. Rep., 417, 1
Buccino A. P., Mauas P. J., 2008, A&A, 483, 903
Bullard E., Gellman H., 1954, Philos. Trans. Royal Soc. A, 247, 213
Buonaura B., Caccin B., 1982, A&A, 111, 113
Cakirli O., İbanoğlu C., Frasca A., 2007, A&A, 474, 579
Campbell W., 1899, ApJ, 10, 178
Casagrande L., Schoenrich R., Asplund M., Cassisi S., Ramirez I., Melendez J., Bensby T., Feltzing S., 2011, A&A, 530, A138
Castelaz M. W., 1989, AJ, 97, 1184
Chang S.-W., Protopapas P., Kim D.-W., Byun Y.-I., 2013, AJ, 145, 132
Charbonneau P., Steiner O., 2012, Solar and Stellar Dynamos. Springer, Berlin, Heidelberg
Chen P., Liu J., Shan H., 2017, AJ, 153, 218
Childress S., Soward A., 1972, Phys. Rev. Lett., 29, 837
Cincunegui C., Díaz R., Mauas P., 2007, A&A, 469, 309
Conti P. S., 1970, PASP, 83, 207
Cotten T. H., Song I., 2016, ApJS, 225, 15
Cousins A. W. J., 1971, R. Obs. Ann., 7, 86
Cowling T., 1945, MNRAS, 105, 166
David T. J., Hillenbrand L. A., 2015, ApJ, 804, 146
Da Silva R., de Mello G. P., Milone A., da Silva L., Ribeiro L., Rocha-Pinto H., 2012, A&A, 542, A84
Demarque P., Roeder R., 1967, ApJ, 147, 1188
Dempsey R. C., Bopp B. W., Henry G. W., Hall D. S., 1993, ApJS, 86, 293
Docobo J., Andrade M., 2013, MNRAS, 428, 321
Dolag K., Kachelriess M., Ostapchenko S., Tomas R., 2010, ApJ, 727, L4
Donati J.-F., 2003, in Javier T.-B., Jorge S. A., eds, ASP Conf. Ser. Vol. 307, Solar Polarization. Astron Soc. Pac., San Francisco, p. 41
Donati J.-F., Semel M., Rees D., 1992, A&A, 265, 669
Donati J.-F., Semel M., Carter B., Rees D., Cameron A. C., 1997, MNRAS, 291, 658
Donati J.-F., Catala C., Landstreet J., Petit P., 2006a, in Casini R., Lites B. W., eds, ASP Conf. Ser., Vol. 358, Solar Polarization 4. Astron. Soc. Pac., San Francisco, p. 362
Donati J.-F. et al., 2006b, MNRAS, 370, 629
Dravins D., 1982, ARA&A, 20, 61
Dravins D., 2008, A&A, 492, 199
Duncan D. K. et al., 1991, ApJS, 76, 383
Duquennoy A., Mayor M., 1988, A&A, 195, 129
Duquennoy A., Mayor M., Halbwachs J.-L., 1991, ApJS, 88, 281
Edwards T., 1976, AJ, 81, 245
Eggen O. J., 1960, MNRAS, 120, 540
Eggleton P., Pringle J., Division N. A. T. O. S. A., 1985, Interacting Binaries. D. Reidel Pub. Co., Dordrecht
Ertel S. et al., 2016, A&A, 595, A44
Evans D. S., Menzies A., Stoy R., 1957, MNRAS, 117, 534
Fekel F. C., Tomkin J., Williamson M. H., 2009, AJ, 137, 3900
Finsen W., 1955, MNASSA, 14, 84
Fracassini L. P., Pastori L., Covino S., Pozzi A., 2001, A&A, 367, 521
Fuhrmann K., 2008, MNRAS, 384, 173
Gaia collaboration et al., 2018, A&A, 616, A1
García R. A., Mathur S., Salabert D., Ballot J., Régulo C., Metcalfe T. S., Baglin A., 2010, Science, 329, 1032
Gasteyer C., 1954, AJ, 59, 243
Giampapa M. S., Rosner R., 1984, ApJ, 286, L19
Gilman P. A., 1980, IAU Colloquium, Vol 51. Cambridge Univ. Press, Cambridge, p. 19
Glass I. S., 1974, MNSSA, 33, 53
Glebocki R., Gnacinski P., 2005, 13th Cambridge Workshop on Cool Stars, Stellar Systems and the Sun, Vol. 560. Hamburg, Germany, p. 571
Gomez A., Abt H. A., 1982, PASP, 94, 650
Gontcharov G., 2012, Astron. Lett, 38, 771
Gontcharov G. A., Kiyaeva O. V., 2010, New Astron., 15, 324
Gray D., 1980, ApJ, 235, 508
Gray D., 1981, ApJ, 251, 583
Gray D. F., 1982, ApJ, 255, 200
Gray D. F., 1983, PASP, 95, 252
Gray D. F., 1989, PASP, 101, 832
Gray D., 1992, in Page D., Hirsch J. G., eds, ASP Conf. Ser. Vol. 26, Cool Stars, Stellar Systems, and the Sun, Proceedings of the 7th Cambridge Workshop. Astron. Soc. Pac., San Francisco, p. 127
Gray D. F., 2010, ApJ, 710, 1003
Gray D. F., Hatzes A. P., 1997, ApJ, 490, 412
Gray D. F., Nagel T., 1989, ApJ, 341, 421
Gray D. F., Toner C. G., 1986, PASP, 98, 499
Gray R., Napier M., Winkler L., 2001, AJ, 121, 2148
Gray R. O., Corbally C. J., Garrison R. F., McFadden M. T., Bubar E. J., McGahee C. E., O'Donoghue A. A., Knox E. R., 2006, AJ, 132, 161
Griffin R., 1999, Observatory, 119, 272
Griffin R., 2000, Observatory, 120, 1
Grossmann-Doerth U., Schuessler M., Solanki S. K., 1989, A&A, 221, 338
Grunhut J. H. et al., 2017, MNRAS, 465, 2432
Gullikson K., Kraus A., Dodson-Robinson S., 2016, AJ, 152, 40
Hale G. E., 1908, ApJ, 28, 315
Hall D. S., 1991, in Tuominen I., Moss D., Rudiger G., eds, IAU Colloquium, Vol. 130. Cambridge Univ. Press, Cambridge, p. 353
Han I. et al., 2018, MNRAS, 479, 1427
Hartkopf W. I., McAlister H. A., Franz O. G., 1989, AJ, 98, 1014
Hartmann L. W., Noyes R. W., 1987, ARA&A, 25, 271
Hatzes A. P., Cochran W. D., Endl M., McArthur B., Paulson D. B., Walker G. A., Campbell B., Yang S., 2003, ApJ, 599, 1383
Heintz W., 1986, ApJS, 64, 1
Herald D., Sinnott R, 2014, JBAA, 124, 247
Hoffleit D., 1991, Catalogue of bright stars, 3rd edn. Yale University Observatory, New Haven, CT
Howard R., Stenflo J. O., 1972, Sol. Phys., 22, 402
Isaacson H., Fischer D., 2010, ApJ, 725, 875
Jofre P., Heiter U., Maia M., Soubiran C., Worley C., Hawkins K., Blanco-Cuaresma S., Rodrigo C., 2018, Res. Notes AAS, 2, 152
Johnson H., Morgan W., 1953, ApJ, 117, 313
Kochukhov O., 2003, A&A, 404, 669
Kochukhov O., 2016, in Rozelot J.-P., Neiner C., eds, Cartography of the Sun and the Stars. Springer, Berlin, p. 77.
Kochukhov O., Ryabchikova T., Bagnulo S., Curto G. L., 2008, A&A, 479, L29
Kochukhov O. et al., 2017, Astron. Nachr., 338, 428
Konacki M., Muterspaugh M. W., Kulkarni S. R., Hełminiak K. G., 2010, ApJ, 719, 1293
Kraft R. P., 1967, ApJ, 150, 551
Krause F., Radler K., 1980, Mean-Field Magnetohydrodynamics and Dynamo Theory. Akademie-Verlag, Berlin
Kuker M., Rudiger G., 2005, A&A, 433, 1023
Kuker M., Rudiger G., 2007, Astron. Nachr., 328, 1050
Kulander J. L., Jefferies J. T., 1966, ApJ, 146, 194
Kurtz D., 1989, MNRAS, 238, 261

Landstreet J., Kupka F., Ford H., Officer T., Sigut T., Silaj J., Strasser S., Townshend A., 2009, A&A, 503, 973
Lignières F., Petit P., Böhm T., Aurière M., 2009, A&A, 500, L41
Lindegren L., Dravins D., 2003, A&A, 401, 1185
Lipunov V. et al., 2016, A&A, 588, A90
Makaganiuk V. et al., 2011, A&A, 525, A97
Malkov O. Y., Tamazian V. S., Docobo J. A., Chulkov D. A., 2012, A&A, 546, A69
Marsakov V. A., Shevelev Y. G., 1995, Bull. Inf. Cent. Donnees Stellaires, 47, 13
Marsden S., Petit P., Jeffers S., do Nascimento J.-D., Carter B., Brown C., 2013, Proc. IAU Symp. 302, 9, 138
Marsden S. et al., 2014, MNRAS, 444, 3517
Martinez-Arnaiz R., Maldonado J., Montes D., Eiroa C., Montesinos B., 2010, A&A, 520, A79
Mason B. D., Wycoff G. L., Hartkopf W. I., Douglass G. G., Worley C. E., 2001, AJ, 122, 3466
Mathys G., 1995, A&A, 293, 733
McDonald I., Zijlstra A. A., Watson R. A., 2017, MNRAS, 471, 770
McLaughlin D. B., 1947, ApJ, 105, 497
Mengel M. et al., 2016, MNRAS, 459, 4325
Mestel L., 1966, MNRAS, 133, 265
Mestel L., 1967, in Cameron R., ed., Magnetic and Related Stars, Mono Book Corp., p. 101
Mestel L., 2012, International Series of Monographs on Physics, Vol. 154, Stellar Magnetism, 2nd edn. OUP, Oxford
Mestel L., Spitzer L., 1956, MNRAS, 116, 503
Middelkoop F., 1982, A&A, 107, 31
Mizusawa T. F., Rebull L. M., Stauffer J. R., Bryden G., Meyer M., Song I., 2012, AJ, 144, 135
Moffatt H., 1978, Magnetic Field Generation in Electrically Conducting Fluids. Cambridge Univ. Press, Cambridge
Montesinos B. et al., 2016, A&A, 593, A51
Morgenthaler A. et al., 2012, A&A, 540, A138
Moss D., 2001, in Mathys G., Solanki S. K., Wickramasinghe D. T., eds, ASP Conf. Ser. Vol. 248, Magnetic Fields Across the Hertzsprung-Russell Diagram. Astron. Soc. Pac., San Francisco, p. 305
Moutou C. et al., 2007, A&A, 473, 651
Muterspaugh M. W., Lane B. F., Konacki M., Burke B. F., Colavita M. M., Kulkarni S. R., Shao M., 2005, AJ, 130, 2866
Muterspaugh M. W. et al., 2008, AJ, 135, 766
Muterspaugh M. W., Lane B. F., Kulkarni S. R., Konacki M., Burke B. F., Colavita M. M., Shao M., 2010, AJ, 140, 1631
Muterspaugh M. W. et al., 2015, AJ, 150, 140
Neiner C., Lampens P., 2015, MNRAS, 454, L86
Neiner C., Mathis S., Alecian E., Emeriau C., Grunhut J., 2015, IAU Symposium, 305, 61
Neiner C., Wade G., Marsden S., Blazère A., 2017a, in Zwintz K., Poretti E., eds, Second BRITE-Constellation Science Conference, Vol. 5, Polish Astronomical Society, Innsbruck, Austria, p. 86
Neiner C., Wade G., Sikora J., 2017b, MNRAS, 468, L46
Noyes R. W., 1984, Adv. Space Res., 4, 151
O'Toole S., Jones H., Tinney C., Butler R., Marcy G., Carter B., Bailey J., Wittenmyer R., 2009, ApJ, 701, 1732
Olspert N., Lehtinen J. J., Käpylä M. J., Pelt J., Grigorievskiy A., 2018, A&A, 619, A6
Owens M. J., Forsyth R. J., 2013, Living Rev. Sol. Phys., 10, 5
Pace G., 2013, A&A, 551, L8
Parker E. N., 1955, ApJ, 122, 293
Parker E., 1979, Cosmical Magnetic Fields: Their Origin and Their Activity. Clarendon Press, Oxford
Petit P. et al., 2005, MNRAS, 361, 837
Pinsonneault M., DePoy D., Coffee M., 2001, ApJ, 556, L59
Piskunov N., Valenti J., 2002, A&A, 385, 1095
Piskunov N. et al., 2011, Messenger, 143, 7
Preston G. W., Sturch C., 1967, in Cameron R., ed., Magnetic and Related Stars, Mono Book Corp., p. 111
Prieto C.A., Lambert D. L., 1999, Astron. Astrophys., 352, 555
Raghavan D. et al., 2010, ApJS, 190, 1
Reiners A., Basri G., 2009, A&A, 496, 787
Rice J. B., Hill G. a., 1988, PASP, 100, 73
Roberts P. H., Soward A. M., 1992, Annu. Rev. Fluid Mech., 24, 459
Roettenbacher R. M. et al., 2016, Nature, 533, 217
Roman N. G., 1950, ApJ, 112, 554
Ryabchikova T., Piskunov N., Kurucz R., Stempels H., Heiter U., Pakhomov Y., Barklem P. S., 2015, Phys. Scr., 90, 054005
Saar S., 1991, in Tuominen I., Moss D., Rudiger G., eds, IAU Colloquium, Vol 130. Cambridge Univ. Press, Cambridge, p. 389
Saikia S. B. et al., 2018, A&A, 616, A108
Samus N., Kazarovets E., Durlevich O., Kireeva N., Pastukhova E., 2017, Astron. Rep., 61, 80
Sato S., Cuntz M., Olvera C. G., Jack D., Schr'oder K.-P., 2014, Int. J. Astrobiol., 13, 244
Scardia M., 1980, Astron. Nachr., 301, 95
Schatzman E., 1962, Ann. Astrophys., 25, 18
Schmitt J., Golub L., Harnden F., Jr, Maxson C., Rosner R., Vaiana G., 1985, ApJ, 290, 307
Schrijver C., 1987, in Linsky J. L., Stencel R. E., eds, Cool Stars, Stellar Systems, and the Sun. Lecture Notes in Physics, Vol. 291. Springer, Berlin, p. 135
Schrijver C., Dobson A. K., Radick R. R., 1989, ApJ, 341, 1035
Schussler M., 1975, A&A, 38, 263
Schwarzschild M., 1950, ApJ, 112, 222
Semel M., 1989, A&A, 225, 456
Semel M., Li J., 1996, Sol. Phys., 164, 417
Semel M., Donati J.-F., Rees D., 1993, A&A, 278, 231
Semel M., Vélez J. R., González M. M., Ramos A. A., Stift M., Ariste A. L., Leone F., 2009, A&A, 504, 1003
Shultz M. et al., 2019, MNRAS, 490, 4154
Shulyak D., Ryabchikova T., Kochukhov O., 2013, A&A, 551, A14
Sikora J., Wade G., Power J., Neiner C., 2018, MNRAS, 483, 2300
Silvester J., Wade G., Kochukhov O., Bagnulo S., Folsom C., Hanes D., 2012, MNRAS, 426, 1003
Simon T., Fekel F. C., Jr, 1987, ApJ, 316, 434
Skumanich A., 1972, ApJ, 171, 565
Slovak M., Barnes T., 2002, Bull. Am. Astron. Soc., 34, 655
Snik F., Jeffers S., Keller C., Piskunov N., Kochukhov O., Valenti J., Johns-Krull C., 2008, in McLean I. S., Casali M, eds, Proc. SPIE Conf. Ser. Vol. 7014, Ground-based and Airborne Instrumentation for Astronomy II. SPIE, Bellingham, p. 70140O
Solanki S. K., 1993, Space Sci. Rev., 63, 1
Soubiran C., Le Campion J.-F., De Strobel G. C., Caillo A., 2010, A&A, 515, A111
Soubiran C. et al., 2018, A&A, 616, A7
Spitzer L. J., 1958, in Lehnert B., ed., Electromagnetic Phenomena in Cosmical Physics, Vol. 6. Cambridge Univ. Press, Cambridge, p. 169
Spruit H., 2002, A&A, 381, 923
Stenflo J., 1985, in de Jager C., Svestka Z., eds, Progress in Solar Physics. Springer, Berlin, p. 189
Stenflo J. O., 1989, A&AR, 1, 3
Stix M., 1982, in Fricke W., Teleki G., eds, Sun and Planetary System. Astrophysics and Space Science Library, Vol. 96. Springer, Berlin, p. 63
Strassmeier K. G., Fekel F. C., Bopp B. W., Dempsey R. C., Henry G. W., 1990, ApJS, 72, 191
Struve O., 1875, MNRAS, 35, 367
Suchkov A. A., Makarov V. V., Voges W., 2003, ApJ, 595, 1206
Takeda G., Ford E. B., Sills A., Rasio F. A., Fischer D. A., Valenti J. A., 2007, ApJS, 168, 297
Tokovinin A., 2014, AJ, 147, 87
Tokovinin A., Lépine S., 2012, AJ, 144, 102
Toner C., Gray D. F., 1988, ApJ, 334, 1008
Torres G., Andersen J., Giménez A., 2010, A&AR, 18, 67
Trilling D. E. et al., 2007, ApJ, 658, 1289
Trust O., Jurua E., De Cat P., Joshi S., 2020, MNRAS, 492, 3143
Uitenbroek H., 2003, ApJ, 592, 1225

Ulmschneider P., Priest E., Rosner R., 1991, Mechanisms of Chromospheric and Coronal Heating: Proceedings of the International Conference, Heidelberg, June 1990. Springer, Berlin Heidelberg
Vaughan A. H., Preston G. W., Wilson O. C., 1978, PASP, 90, 267
Vican L., 2012, AJ, 143, 135
Voges W. et al., 1999, A&A, 349, 389
Wade G., Donati J.-F., Landstreet J., Shorlin S., 2000, MNRAS, 313, 851
Wade G. A. et al., 2016, MNRAS, 456, 2
Walter F. M., Matthews L. D., Linsky J. L., 1995, ApJ, 447, 353
Watson C. L., Henden A, Price A, 2006, The Society for Astronomical Sciences 25th Annual Symposium on Telescope Science, 25, p. 47
Weber E. J., Davis L., Jr, 1967, ApJ, 148, 217
Wenger M. et al., 2000, A&AS, 143, 9
Wilson E. B., 1927, JASA, 22, 209
Wilson O., 1966, ApJ, 144, 695
Wilson O., 1978, ApJ, 226, 379
Wolff S. C., Wolff R. J., 1970, ApJ, 160, 1049
Wolff S. C., Heasley J. N., Varsik J., 1985, PASP, 97, 707
Worley C. E., Heintz W. D., 1983, PUSNO, 24, 1
Wright C. O., Egan M. P., Kraemer K. E., Price S. D., 2003, AJ, 125, 359
Wright J. T., Marcy G. W., Butler R. P., Vogt S. S., 2004, ApJS, 152, 261
Zeldovich I. B., Ruzmaikin A. A., Sokolov D. D., 1983, Magnetic Fields in Astrophysics. Gordon and Breach, New York

APPENDIX A: NOTES ON INDIVIDUAL STARS

Below is background information and summary of the results for individual 25 transition project stars. Information on the 31 BRITEpol stars used in this paper can be found in Marsden et al. (in preparation). We estimated the rotational period of our stars using literature values for $v \sin i$, stellar radius, and assuming an inclination of 60 deg.

A1 σ Boo

σ Boo (HIP 71284) is a young triple star system with component V magnitudes 4.50, 10.66, 12.08, respectively (Mason et al. 2001). Component B was separated from the primary by 215 arcsec in 2012 and component C by 222 arcsec in 2002 based on data from the continuously updated Washington Double Star Catalogue (Mason et al. 2001). σ Boo is classified as a standard F2V star in the MK classification system Johnson & Morgan (), while Samus et al. (2017) classify it as F3V. Hoffleit (1991) suggests σ Boo is possibly a δ Scuti type variable, although Chang et al. (2013) did not include it in a recent catalogue of 1578 δ Scuti variables.

We obtained fourteen polarized spectra for σ Boo over a 2.6 h interval on 2017 January 14 corresponding to 1.5 per cent of the estimated rotational period of 6.8 d. The mean LSD profile (Fig. B2) combined 6304 lines, and a magnetic detection was obtained from the mean LSD Stokes V profile. We estimated B_l at -1.4 ± 0.4 G. Our radial velocity determination $+0.28 \pm 0.01$ km s^{-1} (Table 5) is similar to the value of $+0.37 \pm 0.09$ km s^{-1} in Anderson & Francis (2012), and our S-index 0.240 $\pm$ 0.004 (Table 5) is within the range 0.156–0.253 from Pace (2013).

A2 ϵ Lib

ϵ Lib (HIP 75379) is a single-lined spectroscopic binary (Tokovinin 2014) first observed by Campbell (1899). The system consists of spectral types F4V (Abt 2009) and K5-M2 (Castelaz 1989) with an orbital period of 229 d (Malkov et al. 2012). The secondary is unresolved by interferometry (Hartkopf, McAlister & Franz 1989).

We obtained fourteen polarized spectra for ϵ Lib over a 3.5 h interval on 2017 March 13, corresponding to 2.2 per cent of the estimated rotational period of 12.7 d. The mean LSD profile (Fig. B3) combined 6829 lines, and shows a magnetic detection. We estimated B_l at -0.5 ± 0.1 G, based on the mean LSD. Our radial velocity determination -13.98 ± 0.70 km s^{-1} (Table 5) is larger than the value of -9.8 ± 0.7 km s^{-1} in Anderson & Francis (2012). We determined an S-index of 0.180 $\pm$ 0.012 (Table 5) and this is the first value in the literature.

A3 ϵ Cet

ϵ Cet (HIP 12390) is a spectroscopic binary (Eggleton, Pringle & Division 1985; Duquennoy & Mayor 1988), consisting of F5V+F6V components (Fuhrmann 2008) with a short orbital period of 2.62 yr (Finsen 1955). The system was described as astrometrically, photometrically, and spectroscopically elusive by Fuhrmann (2008) with the stars being difficult to separate. Early radial velocity measurements of ϵ Cet were useless due to scatter caused by blending of two components of nearly equal brightness (Duquennoy & Mayor 1988). This was due to the high rotational velocity of one of the components, combined with a maximum Doppler displacement of 15 kms^{-1} (Duquennoy & Mayor 1988). The spectra of ϵ Cet are mostly not able to be individually separated, and the use of assumptions are required to untangle them (Docobo & Andrade 2013). The angular separation of the components was 0.1 arcsec in 2015 (Mason et al. 2001).

We obtained sixteen polarized spectra for ϵ Cet over a 6.0 h interval on 2016 September 21, corresponding to 2.5 per cent of the estimated rotational period of 10.2 d. The mean LSD profile (Fig. B4) combined 6693 lines, and a magnetic detection was obtained from the mean LSD Stokes V profile. We are unable to determine whether the magnetic detection was on the F5V or F6V components because the two stars could not be separated spectroscopically. We estimated B_l at $+0.6 \pm 0.1$ G. Our radial velocity determination $+15.81 \pm 0.26$ km s^{-1} (Table 5) is similar to the value of $+15.49 \pm 0.19$ km s^{-1} in Anderson & Francis (2012), and our S-index 0.186 $\pm$ 0.003 (Table 5) was less than 0.219 in Pace (2013).

A4 α Com

α Com (HIP 64241) is a triple star consisting of a double-lined spectroscopic binary (Duquennoy, Mayor & Halbwachs 1991) of F5V and F6V components (Edwards 1976; Soubiran et al. 2018), and a V magnitude 10.2 component with an angular separation of 85 arcsec in 2014 based on data from the continuously updated Washington Double Star Catalogue (WDS) (Mason et al. 2001). The system was first observed by Struve (1875) who reported that occultations were observed (Muterspaugh et al. 2015). Roman (1950) describes α Com as a close visual binary, with equal F5 components, and showing weak lines. Hartkopf et al. (1989) describes α Com as a 'lovely edge-on system' with an orbital inclination close to 90 deg, and suggested a partial eclipse was possibly missed in early 1990. The eclipsing binary has the third longest period known (P = 25.85 yr) (Lipunov et al. 2016), with only eight eclipsing stars having periods longer than 10 yr.

We obtained twenty-seven polarized spectra for α Com over a 3.8 h interval on 2017 February 16, corresponding to 5.3 per cent of the estimated rotational period of 3.0 d. The mean LSD profile (Fig. B5) combined 7628 lines, and a magnetic detection is visible in the Stokes V profile. We are unable to determine whether the magnetic detection was on the F5V or F6V components because the two stars could not be separated spectroscopically.

We estimated B_l at $+3.1 \pm 0.3$ G. Our radial velocity determination -18.02 ± 0.27 km s^{-1} (Table 5) is larger the value of -16.05 ± 0.21 km s^{-1} in Anderson & Francis (2012), and our S-index 0.272 ± 0.008 (Table 5) is smaller than the 0.308 in Pace (2013).

A5 ω Dra

ω Dra (HIP 86201) is a triple star system consisting of double-lined spectroscopic binary (Abt & Levy 1976; Konacki et al. 2010), and a V magnitude 13.2 common proper motion companion with an angular separation of 70 arcsec (Abt & Levy 1976; Fekel, Tomkin & Williamson 2009). The mases of the primary component are 1.46 M$_\odot$ and secondary 1.18 M$_\odot$ (Konacki et al. 2010), which corresponds to spectral types F2V and F8V, respectively. The two F-stars have an orbital period of 5.28 d, with a nearly face-on (i = 151 deg), circular orbit (e = 0.00220) (Konacki et al. 2010).

We obtained sixteen polarized spectra for ω Dra over a 3.6 h interval on 2017 May 5, corresponding to 1.5 per cent of the estimated rotational period of 10.1 d. The spectral lines of two F-stars had a relatively wide separation which enabled us to run LSD analysis and FAP for the two components separately. The F2V star did not show a magnetic detection, while a magnetic field was detected on the F8V component. The mean LSD profile (Fig. B6) for the F8V star combined 9099 lines and a strong signal is visible in the Stokes V profile. We estimated B_l for the F8V component at -2.9 ± 1.2 G and the F2V component $+0.2 \pm 0.1$ G. Our radial velocity determination for the F2V was -47.74 ± 0.71 km s^{-1}, and the F8V $+28.42 \pm 0.89$ km s^{-1} (Table 5). Our S-index estimation for the F2V component was 0.240 ± 0.007 and for the F8V 0.307 ± 0.008 (Table 5) which were both greater than the range of 0.174–0.191 from Pace (2013).

A6 h Dra

h Dra (HIP 82860) is a single-lined spectroscopic binary consisting of F8V and M1V components (Abt 2009). The faint companion orbits with a period of 52.1 d (Abt & Levy 1976) and has an estimated mass of 0.54 M$_\odot$ assuming it is a main-sequence star (Behr et al. 2009). The Yale Bright Star Catalogue (Hoffleit 1991) lists h Dra as a possible δ Scuti-type variable with a V magnitude range of 4.85–4.91, and the star shows an excess emission in the infrared, indicating a possible debris disc (Cotten & Song 2016).

We obtained sixteen polarized spectra for h Dra over a 3.7 h interval on 2017 May 9, corresponding to 1.8 per cent of the estimated rotational period of 6.0 d. The mean LSD profile (Fig. B7) combined 7168 lines, and a strong magnetic detection is visible in the Stokes V profile. We estimated B_l at $+8.3 \pm 0.9$ G. Our radial velocity determination -32.95 ± 0.03 km s^{-1} (Table 5) is larger than the value of -21.00 ± 0.80 km s^{-1} in Anderson & Francis (2012), and our S-index 0.251 ± 0.036 (Table 5) is greater than the range 0.195–0.219 given in Pace (2013).

A7 36 UMa

36 UMa (HIP 51459) is a multiple star system with high proper motion (Wenger et al. 2000). Component A is an F8V star with V magnitude 4.9, forming a wide binary, with an estimated separation of 123 arcsec from the spectroscopic binary BC in 2016, based on data from the continuously updated WDS (Mason et al. 2001). We obtained twelve polarized spectra for 36 UMa over a 2.6 h interval on 2017 January 13, corresponding to 1.2 per cent of the estimated rotational period of 8.2 d. The mean LSD profile (Fig. B8) combined 7058 lines, and showed a magnetic detection. We estimated B_l at -0.3 ± 0.1 G. Our radial velocity determination 8.71 ± 0.01 km s^{-1} (Table 5) is close to the value of 8.69 ± 0.09 km s^{-1} in Anderson & Francis (2012), and our S-index 0.193 ± 0.011 (Table 5) is close to the range of 0.193 to 0.203 given in Pace (2013) in 1978 December and May.

A8 17 Crt

17 Crt (HIP 56280) is a visual double star consisting of two F8V components (Gray, Napier & Winkler 2001) separated by 9.7 arcsec in 2012, based on data from the continuously updated Washington Double Star Catalogue (Mason et al. 2001). We obtained eighteen polarized spectra for 17 Crt A over a 4.4 h interval on 2017 March 5, corresponding to 1.9 per cent of the estimated rotational period of 10.0 d. The mean LSD profile (Fig. B9) combined 8309 lines, and shows a magnetic detection. We estimated B_l at $+0.4 \pm 0.1$ G. Our radial velocity determination $+5.85 \pm 0.01$ km s^{-1} (Table 5) is close to the value of $+5.80 \pm 0.40$ km s^{-1} in Anderson & Francis (2012), and our S-index 0.157 ± 0.013 (Table 5) is lower than the range 0.158–0.167 given in Pace (2013).

A9 γ CrA

γ CrA (HIP 93825) is a close visual double star of equal mass F8V components (Heintz 1986). Components AB have an orbital period of approximately 120 yr (Evans, Menzies & Stoy 1957) and an estimated angular separation of 1.4 arcsec in 2017 based on data from the continuously updated Washington Double Star Catalogue (Mason et al. 2001). According to Raghavan et al. (2010) there is another unresolved companion implied by proper motion acceleration.

We obtained 12 spectra of γ CrA (component B) over a 1.5 h interval on 2017 June 6, corresponding to 0.5 per cent of the estimated rotation period of 12.6 d. Component A was observed on 2017 June 7 and showed no magnetic detection (B_l estimated at -0.1 ± 0.1 G), based on an LSD profile of 14 spectra and 7613 lines. We detected a magnetic field on component B using the mean LSD (Fig. B10) of 12 spectra and combining 7608 lines. We estimated B_l at $+5.6 \pm 0.8$ G. Our radial velocity determination of -52.82 ± 0.06 km s^{-1} (Table 5) was similar to the value of -51.60 ± 0.30 km s^{-1} from Anderson & Francis (2012), and our S-index 0.139 ± 0.015 (Table 5) was smaller than 0.165 found in Pace (2013).

A10 τ Psa

τ Psa (HIP 109422) is a single, high proper motion, F6V star (Wenger et al. 2000) with close to solar metallicity (Soubiran et al. 2010). It has a theoretical stellar convection zone mass of 0.002 M$_\odot$ and convection zone depth of 0.236 M$_\odot$ (Takeda et al. 2007). τ Psa has been identified as a potential candidate to host a debris-disc, as shown by emission of an infrared excess (Ertel et al. 2016). We obtained fourteen polarized spectra for τ Psa over a 4.3 h interval on 2016 October 15, corresponding to 3.5 per cent of the estimated rotational period of 5.1 d. The mean LSD profile (Fig. B11) combined 8637 lines, and a marginal magnetic detection was obtained from the mean LSD Stokes V profile. We estimated B_l at -0.6 ± 0.2 G. Our radial velocity determination -16.11 ± 0.01 km s^{-1} (Table 5) is similar to the value of -16.23 ± 0.09 km s^{-1} in Anderson &

Francis (2012), and our S-index 0.156 ± 0.011 (Table 5) is in the range of 0.144–0.173 from Pace (2013).

A11 10 UMa

10 UMa (HIP 44248) is a multiple star system, previously located in the constellation Ursa Major, but now included in boundaries of Lynx (Griffin 1999). The system is moving as part of the Hyades stream (Eggen 1960) with a high proper motion (Wenger et al. 2000). The primary component is spectral type F3V, and the secondary component G5V (Montesinos et al. 2016). Components AB form a double-lined spectroscopic binary (Muterspaugh et al. 2010) with V magnitudes 4.18 and 6.18, respectively (Mason et al. 2001). Components AB,C form an optical binary with V magnitudes 4.03, 10.06, respectively (Mason et al. 2001). Components AB have an orbital period of 21.8 yr, and angular separation of 0.4 arcsec in 2016, according to the continuously updated WDS (Mason et al. 2001). The *ROSAT* All-Sky Survey Bright Source Catalogue lists 10 UMa as an X-Ray source (Voges et al. 1999), although it was not clear if this was due to the F-type primary, or G-type secondary star.

We obtained twenty-one polarized spectra for 10 UMa over a 3.6 h interval on 2016 December 22, corresponding to 3.4 per cent of the estimated rotational period of 3.9 d. The LSD profile combined 8930 lines and a definite magnetic detection was obtained from the mean Stokes V LSD profile. The magnetic signature visible in the Stokes V profile is aligned with the narrow-lined component of the Stokes I profile. The detection is therefore most likely due to the slower rotating (narrower lined) G5V component. We estimated B_l of 10 UMa at −4.8 ± 1.1 G, is consistent with Marsden et al. (2014) who determined B_l of 3.2 G for G-type stars.

The spectral line analysis and S-index estimation were completed on the blended spectral line, therefore contain a mix from the F3V and G5V components. Our calculated radial velocity of +27.68 ± 0.04 km s^{-1} is similar to the value of +27.80 ± 2.80 km s^{-1} in Anderson & Francis (2012). Our S-index 0.216 ± 0.007 (Table 5) is in the range of values 0.206–0.233 found in Buccino & Mauas (2008). The S-index contrasts with a survey of chromospheric activity by Martinez-Arnaiz et al. (2010) which listed 10 UMa as inactive.

A12 σ Cet

σ Cet (HIP 11783) was first identified as a triple star by McLaughlin (1947). Components AB form a wide binary (separation 346 arcsec in 1999) with common proper motion, and V magnitudes of 4.79, 8.77, respectively (Mason et al. 2001), and spectral types F5V+K2.5V (Tokovinin & Lépine 2012). Component A is a spectroscopic binary with component V magnitudes 4.75 and 10.08 (Tokovinin 2014). Glass (1974) identified σ Cet as a Southern hemisphere standard star for JHKL photometry. σ Cet belongs to a class of older F-type stars identified by Suchkov, Makarov & Voges (2003) which show X-ray emission.

We obtained seven polarized spectra for σ Cet over a 1.5 h interval on 2016 September 20, corresponding to 0.5 per cent of the estimated rotational period of 12.1 d. The mean LSD profile combined 7482 lines, and did not show a magnetic detection. We estimated B_l at 0.0 ± 0.2 G. Our radial velocity determination −29.80 ± 0.01 km s^{-1} (Table 5) is the similar to −27.50 ± 0.90 km s^{-1} in Anderson & Francis (2012). Our S-index 0.160 ± 0.001 (Table 5) is within the range of 0.157–0.197 in Pace (2013).

A13 58 Oph

58 Oph (HIP 86736) is a high proper-motion star which was classified as a standard star by Cousins (1971). It is a possible double star system whose binary nature may have been detected a visual grazing occultation of the moon in 1975 (Hoffleit 1991), however, the binary nature of 58 Oph is elusive, with a lunar occultation in 2011 failing to resolve the stellar system (Herald et al. 2016). Mason et al. (2001) lists the primary star as F5V, V magnitude 5.1, and the secondary with a V magnitude 6.90 corresponding to a spectral type of G5.

We obtained thirteen polarized spectra for 58 Oph over a 2.8 h interval on 2017 May 12, corresponding to 2.4 per cent of the estimated rotational period of 4.7 d. The mean LSD profile combined 6833 lines, and did not show a magnetic detection with an estimated B_l of +0.4 ± 0.2 G. Our radial velocity determination +10.34 ± 0.01 km s^{-1} (Table 5) is the similar to +10.20 km s^{-1} in Anderson & Francis (2012). Our S-index 0.164 ± 0.018 (Table 5) is less than 0.197 in Pace (2013).

A14 ψ Peg

ψ Peg (HIP 112447) is a relatively nearby (16 pc), high proper motion multiple star system. ψ Peg consists of a F6V (4.20 mag) primary (Wenger et al. 2000), and M1V (11.10 mag) secondary (Fracassini et al. 2001). The angular separation of components AB was 11.0 arcsec in 2015 (Mason et al. 2001). The General Catalogue of Variable Stars (Samus et al. 2017) lists ψ Peg as a variable with an amplitude of 0.02. We obtained ten polarized spectra for ψ Peg over a 1.4 h interval on 2016 August 15, corresponding to 0.7 per cent of the estimated rotational period of 9.5 d. The mean LSD profile combined 7499 lines, and did not show a magnetic detection. We estimated B_l at +0.1 ± 0.1 G. Our radial velocity determination −5.73 ± 0.01 km s^{-1} (Table 5) is similar to −5.37 ± 0.08 km s^{-1} in Anderson & Francis (2012). Our S-index 0.148 ± 0.001 (Table 5) is within the range of values 0.121–0.176 from 2002 to 2008 (Isaacson & Fischer 2010).

A15 μ Cyg

μ Cyg (HIP 107310) is a multiple star system with components AB forming an optical double, 1.8 arcsec separation in 2016 (Mason et al. 2001) and spectral type F6V+G2V (Hoffleit 1991). Component AB V magnitudes are 4.75 and 6.18 (Wenger et al. 2000) with an orbital period determined as 507.5 yr (Worley & Heintz 1983) or 840 yr (Fuhrmann 2008). We obtained fifteen polarized spectra for μ Cyg over a 2.8 h interval on 2016 August 12, corresponding to 0.9 per cent of the estimated rotational period of 12.8 d. The mean LSD profile combined 7043 lines, and did not show a magnetic detection. We estimated B_l at −0.4 ± 0.1 G. Our radial velocity determination +16.97 ± 0.02 km s^{-1} (Table 5) is the same as +16.95 ± 0.16 km s^{-1} in Anderson & Francis (2012). Our S-index 0.178 ± 0.001 (Table 5) is greater than the values 0.160 in 1981 and 0.155 in 1982 (Duncan et al. 1991).

A16 ι Psc

ι Psc (HIP 116771) is a triple star system with component V magnitudes 4.18, 14.10, and 12.51 (Mason et al. 2001). Components AB form an optical double (Hoffleit 1991) with an angular separation of 123 arcsec in 2008 (Mason et al. 2001). The International Variable Star Index (Watson 2006) lists ι Psc as a variable star with a small magnitude range of 4.11–4.14, while Johnson & Morgan (1953) list 20 Oph as a F7V standard star. The star is sharp-lined, with an overabundance of rare-earth elements (Rice & Hill 1988), while containing overall abundances less than solar (Adelman et al. 1991). The sharp spectral lines has enabled the star to be used as a radial velocity standard star (Cakirli, İbanoğlu & Frasca 2007). We obtained fourteen polarized spectra for ι Psc over a 2.0 h interval on 2016 August 16, corresponding to 1.2 per cent of the estimated rotational period of 10.5 d. The mean LSD profile combined 7502 lines, and did not show a magnetic detection. We estimated B_l at -0.2 ± 0.1 G. Our radial velocity determination $+5.77 \pm 0.01$ km s^{-1} (Table 5) was close to the value of $+5.95 \pm 0.08$ km s^{-1} in Anderson & Francis (2012). Our S-index 0.161 ± 0.001 (Table 5) is consistent with values of 0.152 in 1984, and 0.170 in 1990 (Buccino & Mauas 2008).

A17 σ02 UMa

σ02 UMa (HIP 45038) is a triple star system with V magnitudes 4.87, 8.85, and 10.32 (Mason et al. 2001). Component AB spectral types are F7IV-V+K2V Hoffleit (1991), and separated by 4.3 arscec in 2016 (Mason et al. 2001). The orbital period of AB is approximately 1500 yr (Scardia 1980). We obtained seven polarized spectra for σ02 Uma over a 2.0 h interval on 2016 December 21–22, corresponding to 0.8 per cent of the estimated rotational period of 11.0 d. The mean LSD profile combined 8648 lines, and did not show a magnetic detection. We estimated B_l at $+0.1 \pm 0.1$ G. Our radial velocity determination -3.13 ± 0.01 km s^{-1} was close to the value of -2.98 ± 0.09 km s^{-1} in Anderson & Francis (2012), and our S-index of 0.135 ± 0.014 (Table 5) was lower than the range 0.138–0.171 from Pace (2013).

A18 δ Equ

δ Equ (HIP 104858) is a well-known visual and spectroscopic binary which has been studied since the first observations by Herschel in the 1880's (Muterspaugh et al. 2005). The binary consists of F7V and G0V components (Wenger et al. 2000), with V magnitudes 5.2 and 5.3 (Hoffleit 1991). The components have an orbital period of 5.7 yr (Malkov et al. 2012) and were estimated to be separated by 0.3 arcsec in 2017 based on data from the continuously updated WDS (Mason et al. 2001). Components AB have nearly identical mass of 1.192 $M_\odot$ and 1.187 $M_\odot$ (Muterspaugh et al. 2008). δ Equ is a useful star for binary studies because it is bright, relatively close (18 pc), and contains a semimajor axis of 0".05. According to Muterspaugh et al. (2005) these features, accompanied by its short orbital period, means that it can be studied both visually and spectroscopically in a short period of time.

We obtained twelve polarized spectra for δ Equ over a 2.3 h interval on 2017 June 6, corresponding to 0.9 per cent of the estimated rotational period of 10.9 d. The mean LSD profile combined 7182 lines, and did not show a magnetic detection. We estimated B_l at $+0.7 \pm 0.2$ G. Our radial velocity determination -15.76 ± 0.05 km s^{-1} (Table 5) was close to the value of -15.85 ± 0.07 km s^{-1} in Anderson & Francis (2012), and our S-index 0.166 ± 0.016 (Table 5) was close to the value of 0.160 from Pace (2013).

A19 6 Cet

6 Cet (HIP 910) is a high proper motion single star used as a radial velocity standard (Gray 1982). It has a wide variety of spectral types quoted in the literature from F5 to F8, with Wenger et al. (2000) listing F8V. We obtained five polarized spectra for 6 Cet over a 1.0 h interval on 2017 August 10, corresponding to 0.3 per cent of the estimated rotational period of 13.1 d. The mean LSD profile combined 7659 lines, and did not show a magnetic detection. We estimated B_l at 0.0 ± 0.1 G. Our radial velocity determination $+15.14 \pm 0.01$ km s^{-1} (Table 5) was close to the value of $+14.81 \pm 0.09$ km s^{-1} in Anderson & Francis (2012), and our S-index 0.174 ± 0.001 (Table 5) is within the range of 0.136–0.180 given in Pace (2013).

A20 ζ Cnc

ζ Cnc (HIP 40167) is one of the best-known multiple star systems in the sky, first identified as a double by Mayer in 1756, and up to five components identified by lunar occultation in 1998 (Griffin 2000). Components A and B form a close visual pair with an angular separation of 1.2 arcsec in 2016 (Mason et al. 2001), and an orbital period of 59.7 yr (Gasteyer 1954). The spectral types of components AB are F8V and G0V (Wenger et al. 2000). As with many multiple star systems, there is some confusion in the literature about the naming of individual components. A comprehensive review of ζ Cnc by Griffin (2000) provides clarification on the naming the components.

We obtained three polarized spectra for ζ Cnc A over an 0.3 h interval on 2017 February 15, corresponding to 0.06 per cent of the estimated rotational period of 20.6 d. The mean LSD profile combined 8813 lines, and did not show a magnetic detection. We estimated B_l at -0.7 ± 0.4 G. Our radial velocity determination -5.24 ± 0.01 km s^{-1} (Table 5) was smaller than the value of -7.93 ± 0.08 km s^{-1} in Anderson & Francis (2012), and our S-index 0.143 ± 0.002 (Table 5) smaller than 0.160 in Pace (2013).

A21 HD 84117

HD 84117 (HIP 47592) is single, nearby, Sun-like star (O'Toole et al. 2009), with a spectral type F9V (Wenger et al. 2000). It exhibits solar-type metallicity ([Fe/H] −0.07), however is deficient in Mn, and enriched in Na and in elements of the s-process (Sr, Y, Zr, and Ba) (Da Silva et al. 2012). HD 84117 was a target for the Anglo-Australian Telescope rocky planet search (O'Toole et al. 2009), and showed a Doppler velocity variability which either indicated the star may contain multiple planets, or belong to a class of stars with unusual velocity variability. We obtained five spectra for HD 84117 over a 1.5 h interval on 2017 March 11, corresponding to 0.5 per cent of the estimated rotational period of 9.1 d. The mean LSD profile combined 8804 lines and did not show a magnetic detection. We estimated B_l at $+0.2 \pm 0.1$ G. Our radial velocity determination of $+34.80 \pm 0.01$ km s^{-1} (Table 5) was similar to the value of $+35.30 \pm 0.44$ km s^{-1} from (Anderson & Francis 2012), and our S-index 0.151 ± 0.006 (Table 5) is within the range of 0.147–0.186 between 2004 and 2009 (Pace 2013).

A22 κ Peg

κ Peg (HIP 107354) is a triple star system comprising components Ba,Bb,A (Docobo & Andrade 2013). The system departs from normal the naming convention by designating component B as the brightest. This has resulted in some confusion in naming in the literature. Spectral type of the components Ba,Bb,A are F5IV, G0V, F0IV, respectively (Docobo & Andrade 2013). Components AB orbit with a period of 11.5 yr, and components Ba,Bb have a short orbital period of 6 d (Behr et al. 2011). The V magnitudes of AB are 4.94 and 5.04 (Mason et al. 2001). The κ Peg system is difficult to observe (Barlow & Scarfe 1977) because of nearly equal magnitudes of the brightest two components, their small angular separation, high orbital inclination, and long orbital period.

We obtained thirty-four polarized spectra for κ Peg over a 5.3 h interval on 2016 August 16, corresponding to 2.4 per cent of the estimated rotational period of 9.0 d. It was difficult to disentangle the spectra, and it was not possible to determine which of the components had the magnetic detection. The mean LSD profile combined 6684 lines, and a magnetic detection was obtained from the mean LSD Stokes V profile. The Stokes V signal shows a double positive lobe, aligning with both the F5V and G0V components. We estimated B_l at $+0.9 \pm 0.3$ G. Our radial velocity determination $-21.45 \pm 2.62\,\mathrm{km\,s^{-1}}$ (Table 5) is different to the value of $-0.80 \pm 0.20\,\mathrm{km\,s^{-1}}$ in Anderson & Francis (2012) due to the binary nature of the system. Our S-index 0.237 ± 0.001 (Table 5) is greater than the value of 0.170 in Pace (2013).

A23 20 Oph

20 Oph (HIP 82369) is an high proper motion, spectroscopic binary consisting of F7V (Wenger et al. 2000) and a secondary later than G2V (Gomez & Abt 1982). Abt & Levy (1976) calculated an orbit of 3.5 yr from radial velocity measurements, however the secondary has never been detected with speckle interferometry (Gontcharov & Kiyaeva 2010). We obtained fifteen polarized spectra for 20 Oph over a 3 h interval on 2016 August 8, corresponding to 1.0 per cent of the estimated rotational period of 12.3 d. The mean LSD profile combined 8378 lines, and a magnetic detection was obtained from the mean LSD Stokes V profile. Due to the blended spectra it was not possible to say which component contained the magnetic detection. We estimated B_l at $+0.7 \pm 0.2$ G. Our radial velocity determination $-0.30 \pm 0.01\,\mathrm{km\,s^{-1}}$ (Table 5) is similar to the value of $-1.60 \pm 0.60\,\mathrm{km\,s^{-1}}$ in Anderson & Francis (2012), and our S-index 0.227 ± 0.001 (Table 5) is the only measurement in the literature.

APPENDIX B: LSD PROFILES FOR STARS WITH A MAGNETIC DETECTION

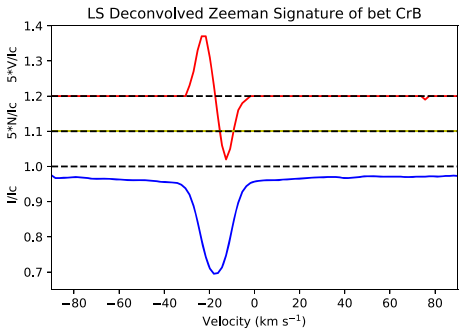

Figure B1. LSD profile (single spectra) for β CrB on 2017 April 23. The upper plot (red) shows the Stokes V profile (y-axis expanded and shifted up by 0.2 to allow better visibility). The middle plot (yellow) shows the null profile (expanded and shifted up by 0.1). The lower plot (blue) shows the Stokes I profile.

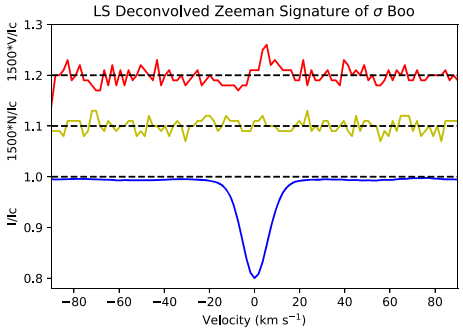

Figure B2. Mean LSD profile (combining 14 spectra) for σ Boo (F3V) on 2017 January 14. The plot is described in Fig. B1.

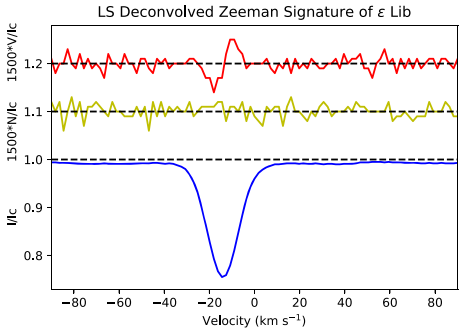

Figure B3. Mean LSD profile (combining 14 spectra) for ϵ Lib (F4V+K5-M2) on 2017 March 13. The plot is described in Fig. B1.

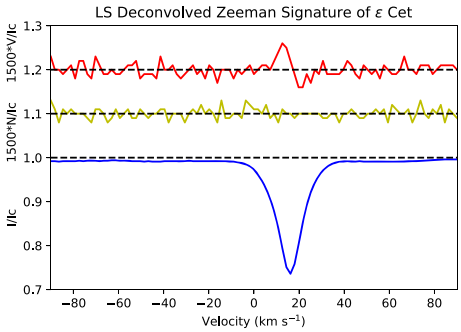

Figure B4. Mean LSD profile (combining 16 spectra) for ϵ Cet (F5V+F6V) on 2016 September 21. The plot is described in Fig. B1.

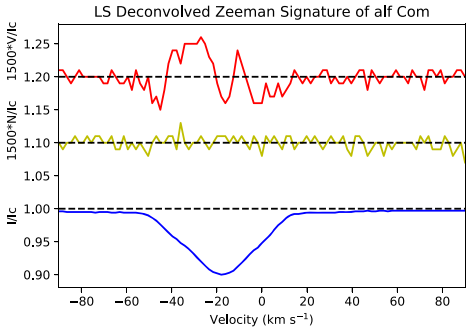

Figure B5. Mean LSD profile (combining 27 spectra) for α Com (F5V+F6V) on 2017 February 16. The plot is described in Fig. B1.

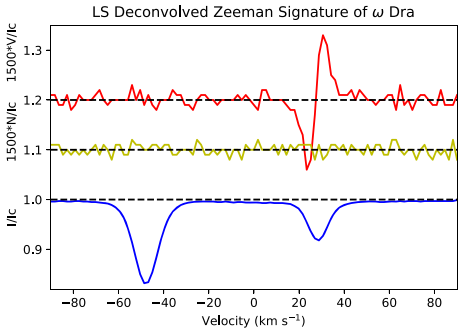

Figure B6. Mean LSD profile (combining 16 spectra) for ω Dra (F2V+F8V) on 2017 May 5. The F8 component with a definite magnetic signature is located at $+28.4\,\mathrm{km\,s^{-1}}$. The plot is described in Fig. B1.

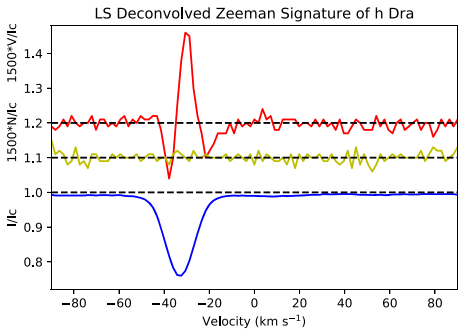

Figure B7. Mean LSD profile (combining 16 spectra) for h Dra (F8V+M1V) on 2017 May 9. The plot is described in Fig. B1.

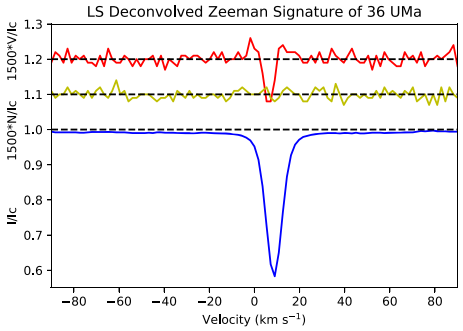

Figure B8. Mean LSD profile (combining 12 spectra) for 36 UMa (F8V+K7) on 2017 January 13. The plot is described in Fig. B1.

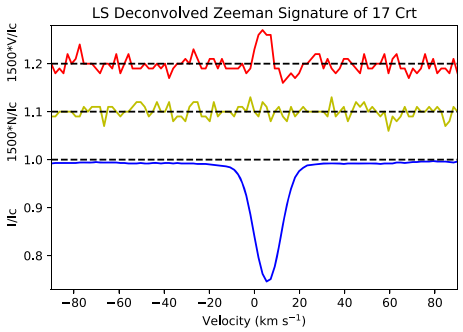

Figure B9. Mean LSD profile (combining 18 spectra) for 17 Crt (F8V+F8V) on 2017 March 5. The plot is described in Fig. B1.

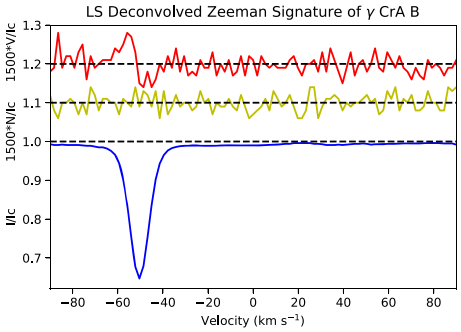

Figure B10. Mean LSD profile (combining 12 spectra) for γ CrA B (F8V) on 2017 June 6. The plot is described in Fig. B1.

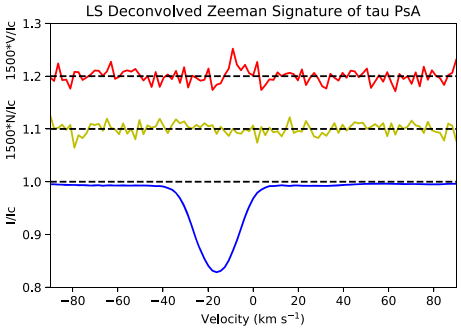

Figure B11. Mean LSD profile (combining 14 spectra) for τ PsA (F6V) on 2016 October 14. The plot is described in Fig. B1.

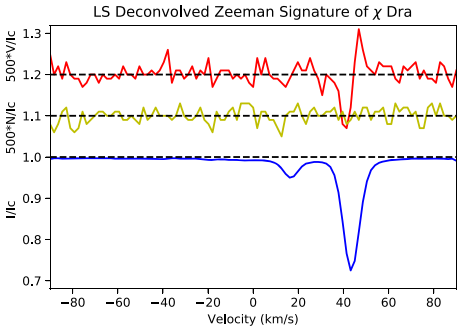

Figure B12. LSD profile (single spectra) for χ Dra (F7V+K1V) on 2015 April 24. The plot is described in Fig. B1.

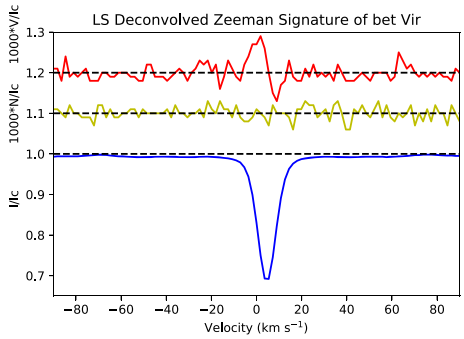

Figure B13. Mean LSD profile (combining two spectra) for β Vir (F9V) on 2017 April 11. The plot is described in Fig. B1.

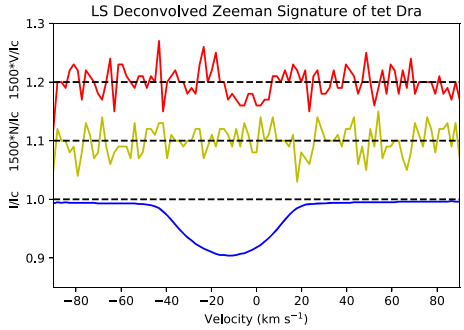

Figure B14. Mean LSD profile (combining three spectra) for θ Dra (F8IV+M2) on 24 April 2017. The plot is described in Fig. B1.

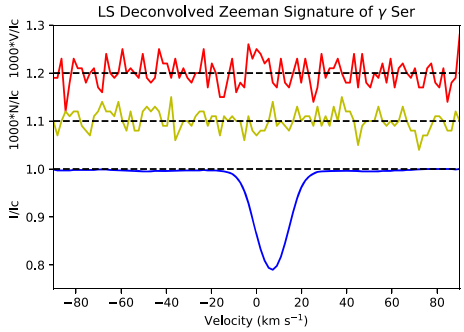

Figure B15. Mean LSD profile (combining two spectra) for γ Ser (F6V) on 2014 August 23. The plot is described in Fig. B1.

This paper has been typeset from a TEX/LATEX file prepared by the author.

2.3 Future Research

This paper has identified two areas for future research. Firstly, a larger number of stars studied in the spectral types F0-F3 will help determine the high temperature boundary for dynamo magnetic fields, and the lower temperature boundary for fossil magnetic fields. Secondly, a detailed analysis of stars in the sample using Zeeman Doppler Imaging over multiple epochs is required to fully classify the detected magnetic fields as being dynamo or weak fossil.

2.4 Additional Comments

Information in this section provides additional comments on Paper 1 and background information on the 31 BRITEpol stars included in the paper.

α CMi (Procyon) is a spectroscopic binary star (Wenger et al., 2000) comprising a F5 IV–V primary (Kervella et al., 2004) and a faint DQZ secondary (Provencal et al., 2002) which orbit each other with a period of 40.8 years and an eccentricity of 0.4 (Bond et al., 2015). The primary component has a mass of 1.5 $M_{\odot}$ (Liebert et al., 2013) and a radius of 2.0 $R_{\odot}$ (Kervella et al., 2004). The stellar system is the fourteenth closest system to the Sun at a distance of 3.51 pc (Van Leeuwen, 2007).

α CrV is an F1V main sequence star Gray et al. (2006) with high proper motion (Wenger et al., 2000). The star has a mass of 1.39 $M_{\odot}$ (Fuhrmann & Chini, 2012) and is considered one of the most metal deficient stars for its age (Da Silva, 1975). The presence of periodic changes in the spectrum of the star indicated it may be a Gamma Doradus-type variable (Fuhrmann & Chini, 2012).

α For is a binary star system consisting of a F6V primary and a G7V secondary Corbally (1984) which orbit each other with a period of 269 years (Hartkopf et al.,

2001). The primary component has a mass of 1.3 $M_{\odot}$ (Santos et al., 2001) and a radius of 2.0 $R_{\odot}$ (Bruntt et al., 2010a). An excess infarred emission indicates the possible presence of a circumstellar debris disk (Oudmaijer et al., 1992).

α Hyi is a high proper motion (Wenger et al., 2000) F0IV star (Rains et al., 2020). The star has a mass of 2.0 $M_{\odot}$ (Malagnini & Morossi, 1990) and a radius of 3.0 $R_{\odot}$ (Rains et al., 2020) and is classified as an x-ray emitter (Schmitt et al., 1985).

β CrB (HIP 75695) is a chemically peculiar (Adelman, 1973), spectroscopic binary with component V magnitudes of 3.68 and 5.20 separated by 0.30 arcsecs (Mason et al., 2001). The primary component has a $T_{\rm eff} = 7980 \pm 180$ K, and the secondary $T_{\rm eff} = 6750 \pm 230$ K (Bruntt et al., 2010b).

β Del is a spectroscopic binary (Wenger et al., 2000) composed of two F5IV stars which orbit each other with a period of 26 years (Söderhjelm, 1999). Component A has a mass of 1.75 $M_{\odot}$ and component B has a mass of 1.47 $M_{\odot}$ (Davidson et al., 2009).

β TrA is a high proper motion (Wenger et al., 2000) F1V star (Gray et al., 2006) with a mass of 1.56 $M_{\odot}$ (David & Hillenbrand, 2015) and a radius of 2.0 $R_{\odot}$ (Rains et al., 2020). Excess infrared emission suggests the possibility of a circumstellar debris disk (Koerner et al., 2010).

β Vir (HIP 57757) is a bright (V=3.60) F9V star (Morgan & Keenan, 1973), with an age of 3.1 ± 0.8 Gyr (Casagrande et al., 2011), metal rich ([Fe/H] = 0.24) (Jofré et al., 2018), and $T_{\rm eff}$ 6083 ± 58 K (Jofré et al., 2018). β Vir is close to the end of its hydrogen burning phase, or just evolved off the main sequence (Eggenberger & Carrier, 2006; North et al., 2009), and is located in a region of the HR diagram where the evolutionary tracks form a loop (Heiter et al., 2015). While β Vir has appeared in planet search programs (Wittenmyer et al., 2006)

no exoplanet companion has been found. β Vir is a frequently studied star in the solar neighbourhood (Gehren, 1978), however the nature of its magnetic field is not well known.

χ Dra is spectroscopic binary system (Wenger et al., 2000) composed of F7V+K1V components (Gray et al., 2001). The primary component has a mass of 1.0 $M_\odot$ and a radius of 1.2 $R_\odot$ (Torres et al., 2010). The secondary component has a mass of 0.75 $M_\odot$ and a radius of 0.73 $R_\odot$ (Torres et al., 2010). The primary component is metal deficient compared to the Sun with Fe/H = -0.41 (Nordström et al., 2004).

δ Aql consists of a primary component with spectral type F1IV-V star (Gray et al., 2001) with a mass of 1.65 $M_\odot$ and a radius of 2.0 $R_\odot$ (Fuhrmann, 2008). A secondary component of possible spectral type K has a mass of 0.67 $M_\odot$ and a radius of 0.61 $R_\odot$ (Fuhrmann, 2008).

δ Cap is an eclipsing binary (Wenger et al., 2000) chemically peculiar star with a spectral type kA5hF0mF2III (Gray et al., 2006). The stellar system contains multiple components with the primary mass of 2.0 $M_\odot$ and a radius of 1.9 $R_\odot$ (Batten & Fletcher, 1992). The secondary component has a mass of 0.7 2.0 $M_\odot$ and a radius of 0.9 $R_\odot$ (Batten & Fletcher, 1992). The sysem is an eclipsing binary (Eggleton & Tokovinin, 2008).

δ Gem is a spectroscopic binary (Wenger et al., 2000) consisting of a F2IV-V primary (Gray et al., 2003) with a mass of 1.57 $M_\odot$ (Shaya & Olling, 2010). The primary and secondary stars form a wide binary system which orbit each other with a period of 1200 years (Abt, 2005).

δ Ser is a double star system comprising a F0IV primary and a F0IV secondary (Abt & Morrell, 1995). Component A is classified as a δ Scuti variable with a mass of 1.58 $M_\odot$ (David & Hillenbrand, 2015) and a radius of 3.0 $R_\odot$ (Massarotti

et al., 2007).

η Cas is a high proper motion (Wenger et al., 2000) double star system consisting of a F9V primary (Abt, 2008a) with a mass of 0.97 $M_\odot$ (Boyujian et al., 2012) and a radius of 1.0 $R_\odot$ (Boyajian et al., 2013). The K7 secondary (Fernandes et al., 1998) has a mass of 0.57 $M_\odot$ (Fernandes et al., 1998) and a radius of 0.66 $R_\odot$ (Johnson & Wright, 1983).

η Lep is a high peoper motion (Wenger et al., 2000) F2V star (Gray et al., 2006) with a mass of 1.42 $M_\odot$ (Casagrande et al., 2011) and a radius of 1.57 $R_\odot$ (Rhee et al., 2007). Excess infrared emission has been detected by the Spitzer Space telescope which indicated a debris disk surrounding the star (Lawler et al., 2009).

γ Cap is a chemically peculiar star classified as spectral type kF0hF1VmF2 (Abt & Morrell, 1995). The star has a mass of 2.44 $M_\odot$ and a radius of 2.35 $R_\odot$ (Glagolevskij, 2019). γ Cap is an alpha2 CVn Variable star (Wenger et al., 2000).

γ Cet is a binary star system comprising F4V+A2Vn components (Skiff, 2014). The primary component is an A2 star with a mass of 1.9 $M_\odot$ (Tokovinin & Kiyaeva, 2015) and a radius of 1.9 $R_\odot$ (Lang, 2006). The secondary F-component has a mass of 1.17 $M_\odot$ (Tokovinin & Kiyaeva, 2015) and is classified as an x-ray source (Schröder & Schmitt, 2007).

γ Del is a binary star system with a F7V primary (Luck, 2016) and a K1IV secondary (Cenarro et al., 2007). The primary component has a mass of 1.99 $M_\odot$ and a radius of 8.43 $R_\odot$ (Maldonado et al., 2013). The secondary has a mass of 1.61 $M_\odot$ and a radius of 2.60 $R_\odot$ (Maldonado et al., 2013). The presence of an exoplanet around the secondary component as suggested by (Irwin et al., 1999) has not been confirmed.

γ Lep is a high proper motion (Wenger et al., 2000) double star system with

a F6V primary (Montes et al., 2001) and a K2 secondary (Abt, 2008a). The primary has a mass of 1.23 $M_\odot$ and a radius of 1.33 $R_\odot$ (Ammler-von Eiff & Guenther, 2009).

γ Ser is a high proper motion (Wenger et al., 2000) F6V star (Gray et al., 2001) with a mass of 1.30 $M_\odot$ and a radius of 1.55 $R_\odot$ (Bruntt et al., 2010a). The star has an age of about 3.5 Gyr (Vican, 2012) and is located at a distance of 11.3 pc (Van Leeuwen, 2007).

γ Tuc is a high proper motion (Wenger et al., 2000) F3IV/V star (Houk, 1978) with a mass of 1.55 $M_\odot$ (Bailer-Jones, 2011) and a radius of 2.2 $R_\odot$ (Allende Prieto & Lambert, 1999).

h UMa is an emission line (Wenger et al., 2000) binary star system with a F0IV primary and a K5 secondary (Boyajian et al., 2013). The primary has a mass of 1.86 $M_\odot$ and a radius of 2.90 $R_\odot$ (Boyajian et al., 2013).

ι Leo is a multiple star system with a F3V primary (Abt, 2008b) and a G3V secondary. The primary component has a mass of 1.62 $M_\odot$ (Bi et al., 2008) and a radius of 2.1 $R_\odot$ (Malagnini & Morossi, 1990).

ι Peg is a double star system with a F5V primary and a G8V secondary which orbit each other with a period of about 10 days (Konacki et al., 2010). The primary has a mass of 1.33 $M_\odot$ (Fuhrmann, 2008) and a radius of 1.53 $R_\odot$ (Van Belle & Von Braun, 2009).

ψ Gem is a high proper motion star with a spectral classification of F5IV-V (Gray et al., 2003) with narrow spectral lines (Hendry, 1981). Fuhrmann et al. (2011) suggested the star may be a spectroscopic binary. The star was considered a probable δ Scuti type variable by Frolov (1970).

ψ Peg is an F6V star (Gray et al., 2001) with high proper motion (Wenger et al., 2000).

ψ Vel is a binary star with an F0IV primary and F3V secondary (Heiter et al., 2015). The primary component has a mass of 1.44 $M_\odot$ (David & Hillenbrand, 2015). The secondary component has been measured as a variable star with magnitudes varying from 4.5 and 5.1 (Samus et al., 2009).

τ Cyg is a δ Scuti Variable (Wenger et al., 2000) comprising of a F2IV primary (Abt & Morrell, 1995) and a G0V secondary which orbit each other with a period of 810 d (Matson et al., 2020). The primary component has a mass of 1.65 $M_\odot$ and a radius of 2.48 $R_\odot$ (Fuhrmann, 2008). The secondary has a mass of 1.03 $M_\odot$ and a radius of 0.93 $R_\odot$ (Fuhrmann, 2008).

θ Dra (HIP 78527) is a bright (V=4.00), spectroscopic binary consisting of an F8IV primary (Pounds et al., 1991) and a late type secondary (Duquennoy & Mayor, 1991; Mazeh et al., 2002) with a mass of 0.62 $M_\odot$ (Tokovinin, 2014) placing it later than spectral type K2. A possible third component was suggested by Mayor & Mazeh (1987) through analysis of radial velocity variations. It is a mature F-star with age = 2.1$\pm$0.2 Gyr (Casagrande et al., 2011), based on Padova isochrones (Bertelli et al., 2008, 2009), a $T_{\rm eff} = 6392 \pm 63$ K (Ramírez et al., 2012), and has been identified as an X-ray source by the Einstein observatory (Maggio et al., 1987).

θ UMa is a high proper motion star (Wenger et al., 2000) consisting of an F6IV primary (Mallik, 1999) and an M-type secondary. The primary component has a mass of 1.41 $M_\odot$ (Fuhrmann, 2008) and a radius of 2.37 $R_\odot$ (Boyujian et al., 2012).

υ UMa is a binary star system consisting of a F2IV primary (De Rosa et al., 2014) which is classified as a δ Scuti variable (Korzennik et al., 1995) and a M-type secondary. The primary component has a mass of 1.57 $M_\odot$ (David & Hillenbrand, 2015) and a radius of 2.79 $R_\odot$ (Korzennik et al., 1995). The secondary has a mass

of 0.44 $M_{\odot}$ Korzennik et al. (1995).

Further information on Paper 1 is presented here to clarify some of the techniques and concepts in the paper. The sampling size for the LSD output velocity are chosen as 1.8 km s^{-1} for all three telescopes used. The velocity grid for HARPSpol observations were chosen to match the lower resolution from NARVAL/ESPaDOnS spectropolarimeters.

In the paper no S-index values were calculated for three stars using the HARPS spectropolarimeter. Since the publication of the paper, the author has become aware of several studies with published fluxes in the Ca H&K lines from HARPS spectra (Alvarado-Gómez et al., 2015, 2018; Boro Saikia et al., 2018a).

A clarification from Section 4.5 of paper 1 on page 65 of the thesis. An advantage in using the S-index for magnetic studies is that it does not suffer from magnetic flux cancellation like the large and small-scale magnetic fields.

A missing reference from Paper 1 in the appendix notes for σ Boo on page 71 is added here for completeness. The revised sentence should read: σ Boo is classified as a standard F2V star in the MK classification system (Johnson & Morgan, 1953), while Samus et al. (2017) classify it as F3V.

One of the values for convection zone depth has incorrect units in appendix notes for τ PsA in Paper 1 on page 72 of the thesis. The corrected sentence should read: It has a theoretical stellar convection zone mass of 0.002 $M_{\odot}$ and convection zone depth of 0.236 $R_{\odot}$ (Takeda et al., 2007).

CHAPTER 3

PAPER 2: THE MAGNETIC FIELDS AND STELLAR WINDS OF THE MATURE LATE F-TYPE STARS: β VIRGINIS AND θ DRACONIS

Published in the Monthly Notices of the Royal Astronomical Society, 2022, Volume 509, pp. 5117–5141 (Seach et al., 2022a).

3.1 Introduction to Paper

Two mature late-type F-stars from the magnetic snapshot survey (Chapter 2) are chosen for a more detailed analysis using ZDI. The stars are β Vir (F9V) and θ Dra (F8IV). The stars are chosen because they are identified as being magnetic

from the snapshot survey, and there are enough spectropolarimetric observations to enable magnetic maps to be produced at multiple epochs.

Magnetic maps displaying the large-scale magnetic field topology for β Vir are obtained at three epochs in 2017. The magnetic field is most likely generated by a dynamo due to the changing topology and varying amount of magnetic energy between epochs. The magnetic maps for the faster rotating θ Dra show more complex magnetic field topology than β Vir, which may be partly due to a greater surface resolution produced by ZDI for faster rotating rotating stars, and also may be due to faster rotation which drives a stronger and more complex dynamo. θ Dra has more magnetic energy stored in the toroidal field compared to the slower rotating β Vir. A possible chromospheric cycle of 83 d is determined for β Vir and possible chromospheric cycles of 183 d and 43 d is determined for θ Dra.

The space weather surrounding β Vir and θ Dra show differences which are related to the strength and orientation of the reconstructed surface radial magnetic field. The average space weather at β Vir at the three observed epochs falls within the range of space weather conditions observed at Earth. θ Dra produces a wind pressure an order of magnitude stronger than the Sun's wind pressure.

3.2 Published Paper

The published paper Seach et al. (2022a), "The magnetic fields and stellar winds of the mature late F-stars: β Virginis and θ Draconis" follows.

Monthly Notices of the ROYAL ASTRONOMICAL SOCIETY

MNRAS **509,** 5117–5141 (2022) https://doi.org/10.1093/mnras/stab3289
Advance Access publication 2021 November 13

The magnetic fields and stellar winds of the mature late F-stars: β Virginis and θ Draconis

J. M. Seach [1]★ S. C. Marsden [1] B. D. Carter [1] D. Evensberget [1] C. P. Folsom,[2,3] C. Neiner [4] and M. W. Mengel [1]

[1] *University of Southern Queensland, Centre for Astrophysics, Toowoomba 4350, Australia*
[2] *Tartu Observatory, University of Tartu, Observatooriumi 1, Tõravere, 61602 Tartumaa, Estonia*
[3] *Department of Physics and Space Science, Royal Military College of Canada, PO Box 17000 Station Forces, Kingston, ON K7K 0C6, Canada*
[4] *LESIA, Paris Observatory, PSL University, CNRA, Sorbonne University, Université Paris, 5 place Jules Janssen, F-92195 Meudon, France*

Accepted 2021 November 9. Received 2021 November 5; in original form 2021 April 26

ABSTRACT

Mapping the large-scale magnetic field in late F-type stars is important for understanding the nature of the stellar dynamo and the dynamics of thin outer convection zones. We use Zeeman Doppler Imaging to produce multi-epoch maps of the surface magnetic field for two mature late F-type stars: β Virginis (F9V) and θ Draconis (F8IV). We also provide a magnetohydrodynamic model for the stellar winds from the corona to the inner astrosphere, which exists in an environment at the hot end of habitability for exoplanets. Our results show that either simple or complex dynamo magnetic fields are present in mature late F-type stars, with shallow outer convection zones. The results of stellar wind modelling show the average space weather for β Vir at a distance of 1 au falls within the range of space weather conditions observed at Earth, while θ Dra produces a wind pressure an order of magnitude stronger than the Sun's wind pressure.

Key words: stars: magnetic field – stars: solar-type – stars: activity – stars: winds, outflows.

1 INTRODUCTION

As part of our study of magnetism in F-type stars, we present surface magnetic maps for β Vir (F9V) and θ Dra, (F8IV) using Zeeman Doppler Imaging (ZDI), and provide a magnetohydrodynamic (MHD) model of their magnetospheres. ZDI (Semel 1989; Donati & Brown 1997; Donati et al. 2006b) is a powerful technique for studying stellar magnetism since it reconstructs both the location and orientation of surface magnetic features (Kochukhov 2016), and is suitable for both fast and slow rotators (Petit et al. 2008). This contrasts with brightness mapping using Doppler imaging (Deutsch 1958; Vogt & Penrod 1983; Vogt et al. 1987) which is best used for fast rotators with $v \sin i \gtrsim 20$ km s^{-1} (Vogt 1988; Rice 2002). ZDI allows the strength, complexity, and axisymmetric nature of the large-scale magnetic field to be determined, including its poloidal, and toroidal components.

The large-scale magnetic field may be described in terms of the poloidal and toroidal components (Elsasser 1946; Chandrasekhar 1961), as well as the axisymmetric/non-axisymmetric and dipole/quadrupole/octupole and higher multipoles (Deutsch 1955; Piskunov & Kochukhov 2002; Donati et al. 2006b). For axisymmetric fields, the poloidal magnetic fields lie in the meridional plane, while toroidal fields have field lines which circle the axis (Elsasser 1956). Both components are expected to be present in stars over the long-term in order to provide magnetic stability, since purely toroidal or purely poloidal fields have been shown to be unstable (Prendergast 1956; Tayler 1973; Wright 1973). Describing the surface magnetic fields in terms of poloidal and toroidal components has been used in dynamo equations (Parker 1955; Backus 1958; Roberts & Stix 1971) and is useful in explaining how stars regenerate, and sustain, a dynamo magnetic field via the $\alpha\Omega$-effect (Parker 1979; Krause & Rädler 1980; Choudhuri et al. 1995; Moffatt & Dormy 2019).

F-star magnetic fields exist in shallow outer convection zones and may have different dynamo properties to solar-type stars (Giampapa & Rosner 1984). The observable effects of magnetism in F-stars differs from later spectral types, and includes strong differential rotation (Barnes et al. 2005a; Reinhold & Reiners 2013; Reinhold & Gizon 2015), weaker X-ray emission (Stern, Schmitt & Kahabka 1995; Lisse et al. 2017; Freund et al. 2020), weaker magnetic fields (Marsden et al. 2014), shorter magnetic cycles (Lopes et al. 2015; Mittag et al. 2019), and inefficiency in producing toroidal magnetic fields (Kitchatinov & Olemskoy 2011). F-stars also span a range of masses where rapid rotational braking occurs (Schatzman 1962; Skumanich 1972; Guedel, Guinan & Skinner 1997; Vidotto et al. 2014c) due to wind-driven angular momentum loss as a consequence of the onset of dynamo magnetic fields (Krause & Rädler 1980; Brandenburg & Subramanian 2005; Moffatt & Dormy 2019) in the outer convection zone. This magnetic braking results in a decrease in rotation from early to late F-stars (Gray 1988; Nielsen et al. 2013) coinciding with an increase in depth of the outer convection zone (Mullan 1972). The properties of stellar winds and the link with magnetic activity is poorly understood in cool stars (Johnstone et al. 2015b), therefore modelling of the stellar magnetosphere (Lammer & Khodachenko 2014; Alvarado-Gómez et al. 2020) is important for

★ E-mail: john.seach@usq.edu.au

understanding how wind properties evolve on the main sequence, and has implications for the habitability of exoplanets (See et al. 2014; Johnstone et al. 2015a). Due to lifespans as short as one billion years, F-stars are considered the hottest stars which allow the possibility of exobiology to develop (Sato et al. 2014).

Relatively little information has been published on the nature of the vector magnetic field in F-stars. Mengel (2005) studied the young, fast rotating F8V star HR 1817 and found a weak complex radial magnetic field with a large rotational shear, which was different from that seen in G and K solar-type stars. The moderately rotating, and hot Jupiter hosting star, τ Boo (F7V) has been studied by several authors with the first magnetic map produced by Catala et al. (2007) who found a predominately poloidal field more complex than that of the Sun, and a high differential rotation rate. Mengel et al. (2016) found a very rapid 120 d chromospheric cycle that was broadly solar-type in contrast to other F-type stars. A chromospheric cycle of 120 d and magnetic cycle of 240 d was found by Jeffers et al. (2018) with the polarity flip of the large-scale magnetic field in phase with the chromospheric cycle. Morgenthaler et al. (2011) found a fast magnetic cycle of ∼3 yr on the slow rotating F9V star HD 78366 and a strong polar radial field and equatorial rotation period of 11.4 d. Fares (2013) presented a magnetic map for the moderately rotating star HD 179949 (F8V) which showed 90 per cent of the magnetic energy in the poloidal component, mainly radial. Waite et al. (2015) showed the young moderately rotating F8V star (HD 35296) contained a complex large-scale magnetic field with significant toroidal component and high level of differential rotation. A short magnetic cycle of 1.06 yr for the F7V star HD75332 was found by Brown et al. (2021), but only a single magnetic field reversal was detected from 12 magnetic map reconstructions over a 12-yr observation period. The authors speculate they may have missed the majority of polarity reversals due to the low frequency of observations. Further studies are needed for F-stars because exactly how the magnetic field topology changes across this spectral class remains to be determined.

In our previous paper (Seach et al. 2020), hereafter called paper I, we determined the longitudinal magnetic field of β Vir ($+1.7 \pm 0.5$ G) and θ Dra ($+7.4 \pm 2.9$ G); however, we were not able to determine if the field was a dynamo, or weak fossil field, from a single night's observation. In this paper, we use ZDI to reconstruct the surface magnetic field of β Vir and θ Dra, and determine equatorial rotation period, differential rotation, and inclination of the rotational axis. We also present a MHD model of their magnetospheres. Maps of the large-scale magnetic field of F-type stars are important for understanding magnetism and convection in stars with thin outer convection zones, and provide input for models of the coronal magnetic field, and stellar winds. Since F-stars span a range of stellar masses where the transition from fossil to dynamo fields is expected to occur (Durney & Latour 1977; Seach et al. 2020), mapping the large-scale magnetic field will offer insight into the magnetic topology of stars with shallow outer convection zones, and constrain dynamo models.

2 OBSERVATIONS AND DATA REDUCTION

2.1 Target selection

β Vir and θ Dra were identified as magnetic stars in our earlier magnetic snapshot survey of F-type stars (paper I) and the original observations contained a sufficient number of spectra to allow this follow up paper reconstructing the large-scale surface magnetic field using ZDI (Section 3.2). Data were obtained as part of the BRITEpol survey (Neiner et al. 2017), which is a systematic spectropolarimetric survey of stars brighter than magnitude $V = 4$, which compliments the optical two-colour photometry collected by the BRITE-Constellation Nanosatellite Space Mission (Handler et al. 2017).

β Vir (HIP 57757) is a bright ($V = 3.60$) F9V star (Morgan & Keenan 1973), with an age of 3.1 ± 0.8 Gyr (Casagrande et al. 2011), metal rich ([Fe/H] = 0.24) (Jofré et al. 2018), and $T_{\rm eff}$ 6083 ± 58 K (Jofré et al. 2018). It is a slow rotator with $v \sin i = 6.1 \pm 2.6$ km s^{-1} (Glebocki & Gnacinski 2005). β Vir is close to the end of its hydrogen burning phase, or just evolved off the main sequence (Eggenberger & Carrier 2006; North et al. 2009), and is located in a region of the HR diagram where the evolutionary tracks form a loop (Heiter et al. 2015). While β Vir has appeared in planet search programs (Wittenmyer et al. 2006) no exoplanet companion has been found. β Vir is a frequently studied star in the solar neighbourhood (Gehren 1978); however, the nature of its magnetic field is not well known.

θ Dra (HIP 78527) is a bright ($V = 4.00$), spectroscopic binary consisting of an F8IV primary (Pounds et al. 1991) and a late type secondary (Duquennoy & Mayor 1991; Mazeh et al. 2002) with a mass of 0.62 $M_\odot$ (Tokovinin 2014) placing it later than spectral type K2. A possible third component was suggested by Mayor & Mazeh (1987) through analysis of radial velocity variations. θ Dra rotates unusually fast for a late F-type star with $v \sin i = 28.1 \pm 0.1$ km s^{-1} (Glebocki & Gnacinski 2005). It is a mature F-star with age = 2.1 ± 0.2 Gyr (Casagrande et al. 2011), based on Padova isochrones (Bertelli et al. 2008, 2009), a $T_{\rm eff} = 6392 \pm 63$ K (Ramírez et al. 2012), and has been identified as an X-ray source by the Einstein observatory (Maggio et al. 1987).

2.2 Observations

Observations of β Vir and θ Dra were obtained between 2017 February 14 and June 18 using the NARVAL spectropolarimeter at the Telescope Bernard Lyot (TBL) at the Observatoire du Pic du Midi, France (Aurière 2003). NARVAL consists of a cross-dispersed, bench mounted, echelle spectrograph, with a wavelength coverage in a single exposure of 370–1050 nm with small gaps at 922.4–923.4, 960.8–963.6, and 1002.6–1007.4 nm. The full spectrum spans 40 grating orders from #22 in the red to #61 in the blue, with a resolving power of ≈68 000 when using the spectropolarimetric mode. The polarimeter consists of a quarter-wave and two half-wave Fresnel rhombs coupled to a Wollaston prism, which is composed of two perpendicular calcite prisms which produce achromatic polarization (Donati et al. 2006a). One stellar observation consists of four sub-exposures which are combined to produce the Stokes I, combined constructively to produce the V spectrum, and combined destructively to give the null spectrum where the Zeeman signature cancels out, and only non-magnetic effects remains in the profile (Semel, Donati & Rees 1993).

We obtained 47 polarized spectra of β Vir over 108 d between 2017 February 14 and April 24 spanning 7.5 rotation cycles. We obtained 105 polarized spectra of θ Dra over 73 d between 2017 April 06 and June 18, spanning 25.3 rotation cycles. On many nights we obtained multiple spectra for θ Dra, therefore individual LSD profiles were combined to produce nightly averages with higher SNR which were used as inputs for the ZDI code. The averaged LSD profiles were obtained over a time period covering less than 2 per cent of the stellar rotational period, and was considered a small enough time frame to avoid rotational smearing of the results. Using mean nightly LSD profiles did not change the magnetic map compared to using individual LSD profiles. A journal of observations for β Vir are shown in Table 1. A journal of nightly averaged observations for θ

Table 1. Journal of observations and magnetic detection for β Vir LSD profiles in 2017, showing date and time of the observation, Stokes *I* profile SNR, rotation cycle with respect to observations starting at HJD = 2457799.6214, radial velocity (RV), chromospheric activity (S-index and H α-index), longitudinal magnetic field (B_l), null value (N_l), and magnetic detection flag for the presence of a magnetic field in individual LSD profiles where *D* is a definite detection, *M* is marginal, and *N* is no detection. The Stokes *V* observations consist of a sequence of four subexposures as described in section. The RV is calculated using the centre of gravity method on the Stokes *I* profiles. The mean RV of our observations is 4.588 ± 0.013 km s^{-1}. For magnetic mapping, we assume a constant RV of 4.6 km s^{-1}.

Date 2017 (local time)	HJD 2450000+	SNR Stokes *I*	Rot. cycle	RV (km s^{-1})	S-index	H α-index	B_l (G)	N_l (G)	Det. N,M,D
Feb 14	7799.6214	534	0.000	4.54	0.162	0.275	1.3 ± 0.4	0.0 ± 0.4	M
Feb 15	7800.6362	548	0.110	4.53	0.161	0.275	0.9 ± 0.3	0.1 ± 0.3	N
Feb 16	7801.5917	548	0.214	4.52	0.162	0.275	0.5 ± 0.2	0.1 ± 0.2	N
Feb 17	7802.6201	548	0.326	4.57	0.162	0.274	0.6 ± 0.3	0.3 ± 0.3	N
Feb 18	7803.6170	543	0.434	4.54	0.162	0.275	0.9 ± 0.3	−0.2 ± 0.3	N
Feb 19	7804.5554	540	0.536	4.50	0.161	0.276	0.4 ± 0.3	−0.4 ± 0.3	N
Feb 20	7805.5919	516	0.649	4.60	0.160	0.275	0.4 ± 0.2	0.2 ± 0.2	N
Feb 21	7806.5967	530	0.758	4.53	0.160	0.276	0.1 ± 0.2	−0.2 ± 0.3	N
Feb 22	7807.5591	526	0.863	4.58	0.162	0.275	1.4 ± 0.5	0.0 ± 0.5	N
Mar 01	7814.5545	526	1.623	4.66	0.161	0.275	1.0 ± 0.3	0.0 ± 0.3	M
Mar 08	7821.4747	493	2.375	4.63	0.162	0.275	3.0 ± 0.7	0.2 ± 0.7	M
Mar 14	7827.5549	494	3.036	4.56	0.161	0.276	0.2 ± 0.3	0.1 ± 0.3	N
Mar 15	7828.4753	563	3.136	4.57	0.159	0.276	0.3 ± 0.2	0.3 ± 0.2	N
Mar 16	7829.4932	525	3.247	4.60	0.160	0.275	0.7 ± 0.2	0.2 ± 0.2	N
Mar 18	7831.5311	529	3.468	4.62	0.157	0.273	0.8 ± 0.2	−0.4 ± 0.2	M
Mar 28	7841.4796	538	4.550	4.58	0.160	0.276	0.5 ± 0.2	0.3 ± 0.2	N
Mar 29	7842.4860	554	4.659	4.59	0.160	0.276	1.3 ± 0.2	0.0 ± 0.2	M
Apr 03	7847.3993	554	5.193	4.56	0.163	0.276	1.0 ± 0.2	0.1 ± 0.2	D
Apr 03	7847.4124	543	5.195	4.55	0.163	0.276	1.6 ± 0.6	0.2 ± 0.6	M
Apr 06	7850.4794	505	5.528	4.59	0.163	0.276	1.0 ± 0.6	0.2 ± 0.6	N
Apr 06	7850.4925	512	5.529	4.58	0.164	0.276	0.8 ± 0.4	−0.1 ± 0.4	N
Apr 07	7851.4844	523	5.637	4.59	0.162	0.276	0.3 ± 0.2	0.1 ± 0.2	N
Apr 07	7851.4974	521	5.639	4.59	0.163	0.276	1.6 ± 0.7	0.4 ± 0.7	N
Apr 08	7852.4197	559	5.739	4.60	0.166	0.275	0.7 ± 0.2	−0.3 ± 0.2	N
Apr 08	7852.4328	561	5.740	4.61	0.166	0.275	0.6 ± 0.3	0.0 ± 0.3	N
Apr 10	7854.5044	514	5.966	4.61	0.162	0.275	1.7 ± 0.4	−0.2 ± 0.4	D
Apr 10	7854.5174	499	5.967	4.61	0.163	0.275	2.4 ± 0.7	−0.5 ± 0.7	D
Apr 11	7855.4529	535	6.069	4.60	0.162	0.274	1.0 ± 0.2	−0.3 ± 0.2	D
Apr 11	7855.4660	522	6.070	4.60	0.162	0.275	2.0 ± 0.6	0.2 ± 0.6	D
Apr 12	7856.4745	524	6.180	4.61	0.163	0.276	3.1 ± 0.6	−0.4 ± 0.6	D
Apr 12	7856.4878	518	6.181	4.62	0.164	0.276	1.1 ± 0.4	−0.1 ± 0.4	D
Apr 16	7860.4455	552	6.611	4.58	0.162	0.276	0.8 ± 0.3	−0.2 ± 0.3	D
Apr 16	7860.4586	555	6.613	4.58	0.163	0.276	0.9 ± 0.3	0.3 ± 0.3	N
Apr 17	7861.3953	546	6.715	4.59	0.162	0.276	0.5 ± 0.2	0.0 ± 0.2	M
Apr 17	7861.4083	559	6.716	4.59	0.161	0.276	0.3 ± 0.2	−0.1 ± 0.2	N
Apr 19	7863.4659	555	6.940	4.52	0.162	0.276	1.7 ± 0.6	0.4 ± 0.6	N
Apr 19	7863.4790	552	6.941	4.52	0.161	0.277	0.9 ± 0.3	−0.1 ± 0.3	N
Apr 20	7864.3500	550	7.036	4.56	0.162	0.277	1.5 ± 0.3	0.2 ± 0.3	D
Apr 20	7864.3631	553	7.037	4.56	0.162	0.277	1.4 ± 0.2	0.0 ± 0.2	D
Apr 21	7865.4823	518	7.159	4.61	0.164	0.277	1.3 ± 0.3	−0.4 ± 0.3	M
Apr 21	7865.4954	518	7.160	4.61	0.164	0.277	2.7 ± 0.8	0.0 ± 0.8	D
Apr 22	7866.3487	543	7.253	4.60	0.164	0.276	1.1 ± 0.5	0.1 ± 0.5	D
Apr 22	7866.3618	555	7.254	4.60	0.164	0.276	1.3 ± 0.3	0.2 ± 0.3	D
Apr 23	7867.4269	549	7.370	4.62	0.164	0.276	1.7 ± 0.3	0.3 ± 0.3	D
Apr 23	7867.4399	553	7.372	4.62	0.163	0.276	1.2 ± 0.3	0.0 ± 0.3	D
Apr 24	7868.3968	512	7.476	4.66	0.165	0.275	1.5 ± 0.2	−0.1 ± 0.2	D
Apr 24	7868.4100	512	7.477	4.66	0.164	0.275	1.8 ± 0.2	−0.2 ± 0.2	D

dra are shown in Table 2, and the full 105 observations are shown in Table A2.

2.3 Spectropolarimetric analysis

We reconstruct surface magnetic maps using circularly polarized spectra (Stokes *V*) and enhance the SNR by the line addition technique of least squares deconvolution (LSD; Donati et al. 1997; Kochukhov, Makaganiuk & Piskunov 2010). LSD analysis combines thousands of individual spectral lines into a single line with mean parameters and is useful in boosting the SNR in our F-stars that are expected to show weak magnetic fields (Marsden et al. 2014). Each observation consists of 4 x 223 s sub-exposures for β Vir and 4 x 320 s sub-exposures for θ Dra. The individual exposures are combined to produce an intensity profile (Stokes *I*), combined constructively to produce a circularly polarized profile (Stokes *V*), and combined

Table 2. Journal of observations and magnetic detection for θ Dra for the nightly averaged LSD profiles in 2017 showing date and time of the observation, number of spectra added for each mean LSD profile, Stokes *I* profile SNR, rotation cycle with respect to observations starting at HJD = 2457850.6525, radial velocity (RV), longitudinal magnetic field (B_l), null value (N_l), and magnetic detection flag for the presence of a magnetic field in the mean LSD profiles, where *D* is a definite detection, *M* is marginal, and *N* is no detection. Each Stokes *V* observation consists of a sequence of four subexposures. The RV is the mean and SD for each night. Table of observations for individual LSD profiles for θ Dra are shown in the Appendix.

Date 2017 (local time)	HJD 2450000+	No. of spectra	SNR Stokes *I*	Rot. cycle	RV (km s^{-1})	B_l (G)	N_l (G)	Det. N,M,D
Apr 06	7850.6525	5	1280	0.00	− 31.65 ± 0.30	3.3 ± 1.2	1.1 ± 1.2	N
Apr 07	7851.5949	5	1271	0.327	− 5.93 ± 1.25	1.8 ± 0.7	0.3 ± 0.7	D
Apr 10	7854.5700	5	1271	1.360	− 10.55 ± 1.23	2.5 ± 0.7	− 0.4 ± 0.7	D
Apr 11	7855.5191	5	1227	1.690	15.59 ± 0.30	0.9 ± 0.8	− 0.3 ± 0.8	N
Apr 12	7856.5422	5	1263	2.045	− 25.32 ± 0.90	0.5 ± 0.5	0.2 ± 0.5	D
Apr 15	7859.5630	5	1334	3.094	− 23.53 ± 1.00	− 0.5 ± 0.6	− 0.6 ± 0.6	D
Apr 16	7860.5115	5	1313	3.423	− 20.13 ± 1.07	2.2 ± 0.7	− 0.4 ± 0.7	D
Apr 17	7861.4817	5	1336	3.760	16.41 ± 0.12	− 1.4 ± 0.8	0.5 ± 0.8	D
Apr 19	7863.5320	5	1320	4.472	− 22.36 ± 1.02	1.2 ± 0.9	0.2 ± 0.9	D
Apr 20	7864.5065	5	1313	4.810	15.93 ± 0.24	1.0 ± 0.7	− 0.2 ± 0.7	N
Apr 21	7865.5798	5	1265	5.183	− 18.27 ± 1.16	− 1.8 ± 0.9	0.3 ± 0.9	M
Apr 22	7866.5141	5	1310	5.508	− 25.64 ± 0.86	1.1 ± 0.6	− 0.2 ± 0.6	D
Apr 23	7867.4924	5	1318	5.847	14.82 ± 0.46	1.3 ± 0.8	− 0.1 ± 0.8	D
Apr 24	7868.5120	3	950	6.201	− 11.60 ± 0.72	− 0.8 ± 0.7	1.0 ± 0.7	D
May 15	7889.4685	5	1134	13.478	12.02 ± 0.70	1.2 ± 1.0	− 0.1 ± 1.0	M
May 16	7890.4275	2	685	13.811	− 28.66 ± 0.24	− 12.6 ± 4.0	3.0 ± 4.0	N
May 20	7894.4558	5	1346	15.209	− 12.43 ± 1.22	− 1.6 ± 0.8	− 0.2 ± 0.8	N
Jun 05	7910.4710	5	1198	20.770	14.60 ± 0.48	− 1.6 ± 0.6	0.4 ± 0.6	N
Jun 14	7919.5162	5	1138	23.911	10.16 ± 0.84	− 1.1 ± 0.8	− 1.2 ± 0.8	N
Jun 16	7921.4964	5	1255	24.599	− 32.00 ± 0.23	0.2 ± 0.5	0.4 ± 0.5	N
Jun 17	7922.4899	5	1291	24.944	6.50 ± 1.19	− 0.7 ± 0.9	0.9 ± 0.9	D
Jun 18	7923.4904	5	1173	25.291	2.90 ± 1.13	− 1.4 ± 0.8	− 0.6 ± 0.8	M

destructively to give a null spectrum. The null spectrum acts as a check to ensure that spurious signals have not contaminated the spectrum. Examples of LSD profiles for β Vir and θ Dra are shown in Fig. 1. See paper I for more details on our spectropolarimetry and extraction of spectra.

We determine the mean longitudinal magnetic field (B_l) for individual Stokes *V* and Null spectra as described in paper I. B_l is the line-of-sight magnetic field component averaged over the stellar disc (Babcock 1947; Schwarzschild 1950). The local magnetic field strength is larger than B_l that suffers from cancellation effects where regions of opposite polarity cancel out, resulting in as little as 5 per cent of the field being detected (Reiners & Basri 2009). Nevertheless, B_l has been a widely used measure of stellar magnetic field strength for many decades due to its relative ease of measurement and because it is measured from the strongest of the Stokes parameters (Stokes *V*). We use an additional method to determine the presence of a stellar magnetic field, the false alarm probability (FAP), which is a statistical method to determine if a magnetic signature is present in the Stokes *V* LSD profile or a spurious signal in the Null profile (Donati et al. 1992, 1997).

2.4 Radial velocity

The radial velocity (RV) is a basic stellar parameter (Lindegren & Dravins 2003) and is determined from the Stokes *I* profile for β Vir and θ Dra using the centre of gravity method (Uitenbroek 2003). The centre of gravity method finds the centroid of the area under an intensity line profile (Rees & Semel 1979) and is considered more accurate than applying a Gaussian fit to the intensity profile, especially for faster rotating stars (Dravins 1975). We use the RV as an input into the ZDI code (Section 3.2) and our determined values are shown in Tables 1, 2, and A2.

3 LARGE-SCALE MAGNETIC FIELD TOPOLOGY

3.1 Brightness map

Doppler Imaging (DI) is a tomographical technique used for mapping bright and dark regions on the surface of a star associated with magnetic activity (Vogt & Penrod 1983; Vogt et al. 1987; Rice et al. 1989; Piskunov & Kochukhov 2002; Rice 2002). We use DI to produce a brightness map for θ Dra to identify regions of enhanced magnetic activity. We are unable to create a brightness map for β Vir, since it rotates too slowly to enable DI to be used. The input parameters for DI are the same as derived for ZDI described in (Section 3.2). The DI code we use (ZDIPY) is the same as described in Folsom et al. (2018), which inverts the Stokes *I* LSD profiles using the maximum entropy fitting routine of Skilling & Bryan (1984) to produce a regularized fit to the data which maximizes entropy and minimizes χ^2. The output of DI produces a map of the stellar surface which we set to show both bright and dark areas compared to the quiet photosphere corresponding to starspots and plages. The rotation cycle for each LSD profile is determined from ZDI using the zero rotation phase as the first observation date for each map. The Stokes *I* maximum entropy fits for θ Dra from DI is shown in Fig. A1, where we plot the observed signatures and modelled lines. The plot allows a visualization of the agreement between observations and model prediction.

3.2 Magnetic maps

We use ZDI to reconstruct the large-scale magnetic field topology of β Vir and θ Dra using the same ZDI code described above for DI, except for magnetic mapping we use a time-series of Stokes *V*

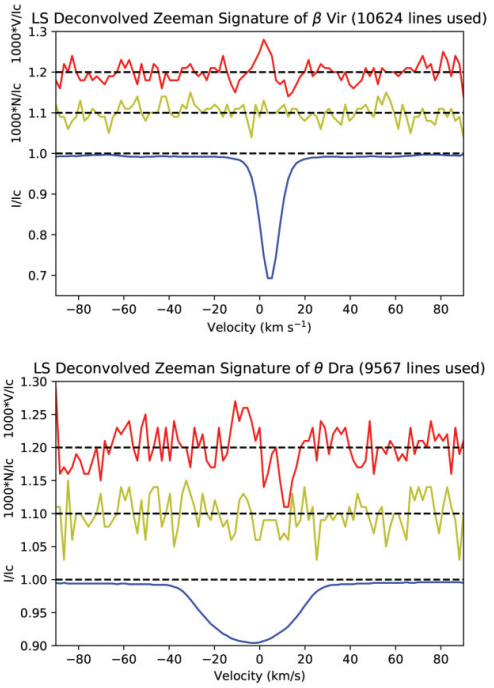

Figure 1. Example of LSD profiles (single spectra) for β Vir on 03 April 2017 (top), and θ Dra on 07 April 2017 (bottom). The upper line (red) shows the Stokes V profile (y-axis expanded by 1000 times and shifted up by 0.2 to allow better visibility). The middle line (yellow) shows the null profile (expanded by 1000 times and shifted up by 0.1), which is used as a check for any spurious signals contaminating the spectra. The lower line (blue) shows the Stokes I profile.

profiles rather than Stokes I profiles. While there are a large number of possible solutions to the inverse problem of reconstructing a magnetic map from Stokes V LSD profiles, a unique map is achieved by imposing a number of criteria. One criteria is to minimize the sum of χ^2 of the model fit of the observations. Secondly, we choose the maximum entropy method (Jaynes 1957a, b) that maximizes the Shannon entropy of Hobson & Lasenby (1998), derived from Skilling & Bryan (1984). The Stokes V data are used to reconstruct the magnetic maps of the radial azimuthal and meridional fields (Piskunov & Kochukhov 2002), using the spherical harmonics expansion of the surface magnetic field (Donati et al. 2006b) that allows the strength of the various field modes determined. The magnetic maps are represented using spherical harmonics. Each map comprises an orthogonal sum of components representing simple oscillations on the sphere. The expansion is parametrized by the degree ℓ, ranging from 1 to $\ell_{\rm max}$, and the order m, ranging from 0 to ℓ. The degree (ℓ) governs the total number of oscillations over the sphere for the spherical harmonics expansion (Ismail-Zadeh & Tackley 2010), so that higher values of ℓ correspond to smaller-scale features on the reconstructed magnetic field. $\ell_{\rm max}$ is the maximum degree of spherical harmonics expansion used in the magnetic map reconstruction and $\ell_{\rm max}$ thus determines the resolution of the magnetogram (Gerth & Yu 2004); however, the resolution is limited in low $v\sin i$ stars (Morin et al. 2010). The order (m) can be considered the number of zeros of the spherical harmonic component in the longitudinal direction (Ismail-Zadeh & Tackley 2010). It also determines if the field is axisymmetric ($m = 0$) or non-axisymmetric ($m > 0$) (Saikia et al. 2016).

The quantities derived from ZDI are the mean unsigned magnetic field ($B_{\rm mean}$), maximal field strength over stellar surface ($B_{\rm max}$), the fraction of the large-scale magnetic energy reconstructed in the poloidal and toroidal field components, the fraction of the magnetic energy in the dipolar ($\ell = 1$), quadrupolar ($\ell = 2$), octopolar ($\ell = 3$), and higher ($\ell > 3$) components. The fraction of the magnetic energy in the axisymmetric field component ($m = 0$), as well as the axisymmetry of the poloidal and toroidal fields are determined which gives an indication of the degree of alignment of the magnetic field with the rotation axis (Lehmann et al. 2019). We calculate the maximum degree of spherical harmonic expansion ($\ell_{\rm max}$) by running ZDI over a range of ℓ values and find the value at the point where no more energy is contained in the higher multipoles. For β Vir, we use $\ell_{\rm max} = 10$, and for θ Dra $\ell_{\rm max} = 20$. For θ Dra, we use the brightness map as an input into the ZDI code to account for suppression of the Zeeman signal in dark spots (Gregory et al. 2010; Johnstone et al. 2010; Morgenthaler et al. 2012; Kochukhov et al. 2017).

Input parameters for ZDI for both stars are initially determined by the methods detailed below, then refined iteratively by χ^2 minimization using the approach of Petit et al. (2002). From the mean FWHM of the Stokes I LSD profiles, we estimate the projected rotational velocity $v\sin i$ (km s^{-1}) (Collier Cameron et al. 2002; Paul et al. 2017):

$$v \sin i = \frac{\rm FWHM}{2\sqrt{\ln 2}}. \quad (1)$$

The rotation period ($P_{\rm rot}$) is estimated using the following equation (Bouvier 2013)

$$P_{\rm rot} = \frac{2\pi R}{v}, \quad (2)$$

where R is the stellar radius from (Stassun et al. 2019).

The inclination (i) of rotation axis in degrees is estimated from the following formula (Simpson et al. 2010; Watson et al. 2010):

$$i = \sin^{-1}\left(\frac{P_{\rm rot}(v\sin i)}{2\pi R}\right), \quad (3)$$

where $P_{\rm rot}$ is in seconds, $v\sin i$ is expressed in km s^{-1}, and R is the stellar radius in km.

Using the stellar parameters estimated by the method above, we then determine optimal values and uncertainties for $v\sin i$, inclination, $P_{\rm rot}$, and dΩ using the entropy landscape method (Petit et al. 2002). For each stellar parameter, we use ZDI to perform a search across a range of stellar parameter values at a fixed χ^2 of 1.0, and find the map with the corresponding maximum entropy. This entropy value is then used as an input into a further search using a fixed entropy and variable χ^2, producing an output of χ^2 versus stellar parameter. We then fit a Gaussian curve to the results and choose the optimal value as the minimum of the Gaussian curve, and the formal 1σ uncertainties are found from the Gaussian curve χ^2 statistics. The optimal stellar parameter derived from both the fixed χ^2 search and fixed entropy search are similar, which adds to the robustness of our results. The values for $P_{\rm rot}$ and dΩ are further estimated from a grid search described in more detail in Section 3.3. The $v\sin i$ for β Vir was taken from Glebocki & Gnacinski (2005), since χ^2 minimization did not produce a well-defined minimum.

The stellar local line model is the Stokes V profile emerging from a point on the stellar surface (Goncharskii et al. 1977, 1982). We use a Voigt profile, using the weak field approximation (Degl'Innocenti &

Landolfi 2004) and calculated using the approximation of Humlícek (1982). The line profiles are weighted using a linear limb darkening law from e.g. Gray (2005),

$$I_c/I_c^0 = 1 - \eta + \eta\cos(\omega), \tag{4}$$

where η is the limb darkening coefficient that matches the effective temperature of the star, I_c/I_c^0 is the brightness relative to the disc centre, and ω is the angle from disc centre. The ZDI code is run with solar local line profiles for Gaussian width and Lorentzian width since the stars have $T_{\rm eff}$ close to solar (<325 K hotter than the Sun). Gaussian width = 2.41 km s^{-1}, Lorentzian width = 0.89. The mean wavelength is obtained from output of LSD analysis, $\lambda_{\rm mean}$ = 536.7 nm (β Vir), $\lambda_{\rm mean}$ = 532.9 nm (θ Dra). Limb darkening coefficients are from fig. 17.6 in Gray (2005), β Vir = 0.60, and θ Dra = 0.58. The Stokes V maximum entropy fits for β Vir and θ Dra from DI is shown in Fig. A2, where we plot the observed signatures and modelled lines. The plot allows a visualization of the agreement between observations and model prediction.

Limitations of ZDI relating to missing information due to axial tilt and only reconstructing the large-scale magnetic field are disused in more detail elsewhere; see for example Gregory et al. (2010), Johnstone et al. (2010), Morgenthaler et al. (2012), and Kochukhov et al. (2017). Despite some limitations, ZDI remains a powerful technique for reconstructing the surface magnetic field in both cool and hot stars (Kochukhov 2016).

3.3 Differential rotation

Differential rotation (dΩ) is one of the key ingredients for creating a large-scale stellar dynamo, whereby non-uniform rotation generates a toroidal field from a poloidal field and helical turbulence recreates the poloidal field (Parker 1955; Steenbeck & Krause 1969; Gilman 1980). A detailed analysis of dΩ is essential for understanding the magnetic activity of the stars (Donahue et al. 1996). While dΩ can be directly measured on the surface of the Sun through sunspot tracing (Kambry & Nishikawa 1990; Beck 2000), different methods must be used to determine stellar surface dΩ due to the inability to directly resolve the stellar surface.

We use ZDI to determine the amplitude of dΩ by applying a solar-type differential rotation law (Donati et al. 2000; Waite et al. 2015), where equatorial regions have larger angular velocity than polar regions:

$$\Omega(l) = \Omega_{\rm eq} - {\rm d}\Omega\sin^2 l ({\rm rad\ d}^{-1}), \tag{5}$$

where l denotes the latitude, $\Omega_{\rm eq}$ is the rotation rate at the equator, and dΩ is the rotational shear between the equator and the pole. We constrain the amplitude of the surface dΩ and $\Omega_{\rm eq}$ of our stars by using dΩ and $\Omega_{\rm eq}$ as an input for magnetic map reconstruction. The optimal dΩ and $\Omega_{\rm eq}$ are determined individually by χ^2 minimization at a constant entropy using the method described in Section 3.2. We also determine dΩ and $\Omega_{\rm eq}$ using a ZDI search which involves plotting a grid of $\Omega_{\rm eq}$ versus dΩ using a range of values and then selecting the pair of $\Omega_{\rm eq}$ and dΩ which minimizes the χ^2 (Petit et al. 2002). This method provides both amplitude of dΩ as well as equator-pole lap time.

We also provide an estimate of uncertainty in dΩ by producing a variation ellipse which encompasses all the values and 1σ uncertainties generated by individually varying stellar parameters and determining the corresponding dΩ and $\Omega_{\rm eq}$ pairs. The parameters varied for β Vir are $v\sin i$ ($\pm$ 2.6 km s^{-1}), inclination angle ($\pm$ 2 deg), and χ^2 aim ($\pm$ 0.05), for θ Dra $v\sin i$ ($\pm$ 0.2 km s^{-1}), inclination angle ($\pm$ 2 deg), and χ^2 aim ($\pm$ 0.05). The individual error bars indicate the 1σ errors of a Gaussian fit to the χ^2 landscape.

4 CHROMOSPHERIC ACTIVITY INDICATORS

4.1 S-Index

The S-index introduced by Vaughan et al. (1978) is an indirect measure of stellar magnetic activity and is a measure of dynamo efficiency (Noyes et al. 1984; Soderblom et al. 1993). It measures emission in the cores of Ca II H&K spectral lines formed in the chromosphere which are related to the presence of plage and network features (Schrijver et al. 1989). The S-index is defined as

$$S-{\rm index} = \frac{aF_{\rm H} + bF_{\rm K}}{cF_{R_{\rm HK}} + dF_{V_{\rm HK}}} + e, \tag{6}$$

where $F_{\rm H}$ and $F_{\rm K}$ are the fluxes in the resonance lines from 20 Å-wide channels (with triangular profiles) centred at wavelengths, 396.8492 nm, and 393.3682 nm, respectively (Duncan et al. 1991), compared to the flux at two bands in the continuum on the red and blue side of the H&K line. The coefficients determined for the NARVAL spectropolarimeter (a, b, c, d, e) are taken from Marsden et al. (2014). The S-Index for our stars are shown in Tables 1 and A2. The S-index not only varies between stars, but the same star has also been shown to vary over time in both cyclic and non-periodic manner (Wilson 1978; Duncan et al. 1991; Baliunas et al. 1995; Henry et al. 1996; Wright et al. 2004; Hall et al. 2007, 2009; Boro Saikia et al. 2018). Results from the decades long Mt Wilson survey of chromospheric emission from cool stars indicated that 60 per cent of lower main-sequence stars show periodic variations in chromospheric emission, which is considered akin to the solar cycle (Baliunas et al. 1998).

We investigate presence of chromospheric cycles by applying a generalized Lomb-Scargle (GLS) periodogram (Zechmeister & Kürster 2009) to a time series of our S-index measurements for β Vir and θ Dra. The results are plotted as power versus frequency where the height of the peak is a measure of the goodness of fit of a sine curve to the data. We also calculate the FAP (Baluev 2008; Zechmeister & Kürster 2009) that quantifies the probability of the maximum peak being produced by a signal without a periodic component (VanderPlas 2018). The most likely period is chosen as the peak with the smallest FAP (Baliunas et al. 1995), although it is possible for more than one significant peak to be present which may indicate multiple magnetic cycles (VanderPlas 2018). A detection is considered excellent when FAP is $\leq 10^{-9}$, good 10^{-9} to $\leq 10^{-5}$, fair 10^{-5} to $\leq 10^{-2}$, and poor 10^{-2} to $\leq 10^{-1}$ (Baliunas et al. 1995). The GLS periodogram takes into account measurement errors by introducing weighted sums (Gilliland & Baliunas 1987; Irwin et al. 1989), and a floating mean (Cumming et al. 1999), which allows for statistical fluctuation in the mean. The GLS periodogram is considered more suitable for small numbers of observations, with uneven sampling, and cases where the period is greater than the length of observations (Zechmeister & Kürster 2009). Discussion of our S-index and magnetic cycle determinations are found in (Section 6.5).

4.2 H α Index

The stellar H α line can also be used as a diagnostic of chromospheric activity in cool stars (Cayrel et al. 1983; Zarro 1983; Zarro & Rodgers 1983; Herbig 1985; Cincunegui et al. 2007). We calculate the H α-index in a method similar to Marsden et al. (2014) according to the

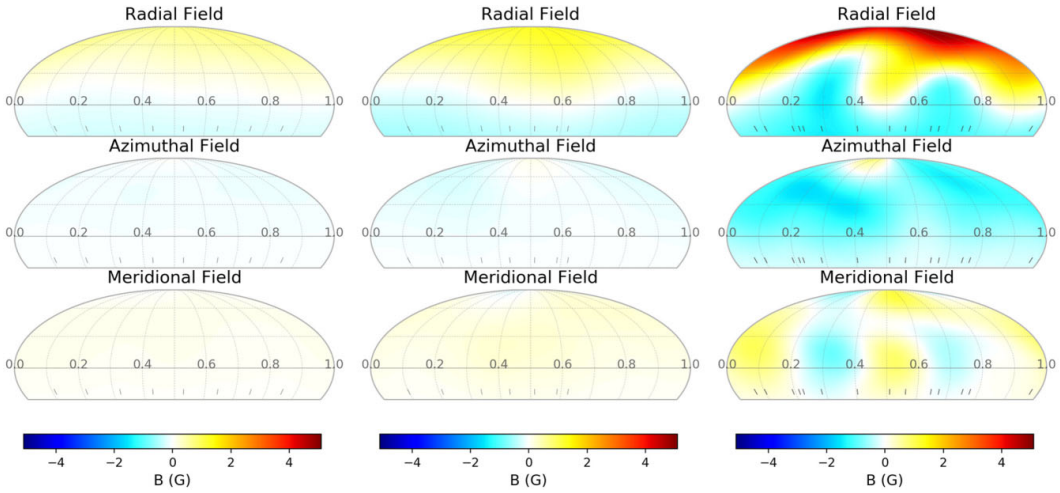

Figure 2. Reconstructed magnetic maps using ZDI for β Vir (F9V) at three epochs in 2017. Figure on left uses observations from February 14 to 22. Middle: March 1–29. Right: April 3–24. The rotational phases of the three maps are aligned with zero rotation phase set to MJD = 2457799.62139 (February map), MJD = 2457827.55489 (March map), and MJD = 2457854.5174 (April map). Tick marks at bottom of figure represent phase of individual observations. The colour bar at bottom indicates the magnetic field strength in Gauss.

equation from Gizis, Reid & Hawley (2002) and Morgenthaler et al. (2012):

$$\mathrm{H}\,\alpha - \mathrm{index} = \frac{F_{\mathrm{H}\alpha}}{F_{V_{\mathrm{H}\alpha}} + F_{R_{\mathrm{H}\alpha}}}. \quad (7)$$

Here, $F_{\mathrm{H}\,\alpha}$ is the flux in a 3.6 Å rectangular bandpass centred on the H α line and $F_{V_{\mathrm{H}\alpha}}$ and $F_{R_{\mathrm{H}\alpha}}$ are the fluxes in two 2.2 Å rectangular bandpasses centred on the continuum points 6558.85 and 6567.30 Å.

5 STELLAR WIND MODELLING

The stellar wind models for β Vir and θ Dra are created using the Alfvén Wave Solar Model (Sokolov et al. 2013; van der Holst et al. 2014) of the Space Weather Modelling Framework (Tóth et al. 2005, 2012) to solve the two-temperature MHD equations along with equation describing the Alfvén wave propagation, reflection, and dissipation along magnetic field lines. We model the wind in two partially overlapping three-dimensional regions. The inner region uses a spherical grid that is irregular in the radial direction; far away from the star the radial spacing is logarithmic, while more radial grid points are added near the star using the methodology of Oran et al. (2013). The outer region uses a Cartesian grid. The wind model covers the regions between the chromosphere and the inner astrosphere, and includes a physical model of the transition region in which the wind is heated to coronal temperatures by Alfvén wave energy emanating from deeper stellar layers, resulting in a Poynting flux $\Pi_{\mathrm{A}} \propto |\mathbf{B}|$ at the inner model boundary. Other heat exchange and cooling terms are also included as they are necessary (Roussev et al. 2003) to reproduce the slow-fast wind bimodality. The radiative cooling is given by $Q_{\mathrm{rad}} = N_{\mathrm{i}} N_{\mathrm{e}} \Lambda(T_{\mathrm{e}})$ where the rate of cooling curve $\Lambda(T_{\mathrm{e}})$ is calculated using the CHIANTI data base (Landi et al. 2013) and Solar elemental abundances.

The radial component of the boundary magnetic field is fixed to the local magnetogram value in Figs 2 and 3. The surface parallel components of the magnetic field varies freely as the MHD solution evolves towards a steady state. The outgoing Alfvén wave energy density at the inner boundary is $(\Pi_{\mathrm{A}}/B)\sqrt{\mu_0 \rho}$. The model and boundary conditions are similar to the ones in Evensberget et al. (2021); i.e. Solar values are used for the chromospheric base temperature and density, the Poynting flux-to-field ratio, the turbulence transverse correlation length and the Coloumb logarithm (see Table 3). The last three of these parameters control the supply of Alfvén wave energy, the Alfvén wave dissipation rate, and the rate of ion-electron heat exchange respectively. These values have been chosen to reproduce observed Solar conditions, see Sokolov et al. (2013), van der Holst et al. (2014). The simulation is stepped forward until a steady state is reached, in which the magnetic and hydrodynamic forces are in balance.

6 RESULTS

6.1 Magnetic maps for β Vir

The large-scale magnetic field topology for β Vir at three epochs derived using ZDI is shown in Fig. 2. The stellar parameters used to construct the map are $v \sin i = 6.1$ km s^{-1}, inclination = 36 deg, and $\mathrm{d}\Omega = 0.19$ rad d^{-1}. The spherical harmonics expansion is limited to $\ell_{\mathrm{max}} = 10$, since no further magnetic energy in higher multipoles was found by increasing ℓ further, and the chosen value of χ^2 for β Vir and θ Dra is 0.95. The data sets comprise 9 LSD profiles between 2017 February 14–22, 8 LSD profiles between 2017 March 1–29, and 30 LSD profiles between 2017 April 3–24. We divide observations into three subsets in order to reduce the effects of magnetic field evolution on the final maps, while providing adequate phase coverage to produce a reliable magnetic map. The April map uses more LSD profiles due to the more intensive sampling for that epoch and splitting the data into two maps using a smaller number of LSD profiles does not provide any significant changes in the resulting maps with increased magnetic field complexity still visible in the April β Vir map.

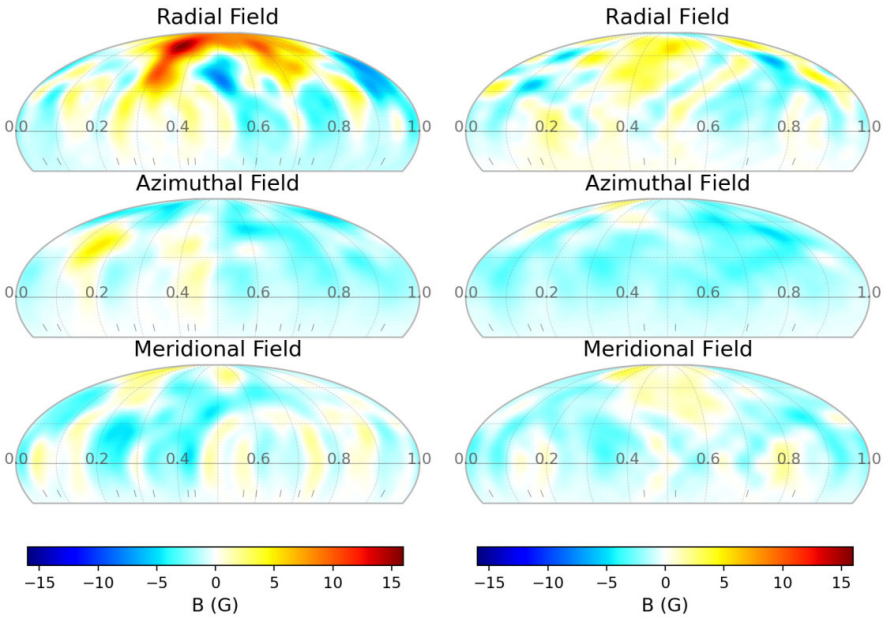

Figure 3. Reconstructed magnetic maps using ZDI for θ Dra at two epochs in 2017. The map at left spans observations from April 6 to 24. The map at right spans observations from 15 May to 18 June. The rotational phases of the two maps are aligned with the zero phase set to MJD = 2457861.4817 (April map) and MJD = 2457910.4710 (May–June map). Tick marks at bottom of figure represent phase of individual observations. The colour bar at bottom indicates the magnetic field strength in Gauss.

The radial field for β Vir shows a relatively simple structure in February and March 2017, while slightly stronger and more complex in April 2017. The increase in magnetic field strength and complexity of the April 2017 map is not an artefact of the larger number of LSD profiles used in the magnetic map reconstruction but appears to be a real change in the surface magnetic field. We verified this by creating a magnetic map using a subset of 8 LSD profiles, and showed that the April map contained the same maximum and mean magnetic field as the reconstruction using 30 LSD profiles. The simple radial field topology may partly be due to a low $v\sin i$ of 6.1 km s^{-1} where the resolution of a map produced by ZDI is dependent on the number of resolved surface elements (Morin et al. 2010). At all three epochs the radial magnetic field is very dipolar, with a single region of positive field in the Northern hemisphere and negative field in the Southern hemisphere. The magnetic field remains very dipolar despite the moderate differential rotation, a feature which was also seen in the F7V star τ Boo (Donati et al. 2008). The azimuthal field is predominantly negative at all epochs with only a small positive region visible near the north pole. The meridional field is mostly positive with a small region of negative field near the north pole.

The complexity of the magnetic field for β Vir is quantified by calculating the fractional strengths of the magnetic field components (Table 5). Most of the magnetic energy for β Vir is stored in the poloidal field (82–98 per cent) while between 2 and 18 per cent of the magnetic energy is toroidal. The high percentage of poloidal field in β Vir is consistent with the finding of Petit et al. (2008) and Jouve, Brown & Brun (2010) who find stars with rotation periods slower than ∼12 d contains predominantly poloidal magnetic fields. The dominant term in the spherical harmonics expansion for β Vir in the three magnetic maps is the dipole (ℓ = 1) with 73–91 per cent of the magnetic energy. The second largest spherical harmonics term is the quadrupole (ℓ = 2) with 8–18 per cent of the magnetic energy. The octupolar and higher components contain less than 7 per cent of the magnetic energy. The poloidal field is predominantly axisymmetric (80–97 per cent) while the toroidal field is also mainly axisymmetric (85–98 per cent). The uncertainties in magnetic quantities are derived by varying the stellar parameters over the 1σ errors for each individual parameter, and taking the extreme values of the results as the variation. The parameter ranges used are inclination (± 2 deg), $v\sin i$ (± 2.6 km s^{-1}), $P_{\rm rot}$ (± 0.4 d), dΩ (± 0.09 rad d^{-1}), and target χ^2 (± 0.05) (see Table 5).

6.2 Brightness maps for θ Dra

The reconstructed brightness maps for θ Dra are shown in Fig. 4. The maps are comprised of 14 LSD profiles between 6–24 April 2017 and 8 LSD profiles between 15 May and 18 June 2017. The fast rotation of θ Dra ($v\sin i$ = 28.1 km s^{-1}) allows us to use Doppler Imaging to produce brightness maps for two epochs. The brightness maps show both bright and dark areas on the stellar surface compared to the average photospheric brightness at the same latitude (Petit et al. 2017). The dark areas correspond to cooler regions on the surface of the star which are likely associated with starspots (Berdyugina 2005; Strassmeier 2009) and are regions of enhanced magnetic activity which suppresses convection, creating cooler, darker regions on the stellar surface (Chugainov 1966; Vogt 1975, 1983). The brighter regions are thought to correspond to plages which are formed in the upper layers of the stellar atmosphere and are regions of enhanced magnetic activity (Linsky 1983).

The April 6–24 map for θ Dra shows the presence of both lighter and darker areas that are smaller and more numerous compared with the 15 May–18 June map. This may be due to the larger number of profiles used in constructing the April 6–24 map, which results in better resolution of the surface features. We see a large dark patch at the north polar region on both maps. Similar dark polar regions have been found on other F-stars; see for example one component of σ 2 CrB, F6V (Strassmeier & Rice 2003), AF Lep, F8V (Marsden et al. 2006a), and τ Boo, F7V (Fares et al. 2009). The presence of a polar spot on θ Dra and other rapid rotators has been described by Schüssler & Solanki (1992) as being the result of a dominance of Coriolis force over buoyancy in the dynamics of magnetic flux tubes. This results in rising flux tubes following a path nearly parallel to the axis of rotation and erupting at higher latitudes. Our brightness maps for θ Dra are used an input for the ZDI reconstruction of the magnetic maps.

6.3 Magnetic maps for θ Dra

The reconstructed magnetic maps for θ Dra are shown in Fig. 3. The maps are comprised of 14 LSD profiles between 2017 April 6 and 24 and 8 LSD profiles between 2017 May 15 and June 18. The stellar parameters used to construct the map are $v \sin i$ = 28.1 km s^{-1}, inclination = 37 deg, and dΩ = 0.18 rad d^{-1}. The spherical harmonic expansion is limited to $\ell_{\rm max}$ = 20, since no further detail is obtained with higher degrees. The large polar spot on the brightness maps (Fig. 4) corresponds to regions of enhanced radial field in the magnetic maps (Fig. 3). The magnetic map for θ Dra in 2017 April has a stronger average magnetic field (2.5 ± 0.2 G) and larger S-index (0.2085 ± 0.0019) compared to 2017 May–June map ($B_{\rm mean}$ = 1.9 ± 0.2 G, S-index = 0.2029 ± 0.0023) (Fig. 3 and Table 4) which also corresponds to the brightness map with the more complex structure. These observations are consistent with θ Dra being more magnetically active in 2017 April compared with 2017 May and June, which indicates θ Dra contains a dynamo magnetic field due to its changing strength over time.

At both epochs the magnetic maps for θ Dra show a strong region of positive radial field at the north polar region, while the mid-northern latitudes shown a mix of positive and negative regions. The azimuthal field is predominantly negative at both epochs with only a small positive regions near the north pole, and a larger region of positive field at mid northern latitudes in April 2017. The meridional field at both epochs contain a mix of positive and negative areas. The complexity of the magnetic field for θ Dra as described by fraction of the large-scale magnetic energy reconstructed in various components is shown in Table 5. The largest terms in the spherical harmonics expansion for θ Dra are dipole (ℓ = 1) with 19–20 per cent of the magnetic energy. The second largest spherical harmonics term is the quadrupole (ℓ = 2) with 14–18 per cent of the magnetic energy, followed by octupolar (ℓ = 3) with 11–16 per cent of magnetic energy. θ Dra has a large amount of magnetic energy stored in the higher multipoles ($\ell > 3$) with values ranging from 47 to 55 per cent, which is consistent with a complex dynamo magnetic field.

The amount of energy contained in higher multipoles for θ Dra compared to β Vir is most likely determined by its faster rotation and therefore the number of resolved surface elements (Morin et al. 2010). An increase in surface resolution results in an ability to reconstruct smaller scale magnetic features and therefore higher multipoles. The uncertainties in magnetic quantities are derived by varying the stellar parameters over the 1σ errors for each individual parameter, and taking the extreme values of the results as the variation. The parameter ranges used are inclination (± 2 deg), $v \sin i$ (± 0.2 km s^{-1}), $P_{\rm rot}$ (± 0.02 d), dΩ (± 0.02 rad d^{-1}), and target χ^2 (± 0.05) (see Table 5).

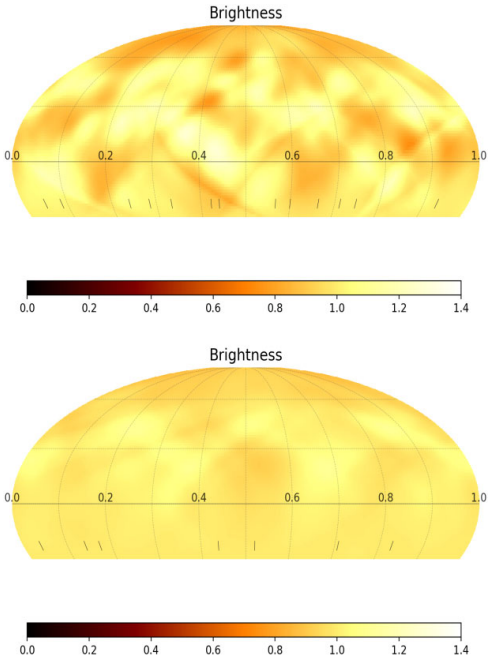

Figure 4. Brightness map for θ Dra at two epochs in 2017. Observations of the top Fig span from 2017 April 6–24. Bottom: Observations span from 2017 May 15 to June 18. The rotational phases of the two maps are aligned with the zero phase set to MJD = 2457861.4817 (April map) and MJD = 2457910.4710 (May–June map). The colour bar at bottom indicates the pixel brightness on a linear scale, where a value of 1.0 represents the quiet photosphere, values less than one are cool spots and values greater than one are bright spots.

6.4 Differential rotation

All stars with an outer convection zone are expected to show surface differential rotation (Hall & Henry 1990; Henry et al. 1995), and it has been suggested that stars with thin convection zones may show different patterns of dΩ (Gilman 1980). Balona & Abedigamba (2016) report a rate of dΩ detection for F-stars of 25 per cent. Theoretical studies have indicated that dΩ increases with increasing effective temperature (Kitchatinov & Rüdiger 1995, 1999a; Küker & Rüdiger 2005b, 2007; Küker et al. 2011). Barnes et al. (2005a) developed a power law relating stellar dΩ to $T_{\rm eff}$ which was confirmed for F-stars by (Reiners 2006),

$$\mathrm{d}\Omega = 0.053 \left(\frac{T_{\rm eff}}{5130K} \right)^{8.6} \ \mathrm{rad\ d^{-1}}. \quad (8)$$

We use the above formula to calculate a theoretical expected rate of dΩ of 0.23 rad d^{-1} for β Vir ($T_{\rm eff}$ = 6083 ± 58 K) and 0.24 rad d^{-1} for θ Dra ($T_{\rm eff}$ = 6105 ± 271 K). Using χ^2 minimization with a fixed entropy, we determine dΩ of 0.23 ± 0.09 rad d^{-1} for β Vir and 0.18 ± 0.03 rad d^{-1} for θ Dra (Fig. 5). The 1σ uncertainties are calculated by fitting a Gaussian fit to the χ^2 landscape. Our determined dΩ values closely matches equation (8), and is slightly

Table 3. Parameters for β Vir (2017 April 3–24) and θ Dra (2017 April 6–24) derived from the maximum-entropy image reconstructions, wind modelling inputs, and magnetic cycle determination using GLS periodogram of S-index. All parameters are from this work except where marked. ZDI determined parameters use Stokes *V* data except where marked and include χ^2 minimization and Ω_{eq} versus dΩ grid search.

Parameter	β Vir	θ Dra
zdi determined parameters		
Inclination (deg) (χ^2 min)	36 ± 2	37 ± 2
$v\sin i$ (km s^{-1}) (χ^2 min)	6.1 ± 2.6^a	28.1 ± 0.2
P_{rot} (d) (χ^2 min)	9.2 ± 0.2^b	2.88 ± 0.02
P_{rot} (d) (grid search)	9.1 ± 0.4	2.88 ± 0.02
dΩ (rad d^{-1}) (χ^2 min)	0.21 ± 0.02	0.18 ± 0.02
dΩ (rad d^{-1}) (grid search)	0.23 ± 0.09	0.18 ± 0.03
Eq-pole lap time (d)	$29.9^{+3.1}_{-2.6}$	$34.9^{+4.4}_{-3.9}$
S-index cycle		
No. observations	49	105
Observation baseline (d)	68	73
Cycle length (d)	83 ± 14	43 ± 2
No. cycles observed	0.8	1.7
FAP	$<10^{-3}$	$<10^{-9}$
Wind model input		
Stellar mass ($M_\odot$)[c]	1.13	1.17
Stellar radius ($R_\odot$)[c]	1.75	2.67
Wind model parameter		***Value***
Chromospheric base temperature, T_{chr}		5×10^4 K
Chromospheric base density, n_{chr}		2×10^{17} m^{-3}
Poynting flux-to-field ratio, Π_A/B		1.1×10^6 Watt m^{-2} T^{-1}
Turbulence trans. corr. length, $L_\perp\sqrt{B}$		1.5×10^5 m T$^{1/2}$
Coulomb logarithm, Λ_C		20

[a] $v\sin i$ value taken from Glebocki & Gnacinski (2005) since the χ^2 minimization did not produce a well-defined minimum. [b] P_{rot} value of 9.2 d used in final maps. [c] Stassun et al. (2019).

higher than the mean d$\Omega = 0.159$ rad d^{-1} found in a sample of 969 F6-G0 stars using photometry by Balona & Abedigamba (2016).

6.5 Chromospheric emission

6.5.1 S-index

The S-index determinations for β Vir over the 83 d observation period are shown in Table 1. The S-index varies from 0.1593 to 0.1658 that indicates the star is only showing weak chromospheric activity. The S-index range during our observation period is within the range of values for β Vir published in the literature of 0.138–0.186 (Pace 2013). A plot of the S-index versus rotational phase for β Vir (Fig. 6) shows a possible difference between the three epochs of observations, and the map with the highest S-index (April 3–24) corresponds to the map with the largest mean magnetic field strength (Fig. 7). The S-index determinations for θ Dra are shown as nightly means in Table 2, while the full 105 observations are shown in Table A2. The S-index variation over the observation period of 73 d is from 0.1990 to 0.2144 which indicates the star is showing strong chromospheric activity. Our S-index values for θ Dra are within the published range of 0.164–0.271 by Pace (2013) and indicates the star displays a large range of chromospheric activity. A plot of the S-index versus rotational phase for θ Dra (Fig. 6) shows a difference between the two epochs of observations, and the map with the highest S-index (April 6–24) corresponds with the largest mean magnetic field strength (Fig. 7). The higher S-index for θ Dra compared to β Vir is consistent with observations (Pallavicini et al. 1981) that a faster rotating star is more likely to produce stronger magnetic activity.

6.5.2 Chromospheric activity cycles

Results of our GLS periodogram search for chromospheric activity cycles for β Vir and θ Dra are shown in Table 3 and Fig. 8. Since nightly observations may lead to a window function which can create a signal in the periodogram (VanderPlas 2018), we need to look for its presence in our data. We calculate a window function for both stars by applying a Lomb–Scargle periodogram to the data while setting the S-index values to unity. For β Vir, we find a window function with a period of 688 d. Since the window function is much larger than the observation baseline, it does not have a significant effect on the chromospheric cycle period determination for β Vir. For θ Dra, we find a window function with a period of 729 d which is a possibly an harmonic of the highest peak found in the power versus frequency plot that shows the highest peak corresponding to a period of 183 d. We can possibly discount this peak as being an artefact of the nightly observations; however, in Fig. 8, we plot a sine curve with a period of 183 d since this appears to fit the S-index data better than a period of 43 d. On the power versus frequency plots there are no peaks coinciding with the P_{rot} for β Vir of 9.2 d, ($f = 0.109$), and 2.88 d ($f = 0.347$) for θ Dra; therefore, we did not remove any rotational signal from the periodograms.

We estimate a chromospheric cycle of 83 ± 14 d for β Vir by applying a GLS periodogram to 49 S-index values over a period of 68 d from 06 January 2017 to 24 April 2017. A FAP of $<10^{-3}$

Table 4. Stellar parameters for β Vir and θ Dra in 2017 determined from our ZDI analysis including 1σ uncertainties. All values are determined using Stokes *V* data except where marked.

Star Epoch	Obs Rot. cycles	No. LSD profiles	Incl (deg)	$v\sin i$ (km s^{-1})	*P*rot Using χ^2 min (d)	dΩ Using χ^2 min (rad d^{-1})	S-index[a] (mean)	H α-index[a] (mean)
β Vir Feb 14–22	0.9	9	[b]	[c]	[b]	[b]	0.1613 ± 0.0006	0.2752 ± 0.0005
β Vir Mar 1–29	3.0	8	[b]	c	[b]	[b]	0.1604 ± 0.0008	0.2753 ± 0.0010
β Vir Apr 3–24	2.3	30	36 ± 2	[c]	9.2 ± 0.4	0.21 ± 0.02	0.1623 ± 0.0011	0.2760 ± 0.0006
θ Dra Apr 6–24	6.2	14	37 ± 2	28.1 ± 0.2	2.88 ± 0.02	0.18 ± 0.02	0.2085 ± 0.0019	0.2856 ± 0.0008
θ Dra May 15–Jun 18	11.8	8	41 ± 2^d	28.1 ± 0.2	2.93 ± 0.02^d	0.21 ± 0.02^d	0.2029 ± 0.0023	0.2842 ± 0.0011

[a] Determined from Stokes *I* data. [b] For these inclination values χ^2 minimization does not produce a well-defined minimum, therefore we use the parameters from the April 3–24 map. [c] $v\sin i$ of $6.1.1 \pm 2.6$ used from Glebocki & Gnacinski (2005). [d] For the θ Dra 15 May–18 June map, we use the parameters determined from April 6–24 map, since it is reconstructed using a larger number of LSD profiles.

Table 5. Fraction of the large-scale magnetic energy reconstructed in the poloidal and toroidal field components for β Vir (2017) and θ Dra (2017). The quantities derived from ZDI are the mean unsigned magnetic field (B_{mean}), maximal field strength over stellar surface (B_{max}), the fraction of the large-scale magnetic energy reconstructed in the poloidal and toroidal field components, the fraction of the magnetic energy in the dipolar ($\ell = 1$), quadrupolar ($\ell = 2$), octopolar ($\ell = 3$), and higher ($\ell > 3$) components, the fraction of the magnetic energy in the axisymmetric field component ($m = 0$), as well as the axisymmetry of the poloidal and toroidal fields. The uncertainties are derived by varying the stellar parameters over the 1σ errors for each individual parameter, and taking the extreme values of the results as the variation. The parameter ranges used for β Vir are: inclination ($\pm$ 2 deg), $v \sin i$ ($\pm$ 2.6 km s^{-1}), P_{rot} ($\pm$ 0.4 d), dΩ ($\pm$ 0.09 rad d^{-1}), and target χ^2 ($\pm$ 0.05). The parameter ranges used for θ Dra are: inclination ($\pm$ 2 deg), $v \sin i$ ($\pm$ 0.2 km s^{-1}), P_{rot} ($\pm$ 0.02 d), dΩ ($\pm$ 0.02 rad d^{-1}), and target χ^2 ($\pm$ 0.05).

Star	B_{mean} (G)	B_{max} (G)	Pol (% tot)	Tor (% tot)	Dipolar (% pol)	Quad. (% pol)	Oct. (% pol)	($\ell > 3$) (% pol)	Axisym. (% tot)	Axi-pol (% pol)	Axi-tor (% tor)
β Vir 14–22 Feb	$0.3^{+0.3}_{-0.0}$	$0.7^{+1.0}_{-0.0}$	98^{+2}_{-0}	$2^{+0.0}_{-2}$	90^{+1}_{-2}	9^{+1}_{-1}	1^{+0}_{-0}	0^{+0}_{-0}	97^{+0}_{-5}	97^{+0}_{-5}	98^{+0}_{-16}
β Vir 1–29 Mar	$0.5^{+0.1}_{-0.1}$	$1.3^{+0.1}_{-0.1}$	98^{+0}_{-0}	2^{+0}_{-0}	91^{+1}_{-2}	8^{+2}_{-1}	1^{+1}_{-0}	0^{+0}_{-0}	94^{+1}_{-2}	94^{+1}_{-8}	87^{+9}_{-4}
β Vir 3–24 Apr	$1.6^{+0.2}_{-0.1}$	$4.9^{+1.8}_{-1.0}$	82^{+4}_{-10}	18^{+10}_{-4}	73^{+5}_{-8}	18^{+3}_{-2}	6^{+4}_{-2}	3^{+2}_{-1}	81^{+3}_{-12}	80^{+4}_{-15}	85^{+2}_{-6}
θ Dra 6–24 Apr	$2.5^{+0.2}_{-0.2}$	$16.2^{+1.0}_{-1.0}$	84^{+1}_{-1}	16^{+1}_{-1}	19^{+1}_{-1}	18^{+1}_{-1}	16^{+0}_{-1}	47^{+2}_{-2}	38^{+2}_{-3}	38^{+2}_{-4}	38^{+3}_{-2}
θ Dra 15 May–18 Jun	$1.9^{+0.2}_{-0.2}$	$7.7^{+0.8}_{-0.7}$	56^{+2}_{-1}	44^{+1}_{-2}	20^{+1}_{-2}	14^{+4}_{-2}	11^{+1}_{-1}	55^{+13}_{-6}	48^{+1}_{-1}	26^{+3}_{-2}	76^{+1}_{-1}

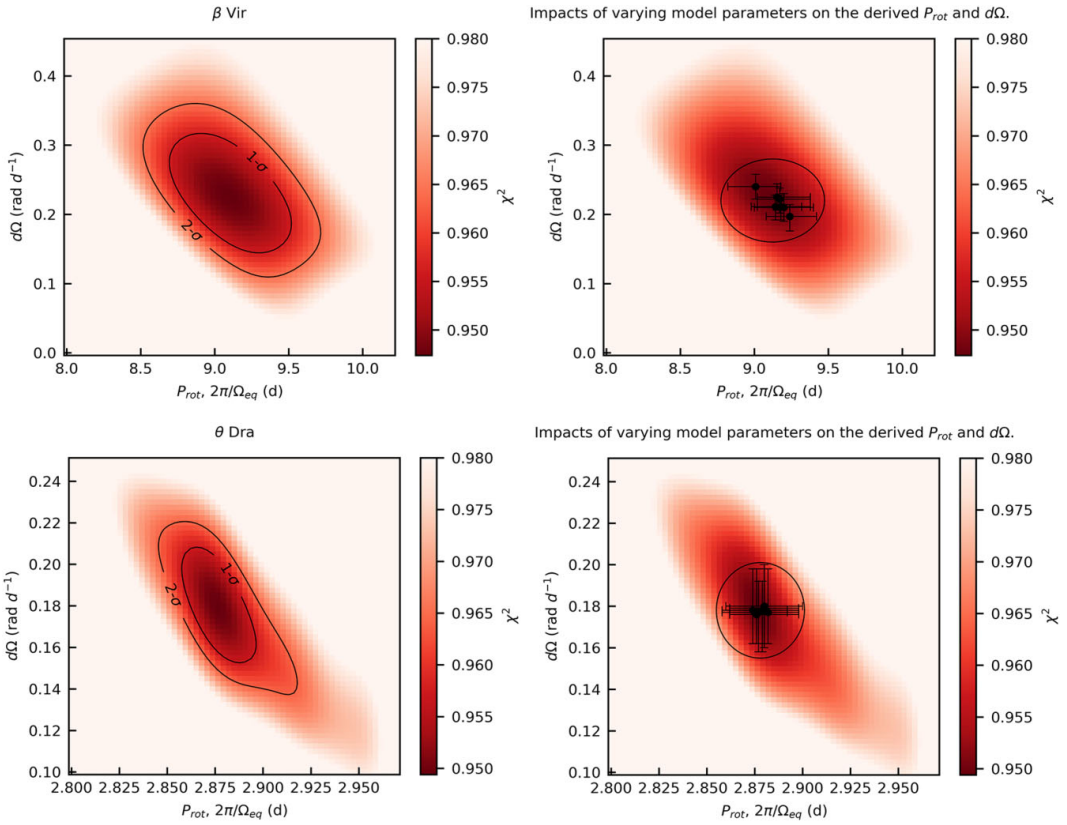

Figure 5. Figures at left: Surface differential rotation contour plot for β Vir 2017 April 3–24 (top) and θ Dra 6–2017 April 24 (bottom) with 1σ, and 2σ confidence contours marked with black lines. From the χ^2 landscape we determine the rotation period at the 1σ level of β Vir as 9.1 $\pm$ 0.4 d and θ Dra 2.88 $\pm$ 0.02. The dΩ for β Vir is 0.23 $\pm$ 0.09 rad d^{-1} and θ Dra 0.18 $\pm$ 0.03 rad d^{-1}. Figures at right: Surface differential rotation using χ^2 minimization landscape of Stokes V profiles for β Vir (top) and θ Dra (bottom). The variation ellipse is generated by individually varying stellar parameters and determining the corresponding Ω_{eq} and dΩ pairs. The parameters varied for β Vir are $v \sin i$ ($\pm$ 2.6 km s^{-1}), inclination angle ($\pm$ 2 deg), and χ^2 aim ($\pm$ 0.05), for θ Dra $v \sin i$ ($\pm$ 0.2 km s^{-1}), inclination angle ($\pm$ 2 deg), and χ^2 aim ($\pm$ 0.05). The individual error bars indicate the 1σ errors of a Gaussian fit to the χ^2 landscape.

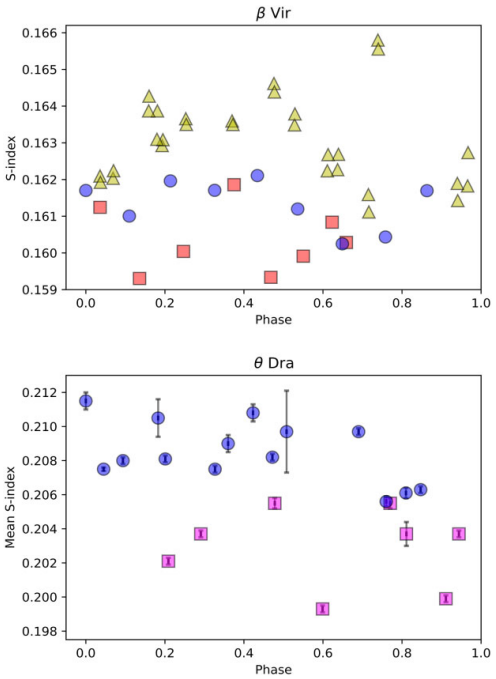

Figure 6. Top: S-index versus rotational phase for β Vir (top). Blue circle indicates data from 2017 February 14 to 22. Red squares indicates data from 2017 March 1 to 29 . Yellow triangle indicates data from 2017 April 3 to 24. The data hint at a possible difference between the three epochs; however, there is no significant difference between the mean S-index of each epoch (see Fig. 7). Bottom: Nightly averaged S-index versus rotational phase for θ Dra. Blue circles indicate data from 2017 April 6 to 24. Pink squares represent data for 2017 May 15 to June 18. The map with the strongest mean magnetic field (see Fig. 7) has a significantly higher S-index.

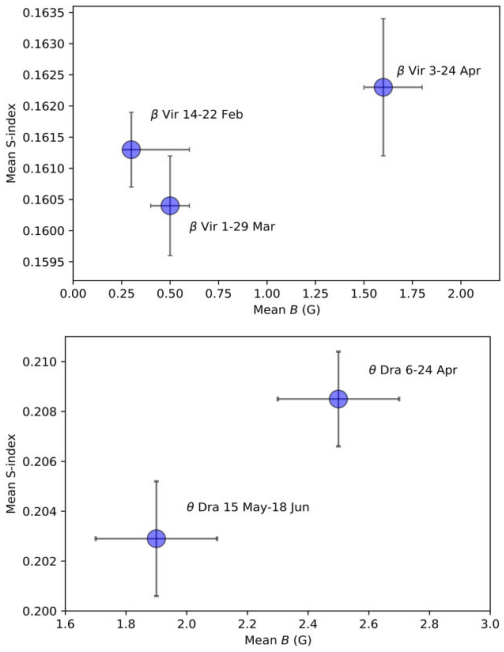

Figure 7. Mean S-index versus mean magnetic field strength (from ZDI) for β Vir (top) and θ Dra (bottom). There is no significant difference between the mean S-index of the 3 maps for β Vir, while there is a significantly larger mean magnetic field strength for the April map. For θ Dra there is a significantly larger mean S-index for the April map that coincides with stronger magnetic field strength (Table 5).

indicates the detection is considered fair. For θ Dra, we apply a GLS periodogram to 105 S-index values over a period of 73 d from 2017 April 06 to 2017 June 18. We see two peaks with a FAP $\leq 10^{-9}$. The peak corresponding to a cycle length of 43 $\pm$ 2 d is chosen as the possible chromospheric cycle length since the highest peak is discounted as an observational artefact as described above. Since we have a short baseline of observation of S-index for β Vir of 69 d (0.8 chromospheric cycles), and for θ Dra 73 d, which is 0.4 or 1.7 cycles (depending on which cycle length is chosen), we can only consider our determination of chromospheric activity cycles for the two stars as a lower limit. A longer baseline of S-index measurements is needed to verify these short cycles.

Our chromospheric activity cycles compared with other F-stars are shown in Fig. 9 and Table A1. The chromospheric cycle periods of 83 $\pm$ 14 d for β Vir and 43 $\pm$ 2 d for θ Dra are potentially shorter than cycles for other F-stars with published values ranging from 109 d for CoRoT 102780281 (F8V) determined by photometry (Lopes et al. 2015), and 120 d for τ Boo from chromospheric emission (Mengel et al. 2016), to a maximum of 21 yr for KIC 5955122 (F9V) determined by photometry (Bonanno et al. 2014). The older Mt Wilson survey data (Baliunas & Vaughan 1985; Baliunas et al. 1995) may have missed short cycles in some F-stars. The previous biasing of data towards longer chromospheric cycles may be hinted at from Fig. 9, where generally longer cycle lengths are visible in the older data.

6.5.3 *H α index*

Along with emissions in the core of Ca II H and K lines and Ca II triplet lines λ8498, 8542, 8662, the H α-index is one of the best indicators of stellar activity in solar-type stars (Gray & Corbally 2009). In Fig. 10, we show a plot of S-index and H α-index for both β Vir and θ Dra. We see a weak correlation between the two measures of chromospheric activity for β Vir with a Pearson correlation coefficient of $r = 0.31$, while there is a stronger correlation for θ Dra with correlation coefficient of $r = 0.63$. The correlation between S-index and H α-index for β Vir and θ Dra is consistent with the trend found in G and K-type stars by Zarro (1983), where the H α absorption increases with Ca II K strength. We find θ Dra has a larger H α index compared to β Vir and this trend has been observed in K, G, and F stars by Cram & Giampapa (1987), where the strength of the photospheric absorption line increases with increasing $T_{\rm eff}$. The increased scatter observed in the S-index for β Vir compared to θ Dra may be due to the low values measured for β Vir which range from 0.159 to 0.166 and may contain a lower relative SNR.

6.6 B_l versus rotational phase

The nightly average of B_l versus rotational phase for β Vir is shown in Fig. 11. The figure indicates there is no significant change in B_l between the three maps. There is a large scatter in B_l during

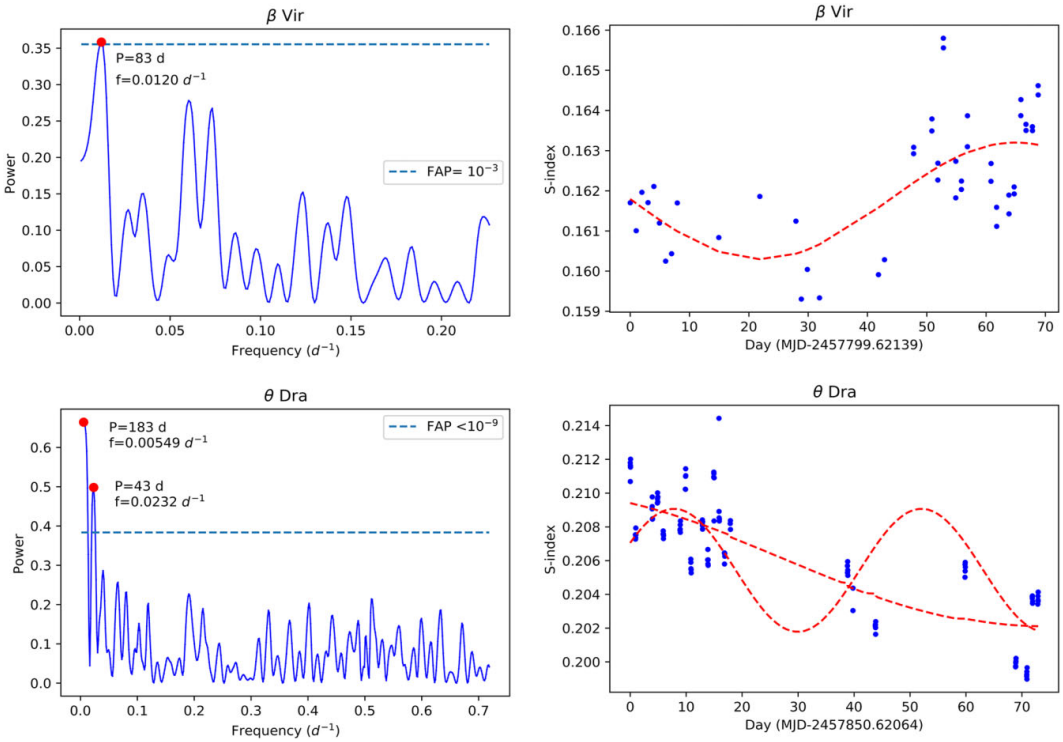

Figure 8. Chromospheric cycle determinations for β Vir 2017 (top) and θ Dra 2017 (bottom) applying a GLS periodogram a time-series of S-index measurements. The figures at left show the power versus frequency and FAP, with the highest peaks marked with a red circle, and text describes the associated period and frequency. The dashed horizontal line represents a FAP of $<10^{-3}$ for β Vir and $<10^{-9}$ for θ Dra. The figures at right show individual S-index measurements shown with blue circles. The red dashed curves indicate the fitted cycle using a GLS periodogram, and assumes a strictly periodic sine curve with a period of 83 d for β Vir. For θ Dra both 183 d and 43 d sine curves are plotted. The figures at right have the zero day set to the first date of S-index measurements for each star.

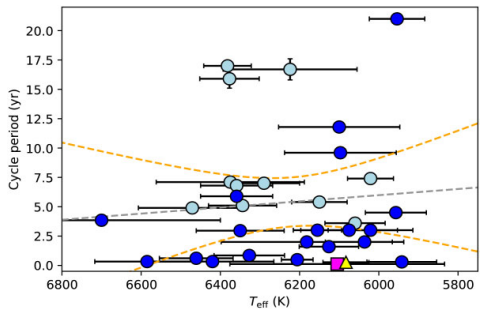

Figure 9. Chromospheric cycle determined from S-index for β Vir and θ Dra versus $T_{\rm eff}$ compared with 30 F-stars from the literature. Data from Mt Wilson survey papers (Baliunas & Vaughan 1985; Baliunas et al. 1995) are shown in light blue, which may have missed short cycles for F-stars. β Vir data is shown as yellow triangle (period 83 $\pm$ 14 d) and θ Dra data are shown as pink square (43 $\pm$ 2 d). The dashed grey trend line and orange 95 per cent confidence intervals are shown. No significant trend observed. The data are shown in Table A1.

2017 April, which is not accounted for by a magnetic field evolution over the two rotational cycles of observations. This was checked by separating the B_l observations into different rotational cycles and observing that the scatter in B_l remained. The scatter in B_l for β Vir in April 2017 is possibly due to the more complex nature of the magnetic field geometry and the location of the fields on the visible surface during an observation may lead to more or less cancellation effects. The nightly average of B_l versus rotational phase for θ Dra is shown in Fig. 11, which also indicates there is no significant difference in B_l between the two maps.

A possible reason no difference in B_l is observed between the two epochs for θ Dra, while the mean S-index for magnetic maps show a significant difference, is that B_l suffers from cancellation effects from regions of opposite polarity, which does not occur for the S-index. We also find that unlike B_l, the calculation of $B_{\rm mean}$ using ZDI does show a significant difference between the two maps. This difference may be explained by the reduced amount of flux cancellation that occurs when calculation $B_{\rm mean}$ using ZDI in faster rotating stars (Lehmann et al. 2019) where θ Dra is a reasonably fast rotator with $v \sin i$ = 28.1 km s^{-1}. Another possible reason for the lack of visible change in B_l between the two θ Dra maps is that the error bars are a similar magnitude to B_l.

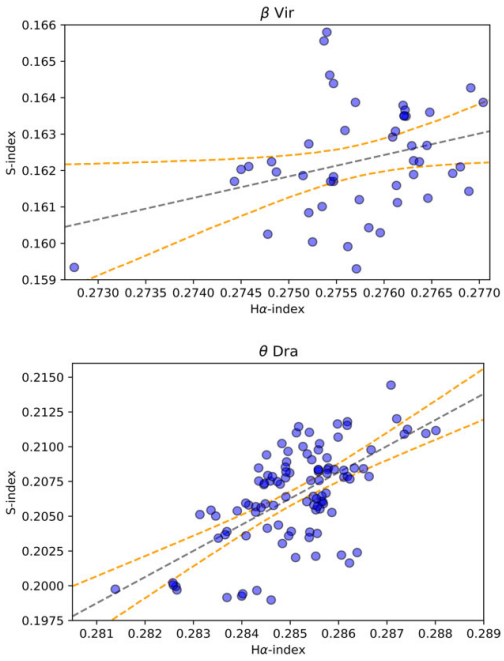

Figure 10. Individual S-index versus individual H α index for β Vir (top) and θ Dra (bottom). The dashed grey trend line and orange 95 per cent confidence intervals are shown. Significant trend observed for both plots with a Pearson correlation coefficient of $r = 0.31$ for β Vir and $r = 0.63$ for θ Dra. These plots indicate the correlation between S-index versus individual H α index holds for late F-stars.

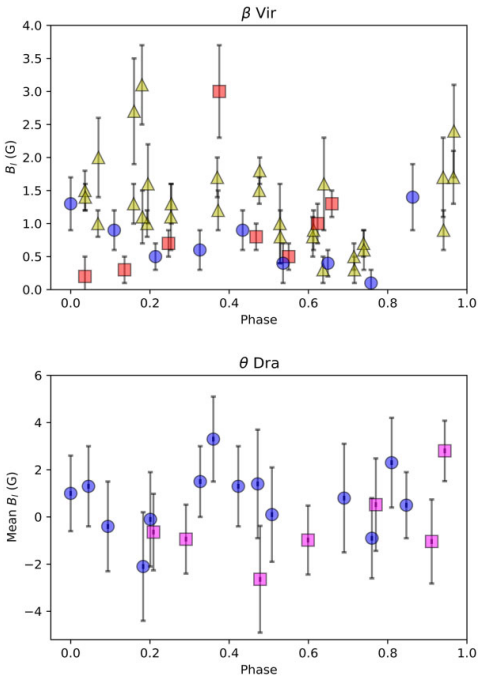

Figure 11. B_l versus rotational phase for β Vir (top) and θ Dra (bottom). Symbols are the same as Fig. 6. There is no significant difference between the means within the data set for each star. The B_l observations for θ Dra with a mean B_l of -13.1 ± 5.1G at rotation phase 0.811 was cropped from the figure to allow better visibility of data. This value with large errors was caused by cloud interference resulting in an V mag extinction ∼3.

6.7 Stellar wind modelling

The coronal magnetic field structure when the wind model has reached as steady state is shown in Fig. 12. The mostly dipolar surface magnetic field of β Vir (see Fig. 2) produces a region of closed magnetic field lines surrounding the surface $B_r = 0$ line, and two regions of open field lines around the north and south magnetic poles. The alignment of the magnetic dipole appears to vary somewhat between the February 14–22 observations and the other two. The region of closed field lines appears smaller for the Febuary 14–22 observation, where the magnetic field is at its weakest. The more complex surface magnetic field geometry of θ Dra (see Fig. 3) gives rise to a similarly complex coronal field; no clear dipolar structure is visible in the coronal field. At both epochs, θ Dra exhibits a large, uniform region of open field lines in the lower hemisphere; this is likely caused by the ZDI regularization in unobservable regions of the star past ∼140°.

The wind accelerates as it flows away from the star, and eventually the wind speed exceeds the Alfvén wave speed $v_A = B/\sqrt{\mu_0 \rho}$ (Alfvén 1942). The surface where this first occurs is shown in Fig. 13. The wind states, as it crosses this Alfvén surface determines the stellar angular momentum loss, as the surface functions as an effective lever arm (Schatzman) increasing the torque effected by the wind upon the star. The xz plane and the Alfvén surface are coloured by the local wind speed. A two-lobed Alfvén surface develops for β Vir at all three epochs; this is typical for a dipole-dominated magnetic field. θ Dra exhibits an irregular Alfvén surface; this is associated with a more complex magnetic field. Fig. 13 also shows the current sheet (Schatten 1972), which we characterize by the radial magnetic field B_r changing sign. The inner current sheet of β Vir appears quite flat but with slightly varying inclinations (see Table 6). The current sheet of θ Dra has multiple kinks and undulations, reflecting the complex magnetic geometry.

The wind pressure in the stellar equatorial plane is shown in Fig. 14. The non-uniformity of the coronal field creates regions of varying wind pressure as the wind density and acceleration is affected by local differences in the magnetic field. The stellar rotation shapes these regions into spirals. The dipolar coronal field of β Vir creates two spiral co-rotating interaction regions (CIRs) of locally overdense wind, while the θ Dra cases are more complex, showing up to four spiral CIRs. The faster rotation of θ Dra creates a more tightly wound spiral in comparison to β Vir.

The wind models permit the calculation of a range of wind-related parameters; we give some of these parameters in Table 6. The surface magnetic flux Φ_0 is the total magnetic flux emerging from the stellar surface, and the open magnetic flux fraction $\Phi_{\rm open}$ is the fraction of Φ_0 that extends past the Alfvén surface. This parameter has been studied by Vidotto et al. (2014a) and Réville et al. (2015a, b) as a proxy for wind mass loss and angular momentum loss. A related parameter is the open surface fraction $S_{\rm open}$, which quantifies the fraction of the stellar surface from which open magnetic field lines emanate. The current sheet inclination i_{B_r} gives a quantitative indication of the tilt of the current sheet and Alfvén surface lobes relative to the stellar axis

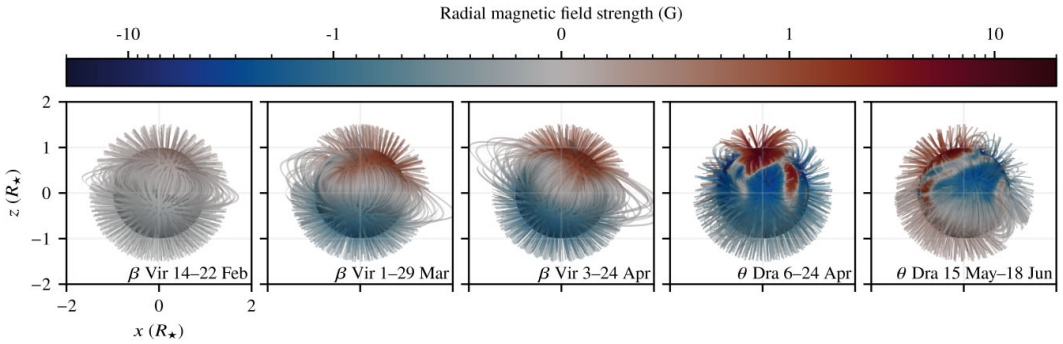

Figure 12. Coronal field structure and radial field strength for the wind model. The open field lines are truncated at two stellar radii. The stellar surface and the field lanes are coloured according to the local radial magnetic field strength. Note that the colour scale is linear from −1 G to 1 G and logarithmic outside of this range. β Vir, which occupies the three leftmost panels, exhibits a typical dipolar coronal field at all three epochs. A strengthening of the surface field may be observed between the first epoch February 14–22 and the second epoch March 1–29. The increase in field strength is accompanied by an increase in the size of the regions of closed magnetic field lines. θ Dra exhibits similar magnetic field strengths at both epochs. The change in polarity around the south pole region of the star can be seen between April 6–24 and May 15–Jun 18.

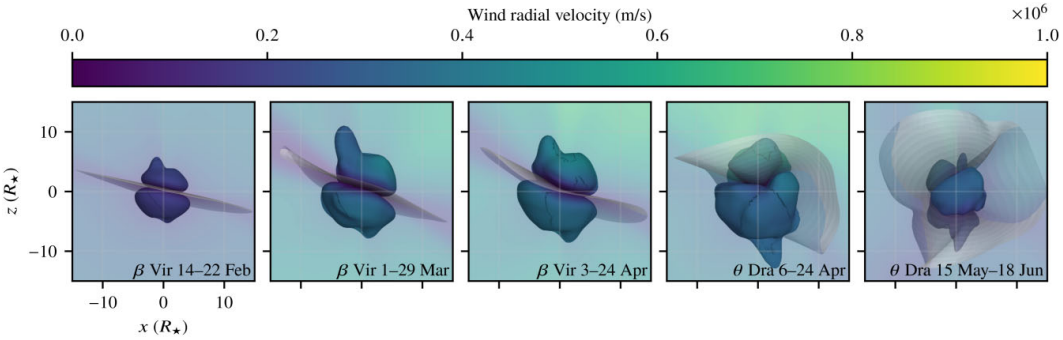

Figure 13. Alfvén surface and inner current sheet. The z-axis coincides with the stellar axis of rotation, and we show the inner current sheet edge-on to emphasize the two-lobed structure of the Alfvén surface. The Alfén surface and the plane of sky (i.e. the xz plane) is coloured according to the wind radial velocity u_r. The current sheet is truncated at $30R_\star$. β Vir exhibits a two-lobed Alfvén surface at all three epochs. An increase of the average Alfvén radius and of the current sheet inclination is seen between February 14 and 22 and the two other epochs, see the aggregate quantities in Table 6. The complicated magnetic field geometry of θ Dra gives rise to a multi-lobed Alfvén surface at both epochs. A decrease in the average Alfvén radius is observed between April 6–24 and May 15–June 18.

Table 6. Overview of the wind aggregates quantities considered. Φ_0 is the absolute amount of magnetic flux exiting the stellar surface, $\Phi_{\rm open}/\Phi_0$ is the fraction of Φ_0 contained in open field lines, $S_{\rm open}/S$ is the fraction of the stellar surface area where the field lines are open, $i_{B_r=0}$ is the angle between the inner current sheet and the stellar axis of rotation; this corresponds to the dipole inclination for a dipolar magnetic field, $\Phi_{\rm axi}/\Phi_{\rm open}$ is the axisymmetric open flux fraction, $R_{\rm A}$ is the distance to the Alfvén surface averaged over the stellar surface, $|\boldsymbol{r}_{\rm A}\times\hat{\boldsymbol{z}}|$ is the torque arm length at the Alfvén surface averaged over the stellar surface, $\dot{M}$ is the stellar mass-loss, $\dot{J}$ is the stellar angular momentum loss, $P_{\rm W}^{\oplus}$ is the average wind pressure for an Earth-like planet at 1 au, and $R_{\rm mag}/R_{\rm p}$ is the magnetospheric stand-off distance in Earth radii for an Earth-like planet.

Case	Φ_0 (Wb)	$\Phi_{\rm open}$ (Φ_0)	$S_{\rm open}$ (S)	$i_{B_r=0}$ (°)	$\Phi_{\rm axi}$ ($\Phi_{\rm open}$)	$R_{\rm A}$ ($R_\star$)	$\lvert\boldsymbol{r}_{\rm A}\times\hat{\boldsymbol{z}}\rvert$ ($R_\star$)	$\dot{M}$ ($\mathrm{kg\,s^{-1}}$)	$\dot{J}$ (N m)	$P_{\rm W}^{\oplus}$ (Pa)	$R_{\rm mag}$ ($R_{\rm p}$)
β Vir 14–Feb 22	$2.9\times10^{+14}$	0.86	0.56	13.6	0.90	4.3	3.3	$8.8\times10^{+8}$	$1.2\times10^{+23}$	1.0×10^{-9}	11.1
β Vir 1– Mar 29	$1.3\times10^{+15}$	0.66	0.32	24.5	0.82	6.1	4.7	$4.2\times10^{+9}$	$1.1\times10^{+24}$	4.9×10^{-9}	8.6
β Vir 3– Apr 24	$1.6\times10^{+15}$	0.68	0.37	23.0	0.81	6.4	4.9	$5.4\times10^{+9}$	$1.5\times10^{+24}$	6.1×10^{-9}	8.3
θ Dra 6– Apr 24	$7.7\times10^{+15}$	0.81	0.32	30.2	0.69	6.5	5.0	$2.5\times10^{+10}$	$4.2\times10^{+25}$	3.4×10^{-8}	6.2
θ Dra May 15–Jun 18	$3.8\times10^{+15}$	0.90	0.35	82.1	0.34	4.6	3.6	$2.0\times10^{+10}$	$1.8\times10^{+25}$	1.6×10^{-8}	7.1

of rotation. The axisymmetric magnetic flux fraction modulates the amount of galactic cosmic rays in the vicinity of the star (see Wang, Sheeley Jr & Rouillard 2006; Vidotto et al. 2014b). The average Alfvén surface $R_{\rm A}$ and the torque-averaged Alfvén surface $|\boldsymbol{r}_{\rm A}\times\hat{\boldsymbol{z}}|$ are used in lower-dimensional models and empirical scaling laws, e.g. Weber & Davis (1967), Mestel (1984), Kawaler (1988), and Finley & Matt (2018). A more detailed description of the calculation of these parameters is described in Evensberget et al. (2021).

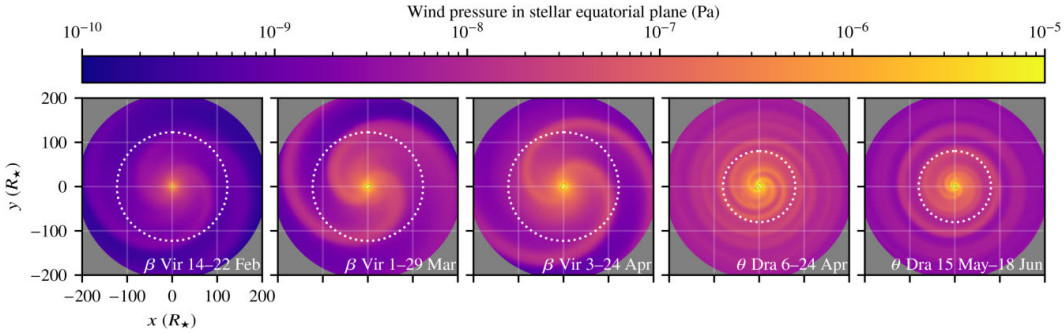

Figure 14. Wind pressure in the star's equatorial plane from the corona to the inner astrosphere. The dotted circle corresponds to an orbital distance of 1 au. The dipolar magnetic field of β Vir gives rise to two spiral 'arms' of overdense wind. These co-rotating interaction regions (CIRs) form when regions of fast, tenuous wind collide with regions of slower, denser wind. The complex field of θ Dra gives rise to multiple CIRs; for the April 6–24 epoch these CIRs persist past 1 au, while the CIRs appear to coalesce into a single spiral at the May 15–June 18 epoch.

The wind mass-loss $\dot{M}$ and the wind angular momentum loss is calculated by integrating the flux across the Alfvén surface. The Alfvén surface is chosen for its uniqueness, but the quantities could also be calculated across a spherical surface giving similar results. The $\dot{M}$ values of β Vir increase from 1–4 times the average solar wind mass loss rate of $\dot{M}_\odot = 1 \times 10^9$ kg s^{-1} (e.g. Wood 2004; Mishra et al. 2019), while the angular momentum loss $\dot{J}$ increases from about 1–5 times the average solar values of 2×10^{23} N m (Finley et al. 2019) between the first observation and the last two observations. The biggest change occurs between February 14–22 and March 1–29. θ Dra is does not exhibit as much variation as β Vir; the $\dot{M}$ values only change by 25 per cent, while the $\dot{J}$ changes by a factor of about 2. θ Dra's large radius of 2.67R$_\odot$ and rapid rotation of 2.88 d means that this star is not quite Sun-like. The numerical model used has mainly been validated for the solar case so some caution should be taken in interpreting θ Dra's $\dot{M}$ values which range from 20 to 25 $\dot{\mathrm{M}}_\odot$ and $\dot{J}$ values which range from 90 to 240 $\dot{\mathrm{J}}_\odot$, although it can be expected that this large, rapidly rotation star should have high values for both $\dot{M}$ and $\dot{J}$. Compared to the 86 G sub-giant of Ó Fionnagáin et al. (2021) our mass-loss values are lower, and our angular momentum loss values are significantly lower. This is however to be expected due to the sensitivity of $\dot{J}$ to the magnetic field strength.

We also include the wind pressure for an Earth-like planet at 1 au and the magnetospheric stand-off distance for an Earth-like planet; these quantities permit comparison to the local Earth space weather. The wind pressure is dominated by the wind radial velocity, $P_\mathrm{w} \approx \rho u_r^2$. The magnetospheric stand-off distance is calculated from a pressure balance argument similar to Vidotto et al. (2009). The wind pressure and stand-off distance at β Vir is comparable to Earth conditions, where the wind pressure varies from ∼0.1 nPa to ∼10 nPa (King & Papitashvili 2005). The conditions at θ Dra are characterized by more powerful winds; however, they are still comparable to the strong Solar wind conditions when the Sun is at Solar maximum.

7 DISCUSSION

A detailed understanding of surface magnetism and space weather surrounding mature late F-stars has been lacking in the literature, and our study provides an insight into magnetism in stars with thin outer convection zones. The reconstructed surface magnetic maps for β Vir and θ Dra allow us to compare dynamo magnetic fields in fast and slowly rotating late F-stars. The large-scale magnetic topology for the slowly rotating β Vir is relatively simple, and is mostly poloidal and dipolar. The surface field shows some changes between the three epochs and is slightly more complex in the 2017 April 3–24 map, compared with the two earlier maps, which is possibly partly due to a more complete rotational phase coverage of the map. The relatively simple magnetic structure is most likely a dynamo magnetic field due to the changing topology and varying amount of magnetic energy contained in the spherical harmonic modes between epochs. Both the maximum and mean magnetic field strength is significantly larger in the April 3–24 map compared to the two earlier maps, which is also consistent with a dynamo magnetic field present for β Vir.

The magnetic maps for the faster rotating θ Dra show more complex magnetic field topology than β Vir, which may be partly due to a greater surface resolution produced by ZDI for faster rotating stars, and also may be due to faster rotation which drives a stronger and more complex dynamo (Noyes et al. 1984; Pizzolato et al. 2003). θ Dra also has a greater mean magnetic field strength than β Vir due to a higher $v \sin i$, where a strong correlation exists between $v \sin i$ and magnetic activity for late F-stars (Wolff et al. 1986) and other cool stars (Noyes et al. 1984). θ Dra has more magnetic energy stored in the toroidal field compared to the slower rotating β Vir, which is consistent with finding by Petit et al. (2008) and Jouve et al. (2010) where the proportion of toroidal energy increases with rotation rate.

F-stars are expected to show faster dΩ compared to cooler stars. Our determinations of dΩ for β Vir (F9V) and θ Dra (F8IV) are smaller than 0.50 ± 0.12 rad d^{-1} for τ Boo (F7V) (Donati et al. 2008) and comparable to the 0.25 rad d^{-1} for HD75332 (F7V) (Brown et al. 2021). This is consistent with the trend of increasing dΩ with increasing T_eff (Kitchatinov & Rüdiger 1999b; Barnes et al. 2005a; Küker & Rüdiger 2005a; Reiners 2006; Marsden et al. 2006b; Collier Cameron 2007; Marsden et al. 2011; Waite et al. 2011). Both β Vir and θ Dra have similar dΩ despite their large differences in $v \sin i$ of 28.1 ± 0.2 km s^{-1} and 6.1 ± 0.2 km s^{-1}, respectively. Our results are consistent with findings that dΩ only shows a weak correlation with rotation (Hall 1991; Donahue et al. 1996; Messina & Guinan 2003; Reiners & Schmitt 2003b; Barnes et al. 2005a; Küker & Rüdiger 2005a; Reinhold, Reiners & Basri 2013).

There is evidence that dΩ can vary over short and medium timescales (Cameron & Donati 2002; Donati et al. 2003; Marsden, Carter & Donati 2005; Barnes et al. 2005b; Yu et al. 2019). We do not detect a change in dΩ for β Vir from 2017 February–April, which may be partly due to its slow rotation ($v \sin i = 6.1 \pm 0.2$ km s^{-1}), resulting

in a reduced spatial resolution of the stellar surface by ZDI, resulting in larger uncertainties in dΩ determination (Fig. 5). Similarly, no change is observed in dΩ for θ Dra between 2017 May–June, even with an increased spatial resolution of the surface compared to β Vir due to its faster rotation ($v \sin i = 28.1 \pm 0.2$ km s^{-1}). The lack of change in dΩ shows a repeatability in our measurements, which often can be difficult to reliably measure.

Another measure of photospheric shear is the equator-pole lap time (Donati & Cameron 1997), which is an absolute value measuring the time for the equatorial region to lap the pole, and is often used as an indicator of dynamo efficiency (Reiners & Schmitt 2003a). This value measures the lap time in days 1/dΩ rather than the relative term Ω/dΩ that measures the lap time in rotation cycles (Donati & Cameron 1997) and is a useful comparison of surface shear between stars. We determine equator-pole lap times of $29.9^{+3.1}_{-2.6}$ d for β Vir and $34.9^{+4.4}_{-3.9}$ d for θ Dra (Table 3), which are both shorter than the 130 d for the Sun (Reiners & Schmitt 2003b). The short lap times in our late F-stars is consistent with the trend that equator-pole lap time decreases with increasing $T_{\rm eff}$ (Barnes et al. 2005a). Similar short equator-pole lap times have been shown in other F-stars, for example; HD 67483 (F3V, lap time 5.7 d) (Reiners & Schmitt 2003b), τ Boo (F7V, lap time 12 d) (Donati et al. 2008), and HD 75332 (F7V, lap time 25 d) (Brown et al. 2021).

The discovery of short magnetic cycles in F-stars has occurred more recently. For example, τ Boo was originally found to have a magnetic cycle 11.6 ± 0.5 yr (Baliunas et al. 1995), but more recently Mengel et al. (2016) found a very short cycle of 120 d. Using re-analysed Mt Wilson Ca II H& K data, Olspert et al. (2018) found magnetic cycles for 10 F-type stars with periods ranging from 3.6 to 16.6 yr. These are longer than our magnetic cycle determination for β Vir and θ Dra, but are mostly shorter than the solar value of approximately 11 yr (Charbonneau 2014). Calculations using mixing-length theory by Belvedere et al. (1980) have predicted magnetic cycles for a G5 star is 9.5 yr and decreases to 0.88 yr for an F5, which is roughly consistent with the literature values shown in Fig. 9.

The short observation baseline for our S-index measurements of approximately 0.8 cycles for β Vir and 0.4 or 1.7 cycles for θ Dra means our cycle determinations can only be considered tentative, and may be considered a lower limit on the chromospheric activity cycle. The limitations of our cycle determinations are the short observation spans of the stars, and the use of periodograms that assume strictly periodic cycles. It is known from solar studies that the magnetic cycle of the Sun varies from 8–14 years and does not follow a strict period (Olspert et al. 2018). Many cool stars from spectral type F-K have been shown to exhibit chaotic chromospheric activity which cannot be represented by a regular cycle (Bruevich et al. 2001). It is also known that cool stars may show multiple magnetic cycles of different lengths operating simultaneously (Baliunas et al. 1996; Oláh et al. 2009; Vida, Oláh & Szabó 2014). F-stars provide good targets for studying magnetic activity cycles, because in some cases, it is possible to observe a full cycle in less than a year compared to more than a decade for the Sun. Due to its simple magnetic topology, β Vir may be a good target to study magnetic polarity reversals, however we did not observe any polarity reversal for β Vir in our 3 magnetic maps reconstructed over an 83 d timescale. A possible reason we did not find a magnetic polarity reversal for β Vir is that the chromospheric cycle we determined is very uncertain and possibly a longer observation period is required to see a polarity reversal.

The H α line core brightening and Ca II line strength are usually used interchangeably as indicators of stellar activity (Zarro 1983; Giampapa et al. 1989; Robinson et al. 1990; Strassmeier et al. 1990; Montes et al. 1995); however, Da Silva et al. (2011) noted it is not clear if this correlation holds for all stellar types or levels of activity. Cincunegui et al. (2007) studied these two indices for a sample of 109 stars ranging in spectral type from F6 to M5 and found the correlation between H α and Ca II flux held for the sample as a whole, but individual variations were noted between stars, with behaviours ranging from tight correlations with different slopes to anticorrelations, and in some cases no correlations were found. In a sample of M-dwarfs Walkowicz & Hawley (2009) found the relationship between H α and Ca II is not linear and weak absorption of the H α line can be associated with both weak and moderate Ca K emission as suggested by Cram & Giampapa (1987) and observed in M dwarfs by Stauffer & Hartmann (1986) and Da Silva et al. (2011). We find for β Vir there is a weak correlation between H α-index and S-index, while for θ Dra there is a stronger correlation (Fig. 10) where a correlation between the two indicators of stellar activity is consistent with the generally accepted trend.

The space weather surrounding β Vir and θ Dra show differences that are related to the strength and orientation of the reconstructed surface radial magnetic field. The stellar wind pressure at a distance of 1 au and the size of the magnetosphere for an Earth-like planet give an indication of the space weather surrounding β Vir and θ Dra compared to our own Solar system. Considering an average solar wind pressure of 2 nPa and a planetary magnetosphere size of 10 Earth radii, the average space weather at β Vir at the three observed epochs falls within the range of space weather conditions observed at Earth. θ Dra produces a wind pressure an order of magnitude stronger than the Sun's wind pressure; this does, however, not strongly affect the size of the magnetosphere as $R_{\rm m}/R_{\rm p} \propto (P_{\rm w}^{\oplus})^{-1/6}$. As always when modelling the steady state wind, it should be remembered that transient phenomena such as flares and coronal mass ejections may contribute significantly to the wind mass- and angular momentum loss; these effects cannot be accounted for by a steady-state model.

8 CONCLUSIONS

We use ZDI to reconstruct surface magnetic maps for two mature late F-type stars, β Vir (F9V), and θ Dra (F8IV). The magnetic field in the slower rotating β Vir shows a simple radial magnetic field which is predominately dipolar and axisymmetric. The azimuthal field shows two areas of stronger magnetic field in the 0–30 deg north latitude, while the meridional field shows two areas of stronger field about 30 deg north latitude. Due to its simple magnetic topology, β Vir may be a good target to look for polarity reversals. The faster rotating star θ Dra shows a more complex surface magnetic field with a strong radial field in the north polar region. The azimuthal field is predominately negative, while the meridional field shows a mix of both positive and negative regions. Our observations of β Vir and θ Dra indicate dynamo magnetic fields are present these two late F-stars with shallow outer convection zones. The space weather conditions surrounding β Vir at 1 au are similar to the conditions observed at Earth, while for θ Dra the wind pressure is an order of magnitude stronger than the Sun's wind pressure. Further magnetic mapping, and wind modelling needs to be done for early to mid F-type stars to better understand the transition between fossil and dynamo magnetic fields, and the space weather environment surrounding stars at the hot end of habitability for exoplanets.

ACKNOWLEDGEMENTS

This work is based on observations obtained at the Bernard Lyot Telescope (TBL, Pic du Midi, France) of the Midi-Pyrénées Ob-

servatory, which is operated by the Institut National des Sciences de l'Univers of the Centre National de la Recherche Scientifique of France. This research was supported by an Australian Government Research Training Program (RTP) Scholarship. This research has made use of the SIMBAD data base, operated at CDS, Strasbourg, France, and the VizieR catalogue access tool, CDS, Strasbourg, France.

DATA AVAILABILITY

All NARVAL data presented here are publicly available through the PolarBase data base (http://polarbase.irap.omp.eu/).

REFERENCES

Alfvén H., 1942, Nature, 150, 405
Alvarado-Gómez J. D., Drake J. J., Garraffo C., Cohen O., Poppenhaeger K., Yadav R. K., Moschou S. P., 2020, ApJ, 902, L9
Aurière M., 2003, EAS, 9, 105
Babcock H. W., 1947, ApJ, 105, 105
Backus G., 1958, Ann. Phys., 4, 372
Baliunas S. L., Vaughan A. H., 1985, ARA&A, 23, 379
Baliunas S. L. et al., 1995, ApJ, 438, 269
Baliunas S. L., Nesme-Ribes E., Sokoloff D., Soon W. H., 1996, ApJ, 460, 848
Baliunas S. L., Donahue R. A., Soon W., Henry G. W., 1998, in Bookbinder R. A.,Donahue J. A., eds, ASP Conf. Ser. 154, Cool Stars, Stellar Systems, and the Sun. Astron. Soc. Pac., San Francisco, p. 153
Balona L. A., Abedigamba O. P., 2016, MNRAS, 461, 497
Baluev R. V., 2008, MNRAS, 385, 1279
Barnes J. et al., 2005a, MNRAS, 357, L1
Barnes J. et al., 2005b, in Favata F., Hussain G. A. J., Battrick B., eds, ESA SP-560: Proc. 13th Cambridge Workshop on Cool Stars, Stellar Systems and the Sun. ESA, Noordwijk, p. 95
Beck J. G., 2000, Sol. Phys., 191, 47
Belvedere G., Paterno L., Stix M., 1980, A&A, 91, 328
Berdyugina S. V., 2005, Living Rev. Solar Phys., 2, 8
Bertelli G., Girardi L., Marigo P., Nasi E., 2008, A&A, 484, 815
Bertelli G., Nasi E., Girardi L., Marigo P., 2009, A&A, 508, 355
Bonanno A. et al., 2014, A&A, 569, A113
Boro Saikia S. et al., 2018, A&A, 616, A108
Bouvier J., 2013, EAS Publ. Ser., 62, 143
Brandenburg A., Subramanian K., 2005, Phys. Rep., 417, 1
Brown E. L. et al., 2021, MNRAS, 501, 3981
Bruevich E. A., Katsova M. M., Sokolov D. D., 2001, Astron. Rep., 45, 718
Cameron A. C., Donati J.-F., 2002, MNRAS, 329, L23
Casagrande L., Schönrich R., Asplund M., Cassisi S., Ramírez I., Meléndez J., Bensby T., Feltzing S., 2011, A&A, 530, A138
Catala C., Donati J.-F., Shkolnik E., Bohlender D., Alecian E., 2007, MNRAS, 374, L42
Cayrel R., de Strobel G. C., Campbell B., Mein N., Mein P., Dumont S., 1983, A&A, 123, 89
Chandrasekhar S., 1961, International Series of Monographs on Physics. Oxford, Clarendon, p. 1
Charbonneau P., 2014, ARA&A, 52, 251
Choudhuri A. R., Schussler M., Dikpati M., 1995, A&A, 303, L29
Chugainov P. F., 1966, Inf. Bull. Var. Stars, 122, 1
Cincunegui C., Díaz R. F., Mauas P. J. D., 2007, A&A, 469, 309
Collier Cameron A., 2007, Astron. Nachr., 328, 1030
Collier Cameron A., Donati J.-F., Semel M., 2002, MNRAS, 330, 699
Cram L. E., Giampapa M. S., 1987, ApJ, 323, 316
Cumming A., Marcy G. W., Butler R. P., 1999, ApJ, 526, 890
Da Silva J. G. et al., 2011, A&A, 534, A30
Degl'Innocenti M., Landolfi M., 2004, Polarization in Spectral Lines. Springer, Netherlands
Deutsch A. J., 1955, Ann. Astrophys., 18, p. 1
Deutsch A. J., 1958, Symposium-International Astronomical Union. Cambridge Univ. Press, Cambridge, p. 209
Donahue R. A., Saar S. H., Baliunas S. L., 1996, ApJ, 466, 384
Donati J.-F., Brown S. F., 1997, A&A, 326, 1135
Donati J.-F., Cameron A. C., 1997, MNRAS, 291, 1
Donati J.-F., Semel M., Rees D. E., 1992, A&A, 265, 669
Donati J.-F., Semel M., Carter B. D., Rees D. E., Collier Cameron A., 1997, MNRAS, 291, 658
Donati J.-F., Mengel M., Carter B. D., Marsden S., Collier Cameron A., Wichmann R., 2000, MNRAS, 316, 699
Donati J.-F., Collier Cameron A., Petit P., 2003, MNRAS, 345, 1187
Donati J.-F., Catala C., Landstreet J., Petit P., 2006a, In Cassini R., Lites B., eds, Solar Polarization 4, in ASP Conf. Ser., ASP, San Francisco, p. 362
Donati J.-F. et al., 2006b, MNRAS, 370, 629
Donati J.-F. et al., 2008, MNRAS, 385, 1179
Dravins D., 1975, A&A, 43, 45
Duncan D. K. et al., 1991, ApJS, 76, 383
Duquennoy A., Mayor M., 1991, A&A, 248, 485
Durney B. R., Latour J., 1977, Geophys. Astrophys. Fluid Dyn., 9, 241
Eggenberger P., Carrier F., 2006, A&A, 449, 293
Elsasser W. M., 1946, Phys. Rev., 69, 106
Elsasser W. M., 1956, Rev. Mod. Phys., 28, 135
Evensberget D., Carter B. D., Marsden S. C., Brookshaw L., Folsom C. P., 2021, MNRAS, 506, 2309
Fares R., 2013, Proc. Int. Astron. Union, 9, 180
Fares R. et al., 2009, MNRAS, 398, 1383
Finley A. J., Matt S. P., 2018, ApJ, 854, 78
Finley A. J., Hewitt A. L., Matt S. P., Owens M., Pinto R. F., Réville V., 2019, ApJ, 885, L30
Folsom C. P. et al., 2018, MNRAS, 474, 4956
Freund S., Robrade J., Schneider P. C., Schmitt J. H. M. M., 2020, A&A, 640, A66
Gaia collaboration et al., 2018, A&A, 616, A1
García R. A., Mathur S., Salabert D., Ballot J., Régulo C., Metcalfe T. S., Baglin A., 2010, Science, 329, 1032
Gehren T., 1978, A&A, 65, 427
Gerth E., Yu G., 2004, Magnetic Stars, 152, 165
Giampapa M. S., Rosner R., 1984, ApJ, 286, L19
Giampapa M. S., Cram L. E., Wild W. J., 1989, ApJ, 345, 536
Gilliland R. L., Baliunas S. L., 1987, ApJ, 314, 766
Gilman P. A., 1980, In Gray D., Linsky J., eds, Stellar turbulence. Springer-Verlag, New York, p. 19
Gizis J. E., Reid I. N., Hawley S. L., 2002, AJ, 123, 3356
Głębocki R., Gnaciński P., 2005, ESA SP-560: Proc. 13th Cambridge Workshop on Cool Stars, Stellar Systems and the Sun. ESA, Noordwijk, p. 571
Goncharskii A. V., Stepanov V. V., Kokhlova V. L., Yagola A. G., 1977, SvAL, 3, 147
Goncharskij A. V., Stepanov V. V., Khokhlova V. L., Yagola A. G., 1982, AZh, 59, 1146
Gray D., 1988, Lectures on Spectral-line Analysis: F, G, and K Stars. The Publisher, Arva
Gray D., 2005, The Observation and Analysis of Stellar Photospheres. Cambridge Univ. Press, Cambridge
Gray R., Corbally C., 2009, Stellar Spectral Classification. Princeton Univ. Press, Princeton
Gregory S. G., Jardine M., Gray C. G., Donati J.-F., 2010, Rep. Prog. Phys., 73, 126901
Güdel M., Guinan E. F., Skinner S. L., 1997, ApJ, 483, 947
Hall D. S., 1991, In Tuominen I., Moss D., Rudiger G., eds, The Sun and Cool Stars. Activity, Magnetism, Dynamos. Springer-Verlag, New York, p. 353
Hall D. S., Henry G. W., 1990, In Ibanoglu C., ed., Active Close Binaries. Kluwer, Dordrecht, p. 287
Hall J. C. et al., 2007, AJ, 133, 862
Hall J. C. et al., 2009, AJ, 138, 312
Handler G. et al., 2017, EPJ Web of Conferences, Seismology of the Sun and the Distant Stars II. EDP Sciences, p. 1001

Heiter U., Jofré P., Gustafsson B., Korn A. J., Soubiran C., Thévenin F., 2015, A&A, 582, A49
Henry G. W., Eaton J. A., Hamer J., Hall D. S., 1995, ApJS, 97, 513
Henry T. J., Soderblom D. R., Donahue R. A., Baliunas S. L., 1996, AJ, 111, 439
Herbig G. H., 1985, ApJ, 289, 269
Hobson M. P., Lasenby A. N., 1998, MNRAS, 298, 905
Humlícek J., 1982, J. Quant. Spectrosc. Radiat. Transfer, 27, 437
Irwin A. W., Campbell B., Morbey C. L., Walker G. A. H., Yang S., 1989, PASP, 101, 147
Ismail-Zadeh A., Tackley P., 2010, Computational Methods for Geodynamics. Cambridge Univ. Press, Cambridge
Jaynes E. T., 1957a, Phys. Rev., 106, 620
Jaynes E. T., 1957b, Phys. Rev., 108, 171
Jeffers S. V. et al., 2018, MNRAS, 479, 5266
Jofré P. et al., 2018, Research Notes of the AAS, 2, 152
Johnstone C. et al., 2010, MNRAS, 404, 101
Johnstone C. et al., 2015a, A&A, 577, A27
Johnstone C. et al., 2015b, A&A, 577, A28
Jouve L., Brown B., Brun A., 2010, A&A, 509, A32
Kambry M. A., Nishikawa J., 1990, Sol. Phys., 126, 89
Kawaler S. D., 1988, ApJ, 333, 236
King J. H., Papitashvili N. E., 2005, JGRA, 110, A02104
Kitchatinov L. L., Olemskoy S. V., 2011, MNRAS, 411, 1059
Kitchatinov L. L., Ruediger G., 1995, A&A, 299, 446
Kitchatinov L., Rüdiger G., 1999a, A&A, 344, 911
Kitchatinov L., Rüdiger G., 1999b, A&A, 344, 911
Kochukhov O., 2016, In Rozelot J-P., Neiner C., eds, Cartography of the Sun and the Stars. Springer, Switzerland, p. 177
Kochukhov O., Makaganiuk V., Piskunov N., 2010, A&A, 524, A5
Kochukhov O. et al., 2017, Astron. Nachr., 338, 428
Krause F., Rädler K., 1980, Mean-Field Magnetohydrodynamics and Dynamo Theory. Akademie-Verlag, Berlin
Küker M., Rüdiger G., 2005a, A&A, 433, 1023
Küker M., Rüdiger G., 2005b, Astron. Nachr., 326, 265
Küker M., Rüdiger G., 2007, Astron. Nachr., 328, 1050
Küker M., Rüdiger G., Kitchatinov L. L., 2011, A&A, 530, A48
Lammer H., Khodachenko M., 2014, Characterizing Stellar and Exoplanetary Environments. Springer, Switzerland
Landi E. et al., 2013, ApJ, 763, 86
Lehmann L. T., Hussain G. A. J., Jardine M. M., Mackay D. H., Vidotto A. A., 2019, MNRAS, 483, 5246
Lindegren L., Dravins D., 2003, A&A, 401, 1185
Linsky J. L., 1983, IAU Colloquium No. 71. Cambridge Univ. Press, Cambridge, p. 39
Lisse C. et al., 2017, AJ, 153, 62
Lopes C. F. et al., 2015, A&A, 583, A134
Maggio A., Sciortino S., Vaiana G. S., Majer P., Bookbinder J., Golub L., Harnden F. R., Rosner R., 1987, ApJ, 315, 687
Marsden S. C., Carter B. D., Donati J.-F., 2005, In: ESA SP-560: 13th Cambridge Workshop on Cool Stars, Stellar Systems and the Sun. ESA, Noordwijk, p. 799
Marsden S. C. et al., 2006a, Solar Polarization 4. p. 401
Marsden S. et al., 2006b, MNRAS, 370, 468
Marsden S. C. et al., 2011, MNRAS, 413, 1939
Marsden S. C. et al., 2014, MNRAS, 444, 3517
Mathur S. et al., 2014, A&A, 562, A124
Mayor M., Mazeh T., 1987, A&A, 171, 157
Mazeh T., Prato L., Simon M., Goldberg E., Norman D., Zucker S., 2002, ApJ, 564, 1007
Mengel M., 2005, Master's thesis, Department of Biological and Physical Sciences, University of Southern Queensland
Mengel M. W. et al., 2016, MNRAS, 459, 4325
Messina S., Guinan E. F., 2003, A&A, 409, 1017
Mestel L., 1984, In Baliunas S., Hartmann L., eds, Cool Stars, Stellar Systems, and the Sun. Springer, Berlin, p. 49
Metcalfe T. S., Basu S., Henry T. J., Soderblom D. R., Judge P. G., Knölker M., Mathur S., Rempel M., 2010, ApJ, 723, L213
Mishra W., Srivastava N., Wang Y., Mirtoshev Z., Zhang J., Liu R., 2019, MNRAS, 486, 4671
Mittag M., Schmitt J. H. M. M., Hempelmann A., Schröder K.-P., 2019, A&A, 621, A136
Moffatt K., Dormy E., 2019, Self-Exciting Fluid Dynamos. Cambridge Univ. Press, Cambridge
Montes D., Fernandez-Figueroa M. J., de Castro E., Cornide M., 1995, A&A, 294, 165
Montet B. T., Tovar G., Foreman-Mackey D., 2017, ApJ, 851, 116
Morgan W. W., Keenan P. C., 1973, ARA&A, 11, 29
Morgenthaler A., Petit P., Morin J., Aurière M., Dintrans B., Konstantinova-Antova R., Marsden S., 2011, Astron. Nachr., 332, 866
Morgenthaler A. et al., 2012, A&A, 540, A138
Morin J., Donati J.-F., Petit P., Delfosse X., Forveille T., Jardine M. M., 2010, MNRAS, 407, 2269
Mullan D. J., 1972, Astrophys. Lett., 12, 13
Neiner C., Wade G. A., Marsden S. C., Blazère A., 2017, Second BRITE Constellation Science Conference, Small Satellites, Big Science, Vol. 5. Polish Astron. Soc., Warsaw, p. 86
Nielsen M. B., Gizon L., Schunker H., Karoff C., 2013, A&A, 557, L10
North J. R. et al., 2009, MNRAS, 393, 245
Noyes R. W., Hartmann L. W., Baliunas S. L., Duncan D. K., Vaughan A. H., 1984, ApJ, 279, 763
Ó Fionnagáin D., Vidotto A., Petit P., Neiner C., Manchester IV W., Folsom C., Hallinan G., 2021, MNRAS, 500, 3438
Oláh K. et al., 2009, A&A, 501, 703
Olspert N., Lehtinen J. J., Käpylä M. J., Pelt J., Grigorievskiy A., 2018, A&A, 619, A6
Oran R., van der Holst B., Landi E., Jin M., Sokolov I. V., Gombosi T. I., 2013, ApJ, 778, 176
Pace G., 2013, A&A, 551, L8
Pallavicini R., Golub L., Rosner R., Vaiana G. S., Ayres T., Linsky J. L., 1981, ApJ, 248, 279
Parker E. N., 1955, ApJ, 122, 293
Parker E., 1979, Cosmical Magnetic Fields: Their Origin and Their Activity. Clarendon Press, Oxford
Paul K. T., Shruthi S. B., Subramaniam A., 2017, JA&A, 38, 6
Petit P., Donati J.-F., Collier Cameron A., 2002, MNRAS, 334, 374
Petit P. et al., 2008, MNRAS, 388, 80
Petit P., Hébrard E. M., Böhm T., Folsom C. P., Lignières F., 2017, MNRAS, 472, L30
Pinsonneault M. H., An D., Molenda-Żakowicz J., Chaplin W. J., Metcalfe T. S., Bruntt H., 2012, ApJS, 199, 30
Piskunov N., Kochukhov O., 2002, A&A, 381, 736
Pizzolato N., Maggio A., Micela G., Sciortino S., Ventura P., 2003, A&A, 397, 147
Pounds K. A. et al., 1991, MNRAS, 253, 364
Prendergast K. H., 1956, ApJ, 123, 498
Ramírez I., Fish J., Lambert D. L., Prieto C. A., 2012, ApJ, 756, 46
Rees D. E., Semel M. D., 1979, A&A, 74, 1
Régulo C., García R. A., Ballot J., 2016, A&A, 589, A103
Reiners A., 2006, A&A, 446, 267
Reiners A., Basri G., 2009, A&A, 496, 787
Reiners A., Schmitt J., 2003a, A&A, 398, 647
Reiners A., Schmitt J., 2003b, A&A, 412, 813
Reinhold T., Gizon L., 2015, A&A, 583, A65
Reinhold T., Reiners A., 2013, A&A, 557, A11
Reinhold T., Reiners A., Basri G., 2013, A&A, 560, A4
Réville V. et al., 2015a, ApJ, 798, 116
Réville V., Brun A. S., Strugarek A., Matt S. P., Bouvier J., Folsom C. P., Petit P., 2015b, ApJ, 814, 99
Rice J. B., 2002, Astron. Nachr., 323, 220
Rice J. B., Wehlau W. H., Khokhlova V. L., 1989, A&A, 208, 179
Roberts H., Stix M., 1971, Technical Report, The Turbulent Dynamo. National Center for Atmospheric Research, Boulder, CO
Robinson R. D., Cram L. E., Giampapa M. S., 1990, ApJS, 74, 891
Roussev I. I. et al., 2003, ApJ, 595, L57
Saikia S. B. et al., 2016, A&A, 594, A29

Sato S., Cuntz M., Olvera C. G., Jack D., Schröder K.-P., 2014, Int. J. Astrobiol., 13, 244
Schatten K. H., 1972, NASA Special Publication, 308, 44
Schatzman E., 1962, Annales d'astrophysique, 25, 18
Schrijver C. J., Cote J., Zwaan C., Saar S. H., 1989, ApJ, 337, 964
Schuessler M., Solanki S. K., 1992, A&A, 264, L13
Schwarzschild M., 1950, ApJ, 112, 222
Seach J. M., Marsden S. C., Carter B. D., Neiner C., Folsom C. P., Mengel M. W., Oksala M. E., Buysschaert B., 2020, MNRAS, 494, 5682
See V., Jardine M., Vidotto A. A., Petit P., Marsden S. C., Jeffers S. V., do Nascimento J. D., 2014, A&A, 570, A99
Semel M., 1989, A&A, 225, 456
Semel M., Donati J.-F., Rees D. E., 1993, A&A, 278, 231
Simpson E. K., Baliunas S. L., Henry G. W., Watson C. A., 2010, MNRAS, 408, 1666
Skilling J., Bryan R. K., 1984, MNRAS, 211, 111
Skumanich A., 1972, ApJ, 171, 565
Soderblom D. R., Stauffer J. R., Hudon J. D., Jones B. F., 1993, ApJS, 85, 315
Sokolov I. V. et al., 2013, ApJ, 764, 23
Soubiran C. et al., 2018, A&A, 616, A7
Stassun K. G. et al., 2019, AJ, 158, 138
Stauffer J. R., Hartmann L. W., 1986, ApJS, 61, 531
Steenbeck M., Krause F., 1969, Astron. Nachr., 291, 49
Stern R. A., Schmitt J. H. M. M., Kahabka P. T., 1995, ApJ, 448, 683
Strassmeier K. G., 2009, A&AR, 17, 251
Strassmeier K. G., Rice J. B., 2003, A&A, 399, 315
Strassmeier K. G., Fekel F. C., Bopp B. W., Dempsey R. C., Henry G. W., 1990, ApJS, 72, 191
Tayler R. J., 1973, MNRAS, 161, 365
Tokovinin A., 2014, AJ, 147, 87
Tóth G. et al., 2005, JGRA, 110, A12226
Tóth G. et al., 2012, J. Comput. Phys., 231, 870
Uitenbroek H., 2003, ApJ, 592, 1225
VanderPlas J. T., 2018, ApJS, 236, 16
van der Holst B., Sokolov I. V., Meng X., Jin M., Manchester W. B., Tóth G., Gombosi T. I., 2014, ApJ, 782, 81
Vaughan A. H., Preston G. W., Wilson O. C., 1978, PASP, 90, 267
Vida K., Oláh K., Szabó R., 2014, MNRAS, 441, 2744
Vidotto A. A., Opher M., Jatenco-Pereira V., Gombosi T. I., 2009, ApJ, 703, 1734
Vidotto A. et al., 2014a, MNRAS, 438, 1162
Vidotto A., Jardine M., Morin J., Donati J., Opher M., Gombosi T. I., 2014b, MNRAS, 438, 1162
Vidotto A. et al., 2014c, MNRAS, 441, 2361
Vogt S. S., 1975, ApJ, 199, 418
Vogt S. S., 1983, International Astronomical Union Colloquium. Cambridge Univ. Press, Cambridge, p. 137
Vogt S. S., 1988, In de Strobel G. C., Spite M., eds, The Impact of Very High S/N Spectroscopy on Stellar Physics. Springer, Netherlands, p. 253
Vogt S. S., Penrod G. D., 1983, PASP, 95 565
Vogt S. S., Penrod G. D., Hatzes A. P., 1987, ApJ, 321, 496
Waite I. A., Marsden S. C., Carter B. D., Hart R., Donati J.-F., Ramírez Vélez J. C., Semel M., Dunstone N., 2011, MNRAS, 413, 1949
Waite I. A., Marsden S. C., Carter B. D., Petit P., Donati J.-F., Jeffers S. V., Boro Saikia S., 2015, MNRAS, 449, 8
Walkowicz L. M., Hawley S. L., 2009, AJ, 137, 3297
Wang Y.-M., Sheeley N. R., Jr, Rouillard A. P., 2006, ApJ, 644, 638
Watson C. A., Littlefair S. P., Collier Cameron A., Dhillon V. S., Simpson E. K., 2010, MNRAS, 408, 1606
Weber E. J., Davis L., 1967, ApJ, 148, 217
Wenger M. et al., 2000, A&AS, 143, 9
Wilson O., 1978, ApJ, 226, 379
Wittenmyer R. A. et al., 2006, AJ, 132, 177
Wolff S. C., Boesgaard A. M., Simon T., 1986, ApJ, 310, 360
Wood B. E., 2004, Living Rev. Sol. Phys., 1, 2
Wright G. A. E., 1973, MNRAS, 162, 339
Wright J. T., Marcy G. W., Butler R. P., Vogt S. S., 2004, ApJS, 152, 261
Yu L. et al., 2019, MNRAS, 489, 5556
Zarro D. M., 1983, ApJ, 267, L61
Zarro D. M., Rodgers A. W., 1983, ApJS, 53, 815
Zechmeister M., Kürster M., 2009, A&A, 496, 577

APPENDIX A: ADDITIONAL RESULTS

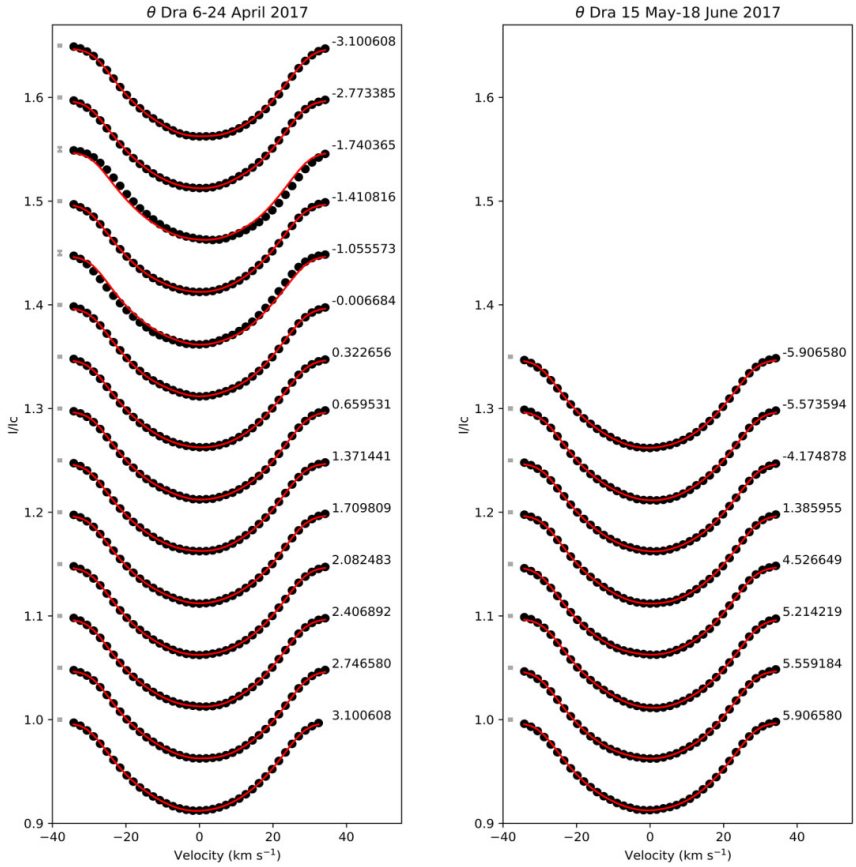

Figure A1. Stokes *I* maximum entropy fit for θ Dra. The black circles represent the observed signatures, while the red lines represent the modelled lines. The radial velocity range of the individual line profiles are shifted to the same range, and line profiles are separated vertically to allow better visibility. The 1.0σ error bars are shown on the left. The rotation cycle is shown on the right with the zero rotation cycle set to the mid JD of observations for each map and assumes $P_{\rm rot} = 9.3$ d for β Vir and $P_{\rm rot} = 2.88$ d for θ Dra. All figures are set to the same scale.

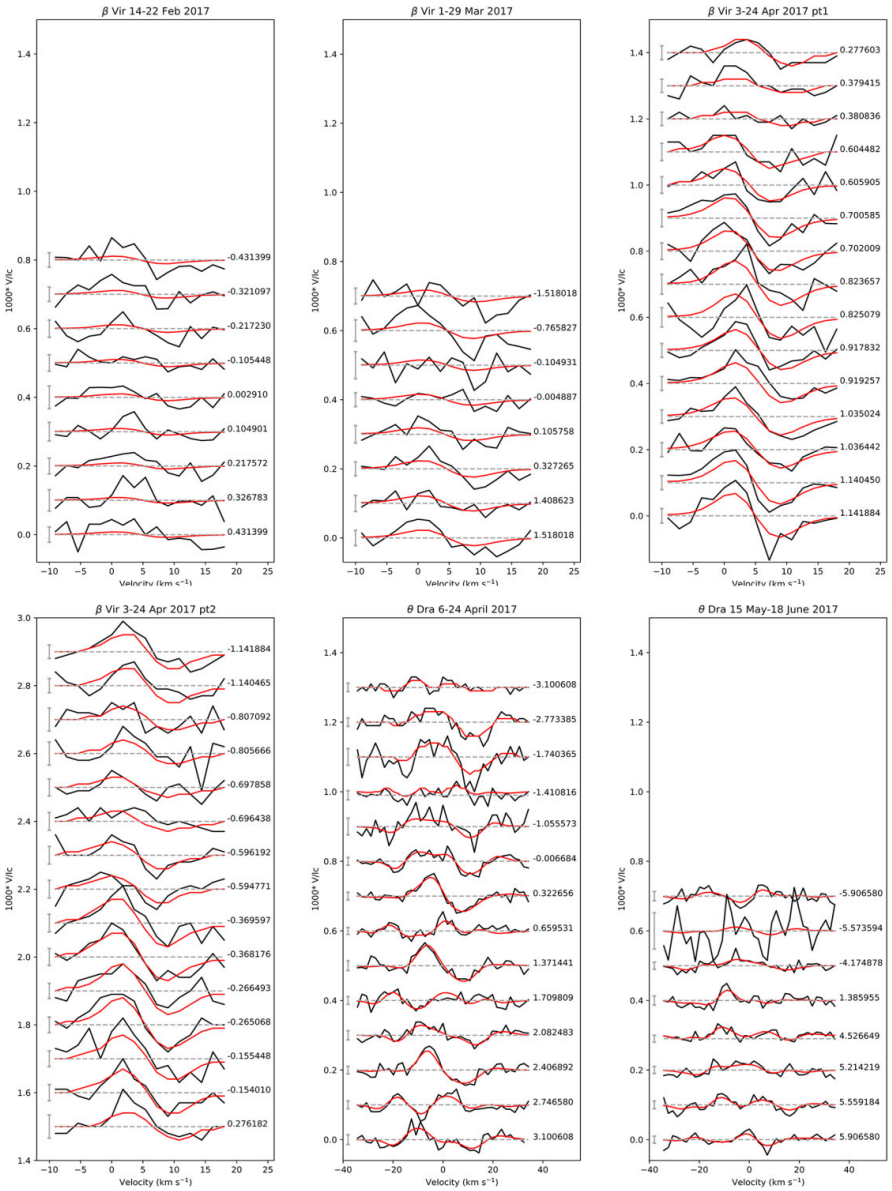

Figure A2. Stokes V maximum entropy fit for β Vir and θ Dra. The black lines represent the observed Zeeman signatures, while the red lines represent the modelled lines. The radial velocity range of the individual line profiles are shifted to the same range, and line profiles are separated vertically to allow better visibility. The 1.0σ error bars are shown on the left. The rotation cycle is shown on the right with the zero rotation cycle set to the mid JD of observations for each map and assumes $P_{\rm rot} = 9.3$ d for β Vir and $P_{\rm rot} = 2.88$ d for θ Dra. All figures are set to the same scale.

Table A1. Magnetic cycle periods for our two F-stars (β Vir, θ Dra) tabulated together with available literature values for other F-stars. Spectral type from Wenger et al. (2000), $T_{\rm eff}$ from Gaia collaboration et al. (2018).

Star	Spectral type	$T_{\rm eff}$ (K)	Mag. cycle (yr)	Cycle det. method	Reference
HD 3229	F2V	6471 ± 136	4.9 ± 0.1	S-index	Baliunas et al. (1995)
HD 76572	F3V	6375 ± 187	7.1 ± 0.2	S-index	Baliunas et al. (1995)
HD 49933	F3V	6585 ± 132	0.33	Asteroseismology	García et al. (2010)
HD 18256	F5V	6359 ± 91	6.8 ± 0.2	S-index	Baliunas et al. (1995)
HD 157856	F5V	6377 ± 75	15.9 ± 0.8	S-index	Baliunas et al. (1995)
HD 194012	F5V	6224 ± 169	16.7 ± 0.9	S-index	Baliunas et al. (1995)
HD 100563	F5.5V	6461 ± 93	0.61	S-index	Mittag et al. (2019)
HD 178971	F5IV-V	6787 ± 77[a]	3.85	Modified S-index ($S_{\rm ph}$)	Mathur et al. (2014)
HD 175226	F6IV	6350 ± 111[b]	2.96	Asteroseismology	Régulo et al. (2016)
HD 207978	F6IV-V	6382 ± 60	17	S-index	Baliunas & Vaughan (1985)
KIC 11415049	F6V	6182 ± 216	2	Photometry	Montet et al. (2017)
HD 18256	F6V	6359 ± 91	5.89	S-index	Boro Saikia et al. (2018)
HD 182101	F6V	6344 ± 86	5.1 ± 0.1	S-index	Baliunas et al. (1995)
HD 111456	F6V	6290 ± 90	7.0	S-index	Baliunas et al. (1995)
HD 100180	F7	6060 ± 76	3.56 ± 0.04	S-index	Baliunas et al. (1995)
HD 120136	F7	6420 ± 155	0.33	S-index	Mengel et al. (2016)
HD 75332	F7	6206 ± 40	0.49	S-index	Mittag et al. (2019)
θ Dra	F8IV	6105 ± 271	0.12 ± 0.01	S-index	This work
HD 154417	F8V	6021 ± 58	7.4 ± 0.2	S-index	Baliunas et al. (1995)
HD 17051	F8V	6126 ± 75	1.6	S-index	Metcalfe et al. (2010)
HD 16673	F8V	6327 ± 89	0.85	S-index	Mittag et al. (2019)
HD 115383	F8V	6100 ± 153	11.79	S-index	Boro Saikia et al. (2018)
CoRoT 102780281	F8V	5942 ± 88	0.3	Photometry	Lopes et al. (2015)
KIC 8043142	F8V	5957 ± 77	4.5	Photometry	Montet et al. (2017)
HD 187691	F8V	6150 ± 70	5.4 ± 0.1	S-index	Baliunas et al. (1995)
KIC 2694810	F8V-VI	6036 ± 99	2	Photometry	Montet et al. (2017)
HD 234856	F9IV-V	6155 ± 61	3	CaII H line	Morgenthaler et al. (2011)
HD 114710	F9V	6097 ± 141	9.6	S-index	Metcalfe et al. (2010)
β Vir	F9V	6083 ± 58	0.23 ± 0.04	S-index	This work
KIC 5955122	F9V	5954 ± 70	21	Photometry	Bonanno et al. (2014)
KIC 7272437	F9IV-V	6075 ± 122	3	Photometry	Montet et al. (2017)
KIC 10921242	F9IV-V	6021 ± 107	3	Photometry	Montet et al. (2017)

[a] $T_{\rm eff}$ from Mathur et al. (2014); [b] $T_{\rm eff}$ from Pinsonneault et al. (2012).

Table A2. Journal of individual observations and magnetic detection for θ Dra LSD profiles in 2017, showing date and time of the observation, Stokes *I* profile SNR, rotation cycle with respect to observations starting at HJD = 2457850.6206, radial velocity (RV), chromospheric activity (S-index and H α-index), longitudinal magnetic field (B_l), null value (N_l), and magnetic detection flag for the presence of a magnetic field in individual LSD profiles where *D* is a definite detection, *M* is marginal, *N* is no detection. The Stokes *V* observations consist of a sequence of four exposures as described in Section 2.1.

Date 2017 (local time)	HJD 2450000+	SNR Stokes *I*	Rot. cycle	RV[a] (km s^{-1})	S-index	Hα-index	B_l (G)	N_l (G)	Det. N, M, D
Apr 06	7850.6206	576	0.000	− 31.17	0.212	0.286	4.4 ± 1.9	0.5 ± 1.9	N
Apr 06	7850.6366	579	0.006	− 31.39	0.210	0.286	1.9 ± 1.6	− 0.6 ± 1.6	N
Apr 06	7850.6524	574	0.011	− 31.61	0.212	0.286	2.3 ± 1.4	0.8 ± 1.4	N
Apr 06	7850.6683	567	0.017	− 31.82	0.212	0.286	− 2.8 ± 1.7	− 0.5 ± 1.7	N
Apr 06	7850.6843	568	0.022	− 32.00	0.212	0.287	− 0.8 ± 1.3	0.5 ± 1.3	N
Apr 07	7851.5594	569	0.326	− 7.71	0.208	0.285	− 1.6 ± 1.6	0.7 ± 1.6	M
Apr 07	7851.5772	576	0.332	− 6.74	0.207	0.284	3.5 ± 1.4	− 0.1 ± 1.4	D
Apr 07	7851.5949	567	0.338	− 5.92	0.207	0.284	1.2 ± 1.7	1.6 ± 1.7	N
Apr 07	7851.6127	560	0.344	− 5.05	0.208	0.285	2.0 ± 1.4	1.5 ± 1.4	N
Apr 07	7851.6305	570	0.351	− 4.12	0.208	0.284	2.4 ± 1.5	1.9 ± 1.6	D
Apr 10	7854.5346	559	1.359	− 12.31	0.209	0.285	4.8 ± 2.0	− 1.1 ± 2.0	D
Apr 10	7854.5524	563	1.365	− 11.58	0.209	0.286	3.0 ± 2.4	0.5 ± 2.4	M
Apr 10	7854.5701	550	1.371	− 10.65	0.210	0.287	2.7 ± 1.7	− 1.3 ± 1.7	D
Apr 10	7854.5877	588	1.377	− 9.73	0.208	0.286	4.1 ± 1.4	0.2 ± 1.4	D
Apr 10	7854.6055	582	1.384	− 8.91	0.208	0.286	1.9 ± 1.3	0.0 ± 1.3	D
Apr 11	7855.4836	537	1.689	15.94	0.209	0.285	4.4 ± 2.9	2.7 ± 2.9	N
Apr 11	7855.5013	561	1.695	15.76	0.210	0.285	3.0 ± 2.5	− 0.3 ± 2.5	N
Apr 11	7855.5191	541	1.701	15.57	0.210	0.285	− 2.9 ± 2.6	− 1.0 ± 2.6	N
Apr 11	7855.5369	556	1.707	15.38	0.209	0.285	− 2.6 ± 2.0	− 0.5 ± 2.0	N
Apr 11	7855.5546	549	1.713	15.08	0.210	0.286	2.1 ± 1.5	− 0.3 ± 1.5	N
Apr 12	7856.5068	556	2.044	− 24.00	0.208	0.285	3.4 ± 2.0	− 0.7 ± 2.1	M
Apr 12	7856.5244	572	2.050	− 24.66	0.208	0.285	2.4 ± 1.2	− 0.4 ± 1.2	D
Apr 12	7856.5422	573	2.056	− 25.31	0.208	0.286	2.3 ± 2.1	1.0 ± 2.2	N
Apr 12	7856.5599	555	2.062	− 25.94	0.207	0.285	1.2 ± 1.7	0.0 ± 1.7	D
Apr 12	7856.5776	570	2.068	− 26.53	0.207	0.285	− 3.0 ± 1.5	− 1.0 ± 1.5	N
Apr 15	7859.5275	601	3.093	− 22.15	0.208	0.286	− 2.0 ± 1.7	− 0.6 ± 1.8	M
Apr 15	7859.5452	598	3.099	− 22.88	0.208	0.286	1.9 ± 1.7	0.2 ± 1.7	M
Apr 15	7859.5630	589	3.105	− 23.59	0.208	0.285	3.5 ± 2.3	− 1.9 ± 2.3	N
Apr 15	7859.5808	602	3.111	− 24.30	0.207	0.286	− 1.5 ± 1.3	− 0.1 ± 1.3	N
Apr 15	7859.5986	594	3.117	− 24.97	0.208	0.286	− 3.7 ± 2.3	1.3 ± 2.3	N
Apr 16	7860.4760	598	3.422	− 21.61	0.210	0.285	3.1 ± 2.1	− 1.1 ± 2.2	D
Apr 16	7860.4937	595	3.428	− 20.84	0.210	0.286	0.9 ± 1.2	0.1 ± 1.2	M
Apr 16	7860.5116	589	3.434	− 20.11	0.211	0.285	− 3.0 ± 2.3	− 0.2 ± 2.3	D
Apr 16	7860.5293	579	3.441	− 19.34	0.211	0.285	6.3 ± 1.8	− 2.9 ± 1.8	M
Apr 16	7860.5470	576	3.447	− 18.59	0.211	0.285	− 1.0 ± 1.3	0.2 ± 1.3	N
Apr 17	7861.4462	593	3.759	16.13	0.206	0.286	− 0.8 ± 1.2	− 0.1 ± 1.2	N
Apr 17	7861.4639	598	3.765	16.30	0.206	0.286	1.7 ± 1.8	− 0.5 ± 1.9	M
Apr 17	7861.4816	605	3.771	16.41	0.206	0.286	− 2.7 ± 1.6	− 0.3 ± 1.6	N
Apr 17	7861.4994	596	3.777	16.44	0.205	0.286	− 4.3 ± 2.0	0.4 ± 2.0	N
Apr 17	7861.5171	596	3.784	16.48	0.205	0.286	1.8 ± 2.1	− 1.6 ± 2.2	N
Apr 19	7863.4966	594	4.471	− 23.78	0.208	0.286	1.6 ± 1.7	− 1.0 ± 1.7	N
Apr 19	7863.5144	585	4.477	− 23.07	0.208	0.287	2.4 ± 2.4	− 0.1 ± 2.4	N
Apr 19	7863.5320	590	4.483	− 22.34	0.208	0.286	5.6 ± 2.8	0.5 ± 2.8	M
Apr 19	7863.5497	590	4.489	− 21.62	0.208	0.287	3.7 ± 1.6	− 0.8 ± 1.6	M
Apr 19	7863.5674	594	4.495	− 20.88	0.208	0.286	− 6.1 ± 3.2	− 4.0 ± 3.2	N
Apr 20	7864.4710	589	4.809	15.59	0.206	0.285	1.6 ± 1.5	1.4 ± 1.5	N
Apr 20	7864.4887	585	4.815	15.78	0.207	0.286	1.7 ± 1.5	− 2.3 ± 1.5	N
Apr 20	7864.5065	578	4.821	15.95	0.206	0.285	8.6 ± 2.4	2.8 ± 2.4	N
Apr 20	7864.5242	595	4.828	16.14	0.206	0.286	− 2.7 ± 1.9	− 0.5 ± 1.9	N
Apr 20	7864.5420	590	4.834	16.25	0.206	0.286	2.2 ± 2.4	− 2.7 ± 2.4	N
Apr 21	7865.5442	580	5.182	− 16.65	0.211	0.288	− 4.4 ± 2.5	− 1.9 ± 2.5	N
Apr 21	7865.5619	569	5.188	− 17.44	0.211	0.287	− 5.4 ± 2.7	− 0.6 ± 2.7	N
Apr 21	7865.5797	555	5.194	− 18.31	0.211	0.288	2.0 ± 2.7	− 0.2 ± 2.7	N
Apr 21	7865.5975	563	5.200	− 19.09	0.208	0.286	− 3.5 ± 2.0	− 0.5 ± 2.0	N
Apr 21	7865.6154	563	5.206	− 19.92	0.211	0.287	0.9 ± 1.5	3.5 ± 1.5	N
Apr 22	7866.4785	584	5.506	− 26.80	0.214	0.287	3.5 ± 2.2	− 1.6 ± 2.2	M
Apr 22	7866.4964	586	5.512	− 26.24	0.209	0.285	− 4.4 ± 2.4	− 1.3 ± 2.4	D
Apr 22	7866.5141	576	5.519	− 25.64	0.209	0.285	4.0 ± 1.9	1.0 ± 1.9	D
Apr 22	7866.5319	589	5.525	− 24.98	0.208	0.286	− 3.0 ± 1.6	− 1.0 ± 1.6	D

Table A2 – *continued*

Date 2017 (local time)	HJD 2450000+	SNR Stokes *I*	Rot. cycle	RV[a] (km s^{-1})	S-index	Hα-index	B_l (G)	N_l (G)	Det. N, M, D
Apr 22	7866.5496	596	5.531	− 24.38	0.208	0.284	0.6 ± 2.0	− 0.2 ± 2.0	D
Apr 23	7867.4570	593	5.846	14.13	0.206	0.286	− 1.1 ± 1.6	− 0.8 ± 1.7	N
Apr 23	7867.4747	601	5.852	14.48	0.206	0.284	− 2.6 ± 1.2	− 0.4 ± 1.2	N
Apr 23	7867.4924	582	5.858	14.83	0.206	0.285	1.8 ± 1.3	0.2 ± 1.3	N
Apr 23	7867.5101	578	5.864	15.16	0.206	0.285	2.0 ± 1.2	− 0.9 ± 1.2	M
Apr 23	7867.5279	595	5.871	15.41	0.206	0.286	2.6 ± 1.8	0.6 ± 1.8	M
Apr 24	7868.4942	552	6.206	− 10.73	0.208	0.285	− 2.1 ± 2.3	1.6 ± 2.3	N
Apr 24	7868.5119	546	6.212	− 11.65	0.208	0.286	− 1.1 ± 1.3	0.1 ± 1.3	N
Apr 24	7868.5297	549	6.218	− 12.48	0.208	0.285	2.9 ± 2.5	2.0 ± 2.5	N
May 15	7889.4331	496	13.477	12.99	0.206	0.284	− 4.2 ± 2.9	− 0.8 ± 2.9	N
May 15	7889.4508	497	13.483	12.53	0.205	0.284	− 4.6 ± 2.4	− 0.3 ± 2.4	N
May 15	7889.4685	499	13.489	12.03	0.206	0.284	− 7.4 ± 2.9	− 0.6 ± 2.9	N
May 15	7889.4862	515	13.495	11.50	0.205	0.283	− 1.0 ± 1.4	2.0 ± 1.4	N
May 15	7889.5038	530	13.501	11.02	0.205	0.283	4.0 ± 1.7	4.0 ± 1.7	N
May 16	7890.4187	483	13.819	− 28.43	0.203	0.285	− 13.0 ± 5.6	2.3 ± 5.6	N
May 16	7890.4364	486	13.825	− 28.91	0.204	0.285	− 13.1 ± 4.7	3.3 ± 4.7	N
May 20	7894.4204	604	15.208	− 14.12	0.202	0.286	2.0 ± 1.4	− 1.2 ± 1.4	N
May 20	7894.4381	609	15.214	− 13.30	0.202	0.286	3.9 ± 2.2	1.2 ± 2.2	N
May 20	7894.4558	598	15.221	− 12.42	0.202	0.285	− 4.1 ± 1.7	− 0.6 ± 1.7	N
May 20	7894.4735	602	15.227	− 11.55	0.202	0.286	− 2.9 ± 1.5	− 0.3 ± 1.5	N
May 20	7894.4911	598	15.233	− 10.68	0.202	0.286	− 2.1 ± 1.3	0.9 ± 1.3	N
Jun 05	7910.4354	548	20.769	13.87	0.205	0.283	− 2.6 ± 1.2	− 0.3 ± 1.2	N
Jun 05	7910.4532	522	20.775	14.19	0.206	0.285	2.3 ± 2.3	4.3 ± 2.3	N
Jun 05	7910.4711	529	20.781	14.64	0.205	0.284	3.3 ± 2.6	0.1 ± 2.6	N
Jun 05	7910.4889	549	20.788	14.97	0.206	0.284	− 3.5 ± 1.3	− 0.2 ± 1.3	M
Jun 05	7910.5066	532	20.794	15.19	0.206	0.284	3.1 ± 2.4	− 2.4 ± 2.4	N
Jun 14	7919.4807	513	23.910	8.94	0.200	0.283	3.1 ± 1.8	− 1.2 ± 1.8	N
Jun 14	7919.4984	512	23.916	9.56	0.200	0.281	− 2.1 ± 2.0	− 0.5 ± 2.0	N
Jun 14	7919.5161	509	23.922	10.14	0.200	0.283	3.3 ± 2.0	− 1.5 ± 2.0	N
Jun 14	7919.5339	504	23.928	10.76	0.200	0.282	− 2.8 ± 1.5	− 3.2 ± 1.5	N
Jun 14	7919.5517	508	23.934	11.31	0.200	0.283	− 0.5 ± 1.6	− 0.1 ± 1.6	N
Jun 16	7921.4609	562	24.597	− 32.37	0.199	0.284	2.7 ± 1.6	1.0 ± 1.6	N
Jun 16	7921.4786	553	24.603	− 32.21	0.199	0.284	− 3.3 ± 1.5	1.8 ± 1.5	N
Jun 16	7921.4964	562	24.610	− 32.09	0.199	0.284	5.0 ± 1.9	1.3 ± 1.9	N
Jun 16	7921.5142	566	24.616	− 31.91	0.199	0.285	− 0.3 ± 1.2	0.1 ± 1.2	N
Jun 16	7921.5320	565	24.622	− 31.71	0.200	0.284	0.8 ± 1.1	1.5 ± 1.1	N
Jun 17	7922.4543	582	24.942	4.43	0.204	0.285	− 1.9 ± 1.1	0.8 ± 1.2	N
Jun 17	7922.4720	565	24.948	5.75	0.204	0.286	− 1.8 ± 1.2	2.2 ± 1.3	N
Jun 17	7922.4898	583	24.955	6.51	0.204	0.285	2.2 ± 1.1	0.2 ± 1.2	N
Jun 17	7922.5076	584	24.961	7.19	0.203	0.285	3.8 ± 1.6	− 0.3 ± 1.6	N
Jun 17	7922.5255	573	24.967	7.88	0.204	0.285	− 0.9 ± 1.4	2.3 ± 1.4	N
Jun 18	7923.4549	532	25.290	4.45	0.203	0.284	− 2.1 ± 1.2	− 2.1 ± 1.2	N
Jun 18	7923.4727	523	25.296	3.65	0.204	0.284	− 4.8 ± 2.0	0.1 ± 2.0	N
Jun 18	7923.4905	519	25.302	2.83	0.204	0.284	− 1.7 ± 1.5	− 1.1 ± 1.5	N
Jun 18	7923.5083	530	25.308	2.08	0.204	0.284	1.9 ± 1.3	− 0.1 ± 1.3	N
Jun 18	7923.5259	521	25.314	1.23	0.204	0.285	2.0 ± 1.3	− 2.4 ± 1.3	N

[a]The RV precision of NARVAL is 0.018 km s^{-1} (Soubiran et al. 2018).

This paper has been typeset from a TEX/LATEX file prepared by the author.

3.3 Future Research

Further magnetic mapping, and wind modelling for early to mid F-type stars will enable a better understanding of the transition between fossil and dynamo magnetic fields, and the space weather environment surrounding stars at the hot end of habitability for exoplanets.

3.4 Additional Comments

Information in this section provides additional comments on Paper 2.

The description of the brightness map for θ Dra could be made more accurate in Section 6.2 of Paper 2, page 95 of the thesis. The revised sentence should read: The April 6–24 map for θ Dra shows the presence of both brighter and darker areas that are smaller and more numerous compared with the 15 May–18 June map.

A missing reference was found in Paper 2, Section 6.7 on stellar wind modelling. The corrected sentence should read: The surface where this first occurs is shown in Fig. 13. The wind states, as it crosses this Alfvén surface determines the stellar angular momentum loss, as the surface functions as an effective lever arm (Schatzman, 1962) increasing the torque effected by the wind upon the star.

A revised sentence which includes a reference to the original Chapman-Ferraro formula from 1931 is presented here for section 6.7 of Paper 2 on page 102 of the thesis. The revised sentence reads: The magnetospheric stand-off distance is calculated from a pressure balance argument similar to a formula introduced by (Chapman & Ferraro, 1931) and used in Vidotto et al. (2009).

CHAPTER 4

PAPER 3: THE MAGNETIC FIELDS OF β CORONA BOREALIS AND THE EARLY F-STAR σ BOOTIS

Published in the Monthly Notices of the Royal Astronomical Society, 2022, Volume 513, pp. 4278–4294 (Seach et al., 2022b).

4.1 Introduction to Paper

In this chapter, two stars which are possibly located on either side of the transition between fossil and dynamo magnetic fields are chosen for further detailed analysis using ZDI. The stars are chosen because one contains a known fossil magnetic fields (β CrB), and the other (σ Boo, F3V) contains a possible dynamo magnetic field close to the boundary. β CrB had enough spectropolarimetric observations

to enable magnetic maps to be produced at multiple epochs from 2015-2018, while σ Boo had observations at one epoch in 2021.

This thesis produces magnetic maps of β CrB using ZDI for the first time. The large-scale magnetic field shows a relatively complex topology which is unusual, but has been previously observed in several other other hot stars. The complex magnetic field topology is consistent with previous studies which suggested the magnetic field could not be modelled by a simple dipole.

The early F-star σ Boo is mapped using ZDI at a single epoch in 2021. The large-scale magnetic field topology shows a relatively simple in structure which is axisymmetric and poloidal. Less than 4 per cent of the magnetic energy is contained in the higher multipoles ($\ell > 2$). A complex surface topology does not appear to be a common feature of F-star dynamo magnetic fields. This may possibly be due to the shallow outer convection zones, which do not allow for complex twisting of the flux tubes on their rise to the surface.

Solid body rotation is found in β CrB which is consistent with that found in other hot stars. The lack of differential rotation in σ Boo may be due to the weak magnetic field which does not allow magnetic features to be tracked.

4.2 Published Paper

The published paper Seach et al. (2022b), "The Magnetic Fields of β Coronae and the Early F-star σ Bootis" follows.

Monthly Notices of the ROYAL ASTRONOMICAL SOCIETY

MNRAS **513,** 4278–4294 (2022) https://doi.org/10.1093/mnras/stac1173
Advance Access publication 2022 April 29

The magnetic fields of β Coronae Borealis and the early F-star σ Bootis

J. M. Seach [1]★ S. C. Marsden [1] B. D. Carter [1] C. Neiner [2] and C. P. Folsom [3]

[1] *Centre for Astrophysics, University of Southern Queensland, Toowoomba 4350, Australia*
[2] *LESIA, Paris Observatory, PSL University, CNRS, Sorbonne University, Université de Paris, 5 place Jules Janssen, F-92195 Meudon, France*
[3] *Tartu Observatory, University of Tartu, Observatooriumi 1, Tõravere 61602, Estonia*

Accepted 2022 April 25. Received 2022 April 25; in original form 2022 February 25

ABSTRACT

The study of magnetism in stars close to the transition from fossil to dynamo magnetic fields is important for understanding the nature of the stellar dynamo and dynamics of the outer atmosphere. We present surface magnetic maps for two stars that are located on opposite sides of the suspected transition zone: the chemically peculiar late A-star β Coronae Borealis (A9SrEuCr) and the early F-star σ Bootis (F3V). The large-scale magnetic field reconstructed at six epochs for β Coronae Borealis shows a complex fossil magnetic field, which is highly poloidal, and contains almost half the magnetic energy in higher multipoles ($\ell >$ 1). In contrast, the single epoch magnetic map for σ Bootis contains a simple surface magnetic topology that is mostly poloidal, and predominantly dipolar, and is consistent with observations of other mature late F-stars.

Key words: stars: activity – stars: early-type – stars: magnetic field – stars: solar-type.

1 INTRODUCTION

We present the third paper in our series on magnetic fields in F-type stars. In the first paper, we published a magnetic snapshot survey of F-type stars (Seach et al. 2020, hereafter Paper 1), and in the second paper we reconstructed surface magnetic maps and created wind models for two late F-type stars β Vir (F9V) and θ Dra (F8IV) (Seach et al. 2022, hereafter Paper 2). In this paper, we present surface magnetic maps for the chemically peculiar star β Coronae Borealis (β CrB) and the F3V star σ Bootis (σ Boo). β CrB is a chemically peculiar star, classified as A9SrEuCr by Renson & Manfroid (2009), which is located on the hot side of the transition between fossil and dynamo magnetic fields. F-type stars are important targets for stellar magnetic studies since they span a range of masses where the transition from fossil to dynamo magnetic fields is believed to occur (Schatzman 1962; Mullan 1972; Schmitt et al. 1985; Wolff, Boesgaard & Simon 1986; Walter & Schrijver 1987; Seach et al. 2022).

Fossil fields (Cowling 1945; Spitzer 1958; Mestel 1967; Dudorov & Khaibrakhmanov 2015) are found in hot stars with little or no outer convection zone. The fields are thought to be left over from the star's formation where it undergoes gravitational collapse from a molecular cloud (Mestel & Spitzer 1956; Mestel 1966), from stellar mergers (Schneider et al. 2019), or from pre-main-sequence dynamos (Moss 2001). Fossil fields are frozen (Cowling 1957; Alfven, Alfvén & Fälthammar 1963) into the stellar atmosphere and essentially remain unchanged over the lifetime of the star. Classically, fossil fields have strengths ranging from a few hundred gauss up to 34 kG (Babcock 1960) and have been found in about 10 per cent of hot stars (Fossati et al. 2015; Grunhut et al. 2016; Sikora et al. 2019). More recently, another class of magnetic fields have been discovered in Ap and Fp stars with sub-gauss magnetic strengths and are possibly fossil in origin (Lignières et al. 2009; Petit et al. 2010; Neiner, Wade & Sikora 2017). Like the stronger fossil fields, these ultra-weak fields are possibly unchanged over long periods of time (Neiner et al. 2017).

Dynamo magnetic fields are located in the outer convection zone of cool stars where they are most efficiently generated by the action of turbulent convection and stellar rotation (Parker 1955, 1987). The presence of a deepening outer convection zone around early to mid-F-stars corresponds to the onset of dynamo-generated magnetic fields. There is an extensive literature on dynamo magnetic fields; e.g. see reviews by Moffatt (1978), Parker (1979), Krause & Radler (1980), Zeldovich, Ruzmaikin & Sokolov (1983), Roberts (1992), Brandenburg & Subramanian (2005), Mestel (2012), and Moffatt & Dormy (2019). Dynamo-generated magnetic fields are seen on the Sun and other solar-type stars where they are responsible for magnetic features like cool surface spots (Berdyugina 2005; Strassmeier 2009), flares (Pettersen 1989), stellar winds, and space weather phenomenon (Bothmer & Daglis 2007; Hanslmeier 2007; Singh et al. 2021). Increasing interest is developing in the field of exoplanet research (Perryman 2018) where the host star magnetic field has an important influence in the exoplanetary environment (Lammer & Khodachenko 2014; Linsky 2019). Dynamo magnetic fields are distinguished from fossil fields by their dynamic and changing nature with short decay times (Pevtsov, Canfield & Metcalf 1994; Burnette, Canfield & Pevtsov 2004).

β CrB is a well-known magnetic star (Babcock 1949, 1958; Stibbs 1950; Preston & Sturch 1967; Wolff & Wolff 1970) with a fossil field that has not been previously mapped using Zeeman Doppler imaging (ZDI). The star is suitable for magnetic studies due to its brightness and sharp spectral lines (Glagolevskij & Gerth 2003). Wolff & Wolff (1970) noted that the magnetic field of β CrB cannot be represented as a simple dipole and contains a geometry where one pole is stronger than the other. Stift (1975) explained that the shape of the longitudinal magnetic field (B_l) is not consistent with axisymmetric morphology,

★ E-mail: john.seach@usq.edu.au

and this was interpreted by Oetken (1977) as corresponding to a superposition of a dipole and a quadrupole magnetic field with their axes perpendicular to the rotation axis.

The lack of magnetic field symmetry around the rotation axis for β CrB is further discussed by Mathys (1993), and Mathys & Hubrig (1997) indicated that magnetic field is unusual and appears quite complex. A study of magnetic curves by Bagnulo et al. (2000) indicated that the magnetic topology of β CrB is characterized by a multipole expansion of a dipole and an arbitrarily oriented quadrupole. We include β CrB in this paper since it is one of the coolest magnetic Ap stars that is located close to the transition between fossil and dynamo magnetic fields. It provides a contrast with σ Boo that possibly is located on the cool side of the magnetic transition.

σ Boo was identified in our magnetic snapshot survey of F-type stars (Paper 1) as the hottest star in our sample having a possible dynamo magnetic field. Dynamo magnetic fields have been mapped on the surface of several late F-stars; see e.g. HR 1817, F7/8 (Marsden et al. 2006; Järvinen et al. 2015), τ Boo, F7V (Donati et al. 2008; Fares et al. 2009; Jeffers et al. 2018), HD 75332, F7V (Brown et al. 2021), HD 179949, F8V (Fares et al. 2012), θ Dra, F8IV, and β Vir, F9V (Paper 2). Mapping the surface magnetic field of σ Boo (F3V) is important for an understanding of magnetism in early F-stars close to the hot limit of dynamo magnetic fields and helps constrain dynamo models that provide insights into magnetism in stars with shallow outer convection zones.

2 OBSERVATIONS

2.1 Target selection

β CrB (HIP 75695) is a chemically peculiar (Adelman 1973), spectroscopic binary with component V magnitudes of 3.68 and 5.20 separated by 0.30 arcsec (Mason et al. 2001). The primary component has $T_{\rm eff} = 7980 \pm 180$ K, and the secondary component has $T_{\rm eff} = 6750 \pm 230$ K (Bruntt et al. 2010). The star was included in our earlier paper (Paper 1) and identified as a good target for magnetic mapping due to the availability of polarized spectra over multiple epochs.

σ Boo (HIP 71284), $T_{\rm eff} = 6720 \pm 144$ K (Gaia collaboration 2018), is a 1.6 ± 0.3 Gyr old (Casagrande et al. 2011) triple star system with component V magnitudes 4.50, 10.66, and 12.08, respectively (Mason et al. 2001). σ Boo is classified as a standard F2V star in the MK classification system (Johnson & Morgan 1953), while Samus et al. (2017) classify it as F3V. The star was detected as magnetic in our earlier magnetic snapshot survey (Paper 1). There has been increasing interest in σ Boo as a host F-type star used in exoplanet weather modelling (Segura et al. 2003; Godolt et al. 2019; Rushby, Shields & Joshi 2019; Schwieterman et al. 2019; Palubski, Shields & Deitrick 2020; Kaltenegger & Lin 2021).

2.2 Observations

Polarized spectra of β CrB were obtained from the PolarBase data base (Petit et al. 2014), which is a publicly available data base containing stellar data collected with the ESPaDOnS (Donati et al. 2006a) and NARVAL (Aurière 2003) high-resolution ($R = 65\,000$) spectropolarimeters. The β CrB data consist of 143 spectra from 2015 April 13 to 2018 July 28 (Table 1) obtained with the NARVAL spectropolarimeter at the Telescope Bernard Lyot (TBL) at the Observatoire du Pic du Midi, France. Observations of β CrB in 2015–2017 were obtained using both circularly polarized (Stokes V) and linear (Stokes UQ) polarized spectra, while observations in 2018 were only obtained in circular polarization. In this paper, we present magnetic maps using circular polarization only, whereas the linear polarization observations are left for future work.

We obtained polarized spectra for σ Boo using the ESPaDOnS spectropolarimeter at the Canada–France–Hawaii Telescope (CFHT) observing in Stokes V. The observations consist of 105 polarized spectra over 11 nights from 2021 May 18 to 28, corresponding to an estimated 1.2 rotational cycles (Tables 2 and A1).

3 MAGNETIC FIELD MEASUREMENTS

3.1 Magnetic Zeeman signatures

The line addition technique of least squares deconvolution (LSD; Donati et al. 1997, 2006b) is used to enhance the Stokes V signal, by combining thousands of individual lines into a single line with mean parameters. LSD profiles are created using line masks from VALD3 (Ryabchikova et al. 2015) where the masks contain the wavelength, depths, and effective Landé factors to be used for the LSD code. We normalized the LSD profiles with the values taken from the means of a typical line mask (Folsom et al. 2016). The number of lines used in LSD analysis varies from 17488 to 17652 for β CrB (Table 1) and 17646 to 17654 for σ Boo (Tables 2 and A1). For σ Boo, we added the nightly LSD profiles into a single mean profile that further enhances the SNR and enables a magnetic detection from an otherwise weak magnetic field. The time between the first and last exposure used in each mean LSD profile is less than 2 h which is less than 1 per cent of the estimated rotation period. This was short enough time-span to avoid smearing of the profiles.

We use the statistical criteria of FAP to determine whether the Stokes V profile has a magnetic signal, or whether the Null profile has a spurious signal (Donati, Semel & Rees 1992; Donati et al. 1997). The probability function of Abramowitz & Stegun (1964) is combined with Chi-square (χ^2) statistics inside and outside the spectral lines to give the probability of the Stokes V data differing from a zero magnetic field. The FAP is calculated to determine for the presence of a magnetic field and is defined as being definite if the FAP is smaller than 10^{-5}, marginal if FAP between 10^{-3} and 10^{-5}, and not detected if FAP is greater than 10^{-3}. The FAP is used to check for the presence of a magnetic field in addition to a measurement of the longitudinal magnetic field which is discussed in Section 3.2.

In Fig. 1, we compare two LSD profiles for β CrB at similar phases obtained in different years. The figure displays an LSD profile from 2015 April 23 at rotational phase 0.546, and a profile from 2017 March 8 at rotational phase 0.542. Zeeman signatures are visible in the Stokes V profiles which align with the Stokes I profile. The null spectrum does not show a magnetic signature and acts as a check to ensure that spurious signals have not contaminated the spectrum. The plots show almost identical Stokes V profiles that indicates a stable magnetic field over the 2 yr of observations. The longitudinal magnetic field strength (see Section 3.2) for the 2015 April profile 24 is -501.9 ± 6.2 G, while the value for 2017 March 8 is -496.7 ± 4.7 G. Magnetic signatures are visible in all 143 LSD profiles for β CrB and the FAP indicates a magnetic detection in all profiles.

In Fig. 2, we display an example of the mean Stokes V LSD profile for σ Boo on 2021 May 18. Due to the weak magnetic field, a Zeeman signature is not visible in individual LSD profiles, but is visible in the mean nightly profile due to the enhanced SNR. The FAP indicates a definite magnetic a magnetic detection in one of the mean LSD

Table 1. Journal of observations for β CrB in 2015–2018. Zero rotation cycle is set to our first observation on 2015 April 13. The table displays the date and time of the observation, zero rotation cycle with respect to the first observation on 2015 April 13, Stokes *I* profile, radial velocity (RV), longitudinal magnetic field (B_l), null value (N_l), and the number of lines used in LSD.

Date (UT)	Time (UT)	Mid-HJD 2457000+	Rot. cycle	SNR Stokes *I*	RV (km s^{-1})	B_l (G)	N_l (G)	LSD lines used
2015								
April 13	23:26:15	126.47656	0.000	264	−18.45	608.9 ± 5.9	−1.6 ± 1.9	17 614
April 14	21:58:41	127.41575	0.051	294	−18.39	684.5 ± 7.6	5.4 ± 5.4	17 610
April 21	02:18:00	133.59583	0.385	280	−18.36	−99.8 ± 4.4	1.4 ± 2.0	17 619
April 24	01:43:00	136.57153	0.546	270	−18.44	−501.9 ± 6.2	−1.3 ± 2.0	17 616
April 30	01:12:28	142.55032	0.870	267	−18.42	242.2 ± 4.8	0.2 ± 1.8	17 613
May 12	00:05:35	154.50388	1.516	277	−18.38	−476.7 ± 6.3	5.0 ± 2.9	17 615
May 13	00:14:40	155.51019	1.571	271	−18.31	−518.5 ± 6.5	−4.0 ± 2.6	17 616
May 16	23:52:13	159.49459	1.786	279	−18.36	−65.9 ± 5.0	−0.4 ± 2.1	17 620
May 18	02:47:31	160.61633	1.847	285	−18.36	160.5 ± 5.0	1.9 ± 2.6	17 621
May 26	21:49:46	169.40956	2.322	272	−18.11	127.1 ± 4.1	−1.4 ± 1.9	17 621
May 27	21:36:39	170.40045	2.376	277	−18.17	−79.0 ± 4.4	0.2 ± 2.1	17 621
May 28	20:29:47	171.35402	2.428	278	−18.21	−267.4 ± 5.0	1.2 ± 2.2	17 617
May 31	02:37:08	173.60912	2.550	269	−18.24	−513.3 ± 6.2	−1.9 ± 2.0	17 615
2016								
August 6	20:15:33	607.34413	26.011	293	−17.38	620.1 ± 5.4	0.6 ± 1.6	17 616
August 7	20:19:40	608.34699	26.066	293	−17.31	685.2 ± 5.6	2.0 ± 1.5	17 617
August 8	20:10:53	609.34089	26.119	291	−17.28	676.5 ± 5.5	1.3 ± 1.6	17 617
August 10	20:10:22	611.34053	26.228	299	−17.27	419.5 ± 4.7	−1.9 ± 1.9	17 617
August 11	20:04:07	612.33619	26.281	295	−17.26	224.4 ± 4.2	0.7 ± 1.9	17 616
August 12	20:10:37	613.34071	26.336	300	−17.29	14.2 ± 4.4	−1.0 ± 2.6	17 616
August 18	19:53:21	619.32872	26.660	292	−17.42	−427.6 ± 6.0	−2.3 ± 2.8	17 618
August 21	19:55:18	622.33007	26.822	290	−17.40	57.3 ± 4.4	0.2 ± 2.0	17 616
August 22	21:17:33	623.38719	26.879	292	−17.39	265.4 ± 4.9	−1.5 ± 2.8	17 615
August 23	21:15:09	624.37858	26.933	290	−17.37	440.0 ± 5.0	2.3 ± 2.2	17 615
August 24	21:11:05	625.38270	26.987	292	−17.35	578.1 ± 5.4	0.1 ± 2.0	17 617
2017								
March 2	01:58:41	814.58242	37.221	300	−17.22	440.7 ± 7.5	−0.4 ± 6.4	17 619
March 8	00:06:05	820.50422	37.542	288	−17.35	−496.7 ± 4.7	−2.3 ± 4.8	17 621
March 15	02:01:08	827.58412	37.925	291	−17.33	441.4 ± 4.7	−1.8 ± 0.8	17 620
March 16	00:15:13	828.51057	37.975	297	−17.32	589.7 ± 5.4	−0.5 ± 0.5	17 620
March 17	04:26:03	829.68476	38.038	297	−17.29	697.3 ± 5.5	−0.1 ± 0.5	17 620
March 18	05:17:31	830.72050	38.094	303	−17.29	728.5 ± 5.8	−0.2 ± 0.5	17 621
March 19	04:03:40	831.66921	38.146	295	−17.18	658.5 ± 5.5	1.0 ± 0.5	17 622
March 20	04:10:28	832.67394	38.200	296	−17.17	525.0 ± 4.9	0.1 ± 0.6	17 620
March 29	02:03:06	841.58549	38.682	286	−17.39	−375.1 ± 5.4	0.6 ± 1.9	17 619
March 29	02:43:57	841.61385	38.684	290	−17.38	−385.3 ± 5.2	0.2 ± 0.5	17 618
March 30	01:28:42	842.56160	38.735	292	−17.39	−240.0 ± 5.3	−4.4 ± 2.8	17 617
March 30	02:16:17	842.59464	38.737	296	−17.40	−235.6 ± 4.7	0.2 ± 0.8	17 617
April 3	01:21:32	846.55662	38.951	316	−17.36	513.5 ± 4.7	0.1 ± 0.8	17 620
April 4	01:00:20	847.54190	39.004	297	−17.34	7.2 ± 0.1	0.0 ± 0.0	17 620
April 4	01:10:46	847.54914	39.005	292	−17.35	646.7 ± 5.3	−0.5 ± 0.4	17 620
April 7	00:55:54	850.53882	39.166	300	−17.21	616.4 ± 5.3	0.3 ± 0.6	17 622
April 8	00:40:43	851.52828	39.220	297	−17.20	460.4 ± 4.6	0.4 ± 0.6	17 622
April 9	02:15:17	852.59395	39.278	336	−17.21	227.9 ± 4.4	4.5 ± 2.6	17 620
April 9	02:25:07	852.60078	39.278	325	−17.21	248.0 ± 3.8	0.0 ± 0.6	17 621
April 11	03:24:33	854.64205	39.388	301	−17.29	−144.0 ± 4.4	0.6 ± 0.7	17 623
April 12	02:29:46	855.60400	39.440	298	−17.31	−376.7 ± 4.9	0.2 ± 0.5	17 620
April 13	03:00:24	856.62528	39.496	298	−17.32	−497.8 ± 5.6	0.3 ± 0.5	17 623
April 16	03:27:12	859.64389	39.659	290	−17.43	−439.7 ± 5.5	−0.3 ± 0.5	17 623
April 17	03:47:30	860.65799	39.714	291	−17.37	−308.7 ± 4.9	−1.1 ± 0.5	17 620
April 18	01:18:22	861.55442	39.762	293	−17.37	−153.0 ± 4.4	−1.1 ± 0.5	17 620
April 20	02:31:18	863.60507	39.873	297	−17.44	256.6 ± 4.2	0.7 ± 0.9	17 620
April 21	01:54:56	864.57981	39.926	296	−17.37	451.7 ± 4.6	−0.6 ± 0.5	17 621
April 23	02:21:19	866.59814	40.035	294	−17.31	694.7 ± 5.6	−0.3 ± 0.5	17 618
April 24	01:48:26	867.57530	40.088	297	−17.26	726.7 ± 5.6	−0.1 ± 0.4	17 615
2018								
April 14	00:00:38	222.50044	59.287	297	−17.47	4.3 ± 4.5	−3.2 ± 3.0	17 623
April 18	03:36:14	226.65016	59.511	285	−17.54	−442.7 ± 6.5	4.7 ± 4.4	17 623
April 19	03:46:04	227.65699	59.566	278	−17.54	−471.5 ± 6.4	2.7 ± 3.7	17 621
April 24	01:24:37	232.55876	59.831	289	−17.53	61.4 ± 4.7	2.9 ± 3.3	17 617

Table 1 – *continued*

Date (UT)	Time (UT)	Mid-HJD 2457000+	Rot. cycle	SNR Stokes *I*	RV (km s^{-1})	B_l (G)	N_l (G)	LSD lines used
April 24	23:55:42	233.49701	59.882	292	−17.53	203.4 ± 4.7	−4.8 ± 3.6	17 618
May 6	00:27:09	244.51885	60.478	295	−17.52	−423.7 ± 5.7	11.2 ± 2.7	17 618
May 11	00:29:12	249.52028	60.748	298	−17.57	−198.5 ± 5.7	−6.7 ± 2.5	17 623
May 17	01:12:33	255.55038	61.075	289	−17.42	703.3 ± 6.2	0.5 ± 2.4	17 627
June 14	23:45:34	284.48998	62.640	276	−17.59	−462.4 ± 5.9	−1.6 ± 1.9	17 631
June 16	23:13:21	286.46760	62.747	289	−17.65	221.7 ± 5.0	1.2 ± 2.1	17 629
June 17	23:34:11	287.48207	62.802	286	−17.65	−32.8 ± 4.5	1.2 ± 2.1	17 629
June 18	22:55:32	288.45523	62.855	278	−17.64	246.5 ± 6.1	−2.3 ± 4.5	17 629
June 19	21:26:50	289.39363	62.905	288	−17.62	343.9 ± 4.8	−3.8 ± 2.4	17 629
June 24	23:17:23	294.47041	63.180	296	−17.49	564.5 ± 5.6	0.9 ± 2.7	17 650
June 25	22:35:44	295.44148	63.232	279	−17.49	413.7 ± 5.4	−3.5 ± 3.4	17 652
June 30	22:24:02	300.43336	63.502	226	−17.64	−236.0 ± 70.0	−80.3 ± 30.6	17 488
July 9	22:42:15	309.44601	63.990	273	−17.52	571.9 ± 5.5	0.9 ± 1.8	17 637
July 22	23:17:37	322.47057	64.694	271	−17.63	−336.8 ± 6.0	2.5 ± 2.4	17 642
July 23	20:58:50	323.37419	64.743	277	−17.62	−182.9 ± 5.9	−3.9 ± 3.3	17 641
July 26	21:14:16	326.38491	64.906	277	−17.59	420.6 ± 5.5	−3.6 ± 2.8	17 642
July 28	21:03:31	328.37744	65.014	273	−17.55	670.0 ± 6.3	8.8 ± 2.4	17 642

Table 2. Journal of observations for σ Boo in 2021. The table displays the date of the observation, number of LSD profiles combined in the mean profile, zero rotation cycle with respect to the first observation on 2021 May 18, Stokes *I* profile mean SNR, RV, longitudinal magnetic field (B_l), null value (N_l), and magnetic detection flag for the presence of a magnetic field in the mean LSD profiles, where D is a definite detection, M is marginal, and N is no detection calculated using the false alarm probability (FAP). HJD are the mean values of the nightly observations. Rotation cycle is displayed as the mean time of observation for each night. A journal of the individual observations is shown in the appendix.

Date (UT)	Mid-HJD 2459000+	No. LSD profiles	Rot. cycle	SNR Stokes *I*	RV (km s^{-1})	B_l (G)	N_l (G)	Det. N, M, D
May 18	352.82771	12	0.000	2468	0.29 ± 0.01	−1.0 ± 0.2	−0.1 ± 0.2	M
May 19	353.80843	12	0.117	2515	0.34 ± 0.01	−0.7 ± 0.1	0.1 ± 0.2	M
May 20	354.82750	12	0.238	2528	0.34 ± 0.01	−0.7 ± 0.2	−0.4 ± 0.2	D
May 21	355.77625	12	0.351	2171	0.32 ± 0.01	−1.4 ± 0.6	−1.0 ± 0.6	M
May 22	356.74181	3	0.466	1048	0.37 ± 0.01	−2.5 ± 1.0	−0.6 ± 1.2	N
May 24a	358.81633	6	0.713	1609	0.35 ± 0.01	−1.1 ± 0.3	0.0 ± 0.3	N
May 24b	358.94385	6	0.728	1640	0.35 ± 0.01	−1.1 ± 0.4	0.1 ± 0.4	N
May 25	359.81721	6	0.832	1607	0.35 ± 0.01	−0.6 ± 0.2	−0.4 ± 0.3	N
May 26	360.92690	12	0.964	2353	0.30 ± 0.01	−0.4 ± 0.2	0.1 ± 0.2	M
May 27	361.77358	12	1.065	2425	0.36 ± 0.01	−0.3 ± 0.1	−0.2 ± 0.1	N
May 28	362.77587	12	1.184	2369	0.32 ± 0.01	−0.7 ± 0.2	−0.4 ± 0.2	M

profiles, marginal detection in five profiles, and no detection in five profiles (Table 2).

3.2 Longitudinal magnetic field

We determine the longitudinal magnetic field (B_l) according to Donati et al. (1997),

$$B_l = -2.14 \times 10^{11} \frac{\int v V(v) \mathrm{d}v}{\lambda g c \int [I_c - I(v)] \mathrm{d}v}, \quad (1)$$

where B_l is the longitudinal magnetic field in gauss, λ is the mean wavelength of all lines used to calculate the LSD profile in nm, g is the mean value of the Landé factors of all lines used to construct the LSD profile, c is the speed of light (in the same units as v), and I_c is the continuum level of the intensity profile. B_l is defined as the line-of-sight component of the field, which is averaged over the visible stellar disc (Babcock 1947; Schwarzschild 1950), and according to Mathys (1989) and Donati et al. (1997) is measured from the first-order moment of the Stokes *V* LSD profile. As a first-order approximation B_l is considered to be proportional to the shift in wavelength between left and right circularly polarized lines (Mathys 1995).

Stars with a fossil magnetic field are expected to be stable over long periods of time and show smooth sinusoidal rotational modulation of B_l that changes polarity over the rotation cycle as the positive and negative magnetic poles become visible. In contrast, dynamo magnetic fields are complex and dynamic and are not expected to show rotational modulation of B_l synchronized with the rotational cycle over longer periods of time due to evolution of the magnetic field.

We apply a generalized Lomb–Scargle periodogram (GLS; Zechmeister & Kürster 2009) to search for a period in the time-series of B_l measurements. We also calculate the FAP (Baluev 2008), which quantifies the probability of the maximum peak being produced by a signal without a periodic component (VanderPlas 2018). A plot of power versus frequency in Fig. 3 shows a peak with an FAP > 10^{-9} corresponding to an excellent fit of the sine curve to the data. This peak with maximum power corresponds to sine curve with a period of 18.4748 d, which is consistent with the equatorial rotation period of 18.5 d found by Preston (1967a), 18.497 d (Steinitz 1967),

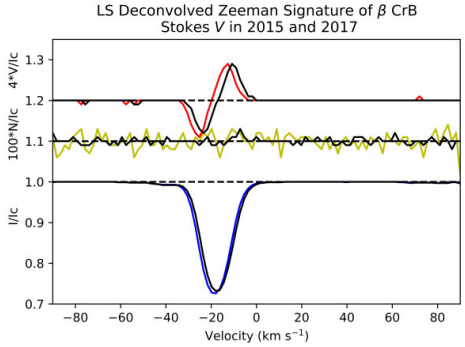

Figure 1. Comparison of two LSD profiles for β CrB at similar phases in different years. The LSD profile from 2015 April 24 at rotational phase 0.546 is displayed with the upper red line showing the Stokes V profile (y-axis expanded 4× and shifted up by 0.2 to allow better visibility). The middle green-yellow line shows the null profile (expanded 100× and shifted up by 0.1). The lower blue line shows the Stokes I profile. The profile from 8 March 2017 at rotational phase 0.542 is overplotted in black. The two plots show almost identical Stokes V profiles and a stable magnetic field over the 2 yr of observations, showing the well-known observation that β CrB contains a fossil magnetic field. The zero rotation phase for both figures is aligned to our first observation of β CrB on 2015 April 13.

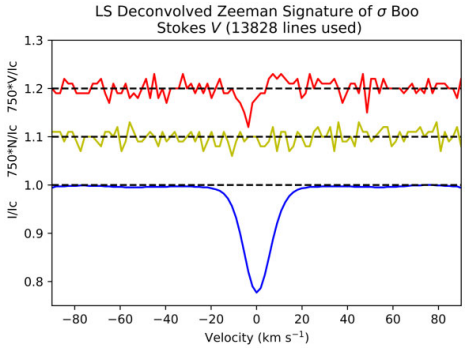

Figure 2. Mean LSD profile for σ Boo on 2021 May 18. The upper line (red) shows the Stokes V profile (y-axis expanded by 750 times and shifted up by 0.2 to allow better visibility). The middle line (green-yellow) shows the null profile (expanded by 750 times and shifted up by 0.1), which is used as a check for any spurious signals contaminating the spectra. The lower line (blue) shows the Stokes I profile.

18.4868 d (Kurtz 1989; Leroy 1995), and 18.4866 d (Bagnulo et al. 2000). We compute the window function (VanderPlas 2018) that is a check for the presence of periods caused by observational biases in the data. The window function is determined by applying a Lomb–Scargle periodogram to the data with the B_l measurements set to 1. The window function is shown in Fig. 3 and indicates there are no patterns in the timing of observations.

We determine 143 B_l values for β CrB over a 4-yr period between 2015 and 2018 (Table 1). A plot of the rotational modulation of B_l (Fig. 4) shows a sinusoidal curve that results from both positive and negative magnetic poles being visible over the rotation cycle. B_l spans a range of values from $+751.6 \pm 5.8$ G at phase 0.08 to -528.8 ± 6.8 G at phase 0.57 that is consistent with the range found by previous studies (Wade et al. 2000; Leone & Catanzaro 2001). Fig. 4 shows the rotational modulation B_l for each epoch which remains stable over the 4 yr of observations that is consistent with the behaviour of a fossil field.

We apply a GLS periodogram to the B_l measurements of σ Boo from 2021 May 18 to 28 (Tables 2 and A1), and find a sine period of 7.7 ± 1.0 d with an FAP of approximately 0.1 (Fig. 5). The window function is shown in Fig. 5, and indicates there are no patterns in the timing of observations. A plot of the rotational modulation of 11 mean nightly values of B_l for σ Boo is shown in Fig. 6, where we overlay a sinusoidal curve with a period that corresponds to an estimated stellar rotation period of 8.4 ± 0.2 d determined from ZDI χ^2 minimization (Table 4). The plot of B_l versus rotation phase shows a possible rotational modulation of the magnetic field; however, the large error bars make the determination uncertain.

4 MAGNETIC FIELD MODELLING

4.1 Longitudinal field modelling

The oblique rotator model (Babcock 1949; Stibbs 1950; Deutsch 1958, 1970; Pyper 1969; Falk & Wehlau 1974) is a useful first step in modelling the longitudinal magnetic field of a hot star where the field is considered to be a simple dipole inclined to the rotation axis. We derive the geometry and strength of the dipole fossil field of β CrB using parameters: inclination of the rotational axis with respect to the observer (i), obliquity of the dipole axis with respect to the rotational axis (β) counted from the positive rotational pole towards the positive magnetic pole, and the polar strength of the surface magnetic field (B_d) calculated at the positive magnetic pole. Following the oblique rotator model of Preston (1967b):

$$\beta = arctan\left[\left(\frac{1-r}{1+r}\right) - \cot i\right], \tag{2}$$

where

$$r = \frac{B_l(min)}{B_l(max)} = \frac{\cos\beta\cos i - \sin\beta\sin i}{\cos\beta\cos i + \sin\beta\sin i}. \tag{3}$$

We calculate the polar field strength (B_d) of following the relation given by Blazère et al. (2020),

$$B_d = B_{max}\left(\frac{15+u}{20(3-u)}(\cos\beta\cos i + \sin\beta\sin i)\right)^{-1} \tag{4}$$

where we use the limb-darkening coefficient $u = 0.57$ from Gray (2005), B_l max $= +751.6 \pm 5.8$ G and B_l min $= -528.8 \pm 6.8$ G calculated from fitting a sinusoidal curve to the data in Fig. 3. The value for $r = 0.70 \pm 0.006$ is calculated using equation (3). The value for $i = 39 \pm 4$ deg is calculated from the mean epoch values determined from ZDI χ^2 minimization, and $\beta = 26 \pm 4$ deg from the mean epoch values calculated using equation (2). We calculate the polar field strength (B_d) of β CrB $= 2423 \pm 51$ G. The values are presented in Table 3.

Schwarzschild (1950) showed the maximum value for a longitudinal magnetic field (B_l) is 30 per cent of the dipolar field. Our B_l max value of $+751.6 \pm 5.8$ G is 31.0 per cent of our calculated B_d of 2423 ± 51 G, which is consistent with Schwarzschild's prediction.

Landstreet & Mathys (2000) and Bagnulo et al. (2002) suggest the dipolar field obliquity (β) is correlated with stellar rotational period, where low-β geometries are more common in slow rotators. Landstreet & Mathys (2000) indicate that stars with rotation periods of about one month have their magnetic and rotation axes aligned within about 20 deg of each other, while faster rotating stars have

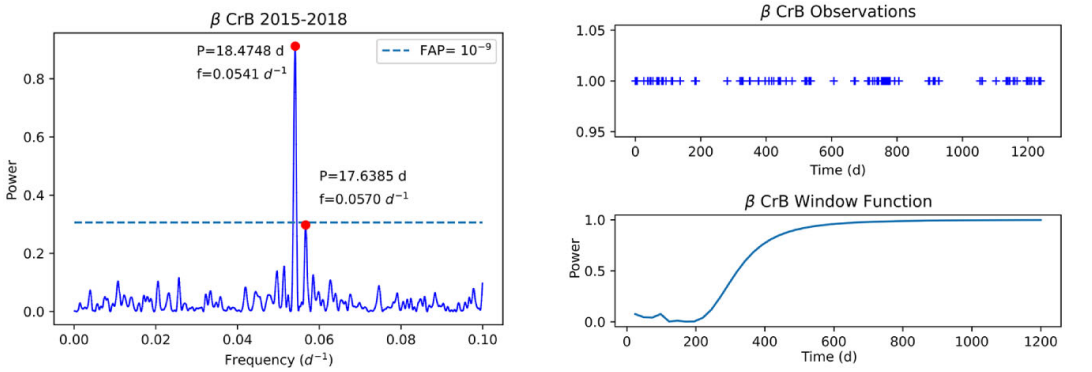

Figure 3. Figure at left: GLS periodogram a time-series of B_l measurements for β CrB spanning 1240 d from 2015 March 7 to 2018 July 28 (Table 1). The figure shows the power versus frequency and FAP, with the highest peaks marked with a red circle, and text describing the associated period and frequency. The FAP quantifies the probability of the maximum peak being produced by a signal without a periodic component. The blue dashed line is FAP 10^{-9} level, which indicates an excellent detection for the period determination. The best sine period determined from the GLS periodogram is 18.4748 ± 0.005 d. The figure at top right shows the time spacing of the observations. Figure at bottom right shows the window function.

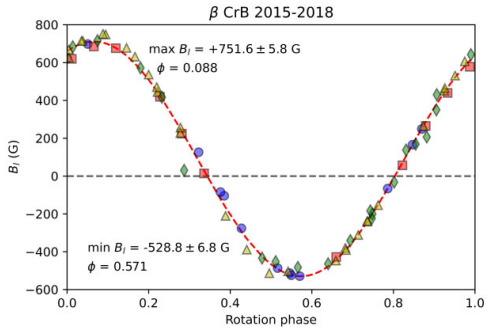

Figure 4. The figure shows the rotational modulation of B_l for β CrB from 73 observations corresponding to magnetic maps from 2015 to 2018. The data from 2015 are shown as blue circle, 2016 red square, 2017 yellow triangle, and 2018 green diamond. The dashed red curve indicates a fitted sine curve to the data with a period period of 18.4868 d that corresponds to the rotation period used in ZDI analysis. The rotation phase ϕ corresponds to the measured maximum and minimum B_l. The figure shows the magnetic field is stable over the 4 yr observation period. The zero day is the first date of B_l measurement on 2018 January 23.

larger values of β. Since β CrB is a slow rotator with a period of 18.5 d (Section 3.2), we may expect that β will be larger 20 deg. We determine β values of 29 ± 3 deg, using equation (2) and 26 ± 4 deg from ZDI χ^2 minimization Section 4.2, which is consistent with the trend from Landstreet & Mathys (2000).

4.2 Zeeman Doppler imaging

The surface magnetic fields of β CrB and σ Boo are reconstructed using the inversion technique of ZDI (Semel 1989; Donati & Brown 1997), using a spherical harmonics expansion of the surface magnetic field (Donati et al. 2006b). Recovery of reliable maps depends on modelling Stokes *I* and *V* profiles and using a model local line profile. ZDI involves an iterative procedure that begins with a zero magnetic field, and parameters are adjusted to optimize the fit (parametrized by reduced χ^2) of the model compared to observations. The local line profile is an approximation to the actual line profile (Piskunov & Rice 1993) and is the function used to calculate the line at one point on the surface of the star. We modelled the local line profile using a Voigt profile (Table 4).

We assume the model star is spherical and divided into approximately equal area surface elements with coordinates of colatitude and longitude. Colatitude increases with distance from the north pole, and longitude increases in the direction of rotation, with the coordinate system aligned with the stellar rotation axis. We use a stellar surface divided into a 4584 point grid, with 120 spatially resolved elements around the equator, and 60 in colatitude similar to Folsom et al. (2018). The minimum χ^2 used in the ZDI code is determined by running the code with increasing values and finding the χ^2 value where there is no increase in magnetic energy as used in Paper 2. Using this method, we adopt a χ^2 of 4.0 for β CrB and 0.95 for σ Boo.

For β CrB, the local line width used are Gaussian width 2.41 km s^{-1}, Lorentzian width 0.89 km s^{-1}, and limb darkening coefficient 0.57. The wavelength 512.6 nm and effective Landé factor 1.195 used for computing Stokes *V* are the normalizing values for the LSD profile. For σ Boo, the local line width used are Gaussian width 2.41 km s^{-1}, Lorentzian width 0.89 km s^{-1}, and limb darkening coefficient 0.70. The wavelength 512.6 nm and effective Landé factor 1.195 used for computing Stokes *V* are the normalizing values for the LSD profile. The profiles for both stars are convolved with a Gaussian instrumental profile of $R = 65\,000$.

4.2.1 *Modelling the LSD stokes profiles*

The Stokes *V* maximum entropy fit for β CrB is shown in Fig. 7. The plot shows a good fit between the observed and modelled profiles that adds weight to the reliability of our magnetic map reconstruction. The Stokes *V* LSD profile for σ Boo (Fig. 2) is produced by co-adding the nightly LSD profiles, which further increases the SNR of the weak magnetic field. The Stokes *V* maximum entropy fit for σ Boo is shown in Fig. 8. The plot shows a moderate fit between the observed and modelled profiles.

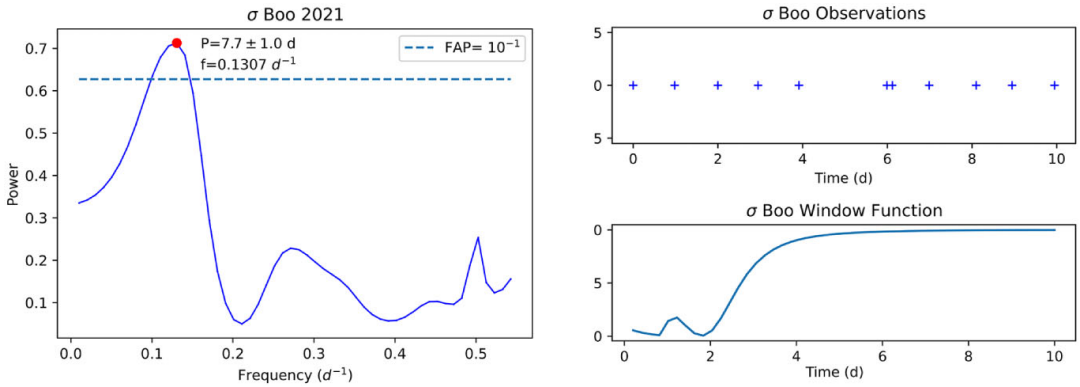

Figure 5. Figure at left: GLS periodogram a time-series of B_l measurements for σ Boo spanning 11 d from 2021 May 18 to 28 (Table 2). The figure shows the power versus frequency and FAP, with the highest peak marked with a red circle, and text describing the associated period and frequency. The blue dashed line is FAP 10^{-1} level. The best sine period determined from the GLS periodogram is 7.7 ± 1.0 d. The figure at top right shows the time spacing of the observations. Figure at bottom right shows the window function.

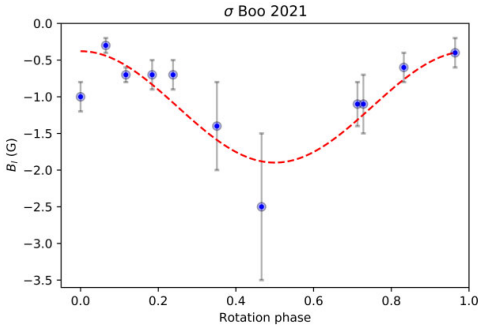

Figure 6. Figure shows the rotational modulation of B_l for σ Boo from 11 observations in 2021 May from the mean LSD profiles from each night. The red dashed line indicates a fitted sine curve to the data with a period of 8.4 d corresponding to an estimated stellar rotation period determined from ZDI.

4.2.2 β CrB magnetic maps

The large-scale magnetic field topology for β CrB at six epochs are shown in Fig. 9. The stellar parameters used to reconstruct the map are determined using a method of χ^2 minimization (Petit, Donati & Collier Cameron 2002) whereby we iteratively change individual parameters and re-run ZDI analysis, to find the parameter with the minimum χ^2 when we fit a Gaussian curve to the χ^2 values. The formal uncertainties in parameter estimation are determined by finding the 1σ uncertainty around Gaussian fit to the χ^2 minimization. The parameters determined by ZDI analysis of each magnetic map are shown in Table 4.

We adopt the same stellar parameters for all β CrB maps displayed in Table 4 that are mean $v \sin i = 9.4$ km s^{-1}, mean inclination = 39 deg, and differential rotation $d\Omega = 0.0$ rad d^{-1}. The mean and 1σ errors are derived from the mean values averaged over the six maps. For P_{rot}, we use the value of 18.4868 d from Kurtz (1989) since this value is within the uncertainty of our ZDI determination of 18.59 ± 0.07 d. The spherical harmonic expansion is limited to $\ell_{max} = 20$ since no further detail is obtained with higher degrees. The rotation phase of all maps is aligned to a common zero date, with the first observation date set to MJD = 2457126.47656 (2015 April 13). The data sets comprise between 8 and 15 LSD profiles (Table 3).

The large-scale magnetic features are similar on all maps and indicate that the field is stable over the 39 month observation period. This is consistent with the fossil field nature of β CrB where the field remains frozen into the stellar atmosphere and is expected to remain unchanged over a long period of time. The radial magnetic field shows a large area of negative polarity in the mid-northern latitudes between phases 0.2–0.6 and a region of positive magnetic field in the northern latitudes between phases 0.8–1.0. The azimuthal magnetic field shows a region of negative polarity that approximately matches the position of negative radial field between 0.2–0.6, and a small region of positive field with strengths of about 1000–2000 G at the north pole.

The complexity of the surface magnetic field for β CrB is quantified by calculating the fractional strength of the magnetic field components that are displayed in Table 5. The calculated percentages from the Stokes V maps are the average squared magnetic field $\langle B^2 \rangle$, which is proportional to the magnetic energy (Reiners 2012). The uncertainties are derived by varying the stellar parameters over the 1σ errors for each individual parameter, and taking the extreme values of the results as the variation. The dominant term in the spherical harmonics expansion is the dipole ($\ell = 1$), which ranges from 50^{+5}_{-0} to 61^{+0}_{-9} per cent over the six epochs from 2015 to 2018. The second largest spherical harmonics term is the quadrupole ($\ell = 2$) with 18^{+2}_{-1} to 21^{+0}_{-4} per cent of magnetic energy. The octupole ($\ell = 3$) contains between 5^{+1}_{-0} and 7^{+0}_{-2} per cent of magnetic energy. The higher multipoles ($\ell > 3$) contain a significant fraction of magnetic energy with 12^{+13}_{-0} to 27^{+0}_{-5} per cent of magnetic energy.

The maximum magnetic field strength of our magnetic map of β CrB, $B_{max} = 4106$ G for the 2017 April 7–24 map, which also has the highest $B_{mean} = 1192$ G. In contrast, the maximum B_l is only +728.5 G. This large difference between B_{max} and B_l values indicates a significant transverse magnetic field component may be present in β CrB, resulting in magnetic flux cancellation. This flux cancellation is consistent with a complex magnetic field structure on the surface of β CrB. The magnetic field configuration is predominately poloidal with values ranging from 73 to 90 per cent (Table 5). The uncertainties are derived by varying the stellar parameters over the 1σ errors for each individual parameter, and taking the extreme values of the results as

Table 3. Stellar parameters for β CrB between 2015 and 2018, and σ Boo in 2021 determined from our ZDI analysis. For β CrB, polar field strength (B_d) and obliquity angle (β) are calculated from a dipole model of the star ($\ell_{max} = 1$). β_{ORM} is calculated from the oblique rotator model using equation (2). β_{ZDI} is calculated using ZDI. B_d is calculated from equation (4) using β from equation (2) and inclination from ZDI χ^2 minimization. Maximum dipolar field strength from ZDI output. For σ Boo, the 11 mean LSD profiles constructed from 105 individual profiles.

Epoch (UT)	Obs. rot cycles	No. LSD profiles	Incl. (deg)	$v \sin i$ (km s^{-1})	Eq rot period (d)	Obliquity angle β_{ORM} (deg)	Obliquity angle β_{ZDI} (deg)	Polar field str. B_d (G)	Dipolar max (G)
β CrB									
13 Apr–30 May 2015	2.5	13	35 ± 2	9.2 ± 0.2	18.475 ± 0.102	32 ± 2	32	2364	1389^{+52}_{-30}
6–24 Aug 2016	1.0	11	35 ± 2	9.8 ± 0.2	18.450 ± 0.020	32 ± 2	22	2364	1469^{+0}_{-110}
2 Mar–4 Apr 2017	0.9	15	42 ± 2	9.1 ± 0.3	18.465 ± 0.020	26 ± 2	21	2481	1406^{+35}_{-47}
7–24 Apr 2017	0.9	14	35 ± 2	9.2 ± 0.2	18.410 ± 0.021	32 ± 2	25	2401	1533^{+0}_{-173}
14 Apr–16 May 2018	1.8	8	46 ± 2	9.6 ± 0.2	18.625 ± 0.022	23 ± 2	28	2489	1281^{+160}_{-0}
14 Jun–28 Jul 2018	2.4	13	39 ± 2	9.4 ± 0.2	18.525 ± 0.022	28 ± 2	25	2440	1339^{+102}_{-0}
Mean	–	–	39 ± 4	9.4 ± 0.2	18.592 ± 0.069	29 ± 3	26 ± 4	2423 ± 51	1403 ± 82
σ Boo									
18–28 May 2021	1.2	11	15 ± 3	3.8 ± 0.3	8.4 ± 0.2	–	20	–	0.8

Table 4. Parameters used to produce the maximum-entropy image reconstructions for β CrB and σ Boo. β CrB P_{rot} from Kurtz (1989).

Parameter	β CrB	σ Boo
ZDI parameters		
Inclination (deg)	39 ± 4	15 ± 3
$v \sin i$ (km s^{-1})	9.4 ± 0.2	3.8 ± 0.3
P_{rot} (this work) (d)	18.50 ± 0.07	8.4 ± 0.2
P_{rot} (literature) (d)	18.4868	–
dΩ (rad d^{-1})	0.0	0.0
χ^2	4.0	0.95
degree ℓ_{max}	20	8

the variation. The parameter ranges used for β CrB are: inclination $\pm$ 4 deg, $v \sin i \pm 0.2$ km s^{-1}, and $P_{rot} \pm 0.07$ d. The Stokes V LSD fits to the observations are shown in Fig. 7 that indicates an excellent match between the observed Zeeman signatures and modelled line profiles, which adds further evidence of the reliability of our reconstructed magnetic maps.

4.2.3 σ Boo magnetic map

The large-scale magnetic field topology for σ Boo in 2021 May is shown in Fig. 10. The stellar parameters used to reconstruct the maps are determined using a method of χ^2 minimization as described in Section 4.2.2 are $v \sin i = 3.8$ km s^{-1}, inclination = 15 deg, rotation period = 8.4 d, and dΩ = 0.0 rad d^{-1}. The spherical harmonic expansion is limited to $\ell_{max} = 8$ since no further details are observed in the maps with higher degrees. The large-scale magnetic field shows a simple topology, which may partly be due to a low $v \sin i$ of 3.8 ± 0.3 km s^{-1} where the resolution is affected by the number of resolution elements (Morin et al. 2010).

The radial field of σ Boo shows a large region of negative polarity in the Northern hemisphere, with a maximum strength of 1.5 G at rotation phase 0.2–0.4. The positive magnetic pole is not visible on the map since it is located near the south polar region in an area that is tilted away from the observer. The azimuthal magnetic field shows mostly weak positive polarity (<0.5 G) that covers most of the surface except of a weak negative patch in the Northern hemisphere between phases 0.5–0.8. The meridional magnetic field shows mostly weak negative polarity (>−0.5 G) that covers most of the surface except of a positive patch at the north pole, and a negative area of approximately −1.0 G in the Northern hemisphere between phases 0.7–1.0.

The simplicity of the surface magnetic field of σ Boo is further indicated by the fractional strength of the magnetic field components that are displayed in Table 5. The dominant term in the spherical harmonics expansion is the dipole ($\ell = 1$) which contains 84 ± 1 per cent of the magnetic energy. The second largest spherical harmonics term is the quadrupole ($\ell = 2$) with 14 ± 1 per cent of the magnetic energy. The octupole ($\ell = 3$) contains between 2^{+0}_{-0} per cent of magnetic energy, while the higher order multipoles ($\ell > 3$) contain 2^{+1}_{-2} per cent of magnetic energy. The uncertainties are derived by varying the stellar parameters over the 1σ errors for each individual parameter and taking the extreme values of the results as the variation. The parameter ranges used for σ Boo are: inclination $\pm$3 deg, $v \sin i \pm 0.3$ km s^{-1}, $P_{rot} \pm 0.2$ d.

The maximum magnetic field strength of our magnetic map of σ Boo, $|B_{max}|$ =1.5 G that is consistent with the expected weak magnetic fields for F-type stars (Marsden et al. 2014) and Paper 1. The magnetic field for σ Boo is mainly poloidal which is consistent with the finding of Petit et al. (2008) who found that stars with $P_{rot} < 12$ d are more likely to have increasing proportion of magnetic energy in the poloidal field. The simple magnetic topology of σ Boo is similar to the slow rotating ($v \sin i = 6.1$ km s^{-1}) F9V star β Vir (Paper 2) that also has a mainly poloidal field with a weak magnetic field (B_{max}=1.6 G).

4.3 Differential rotation

An understanding of differential rotation (dΩ) in hot stars, and the conditions of the atmosphere are incomplete; however, there is evidence from Kepler photometric data that rotational shear is present in about 60 per cent of A-type stars, compared to 75 per cent of F-stars, and 95 per cent of G-stars (Balona & Abedigamba 2016). We do not find evidence of dΩ in β CrB using the method of χ^2 minimization as described in Section 4.2.2. The lack of detected dΩ is consistent with the suggestion that hot stars with strong magnetic fields maintain uniform rotation along field lines (Mathis & Zahn 2005; Zahn 2010). The presence of dΩ in hot stars is also strongly

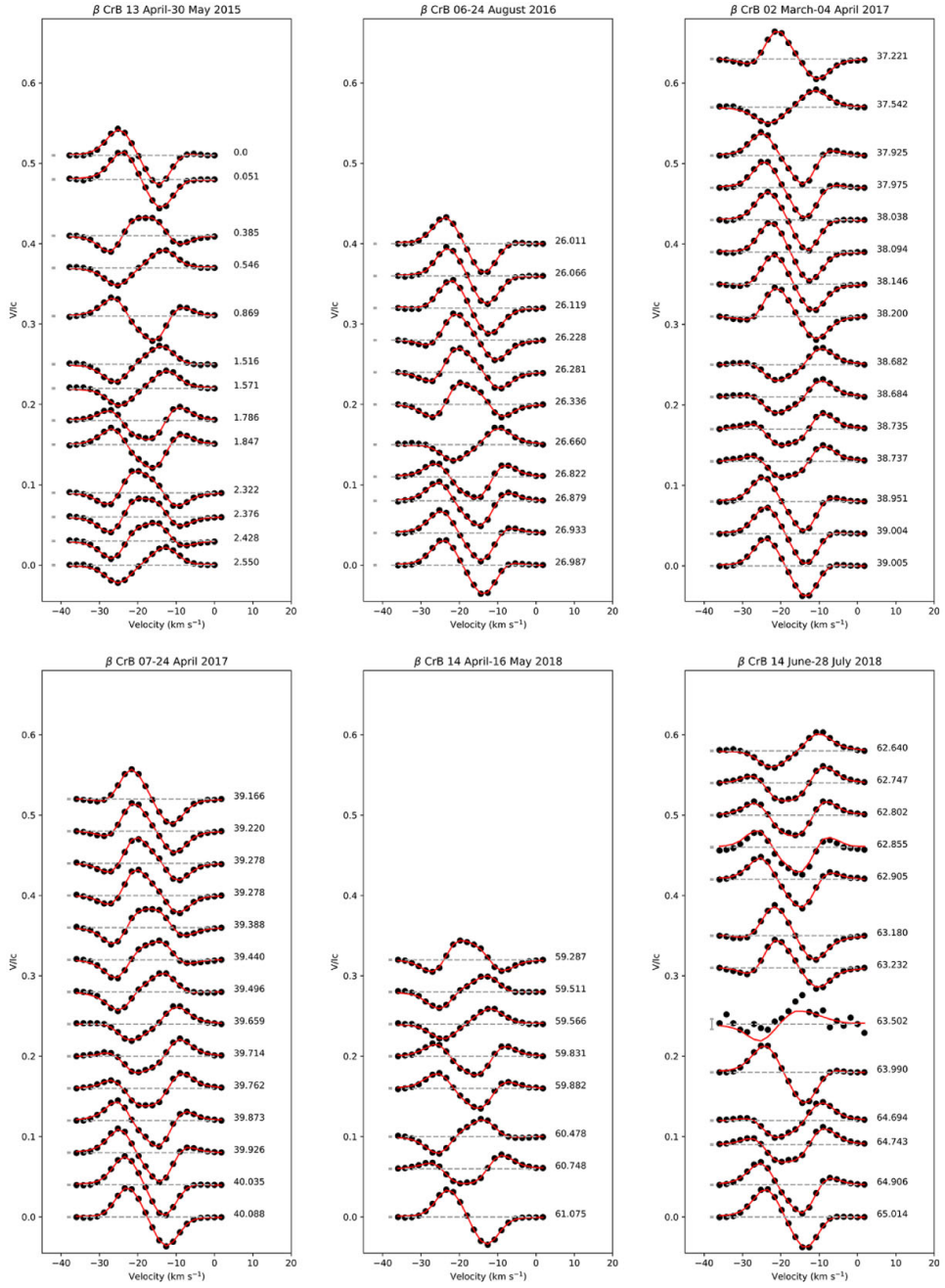

Figure 7. Stokes *V* fit for β CrB corresponding to 2015–2108 magnetic maps. The black lines represent the observed Zeeman signatures, while the red lines represent the modelled line profiles. The 1σ error bars are very small and are shown on the left. The line profiles are arranged vertically by rotation cycle and separated to allow better visibility. The rotation cycle is shown on the right of each profile.

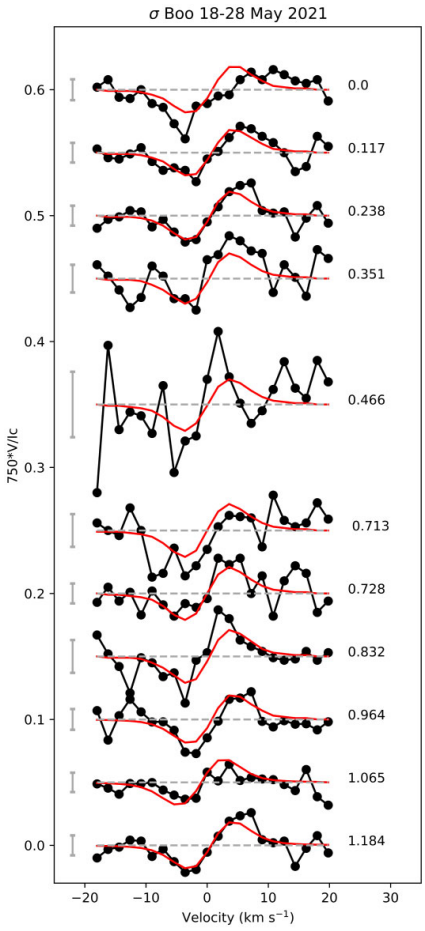

Figure 8. Stokes *V* fit for σ Boo corresponding to the 2021 magnetic maps. The description is the same as Fig. 7.

correlated with rotation rate (Balona & Abedigamba 2016), and with β CrB being a slow rotator ($v \sin i = 9.4$ km s^{-1}), we may therefore expect small or no detectable dΩ.

The presence of dΩ is a common feature of solar-type stars (Hall 1972; Gilman 1980; Rüdiger 1989) and is one of the ingredients in the operation of a solar-type dynamo (Parker 1955; Steenbeck & Krause 1969; Gilman 1980). We determine the amplitude of dΩ by applying a solar-type differential rotation law as described in Donati et al. (2000) where equatorial regions have larger angular velocity than polar regions:

$$\Omega(l) = \Omega_{\rm eq} - {\rm d}\Omega \sin^2 l, \quad (5)$$

where l denotes the latitude, $\Omega_{\rm eq}$ is the rotation rate at the equator, and dΩ is the rotational shear between the equator and the pole expressed in rad d^{-1}. The presence of dΩ in F-type stars was initially questioned by Gray (1982) who failed to find evidence of it in seven stars from F2-F8 using a Fourier transform of the line profiles. However, using a Fourier transform method, Reiners & Schmitt (2003a) detected dΩ was present in F-type stars. Further research has shown that strong dΩ may be present in F-type stars compared to cooler stars (Reiners & Schmitt 2003b; Barnes et al. 2005).

We do not find evidence of dΩ in σ Boo using the method of χ^2 minimization as described in Section 4.2.2. Reiners & Schmitt (2003a) found large dΩ values in comparably slowly rotating stars, therefore we may have expected σ Boo with a $v \sin i = 3.8$ km s^{-1} to have a high dΩ. Higher rates of dΩ are also expected to be present in earlier spectral types (Barnes et al. 2005). There are several possible reasons we did not find differential rotation in σ Boo. First, the magnetic field in σ Boo may have been too weak to allow magnetic features to be tracked on the surface of the star. A second reason is that rigid rotation may exist for σ Boo, therefore no dΩ was present in the star. A third reason for the lack of detection of dΩ may be due to a change in atmospheric conditions in early F-type stars whereby dΩ is inhibited near the transition to A-type stars (Walter 1983; Ammler-von Eiff & Reiners 2012). A fourth reason may be due to the presence of a varying differential rotation rate caused by a variable stellar dynamo (Marsden, Carter & Donati 2005), and σ Boo may have been observed during a period of low dΩ. The most likely reason for the non-detection of dΩ is the low amplitude of the Stokes *V* signal relative to the noise, and observations spanning only 1.2 rotation cycles.

5 CHROMOSPHERIC ACTIVITY INDICATOR

The *S*-index introduced by Vaughan, Preston & Wilson (1978) is an indirect measure of stellar magnetic activity in cool stars. It measures the flux in 20 Å wide triangular profiles centred on two resonance lines at 393.3682 nm (K-line) and 396.8492 nm (H-line) compared to the flux in two bands in the continuum on the red and blue side of the H&K line. The onset of chromospheric emission appears abruptly in solar-type stars (Hall 2008), and has been detected in the hot star Altair, A7 IV-V (Ferrero et al. 1995). Observations using the Far Ultraviolet Spectroscopic Explorer have suggested that chromospheres appear in stars as hot as 8250 K (Simon et al. 2002); however, the chromospheric emission is only a few per cent of the solar value. We do not determine *S*-index for β CrB since the measurement is not used in hot stars due to the absence of significant chromospheres (Hall 2008).

We determine the *S*-index for σ Boo using the method of Vaughan et al. (1978) and coefficients for the ESPaDOnS spectropolarimeter taken from Marsden et al. (2014). The *S*-index values for σ Boo are shown in table 6. We plot the rotational modulation of the mean nightly *S*-index of σ Boo in Fig. 11. The mean nightly *S*-index values vary from 0.248 ± 0.010 to 0.262 ± 0.005 and possibly show small variations in strength over the 11 d observation period. The figure indicates there is no periodic rotational modulation of the *S*-index. We confirm the lack of sinusoidal fit to the *S*-index data by applying a GLS periodogram to the mean *S*-index values and noted an absence of a detectable period to the 0.1 FAP level (see Fig. A1). Chromospheric emission dominates the flux measured in the *S*-index of K-type stars. However, Wolff, Heasley & Varsik (1985) suggest in active early F-type stars it is a minor contributor to the *S*-index. Variability in chromospheric emission may be difficult to detect in F-stars due to possible weakness of chromospheric emission and low contrast relative to the photospheric flux (Baliunas et al. 1995; Knutson, Howard & Isaacson 2010).

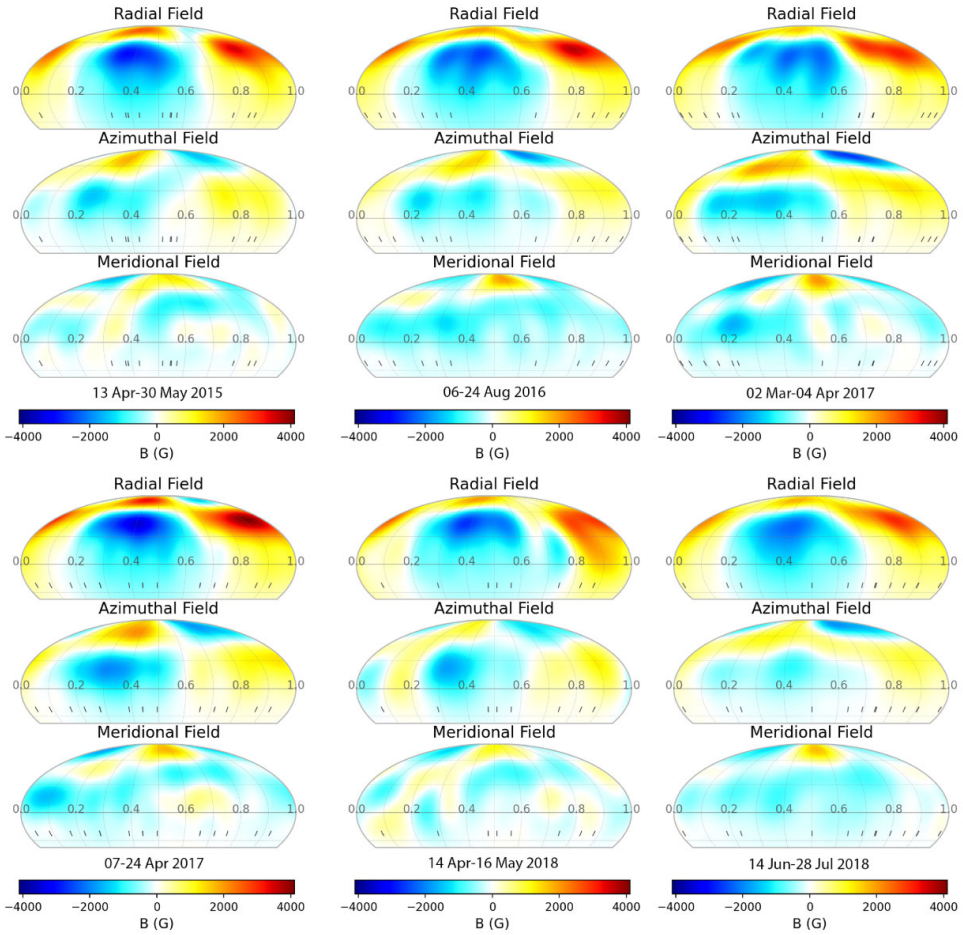

Figure 9. Magnetic maps for β CrB at six epochs from 2015–2018 displayed using a Mollweide projection. The magnetic field strength in gauss is indicated in colour bars below the maps. The radial, azimuthal, and meridional components of the reconstructed large-scale magnetic field are plotted from top to bottom. Tick marks at bottom of map indicate observational phases used in magnetic map reconstruction. The rotation phases for all maps are aligned to the same zero date of MJD = 2457126.47656 (2015 April 13). The map displays the visible surface of the star to −39 deg latitude.

6 DISCUSSION

6.1 β CrB

We have reconstructed for the first time surface magnetic maps for β CrB using ZDI. Our analysis of β CrB provides a rotational modulation of B_l that is consistent with previous studies. We find that the magnetic field is stable over the 4 yr observation period after taking into account the rotation of the magnetic field as a result of the different alignment in rotation and magnetic axes.

Using the simple oblique rotator model for β CrB, we find that our B_l max calculation of $+751.6 \pm 5.8$ G is 31.0 per cent of B_d value of 2423 ± 51 G, which is consistent with Schwarzschild's prediction that B_l should be about a third of the B_d value. Looking into the magnetic field in more detail beyond a simple dipole model, we find a range of maximum strengths of the magnetic field for the maps determined by ZDI from 2660 to 4106 G, which are larger than the B_l values of 902–1120 G. This may be due to some cancellation effects of the B_l where regions of opposite polarity cancel out, while less cancellation effects may occur in ZDI maps (Lehmann et al. 2019). A higher proportion of the magnetic energy is contained in higher multipoles, which is shown in our ZDI analysis that indicates for the six magnetic maps only 54–61 per cent of the magnetic energy is contained in the dipolar magnetic field, while a significant proportion of the energy is contained in the quadrupolar (18–20 per cent) and octupolar (5–8 per cent) components, and higher multipoles ($\ell > 3$) account for 12–27 per cent of magnetic energy. This complex magnetic field for β CrB is also displayed in the magnetic maps that show details beyond a simple dipole. There are areas of positive and negative magnetic regions that are more commonly seen in dynamo fields.

Using arguments from Donati et al. (2006b), there are several reasons we conclude the complex magnetic field of β CrB is fossil in origin and not a dynamo field. First, β CrB is a relative slow rotator

Table 5. Fraction of the large-scale magnetic energy reconstructed in the toroidal and poloidal field components; the fraction of the poloidal field in the dipolar ($\ell = 1$), quadrupolar ($\ell = 2$), and octupolar ($\ell = 3$) components; and the fraction of the energy stored in the axisymmetric component ($m = 0$) for β CrB and σ Boo. The uncertainties are derived by varying the stellar parameters over the 1σ errors for each individual parameter, and taking the extreme values of the results as the variation.

Epoch (UT)	$B_{\rm mean}$ (G)	$B_{\rm max}$ (G)	Poloidal (per cent tot)	Toroidal (per cent tot)	Dipolar (per cent pol)	Quad. (per cent pol)	Oct. (per cent pol)	($\ell > 3$) (per cent pol)	Axisym. (per cent tot)	Poloidal (per cent axi)	Toroidal (per cent axi)
β CrB											
13 Apr–30 May 2015	970^{+44}_{-24}	3462^{+147}_{-87}	88^{+1}_{-1}	12^{+1}_{-1}	54^{+2}_{-2}	18^{+2}_{-1}	5^{+1}_{-0}	23^{+2}_{-2}	9^{+2}_{-2}	10^{+2}_{-2}	3^{+0}_{-0}
6–24 Aug 2016	1050^{+0}_{-104}	3624^{+0}_{-249}	89^{+0}_{-2}	11^{+2}_{-0}	57^{+0}_{-5}	19^{+0}_{-2}	7^{+0}_{-2}	17^{+7}_{-0}	23^{+0}_{-14}	23^{+0}_{-15}	20^{+0}_{-17}
2 Mar–4 Apr 2017	1113^{+0}_{-167}	3666^{+0}_{-179}	73^{+16}_{-0}	27^{+0}_{-16}	55^{+0}_{-3}	20^{+0}_{-3}	7^{+0}_{-2}	18^{+7}_{-0}	19^{+0}_{-12}	17^{+0}_{-9}	26^{+0}_{-23}
7–24 Apr 2017	1192^{+0}_{-246}	4106^{+0}_{-731}	85^{+4}_{-0}	15^{+0}_{-4}	50^{+5}_{-0}	18^{+3}_{-1}	5^{+1}_{-0}	27^{+0}_{-5}	13^{+0}_{-6}	14^{+0}_{-6}	11^{+0}_{-7}
14 Apr–16 May 2018	902^{+112}_{-0}	2660^{+949}_{-0}	90^{+0}_{-3}	10^{+3}_{-0}	54^{+1}_{-2}	20^{+0}_{-3}	8^{+0}_{-3}	18^{+7}_{-0}	7^{+4}_{-0}	7^{+5}_{-0}	7^{+0}_{-4}
14 Jun–28 Jul 2018	905^{+109}_{-0}	2906^{+703}_{-0}	87^{+2}_{-0}	12^{+0}_{-2}	61^{+0}_{-9}	21^{+0}_{-4}	6^{+0}_{-1}	12^{+13}_{-0}	21^{+0}_{-14}	20^{+0}_{-12}	30^{+0}_{-27}
σ Boo											
18–27 May 2021	$0.5^{+0.0}_{-0.0}$	$1.5^{+0.0}_{-0.0}$	95^{+1}_{-2}	5^{+2}_{-1}	84^{+1}_{-1}	14^{+1}_{-1}	2^{+0}_{-0}	2^{+1}_{-2}	88^{+2}_{-2}	92^{+2}_{-2}	10^{+5}_{-4}

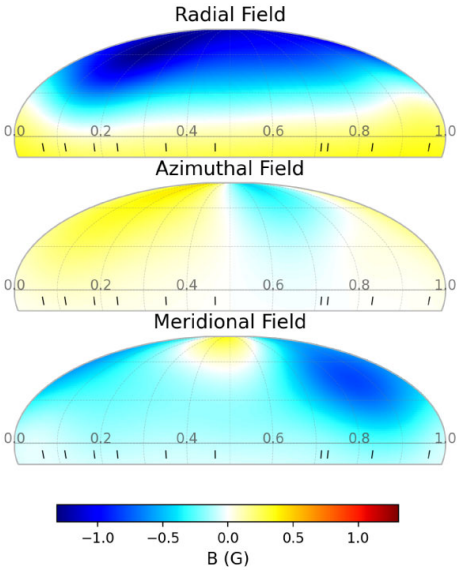

Figure 10. Magnetic map for σ Boo in 2021 reconstructed from mean LSD profiles. Description is the same as Fig. 9. Zero phase for the map is set to the first date of observations HJD = 2459352.82771. The map displays the visible surface of the star to −15 deg latitude.

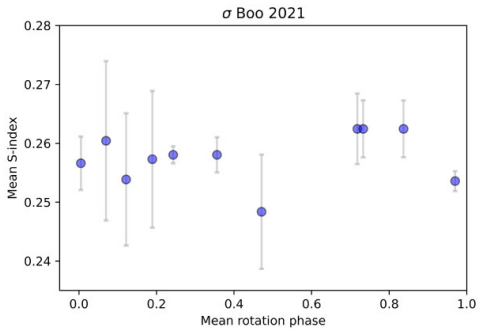

Figure 11. Rotational modulation of 11 mean nightly S-index values for σ Boo in 2021 May. The two closely spaced values at rotational phases 0.72 and 0.73 are observation on the same night separated by 2 h. The figure shows a small variation in S-index over time, but no variation due to rotational modulation.

($v \sin i = 9.4 \pm 0.2$ km s^{-1}) and dynamo-generated magnetic fields are expected to scale with rotation rate (Noyes et al. 1984). The $v \sin i$ is not fast enough to produce a large dynamo magnetic field of the order of several kG in strength. Secondly, we consider the possibility that the field is created by a convective core dynamo (Charbonneau & MacGregor 2001; Brun, Browning & Toomre 2005) that has reached the surface. According to Spruit–Taylor dynamo processes (Spruit 1999, 2002), a core dynamo would only be expected to reach surface strengths of a few gauss in a star rotating as slowly as β CrB. Thirdly, the large-scale magnetic field is stable over at least 3 yr, which contrasts with dynamo fields that are expected to evolve over time.

In order to maintain their stability, stellar fossil fields are thought to contain mixed poloidal and toroidal topology of comparable strength in their interior (Prendergast 1956; Tayler 1973; Wright 1973; Braithwaite & Spruit 2004; Braithwaite & Nordlund 2006). However, at the surface, they are expected to be mainly poloidal (Braithwaite 2009). We find that the surface magnetic field of β CrB is mainly poloidal (approximately 85 per cent) with 15 per cent being toroidal. This agrees with the expectation for a hot star fossil field. We also find that the magnetic field geometry of β CrB is not represented by a simple dipole as described by the oblique rotator model, but is more complex as suggested by Preston (1969), Wolff & Wolff (1970), Mathys & Hubrig (1997), and Bagnulo et al. (2000).

Complex fossil fields are rare, but have been found in several stars previously. τ Sco (B0.2 V) was found by Donati et al. (2006b) to contain an unusually complex surface magnetic field for a massive star that differed significantly from a simple dipole. The magnetic field contained a moderate toroidal component, which is unusual for a fossil field. The B_l varied over the rotation cycle from a minimum of -51.9 ± 5.3 G to a maximum of 87.8 ± 4.2 G. HD 37776 (B2IV) was found to show a complex, non-axisymmetric magnetic

field that differed from a simple dipole (Kochukhov et al. 2011). A quadrupolar component dominated the magnetic field geometry with higher multipoles present up to $\ell = 6$. The magnetic field intensity varied over the surface from ≈5 to ≈30 kG. The authors found that there were similar poloidal and toroidal components to the field, which was an unexpected result for a hot star that is not expected to contain such a high toroidal component.

The δ Scuti star HD 41641 (A5III) was found to contain a complex fossil field (Thomson-Paressant et al. 2021) B_l that varied from -178 ± 112 to 182 ± 273 G, and a simple dipole or dipole + quadrupolar configuration did not fit the data. Our finding of a relatively complex surface magnetic field for β CrB is at odds with the fossil field hypothesis where a complex magnetic field topology has previously been considered to be produced mostly by dynamo fields. Our results for β CrB are consistent with the presence of a complex fossil field and may add to the evidence that complex fossil fields may be more common than previously thought. Another δ Scuti star β Cas (F2III) has recently been shown to be magnetic (Zwintz et al. 2020); however, this time the complex magnetic field was considered to be produced by a dynamo. β Cas is therefore an interesting star for the study of magnetic fields in stars with shallow outer convection zones close to the transition between fossil and dynamo magnetic fields.

6.2 σ Boo

We have reconstructed surface magnetic maps for σ Boo at one epoch in 2021 May using ZDI. The surface magnetic topology is simple in structure, axisymmetric, poloidal (95 per cent), and is dominated by the dipole component (84 per cent) of magnetic energy. Less than 4 per cent of magnetic energy is contained in the higher ($\ell > 2$) multipoles. The simple magnetic field for σ Boo is similar to the late F-star β Vir F9V (Paper 2) and is more like the dipolar fields seen in hot stars. Complex surface topology does not appear to be a common feature of F-star dynamo magnetic fields, and may possibly be due to the shallow outer convection zones, which do not allow for complex twisting of the flux tubes on their rise to the surface.

σ Boo shows a variation of S-index over time, which is not due to rotational modulation. This is possibly due to magnetic areas on the surface of the star varying over time which may indicate a dynamo magnetic field. However, we are not able to definitely say whether the magnetic field of σ Boo is a dynamo field or weak fossil from a single epoch magnetic map. One or more additional epochs are required to characterize the field of σ Boo, and evolution of the large-scale magnetic field will indicate a dynamo field, while an unchanging field over an additional epoch will indicate that a weak fossil field in present.

The spectral type where the transition from fossil to dynamo magnetic fields occurs has not been determined; however, Paper 1 provided some evidence that it may occur as early as spectral type F3. This identifies σ Boo as an important star for magnetic studies. There is some indirect evidence that the F2IV star HD164615 may contain spots (Abt, Bollinger & Burke 1983; Zerbi et al. 1997), and therefore may be generated by a dynamo; however, this was questioned by Hatzes (1998) who concluded that the most likely explanation was non-radial pulsations.

Searching for dynamo magnetic field in stars earlier than F3 will help identify the transition between fossil and dynamo fields. Observing σ Boo at additional epochs will help firmly establish the nature of its magnetic field. Our mapping of a complex fossil field in β CrB and a simple dynamo field in σ Boo adds evidence that magnetic field complexity alone cannot be used to differentiate between fossil and dynamo fields. We need to look at a combination of factors in stars to fully categorize the type of surface magnetic field present. This includes B_l modelling, magnetic mapping, and chromospheric emission analysis.

7 CONCLUSIONS

Using ZDI, we reconstructed surface magnetic maps for β CrB (A9SrEuCr), a hot star with a fossil magnetic field, and σ Boo, an F3V star with either a dynamo field or a weak fossil field. The surface magnetic field of β CrB shows a relatively complex topology that is not commonly seen in hot stars with a fossil field. This adds further evidence that complex fossil fields might be more common than previously recognized. We also reconstruct surface magnetic maps for σ Boo and find that it has a relatively simple surface magnetic field topology. Future studies to search for dynamo magnetic fields in stars earlier than F3 will be valuable in order to learn more about the transition between fossil and dynamo magnetic fields.

ACKNOWLEDGEMENTS

This research was based on observations obtained at the Canada–France–Hawaii Telescope (CFHT), which is operated by the National Research Council of Canada, the Institut National des Sciences de l'Univers of the Centre National de la Recherche Scientifique of France, and the University of Hawaii. This work is based on observations obtained at the Bernard Lyot Telescope (TBL, Pic du Midi, France) of the Midi-Pyrénées Observatory, which is operated by the Institut National des Sciences de l'Univers of the Centre National de la Recherche Scientifique of France. This research was supported by an Australian Government Research Training Program (RTP). This research has made use of the SIMBAD data base, operated at CDS, Strasbourg, France, and the VizieR catalogue access tool, CDS, Strasbourg, France.

DATA AVAILABILITY

All data presented here are publicly available through the PolarBase data base (http://polarbase.irap.omp.eu/).

REFERENCES

Abramowitz M., Stegun A., 1964, Handbook of Mathematical Functions, 9th edn. Dover Press, New York
Abt H., Bollinger G., Burke E.,, Jr, 1983, ApJ, 272, 196
Adelman S. J., 1973, ApJ, 183, 95
Alfven H., Alfvén H., Fälthammar C., 1963, Cosmical Electrodynamics: Fundamental Principles, Clarendon Press, London
Ammler-von Eiff M., Reiners A., 2012, A&A, 542, A116
Aurière M., 2003, in Magnetism and Activity of the Sun and Stars, EDP Sciences, France, p. 105
Babcock H., 1947, ApJ, 105, 105
Babcock H., 1949, The Observatory, 69, 191
Babcock H. W., 1958, ApJS, 3, 141
Babcock H. W., 1960, ApJ, 132, 521
Bagnulo S., Landolfi M., Mathys G., Landi Degl'Innocenti M., 2000, A&A, 358, 929
Bagnulo S., Degl'Innocenti M. L., Landolfi M., Mathys G., 2002, A&A, 394, 1023
Baliunas S. A. et al., 1995, ApJ, 438, 269
Balona L. A., Abedigamba O. P., 2016, MNRAS, 461, 497
Baluev R. V., 2008, MNRAS, 385, 1279

Barnes J., Cameron A. C., Donati J.-F., James D., Marsden S., Petit P., 2005, MNRAS, 357, L1
Berdyugina S. V., 2005, Living Rev. Sol. Phys., 2, 8
Blazère A., Petit P., Neiner C., Folsom C., Kochukhov O., Mathis S., Deal M., Landstreet J., 2020, MNRAS, 492, 5794
Bothmer V., Daglis I., 2007, Space Weather: Physics and Effects, Springer Praxis Books. Springer-Verlag, Berlin
Braithwaite J., 2009, MNRAS, 397, 763
Braithwaite J., Nordlund Å., 2006, A&A, 450, 1077
Braithwaite J., Spruit H. C., 2004, Nature, 431, 819
Brandenburg A., Subramanian K., 2005, Phys. Rep., 417, 1
Brown E. et al., 2021, MNRAS, 501, 3981
Brun A. S., Browning M. K., Toomre J., 2005, ApJ, 629, 461
Bruntt H. et al., 2010, A&A, 512, A55
Burnette A. B., Canfield R. C., Pevtsov A. A., 2004, ApJ, 606, 565
Casagrande L., Schönrich R., Asplund M., Cassisi S., Ramírez I., Melendez J., Bensby T., Feltzing S., 2011, A&A, 530, A138
Charbonneau P., MacGregor K. B., 2001, ApJ, 559, 1094
Cowling T., 1945, MNRAS, 105, 166
Cowling T., 1957, Magnetohydrodynamics, Interscience Tracts on Physics and Astronomy. Interscience Publishers, London
Deutsch A. J., 1958, in Lehnert B., ed., Electromagnetic Phenomena in Cosmical Physics, Cambridge University Press, Cambridge, p. 209
Deutsch A. J., 1970, ApJ, 159, 985
Donati J.-F., Brown S., 1997, A&A, 326, 1135
Donati J.-F., Semel M., Rees D., 1992, A&A, 265, 669
Donati J.-F., Semel M., Carter B. D., Rees D., Cameron A. C., 1997, MNRAS, 291, 658
Donati J.-F., Mengel M., Carter B., Marsden S., Collier Cameron A., Wichmann R., 2000, MNRAS, 316, 699
Donati J.-F., Catala C., Landstreet J., Petit P., 2006a, in Casini R., Lites B. W., eds, ASP Conf. Ser. Vol. 358, Solar Polarization 4. Astron. Soc. Pac., San Francisco, p. 362
Donati J.-F. et al., 2006b, MNRAS, 370, 629
Donati J.-F. et al., 2008, MNRAS, 385, 1179
Dudorov A. E., Khaibrakhmanov S. A., 2015, Adv. Space Res., 55, 843
Falk A. E., Wehlau W. H., 1974, ApJ, 192, 409
Fares R. et al., 2009, MNRAS, 398, 1383
Fares R. et al., 2012, MNRAS, 423, 1006
Ferrero R. F., Gouttebroze P., Catalano S., Marilli E., Bruhweiler F., Kondo Y., Van Der Hucht K., Talavera A., 1995, ApJ, 439, 1011
Folsom C. P. et al., 2016, MNRAS, 457, 580
Folsom C. et al., 2018, MNRAS, 474, 4956
Fossati L. et al., 2015, A&A, 582, A45
Gaia collaboration, 2018, A&A, 616, A1
Gilman P. A., 1980, Differential Rotation in Stars with Convection Zones. Springer-Verlag, Berlin, p. 19
Glagolevskij Y., , 2003, in Piskunov N.et al. eds, Proc. IAU Symp. Modelling of Stellar Atmospheres. Cambridge University Press, Cambridge, UK, p. A3
Godolt M., Tosi N., Stracke B., Grenfell J. L., Ruedas T., Spohn T., Rauer H., 2019, A&A, 625, A12
Gray D., 1982, ApJ, 258, 201
Gray D., 2005, The Observation and Analysis of Stellar Photospheres. Cambridge Univ. Press, Cambridge
Grunhut J. et al., 2016, MNRAS, 465, 2432
Hall D. S., 1972, PASP, 84, 323
Hall J. C., 2008, Living Rev. Sol. Phys., 5, 1
Hanslmeier A., 2007, The Sun and Space Weather, Astrophysics and Space Science Library. Springer, Netherlands
Hatzes A., 1998, MNRAS, 299, 403
Järvinen S. et al., 2015, A&A, 574, A25
Jeffers S. et al., 2018, MNRAS, 479, 5266
Johnson H., Morgan W., 1953, ApJ, 117, 313
Kaltenegger L., Lin Z., 2021, ApJ, 909, L2
Knutson H. A., Howard A. W., Isaacson H., 2010, ApJ, 720, 1569
Kochukhov O., Lundin A., Romanyuk I., Kudryavtsev D., 2011, ApJ, 726, 24
Krause F., Radler K., 1980, Mean-field Magnetohydrodynamics and Dynamo Theory, Pergamon Press, Oxford, UK
Kurtz D., 1989, MNRAS, 238, 261
Lammer H., Khodachenko M., 2014, Characterizing Stellar and Exoplanetary Environments, Astrophysics and Space Science Library. Springer International Publishing, Switzerland
Landstreet J., Mathys G., 2000, A&A, 359, 213
Lehmann L., Hussain G., Jardine M., Mackay D., Vidotto A., 2019, MNRAS, 483, 5246
Leone F., Catanzaro G., 2001, A&A, 365, 118
Leroy J., 1995, A&AS, 114, 79
Lignières F., Petit P., Böhm T., Aurière M., 2009, A&A, 500, L41
Linsky J., 2019, Host Stars and their Effects on Exoplanet Atmospheres: An Introductory Overview, Lecture Notes in Physics. Springer International Publishing, Switzerland
Marsden S., Carter B., Donati J.-F., 2005, in Favata F.ed., 13th Cambridge Workshop on Cool Stars, Stellar Systems and the Sun. ESA, Noordwijk, Netherlands, p. 799
Marsden S. C., Mengel M. W., Donati F., Carter B. D., Semel M., Petit P., 2006, in Casini R.,Lites B., eds Solar Polarization 4. ASP, San Francisco, p. 401
Marsden S. et al., 2014, MNRAS, 444, 3517
Mason B. D., et al., 2001, AJ, 122, 3466
Mathis S., Zahn J.-P., 2005, A&A, 440, 653
Mathys G., 1989, Fundam. Cosm. Phys., 13, 143
Mathys G., 1993, in Dworetsky, M., Castelli, F.,Faraggiana R, eds, Peculiar versus normal phenomena in A-type and related stars. Cambridge University Press, Cambridge, UK, p. 232
Mathys G., 1995, A&A, 293, 733
Mathys G., Hubrig S., 1997, A&AS, 124, 475
Mestel L., 1966, MNRAS, 133, 265
Mestel L., 1967, in Magnetic and Related Stars. Mono Book Corporation, California, p. 101
Mestel L., 2012, Stellar Magnetism. Oxford Univ. Press, Oxford
Mestel L., Spitzer L., 1956, MNRAS, 116, 503
Moffatt H., 1978, Magnetic Field Generation in Electrically Conducting Fluids. Cambridge Univ. Press, Cambridge
Moffatt K., Dormy E., 2019, Self-Exciting Fluid Dynamos, Cambridge Texts in Applied Mathematics. Cambridge Univ. Press, Cambridge
Morin J., Donati J.-F., Petit P., Delfosse X., Forveille T., Jardine M., 2010, MNRAS, 407, 2269
Moss D., 2001, in Wickramasinghe D., et al., eds, Magnetic Fields Across the Hertzsprung-Russell Diagram. ASP, San Francisco, p. 305
Mullan D., 1972, ApL, 12, 13
Neiner C., Wade G., Sikora J., 2017, MNRAS, 468, L46
Noyes R., Hartmann L., Baliunas S., Duncan D., Vaughan A., 1984, ApJ, 279, 763
Oetken L., 1977, Astron. Nachr., 298, 197
Palubski I. Z., Shields A. L., Deitrick R., 2020, ApJ, 890, 30
Parker E. N., 1955, ApJ, 122, 293
Parker E., 1979, Cosmical Magnetic Fields: Their Origin and Their Activity. OUP, Oxford, UK
Parker E., 1987, Sol. Phys., 110, 11
Perryman M., 2018, The Exoplanet Handbook. Cambridge Univ. Press, Cambridge
Petit P., Donati J.-F., Collier Cameron A., 2002, MNRAS, 334, 374
Petit P. et al., 2008, MNRAS, 388, 80
Petit P. et al., 2010, A&A, 523, A41
Petit P., Louge T., Théado S., Paletou F., Manset N., Morin J., Marsden S., Jeffers S., 2014, PASP, 126, 469
Pettersen B., 1989, Sol. Phys., 121, 299
Pevtsov A. A., Canfield R. C., Metcalf T. R., 1994, ApJ, 425, L117
Piskunov N., Rice J., 1993, PASP, 105, 1415
Prendergast K. H., 1956, ApJ, 123, 498
Preston G., 1967a, in Cameron R., ed., Studies of Stellar Magnetism - Past, Present, and Future, in The Magnetic and Related Stars. Mono Book Corporation, California, p. 3
Preston G. W., 1967b, ApJ, 150, 547

Preston G. W., 1969, ApJ, 158, 1081
Preston G. W., Sturch C., 1967, in Magnetic and Related Stars. Mono Book Corporation, California, p. 111
Pyper D. M., 1969, ApJS, 18, 347
Reiners A., 2012, Living Rev. Sol. Phys., 9, 1
Reiners A., Schmitt J., 2003a, A&A, 398, 647
Reiners A., Schmitt J., 2003b, A&A, 412, 813
Renson P., Manfroid J., 2009, A&A, 498, 961
Roberts P. H., 1992, Dynamo Theory. Springer-Verlag, Berlin, p. 237
Rüdiger G., 1989, Differential Rotation and Stellar Convection: Sun and Solar-type Stars, Fluid Mechanics of Astrophysics and Geophysics. Gordon and Breach Science Publishers, New York
Rushby A. J., Shields A. L., Joshi M., 2019, ApJ, 887, 29
Ryabchikova T., Piskunov N., Kurucz R., Stempels H., Heiter U., Pakhomov Y., Barklem P. S., 2015, Phys. Scr., 90, 054005
Samus N., Kazarovets E., Durlevich O., Kireeva N., Pastukhova E., 2017, Astron. Rep., 61, 80
Schatzman E., 1962, Ann. Astrophys., 25, 18
Schmitt J., Golub L., Harnden F. Jr, Maxson C., Rosner R., Vaiana G., 1985, ApJ, 290, 307
Schneider F. R., Ohlmann S. T., Podsiadlowski P., Röpke F. K., Balbus S. A., Pakmor R., Springel V., 2019, Nature, 574, 211
Schwarzschild M., 1950, ApJ, 112, 222
Schwieterman E. W., Reinhard C. T., Olson S. L., Ozaki K., Harman C. E., Hong P. K., Lyons T. W., 2019, ApJ, 874, 9
Seach J., Marsden S., Carter B., Neiner C., Folsom C., Mengel M., Oksala M., Buysschaert B., 2020, MNRAS, 494, 5682 (Paper 1)
Seach J., Marsden S., Carter B., Evensberget D., Folsom C., Neiner C., Mengel M., 2022, MNRAS, 509, 5117 (Paper 2)
Segura A., Krelove K., Kasting J. F., Sommerlatt D., Meadows V., Crisp D., Cohen M., Mlawer E., 2003, Astrobiology, 3, 689
Semel M., 1989, A&A, 225, 456
Sikora J., Wade G., Power J., Neiner C., 2019, MNRAS, 483, 2300
Simon T., Ayres T. R., Redfield S., Linsky J. L., 2002, ApJ, 579, 800
Singh A. K., Bhargawa A., Siingh D., Singh R. P., 2021, Geosciences, 11, 286
Spitzer L., 1958, in Lehnert B., ed, Electromagnetic Phenomena in Cosmical Physics. Cambridge University Press, London, p. 169
Spruit H., 1999, A&A, 349, 189
Spruit H., 2002, A&A, 381, 923
Steenbeck M., Krause F., 1969, Astron. Nachr., 291, 49
Steinitz R., 1967, in Cameron R., ed., The Magnetic Oblique Rotator, in The Magnetic and Related Stars. Mono Book Corporation, California, p. 83
Stibbs D., 1950, MNRAS, 110, 395
Stift M., 1975, MNRAS, 172, 133
Strassmeier K. G., 2009, A&AR, 17, 251
Tayler R., 1973, MNRAS, 161, 365
Thomson-Paressant K., Neiner C., Zwintz K., Escorza A., 2021, MNRAS, 500, 1992
VanderPlas J. T., 2018, ApJS, 236, 16
Vaughan A. H., Preston G. W., Wilson O. C., 1978, PASP, 90, 267
Wade G., Donati J.-F., Landstreet J., Shorlin S., 2000, MNRAS, 313, 851
Walter F., 1983, ApJ, 274, 794
Walter F., Schrijver C., 1987, in Araki H., et al., eds, Cool Stars, Stellar Systems, and the Sun. Springer, London, p. 262
Wolff S. C., Wolff R. J., 1970, ApJ, 160, 1049
Wolff S. C., Heasley J., Varsik J., 1985, PASP, 97, 707
Wolff S. C., Boesgaard A. M., Simon T., 1986, ApJ, 310, 360
Wright G., 1973, MNRAS, 162, 339
Zahn J.-P., 2010, in Neiner C., et al. eds, Active OB stars: structure, evolution, mass loss, and critical limits, Cambridge University Press, Cambridge, UK, p. 14
Zechmeister M., Kürster M., 2009, A&A, 496, 577
Zeldovich I. B., Ruzmaikin A. A., Sokolov D. D., 1983, Magnetic Fields in Astrophysics. Gordon & Breach,, New York
Zerbi F. et al., 1997, MNRAS, 292, 43
Zwintz K. et al., 2020, A&A, 643, A110

APPENDIX A: ADDITIONAL DATA

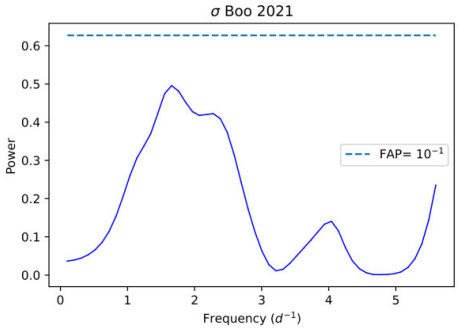

Figure A1. GLS periodogram a time-series of mean nightly *S*-index measurements for σ Boo spanning 11 d from 2021 May 18–28 (Table 2). The figure shows the power versus frequency and FAP, with no peak visible to the 10^{-1} level.

Table A1. Journal of observations for σ Boo in 2021 for the individual spectra. The columns are the same as Table 2.

Date (UT)	Time (UT)	Mid-HJD 2459000+	Rot. cycle	SNR Stokes *I*	RV (km s^{-1})	B_l (G)	N_l (G)	*S*-index	LSD lines used
May 18	06:46:45	352.78642	0.0000	714	0.29	− 1.5 ± 1.5	− 0.9 ± 1.5	0.257	17 654
May 18	06:57:27	352.79386	0.0009	715	0.29	− 0.4 ± 0.5	0.0 ± 0.5	0.256	17 654
May 18	07:08:10	352.80130	0.0018	714	0.30	− 3.0 ± 1.5	− 0.7 ± 1.5	0.253	17 654
May 18	07:18:53	352.80874	0.0027	717	0.29	− 0.6 ± 0.5	0.1 ± 0.5	0.262	17 654
May 18	07:29:36	352.81619	0.0035	717	0.28	− 2.4 ± 1.4	− 1.6 ± 1.4	0.256	17 654
May 18	07:40:20	352.82360	0.0044	714	0.29	− 1.4 ± 0.5	0.4 ± 0.5	0.258	17 654
May 18	07:52:04	352.83179	0.0054	696	0.29	− 3.5 ± 1.5	1.4 ± 1.5	0.247	17 654
May 18	08:02:47	352.83923	0.0063	713	0.31	− 3.8 ± 1.2	− 0.3 ± 1.2	0.262	17 654
May 18	08:13:30	352.84667	0.0072	711	0.30	− 1.2 ± 0.8	0.5 ± 0.8	0.262	17 654
May 18	08:24:13	352.85411	0.0081	715	0.30	− 1.5 ± 0.6	0.0 ± 0.6	0.251	17 654
May 18	08:34:56	352.86155	0.0089	715	0.30	− 1.2 ± 0.5	0.4 ± 0.6	0.255	17 654
May 18	08:45:39	352.86900	0.0098	711	0.30	− 1.3 ± 0.8	1.2 ± 0.8	0.260	17 654
May 19	06:18:56	353.76710	0.1167	719	0.32	− 3.1 ± 1.4	0.3 ± 1.4	0.251	17 653
May 19	06:29:40	353.77455	0.1176	723	0.32	− 2.2 ± 0.6	0.3 ± 0.6	0.263	17 652
May 19	06:40:24	353.78200	0.1185	722	0.32	− 1.6 ± 0.5	0.8 ± 0.5	0.258	17 652
May 19	06:51:08	353.78946	0.1194	726	0.33	− 1.0 ± 0.8	− 0.6 ± 0.8	0.255	17 652
May 19	07:01:52	353.79691	0.1203	731	0.33	− 1.6 ± 0.5	0.4 ± 0.5	0.259	17 652
May 19	07:12:37	353.80437	0.1212	731	0.34	0.7 ± 0.7	− 0.5 ± 0.7	0.253	17 653
May 19	07:24:12	353.81242	0.1221	731	0.34	0.6 ± 0.5	0.6 ± 0.5	0.255	17 652
May 19	07:35:00	353.81992	0.1230	731	0.33	− 0.6 ± 0.5	0.1 ± 0.5	0.261	17 652
May 19	07:45:47	353.82741	0.1240	733	0.34	1.3 ± 1.0	0.4 ± 1.0	0.254	17 652
May 19	07:56:31	353.83487	0.1248	729	0.34	− 2.5 ± 1.3	0.5 ± 1.3	0.257	17 652
May 19	08:07:15	353.84232	0.1257	728	0.36	− 0.8 ± 1.5	0.0 ± 0.5	0.261	17 652
May 19	08:18:04	353.84982	0.1266	711	0.36	− 1.1 ± 0.5	0.1 ± 0.5	0.218	17 652
May 20	06:46:28	354.78620	0.2381	731	0.35	− 1.5 ± 0.9	0.0 ± 0.9	0.256	17 653
May 20	06:57:13	354.79367	0.2390	724	0.35	− 0.5 ± 0.6	0.5 ± 0.6	0.256	17 653
May 20	07:07:57	354.80112	0.2398	726	0.34	2.4 ± 1.6	− 1.4 ± 1.6	0.257	17 652
May 20	07:18:43	354.80860	0.2407	724	0.34	− 1.4 ± 1.0	0.5 ± 1.0	0.258	17 652
May 20	07:29:26	354.81604	0.2416	727	0.35	− 1.1 ± 0.7	0.0 ± 0.7	0.257	17 653
May 20	07:40:12	354.82350	0.2425	732	0.34	− 0.5 ± 0.5	− 0.1 ± 0.5	0.258	17 653
May 20	07:51:43	354.83152	0.2435	728	0.35	− 1.5 ± 0.6	− 0.2 ± 0.6	0.259	17 653
May 20	08:02:27	354.83897	0.2444	722	0.34	− 1.1 ± 0.6	− 1.1 ± 0.6	0.257	17 652
May 20	08:13:10	354.84641	0.2452	730	0.33	− 0.9 ± 0.7	0.0 ± 0.7	0.258	17 652
May 20	08:23:54	354.85386	0.2461	741	0.34	− 1.2 ± 0.5	− 0.1 ± 0.5	0.261	17 652
May 20	08:34:40	354.86134	0.2470	736	0.33	− 0.9 ± 0.6	− 1.3 ± 0.6	0.259	17 652
May 20	08:45:23	354.86878	0.2479	737	0.33	− 2.1 ± 0.6	− 0.8 ± 0.6	0.259	17 651
May 21	05:30:14	355.73325	0.3508	657	0.31	− 3.0 ± 1.5	0.8 ± 1.5	0.249	17 651
May 21	05:41:00	355.74073	0.3517	655	0.31	− 2.0 ± 0.8	− 0.3 ± 0.8	0.249	17 651
May 21	05:51:44	355.74817	0.3526	658	0.31	− 0.4 ± 0.6	− 0.1 ± 0.6	0.254	17 651
May 21	06:02:27	355.75562	0.3535	653	0.30	− 2.7 ± 1.6	− 1.9 ± 1.6	0.255	17 652
May 21	06:13:10	355.76306	0.3544	646	0.31	2.2 ± 1.5	− 1.6 ± 1.5	0.253	17 652
May 21	06:23:53	355.77051	0.3552	643	0.32	− 2.8 ± 1.2	0.1 ± 1.2	0.256	17 652
May 21	06:35:59	355.77890	0.3562	576	0.33	− 4.3 ± 2.6	0.1 ± 2.6	0.258	17 652
May 21	06:52:02	355.79005	0.3576	582	0.32	− 3.6 ± 1.7	2.3 ± 1.7	0.255	17 652
May 21	07:02:45	355.79749	0.3585	608	0.32	− 2.5 ± 0.9	0.9 ± 0.9	0.258	17 652
May 21	07:13:29	355.80494	0.3593	613	0.31	− 1.5 ± 1.6	− 0.5 ± 1.6	0.256	17 651
May 21	07:24:12	355.81239	0.3602	612	0.33	− 4.5 ± 1.8	− 0.9 ± 1.9	0.256	17 651
May 21	07:34:55	355.81983	0.3611	610	0.33	− 3.6 ± 3.3	− 3.4 ± 3.3	0.253	17 652
May 22	05:31:52	356.73437	0.4700	610	0.38	− 3.3 ± 2.2	− 2.4 ± 2.3	0.255	17 652
May 22	05:42:36	356.74181	0.4709	622	0.36	− 3.4 ± 1.8	0.9 ± 1.8	0.235	17 652
May 22	05:53:19	356.74926	0.4718	583	0.37	− 2.2 ± 1.3	1.8 ± 1.3	0.256	17 652
May 24	07:03:08	358.79770	0.7156	618	0.35	− 1.6 ± 0.9	− 0.6 ± 0.9	0.260	17 650
May 24	07:13:52	358.80517	0.7165	659	0.35	− 1.4 ± 0.6	− 0.3 ± 0.6	0.274	17 650
May 24	07:24:36	358.81261	0.7174	671	0.34	− 3.0 ± 1.2	1.1 ± 1.2	0.257	17 650
May 24	07:35:19	358.82006	0.7183	668	0.35	− 1.2 ± 0.6	0.0 ± 0.6	0.262	17 650
May 24	07:46:02	358.82750	0.7192	666	0.35	− 4.1 ± 0.6	− 0.5 ± 1.6	0.264	17 650
May 24	07:56:46	358.83495	0.7201	660	0.35	− 1.3 ± 0.6	− 0.7 ± 0.6	0.256	17 650
May 24	10:06:47	358.92524	0.7308	671	0.35	1.4 ± 1.1	0.7 ± 1.1	0.253	17 651
May 24	10:17:31	358.93269	0.7317	671	0.34	− 1.5 ± 0.9	0.6 ± 0.9	0.257	17 650
May 24	10:28:14	358.94013	0.7326	672	0.34	− 1.2 ± 0.9	0.2 ± 0.9	0.252	17 650
May 24	10:38:57	358.94757	0.7335	673	0.34	− 1.9 ± 1.1	− 1.5 ± 1.1	0.267	17 650
May 24	10:49:40	358.95502	0.7344	661	0.36	− 2.8 ± 1.4	0.3 ± 1.4	0.259	17 650

Table A1 *– continued*

Date (UT)	Time (UT)	Mid-HJD 2459000+	Rot. cycle	SNR Stokes *I*	RV (km s^{-1})	B_l (G)	N_l (G)	*S*-index	LSD lines used
May 24	11:00:23	358.96246	0.7352	671	0.36	0.2 ± 0.6	0.7 ± 0.6	0.260	17 650
May 25	07:04:24	359.79856	0.8348	657	0.34	1.4 ± 1.6	−1.4 ± 1.6	0.251	17 650
May 25	07:15:07	359.80601	0.8357	651	0.35	1.4 ± 1.7	0.3 ± 1.7	0.255	17 650
May 25	07:25:54	359.81349	0.8366	654	0.34	−1.4 ± 0.6	0.0 ± 0.6	0.255	17 650
May 25	07:36:38	359.82095	0.8374	659	0.34	−1.7 ± 1.3	−0.1 ± 1.3	0.245	17 650
May 25	07:47:21	359.82839	0.8383	659	0.35	−2.7 ± 1.0	−0.3 ± 1.0	0.254	17 650
May 25	07:58:08	359.83588	0.8392	658	0.36	1.7 ± 1.5	0.6 ± 1.5	0.261	17 650
May 26	09:15:13	360.88939	0.9646	671	0.30	1.6 ± 1.3	−0.1 ± 1.3	0.251	17 650
May 26	09:25:56	360.89683	0.9655	675	0.30	−1.1 ± 0.8	0.8 ± 0.8	0.251	17 650
May 26	09:36:39	360.90428	0.9664	673	0.31	0.9 ± 0.6	−0.2 ± 0.6	0.256	17 650
May 26	09:47:22	360.91171	0.9673	678	0.30	−0.5 ± 0.5	0.1 ± 0.5	0.254	17 650
May 26	09:58:00	360.91916	0.9682	681	0.30	−0.6 ± 0.6	0.0 ± 0.6	0.255	17 650
May 26	10:08:48	360.92660	0.9691	682	0.30	−1.8 ± 1.4	−0.8 ± 1.4	0.254	17 650
May 26	10:20:33	360.93475	0.9700	684	0.30	−0.6 ± 0.5	0.0 ± 0.5	0.254	17 649
May 26	10:31:16	360.94220	0.9709	687	0.31	1.0 ± 1.0	−0.3 ± 1.0	0.251	17 650
May 26	10:41:59	360.94965	0.9718	687	0.31	2.8 ± 1.4	−1.3 ± 1.4	0.255	17 650
May 26	10:52:43	360.95709	0.9727	679	0.32	−0.8 ± 0.5	0.6 ± 0.5	0.253	17 650
May 26	11:03:26	360.91916	0.9736	675	0.31	−2.6 ± 1.5	−0.1 ± 1.5	0.255	17 650
May 26	11:14:09	360.97198	0.9745	681	0.32	−1.3 ± 0.5	−0.5 ± 0.5	0.252	17 649
May 27	05:29:08	361.73236	1.0650	710	0.36	−1.7 ± 1.4	−1.1 ± 1.4	0.242	17 649
May 27	05:39:52	361.73982	1.0659	713	0.35	−0.6 ± 0.5	−0.6 ± 0.5	0.254	17 648
May 27	05:50:36	361.74727	1.0668	718	0.36	−0.6 ± 0.5	−0.4 ± 0.5	0.265	17 648
May 27	06:01:19	361.75471	1.0677	715	0.36	1.8 ± 1.3	−0.5 ± 1.3	0.256	17 648
May 27	06:12:02	361.76216	1.0685	713	0.37	−2.0 ± 1.3	−0.9 ± 1.4	0.294	17 648
May 27	06:22:45	361.76960	1.0694	720	0.35	−1.5 ± 1.0	0.0 ± 1.0	0.266	17 648
May 27	06:34:11	361.77753	1.0704	719	0.35	−1.6 ± 1.3	−0.9 ± 1.3	0.273	17 648
May 27	06:44:54	361.78498	1.0713	472	0.35	−0.5 ± 1.5	1.2 ± 1.5	0.401	17 648
May 27	06:55:37	361.79242	1.0721	719	0.37	−0.7 ± 0.6	−0.6 ± 0.6	0.259	17 648
May 27	07:06:24	361.79991	1.0730	718	0.36	−0.5 ± 0.5	0.0 ± 0.5	0.258	17 648
May 27	07:17:07	361.80736	1.0739	722	0.36	1.3 ± 1.3	0.2 ± 1.2	0.245	17 648
May 27	07:27:51	361.81481	1.0748	724	0.36	−2.1 ± 0.9	1.4 ± 0.9	0.254	17 648
May 28	05:32:29	362.73466	1.1843	704	0.32	−1.6 ± 1.2	−0.9 ± 1.2	0.258	17 649
May 28	05:43:12	362.74212	1.1852	684	0.32	−5.0 ± 1.6	−1.3 ± 1.6	0.289	17 649
May 28	05:53:56	362.74956	1.1861	701	0.32	−1.0 ± 0.5	−0.9 ± 0.5	0.255	17 650
May 28	06:04:40	362.75701	1.1870	704	0.32	1.2 ± 0.8	−0.2 ± 0.8	0.256	17 650
May 28	06:15:23	362.76446	1.1879	434	0.31	2.2 ± 1.0	−2.5 ± 1.0	NA	17 646
May 28	06:26:06	362.77190	1.1887	712	0.33	−1.5 ± 0.6	−0.5 ± 0.6	0.259	17 650
May 28	06:37:28	362.77979	1.1897	709	0.33	−1.7 ± 0.6	−0.5 ± 0.6	0.256	17 650
May 28	06:48:14	362.78728	1.1906	709	0.33	−0.8 ± 0.5	−0.3 ± 0.5	0.259	17 649
May 28	06:58:58	362.79473	1.1915	708	0.33	−0.2 ± 0.5	−0.4 ± 0.5	0.260	17 649
May 28	07:09:42	362.80218	1.1924	704	0.33	−1.2 ± 0.5	−0.1 ± 0.5	0.246	17 649
May 28	07:20:30	362.80968	1.1932	698	0.32	−0.8 ± 0.5	−0.2 ± 0.5	0.250	17 650
May 28	07:31:13	362.81712	1.1941	694	0.32	0.2 ± 0.5	−0.3 ± 0.5	0.241	17 650

This paper has been typeset from a TEX/LATEX file prepared by the author.

4.3 Future Research

This paper has identified two areas of research will will benefit from follow up. Firstly, magnetic mapping of β CrB using linear polarisation will allow a more complete characterisation of the magnetic field to be obtained. Secondly, it is important to obtain additional spectropolarimetric observations of σ Boo in order to fully characterise the magnetic field as either a dynamo or weak fossil.

4.4 Additional Comments

Information in this section provides additional comments on Paper 3.

A clarification has been added here to more accurately describe the ZDI process as described in Paper 3, section 4.2 on page 121 of the thesis. The revised sentence reads: ZDI involves an iterative procedure that typically begins with a zero magnetic field, and parameters are adjusted to optimize the fit (parametrized by reduced χ^2) of the model compared to observations.

A further note on the validity of the weak field approximation for analysis of β CrB is presented here for extra clarity. The weak field approximation is typically valid for magnetic field strengths up to approximately 1kG (Bagnulo et al., 2002a). Therefore, our magnetic field strengths of approximately 4 kG are considered as sufficiently close to the upper limit to be acceptable in our case of magnetic mapping for β CrB.

An incorrect spelling was noted in Paper 3 section 6.1 on page 128 of thesis. The correct sentence should read: The δ Scuti star HD 41641 (A5III) was found to contain a complex fossil field (Thomson-Paressant et al., 2021) B_l that varied from -178 $\pm$ 112 G to 182 $\pm$ 273 G, and a simple dipole or dipole plus quadrupolar configuration did not fit the data.

CHAPTER 5

DISCUSSION AND CONCLUSION

5.1 Discussion

Magnetic fields are an observable feature of many stars, with F-type stars having a special interest in the search for the transition between fossil and dynamo magnetic fields. The transition is not known exactly but is believed to occur in stars around early-to-mid F in spectral type. A summary of the magnetic detections and ZDI maps from the three papers in this thesis is shown in Fig. 5.1. The figure shows there are no detections of a magnetic field in spectral types F0-F2, and detections in every spectral type from F3-F9. The four stars which were imaged using ZDI are placed on the figure to show their location in relation to the full sample studied. From Fig. 5.1 it is seen that the transition between fossil and dynamo magnetic fields may occur as early as spectral type F3.

The nature of the magnetic fields in the snapshot stars from paper 1 cannot be definitely determined from a single nights observation. A simple explanation

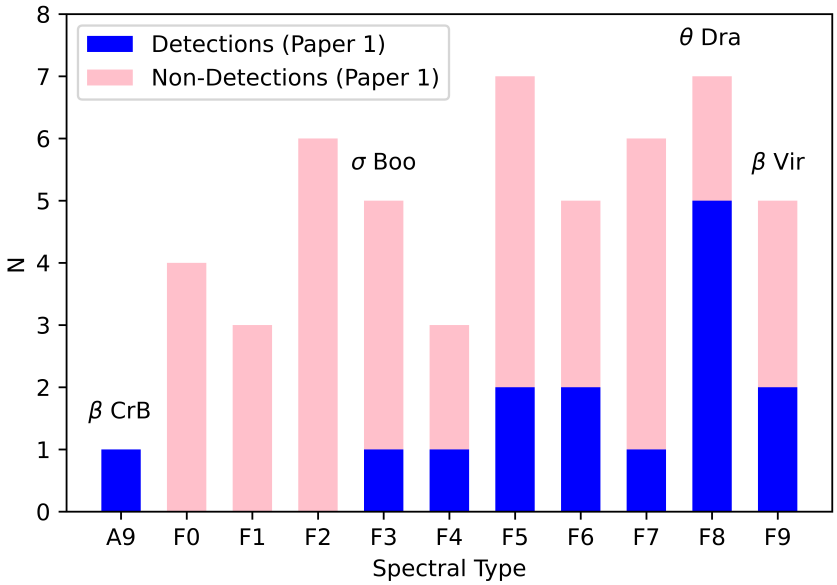

Figure 5.1: Summary of magnetic detections and ZDI maps for stars included in this thesis. The blue histograms indicate the number of stellar magnetic detections for each spectral type from paper 1. The pink histograms indicate the number of stellar non-magnetic detections for each spectral type from paper 1. The four star names on the top of the histograms indicate the spectral types of the stars mapped using ZDI from papers 2 and 3. The lack of magnetic detections from spectral types F0-F2 is obvious.

may be the lack of magnetic detections from spectral types F0-F2 is due to the transition zone being located at F3. The results can be also be interpreted in another way. For example, there are two magnetic detections out of 21 stars observed from spectral types F0-F4. This approximately 10 per cent detection rate is the same as the expected detection rate for fossil fields (Grunhut et al., 2016; Sikora et al., 2019). This highlights the need for further detections and magnetic mapping of early-to-mid F-stars at multiple epochs in order to determine the nature of magnetic fields, and to locate the transition zone.

It remains to be determined if there is a clear boundary between fossil and

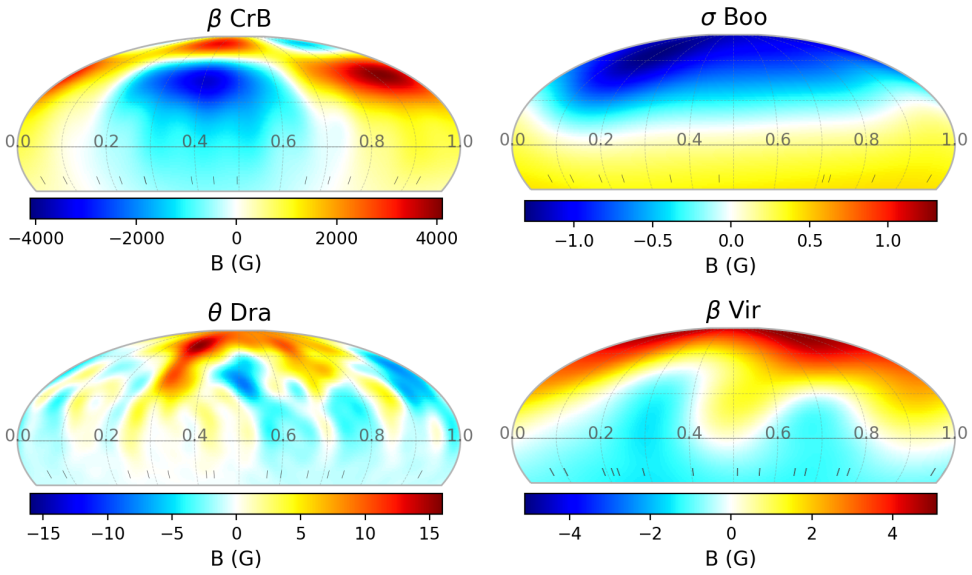

Figure 5.2: Summary of ZDI maps of the large-scale surface radial magnetic fields of all four stars from papers 2 and 3. The dates of the maps are β CrB (A9) 7-24 April 2017, σ Boo (F3V) 18-27 May 2021, θ Dra (F8IV) 06-24 April 2017, and β Vir (F9V) 03-24 April 2017. Map dates correspond to the dates of maximum magnetic field strength. The colour bar at bottom represents the magnetic field strength in Gauss. The radial magnetic fields may be used an inputs for stellar wind modelling.

dynamo fields, or if there are multiple boundaries which depend on stellar parameters like metallicity, rotation rate and age. The recent discovery of hot stars with weak magnetic fields (Lignières et al., 2009; Petit et al., 2010; Neiner et al., 2017) has added a degree of complexity to the search for the transition zone. A larger number of these stars needs to be observed in order to explore the nature of these weak fields, and to determine the range of effective temperatures at which they are found. Theoretical models of stars with shallow outer convection zones (see for example Mullan (1971, 1972); Gilman (1980); Kupka & Montgomery (2002)) need to be further developed to complement observations of fossil fields, weak hot star fields, and dynamo fields around the transition zone.

Mapping the large scale magnetic field topology of stars close to the transition

zone is important for understanding the magnetic topology, and providing constraints of fossil and dynamo models. Fig. 5.1 shows examples of ZDI maps for the four stars imaged in this thesis. The maps show the radial field component which corresponds to the map with maximum magnetic field strength. While the magnetic field scale is different for each map, the figures allows a comparison of the magnetic field topology of the stars. On the hot side of the suspected transition zone, β CrB shows a relatively complex topology for a fossil field, which is more complex than a dipole. In contrast, σ Boo shows a weak field with simple topology. One possible explanation for the simple field is that due to the relatively shallow outer convection zone, rising magnetic flux does not have the ability to twist into complex areas of magnetic field. The surface magnetic field may be expected to be different in stars with shallow outer convection zones compared to cooler stars with deeper outer convection zones. As we move further away from the suspected transition zone to the cooler stars, the magnetic field topology becomes more complex. θ Dra and β Vir show more complex surface fields than σ Boo. There is a difference in the magnetic field complexity between θ Dra and β Vir is that is partly due to the faster rotation for θ Dra which allows a greater resolution of surface elements.

The degree of complexity of the magnetic field is not sufficient alone to classify a stellar field as either fossil or dynamo, as evidenced by the complex field of β CrB (Seach et al., 2022a). Multi-epoch spectropolarimetry is required to conclusively classify the nature of the field. Definitive evidence of the transition from fossil to dynamo field is not able to be determined from single-epoch magnetic maps, and additional maps are required across different epochs to provide evidence for the type of magnetic fields present. Additionally, information is lacking on how stellar mass, rotation and age correlate with the emergence of dynamo fields in stars with shallow convection zones.

Besides σ Boo, which has been identified as a prime target for magnetic mapping located close to the suspected transition zone, there are two other F-stars from this research which are of particular interest. The F8V star h Draconis shows a magnetic signal which is consistent with a dynamo magnetic field, however the magnetic signal is unusually strong for an F-star. The star is possibly a δ Scuti type (Hoffleit, 1991), and further magnetic mapping would be valuable to fully understand the nature of its magnetism. Another interesting star identified from paper 1 is τ Piscis Austrinus (F6V) which is a single star showing a marginal magnetic detection. While this star has a spectral type later than the suspected transition zone, it nevertheless would provide a good target for ZDI mapping since no stars have been mapped from spectral types F4-F6. Imaging this star will help fill a gap in our knowledge of magnetism in mid F-stars.

Previous studies have indicated that chromospheric and magnetic cycles in F-type stars are short (García et al., 2010; Lopes et al., 2015; Mittag et al., 2019) compared to solar values of 11 years and 22 years respectively (Charbonneau, 2014). This thesis adds further evidence for short cycles in F-stars with the finding of a possible chromospheric cycle of 83 ± 14 d for β Vir and 43 ± 2 d for θ Dra. It should be noted that the cycle determinations are subject to uncertainty due to the short baseline of observations however, the values are considered worth reporting because they are consistent with other literature determinations of possible short activity cycles in F-type stars. This highlights the value of F-type stars in studies of magnetic cycles due to the short time frame required for observations. A complete magnetic cycle may be observed in less than a year, in contrast to decades which are required for the Sun and later spectral types. For example short magnetic cycles of 120 d for τ Boo (F7V) (Jeffers et al., 2018) compared to a much longer magnetic cycle of 14 years for 61 Cyg A (K5V) (Boro Saikia et al., 2018b).

The modelling of stellar winds is a growing area of astrophysics research, which is important for studies of exoplanet habitability, and the space weather conditions affecting the Earth. Magnetic maps produced in this thesis provide inputs for wind models for two late F-type stars. The winds surrounding β Vir and θ Dra show differences related to the strength and orientation of the reconstructed surface radial magnetic field. The average wind pressure surrounding β Vir at the three observed epochs falls within the range of space weather conditions observed at Earth. In contrast, θ Dra produces a wind pressure an order of magnitude stronger than the Sun's wind pressure, however this does not strongly affect the size of the magnetosphere. In comparison, stellar wind modelling of τ Boo (F7V) by Nicholson et al. (2016) showed different results than the two late F-stars in this research, with a mass loss of 1-2 orders of magnitude greater than β Vir and θ Dra respectively. This thesis identifies a range of stellar wind pressures surrounding two late F-stars, and this may indicate wind pressures surrounding some F-stars are strong enough to have detrimental effects on the exoplanet atmospheres, and may affect the habitability of exoplanets (See et al., 2014; Vidotto et al., 2015; Linsky, 2019).

5.2 Conclusions

This thesis explores two questions. Firstly, what changes occur, if any, in the strength and detectability of the magnetic fields of F-type stars across spectral types from F0-F9? Secondly, how does the surface magnetic topology differ between early and late F-stars? These results indicate that a transition between fossil and dynamo magnetic fields may occur as early as F3 based on the magnetic snapshot survey of 53 F-type stars. The detected magnetic fields are weak with B_l ranging from 0.3 ± 0.1 G to 8.3 ± 0.9 G, and there is no correlation between

magnetic field strength and stellar parameters except for a positive correlation between Stokes V amplitude and B_l. The second question which is addressed is; how does the surface magnetic topology differ between early and late F-stars? This ZDI mapping finds the surface magnetic field of the early F-star σ Boo (F3V) shows a relatively simple topography, in contrast to the late F-stars θ Dra (F8IV) and β Vir (F9V). A faster rotation is likely the cause of the more complex magnetic field in θ Dra compared to the slower rotating β Vir. Magnetic maps can be successfully produced for stars with a weak magnetic field close to the transition between fossil and dynamo magnetic fields. The study of F-stars in this thesis has provided an insight into the remarkable phenomenon of stellar magnetism, and the physical processes which occur in stars with shallow outer convection zones.

5.3 Future Work

Suggested future work to extend the results of this research include; the study of linear polarization for β CrB, and the reconstruction of surface magnetic maps using Stokes U,Q profiles. This will provide constraints on the transverse components of the magnetic field, and possibly allow small-scale magnetic field structures to be revealed. Mapping stellar magnetic fields using all four Stokes parameters is valuable because it provides the most complete description of the magnetic field (Auer et al., 1977; Mathys, 1999). While studies of linear polarisation are valuable for a full description of the vector magnetic fields, observations are more difficult to obtain than circular polarisation due to the weakness of the features and more cancellation of the transverse field over the stellar surface Wade et al. (2000a,b).

Additionally, this research has identified the early F-type star σ Boo (F3V) as

an interesting target for further study of magnetic fields in stars with shallow outer convection zones. σ Boo is a bright single star, with relatively sharp spectral lines, which makes it an attractive target for spectropolarimetry. The single epoch map produced in 2021 is not sufficient to definitely conclude if the magnetic field is a weak fossil or dynamo field. Further magnetic mapping of the surface magnetic field at one additional epoch at least is necessary to classify the type of magnetic field present. Finally, further DI/ZDI studies of early-to-mid F-type stars are required to increase the number magnetic maps for this interesting class of stars, and to provide further constraints on the nature of magnetism in stars with outer convection zones, close to the boundary of fossil and dynamo magnetic fields.

REFERENCES

The references here are for Chapter 1 and 5.

References for the papers are included in reference sections of the papers.

Abt H. A., 2005, ApJ, 629, 507

Abt H. A., 2008a, ApJS, 176, 216

Abt H. A., 2008b, ApJS, 180, 117

Abt H. A., Morrell N. I., 1995, ApJS, 99, 135

Adelman S., 1973, ApJ, 183, 95

Allende Prieto C., Lambert D., 1999, A&A, 352, 555

Alvarado-Gómez J., et al., 2015, A & A, 582, A38

Alvarado-Gómez J., Hussain G., Cohen O., Drake J., Garraffo C., Grunhut J., Gombosi T., 2016a, A&A, 588, A28

Alvarado-Gómez J. D., Hussain G., Cohen O., Drake J., Garraffo C., Grunhut J., Gombosi T., 2016b, A&A, 594, A95

Alvarado-Gómez J. D., et al., 2018, MNRAS, 473, 4326

Ammler-von Eiff M., Guenther E., 2009, A & A, 508, 677

Auer L., Heasley J., House L., 1977, Sol. Phys., 55, 47

Augustson K. C., Brown B. P., Brun A. S., Miesch M. S., Toomre J., 2012, ApJ, 756, 169

Auvergne M., et al., 2009, A&A, 506, 411

Babcock H. W., 1947, ApJ, 105, 105

Babcock H., 1949, the Observatory, 69, 191

Babcock H., 1961, ApJ, 133, 572

Bagnulo S., Szeifert T., Wade G., Landstreet J., Mathys G., 2002a, A & A, 389, 191

Bagnulo S., Degl'Innocenti M. L., Landolfi M., Mathys G., 2002b, A&A, 394, 1023

Bagnulo S., Landolfi M., Landstreet J., Degl'Innocenti E. L., Fossati L., Sterzik M., 2009, PASP, 121, 993

Bailer-Jones C. A., 2011, MNRAS, 411, 435

Baliunas S. L., Vaughan A. H., 1985, Annu. Rev. Astron. Astrophys., 23, 379

Baliunas S., et al., 1995, ApJ, 438, 269

Baliunas S., Nesme-Ribes E., Sokoloff D., Soon W., 1996, ApJ, 460, 848

Baliunas S. L., Donahue R. A., Soon W., Henry G. W., 1998, in Cool stars, stellar systems, and the sun. p. 153

Balona L. A., Abedigamba O. P., 2016, MNRAS, 461, 497

Barban C., et al., 2009, A&A, 506, 51

Barnes A., 1992, J. Geophys. Res. Space Phys., 97, 12105

Barnes J., Collier Cameron A., James D., Donati J.-F., 2001, MNRAS, 324, 231

Barnes J., et al., 2005, MNRAS Letters, 357, L1

Bars M., Lecoanet D., 2019, Fluid Mechanics of Planets and Stars. CISM International Centre for Mechanical Sciences, Springer International Publishing

Batchelor G. K., 1950, Proc. R. Soc. Lond. A. Mathematical and Physical Sciences, 201, 405

Batten A., Fletcher J., 1992, J R Astron Soc Can, 86, 99

Bertelli G., Girardi L., Marigo P., Nasi E., 2008, A& A, 484, 815

Bertelli G., Nasi E., Girardi L., Marigo P., 2009, A & A, 508, 355

Bi S.-L., Basu S., Li L.-H., 2008, ApJ, 673, 1093

Bigelow F. H., 1890, Am. J. Sci., 40, 343

Blackman E. G., Hubbard A., 2014, MNRAS, 442, 1040

Blazère A., Neiner C., Petit P., 2016, MNRAS: Letters, 459, L81

Böhm-Vitense E., 1958, Zeitschrift fur Astrophysik, 46, 108

Böhm-Vitense E., 1989, Introduction to Stellar Astrophysics: Volume 1. Introduction to Stellar Astrophysics, CUP

Böhm-Vitense E., 1992, Introduction to Stellar Astrophysics: Volume 3. Introduction to Stellar Astrophysics, CUP

Böhm T., et al., 2015, A&A, 577, A64

Bond H. E., et al., 2015, ApJ, 813, 106

Born M., 1935, The Restless Universe. Harper and brothers

Boro Saikia S., et al., 2018a, A&A, 616, A108

Boro Saikia S., et al., 2018b, A&A, 620, L11

Borra E. F., Fletcher J., Poeckert R., 1981, ApJ, 247, 569

Borra E. F., Landstreet J. D., Mestel L., 1982, Annu. Rev. Astron. Astrophys., 20, 191

Bothmer V., Daglis I., 2007, Space Weather: Physics and Effects. Springer Praxis Books, Springer Berlin Heidelberg

Boyajian T. S., et al., 2013, ApJ, 771, 40

Boyujian T. S., et al., 2012, ApJ, 7, 101

Brandenburg A., 2005, ApJ, 625, 539

Brandenburg A., Subramanian K., 2005, Phys. Rep., 417, 1

Brandenburg A., Moss D., Rüdiger G., Tuominen I., 1991, Geophys. Astrophys. Fluid Dyn, 61, 179

Brecht S., Lyon J., Fedder J., Hain K., 1981, Geophys. Res. Lett., 8, 397

Brecht S. H., Lyon J. G., Fedder J. A., Hain K., 1982, J. Geophys. Res. Space Phys., 87, 6098

Bromm V., 2013, Reports on Progress in Physics, 76, 112901

Bromm V., Larson R. B., 2004, Annu. Rev. Astron. Astrophys., 42, 79

Bromm V., Coppi P. S., Larson R. B., 1999, APJL, 527, L5

Brown S., Donati J.-F., Rees D., Semel M., 1991, A&A, 250, 463

Brown E., et al., 2021, MNRAS, 501, 3981

Bruning D. H., 1981, ApJ, 248, 274

Bruno R., Carbone V., 2016, Turbulence in the Solar Wind. Springer International Publishing

Bruntt H., et al., 2010a, MNRAS, 405, 1907

Bruntt H., et al., 2010b, A& A, 512, A55

Budding E., Carter B., Mengel M., Slee O., Donati J.-F., 2002, PASA, 19, 527

Bullard E. C., Gellman H., 1954, Philos. Trans. Royal Soc., 247, 213

Carroll T., Strassmeier K., Rice J., Künstler A., 2012, A&A, 548, A95

Carter B., Brown S., Donati J.-F., Rees D., Semel M., 1996, PASA, 13, 150

Carter B., Marsden S., Waite I., 2014, in Proceedings of the 18th Cambridge Workshop on Cool Stars, Stellar Systems, and the Sun. pp 209–216

Casagrande L., Schönrich R., Asplund M., Cassisi S., Ramírez I., Melendez J., Bensby T., Feltzing S., 2011, A& A, 530, A138

Catala C., Donati J.-F., Shkolnik E., Bohlender D., Alecian E., 2007, MNRAS: Letters, 374, L42

Cattaneo F., Hughes D., Weiss N., 1991, MNRAS, 253, 479

Cenarro A. J., et al., 2007, MNRAS, 374, 664

Chandrasekhar S., 1946a, ApJ, 103, 351

Chandrasekhar S., 1946b, ApJ, 104, 110

Chandrasekhar S., 1947, ApJ, 105, 424

Chapman S., Ferraro V., 1931, Terr. Mag, 36, 171

Charbonneau P., 2013, in , Solar and Stellar Dynamos. Springer, pp 187–214

Charbonneau P., 2014, Annu. Rev. Astron. Astrophys., 52, 251

Charbonneau P., MacGregor K., 1997, ApJ, 486, 502

Chassefière E., Leblanc F., 2004, Planet. Space Sci., 52, 1039

Childress S., Gilbert A., 1995, Stretch, Twist, Fold: The Fast Dynamo. Lecture Notes in Physics Monographs, Springer Berlin Heidelberg

Chugainov P., 1966, Inf. Bull. Var. Stars, 122

Chugainov P., 1971, Inf. Bull. Var. Stars, 520

Clarke D., 2010, Stellar Polarimetry. Wiley

Cohen O., Drake J. J., 2014, ApJ, 783, 55

Cohen O., et al., 2006, ApJ, 654, L163

Cohen O., Kashyap V., Drake J., Sokolov I., Gombosi T., 2011, ApJ, 738, 166

Cohen O., Drake J., Glocer A., Garraffo C., Poppenhaeger K., Bell J., Ridley A., Gombosi T., 2014, ApJ, 790, 57

Cohen O., Ma Y., Drake J. J., Glocer A., Garraffo C., Bell J., Gombosi T. I., 2015, ApJl, 806, 41

Collier Cameron A., et al., 2002, MNRAS, 330, 699

Collins G. W., Truax R. J., 1995, ApJ, 439, 860

Condon E., Shortley G., 1951, The Theory of Atomic Spectra. CUP

Copeland H., Jensen J., Jorgensen H., 1970, A&A, 5, 12

Corbally C. J., 1984, ApJS, 55, 657

Cowling T., 1945, MNRAS, 105, 166

Cowling T., 1953, The Sun. University of Chicago Press, p. 532

Cowling T., 1981, Annu. Rev. Astron. Astrophys., 19, 115

Da Silva L., 1975, A&A, 41, 287

Da Silva J. G., Santos N., Bonfils X., Delfosse X., Forveille T., Udry S., 2011, A&A, 534, A30

Da Silva J. G., et al., 2021, A&A, 646, A77

David T. J., Hillenbrand L. A., 2015, ApJ, 804, 146

Davidson J. W., Baptista B. J., Horch E. P., Franz O., Van Altena W. F., 2009, AJ, 138, 1354

De Loore C., Doom C., 1992, Structure and Evolution of Single and Binary Stars. Astrophysics and Space Science Library, Springer Netherlands

De Rosa R., et al., 2014, MNRAS, 437, 1216

Degl'Innocenti E. L., 1982, Solar Physics, 77, 285

Degl'Innocenti M., Landolfi M., 2004, Polarization in Spectral Lines. Astrophysics and Space Science Library, Springer Netherlands

Deluca E. E., Gilman P. A., 1986, Geophys. Astrophys. Fluid Dyn., 37, 85

Deluca E. E., Gilman P. A., 1988, Geophys. Astrophys. Fluid Dyn., 43, 119

Demarque P., Roeder R., 1967, ApJ, 147, 1188

Deutsch A. J., 1958, in Symposium-IAU. pp 209–221

Dikpati M., Charbonneau P., 1999, ApJ, 518, 508

Dirac P. A. M., 1931, Proceedings of the Royal Society of London. Series A, 133, 60

Donahue R. A., Saar S. H., Baliunas S. L., 1996, ApJ, 466, 384

Donati J.-F., 2001, in , Astrotomography. Springer, pp 207–231

Donati J.-F., Brown S., 1997, A&A, 326, 1135

Donati J.-F., Landstreet J., 2009, Annu. Rev. Astron. Astrophys., 47, 333

Donati J., Semel M., 1990, Sol. Phys., 128, 227

Donati J.-F., Semel M., Praderie F., 1989, A&A, 225, 467

Donati J.-F., Semel M., Rees D., 1992, A&A, 265, 669

Donati J.-F., Semel M., Carter B. D., Rees D., Cameron A. C., 1997, MNRAS, 291, 658

Donati J.-F., Cameron A. C., Hussain G., Semel M., 1999, MNRAS, 302, 437

Donati J.-F., Mengel M., Carter B., Marsden S., Collier Cameron A., Wichmann R., 2000, MNRAS, 316, 699

Donati J.-F., et al., 2006, MNRAS, 370, 629

Donati J.-F., et al., 2008, MNRAS, 385, 1179

Dong C., et al., 2018, ApJL, 859, L14

Dormy E., Soward A., 2007, Mathematical Aspects of Natural Dynamos. The Fluid Mechanics of Astrophysics and Geophysics, CRC Press

Dubrov A., 2013, The Geomagnetic Field and Life: Geomagnetobiology. Springer US

Duncan D. K., et al., 1991, ApJS, 76, 383

Duquennoy A., Mayor M., 1991, A&A, 248, 485

Eberhard G., Schwarzschild K., 1913, ApJ, 38

Egan H., Jarvinen R., Ma Y., Brain D., 2019, MNRAS, 488, 2108

Eggenberger P., Carrier F., 2006, A&A, 449, 293

Eggleton P., Tokovinin A., 2008, MNRAS, 389, 869

Eisberg R., 1961, Fundamentals of Modern Physics. Wiley

Eker Z., et al., 2015, AJ, 149, 131

Elsasser W. M., 1946, Phys. Rev., 69, 106

Elsasser W. M., 1950, Phys. Rev., 79, 183

Evensberget D., Carter B. D., Marsden S. C., Brookshaw L., Folsom C. P., 2021, MNRAS, 506, 2309

Evensberget D., Carter B. D., Marsden S. C., Brookshaw L., Folsom C., Salmeron R., 2022, MNRAS, 510, 5226

Falk A. E., Wehlau W. H., 1974, ApJ, 192, 409

Fares R., et al., 2009, MNRAS, 398, 1383

Fares R., et al., 2012, MNRAS, 423, 1006

Fares R., Moutou C., Donati J.-F., Catala C., Shkolnik E., Jardine M., Cameron A., Deleuil M., 2013, MNRAS, 435, 1451

Fernandes J., Lebreton Y., Baglin A., Morel P., 1998, A&A, 338, 455

Field G. B., Carroll S. M., 2000, Physical Review D, 62, 103008

Fleisch D., 2008, A Student's Guide to Maxwell's Equations. CUP

Fricke W., Teleki G., 1982, Sun and Planetary System

Frolov M., 1970, Information Bulletin on Variable Stars, 427

Fuhrmann K., 2008, MNRAS, 384, 173

Fuhrmann K., Chini R., 2012, ApJS, 203, 30

Fuhrmann K., Chini R., 2015, ApJ, 809, 107

Fuhrmann K., Chini R., Hoffmeister V., Stahl O., 2011, MNRAS, 415, 1240

Fujimura D., Tsuneta S., 2009, ApJ, 702, 1443

Gallet F., Bouvier J., 2013, A&A, 556, A36

Galloway D., Weiss N., 1981, ApJ, 243, 945

Garcia-Alvarez D., et al., 2011, A&A, 533, A30

García R. A., Mathur S., Salabert D., Ballot J., Régulo C., Metcalfe T. S., Baglin A., 2010, Science, 329, 1032

Gargaud M., Irvine W. M., eds, 2011, Magnetic Field. Springer Berlin Heidelberg, Berlin, Heidelberg, pp 939–943

Gehren T., 1978, A&A, 65, 427

Giampapa M., 1984, in Space Research in Stellar Activity and Variability. p. 309

Gilliland R. L., et al., 2010, PASP, 122, 131

Gilman P. A., 1980, Differential rotation in stars with convection zones. Springer, pp 19–37

Glagolevskij Y. V., 2019, Astrophys Bull., 74, 66

Goncharskii A., Stepanov V., Kokhlova V., Yagola A., 1977, Astron. Lett., 3, 147

Gray D., 1984, ApJ, 277, 640

Gray D. F., 1985, PASP, 97, 719

Gray R., Napier M., Winkler L., 2001, AJ, 121, 2148

Gray R., Corbally C., Garrison R., McFadden M., Robinson P., 2003, AJ, 126, 2048

Gray R., Corbally C., Garrison R., McFadden M., Bubar E., McGahee C., O'Donoghue A., Knox E., 2006, AJ, 132, 161

Gregory S., Jardine M., Gray C., Donati J., 2010, Rep. Prog. Phys., 73, 126901

Gronoff G., et al., 2020, Journal of Geophysical Research: Space Physics, 125, e2019JA027639

Groth C., De Zeeuw D., Gombosi T., Powell K., 2000, Adv. Space Res., 26, 793

Grunhut J., et al., 2016, MNRAS, p. stw2743

Hackman T., Lehtinen J., Rosén L., Kochukhov O., Käpylä M. J., 2016, A&A, 587, A28

Haken H., Wolf H., Brewer W., 2005, The Physics of Atoms and Quanta: Introduction to Experiments and Theory. Advanced Texts in Physics, Springer

Hale G. E., 1908, ApJ, 28, 315

Hale G. E., 1912, Terrestrial Magnetism and Atmospheric Electricity, 17, 173

Hale G. E., 1913, The Astrophysical Journal, 38, 27

Hale G., Seares F., van Maanen A., Ellerman F., 1918, Contributions from the Mount Wilson Observatory/Carnegie Institution of Washington, 148, 1

Hall D. S., 1972, PASP, 84, 323

Hall D. S., 1991, in IAU Colloquium. pp 353–369

Hall J. C., 2008, Living Rev. Sol. Phys., 5, 1

Hansen W., 1935, Physical review, 47, 139

Hanslmeier A., 2018, Planetary Habitability And Stellar Activity. Advances In Planetary Science, World Scientific Publishing Company

Hartkopf W. I., Mason B. D., Worley C. E., 2001, AJ, 122, 3472

Hartmann L., 1987, in , Cool Stars, Stellar Systems, and the Sun. Springer, pp 1–9

Heiter U., Jofré P., Gustafsson B., Korn A. J., Soubiran C., Thévenin F., 2015, A& A, 582, A49

Hendry E. M., 1981, AJ, 86, 1540

Herbig G., 1985, ApJ, 289, 269

Herzberg G., Spinks J., 1944, Atomic Spectra and Atomic Structure. A Dover paperback, Dover publications

Hill E., 1954, Am. J. Phys., 22, 211

Hobson M., Lasenby A., 1998, MNRAS, 298, 905

Hoffleit D., 1991, Catalogue of bright stars., 3d rev. ed. edn. Yale University Observatory

Houk N., 1978, Michigan catalogue of two-dimensional spectral types for the HD stars. University of Michigan

Huang S.-S., 1961, ApJ, 133, 130

Huang K., 2007, Fundamental Forces of Nature: The Story of Gauge Fields. World Scientific

Hundhausen A., 1968, Space Sci. Rev., 8, 690

Irwin A. W., VandenBerg D. A., Larson A. M., 1999, in IAU Colloquium. pp 297–307

Jackson J., 1962, Classical Electrodynamics. Wiley

Jacques S., 1977, ApJ, 215, 942

Jardine M., Vidotto A., van Ballegooijen A., Donati J.-F., Morin J., Fares R., Gombosi T. I., 2013, MNRAS, 431, 528

Järvinen S., et al., 2015, A&A, 574, A25

Jaschek C., Jaschek M., 1990, The Classification of Stars. CUP

Jeffers S., et al., 2018, MNRAS, 479, 5266

Jiang J., Cameron R. H., Schmitt D., Schüssler M., 2011, A & A, 528, A83

Jofré P., et al., 2018, Research Notes of the AAS, 2, 152

Johnson H. L., Morgan W., 1953, ApJ, 117, 313

Johnson H., Wright C., 1983, ApJS, 53, 643

Johnstone C., Jardine M., Mackay D., 2010, MNRAS, 404, 101

Johnstone C. P., Lüftinger T., Güdel M., Fichtinger B., 2013, Proceedings of the IAU, 9, 243

Johnstone C., Güdel M., Lüftinger T., Toth G., Brott I., 2015, A&A, 577, A27

Joy A. H., Wilson R. E., 1949, ApJ, 109, 231

Kabanikhin S., 2012, Inverse and Ill-posed Problems: Theory and Applications. Inverse and Ill-Posed Problems Series, De Gruyter

Kaspi V. M., Beloborodov A. M., 2017, Annu. Rev. Astron. Astrophys., 55, 261

Kervella P., Thévenin F., Morel P., Berthomieu G., Bordé P., Provost J., 2004, A&A, 413, 251

Kitchatinov L., Rüdiger G., 1999, A&A, 344, 911

Kitchatinov L., Jardine M., Cameron A. C., 2001, A&A, 374, 250

Kleeorin N., Ruzmaikin A., Sokoloff D., 1983, Astrophys. Space Sci., 95, 131

Knutson H. A., Howard A. W., Isaacson H., 2010, ApJ, 720, 1569

Kochukhov O., 2016, in , Cartography of the Sun and the Stars. Springer, pp 177–204

Kochukhov O., Makaganiuk V., Piskunov N., 2010, A&A, 524, A5

Kochukhov O., Lüftinger T., Neiner C., Alecian E., Collaboration M., et al., 2014, A&A, 565, A83

Koerner D., et al., 2010, ApJL, 710, L26

Koh D., Abel T., Jedamzik K., 2021, ApJL, 909, L21

Konacki M., Muterspaugh M. W., Kulkarni S. R., Hełminiak K. G., 2010, ApJ, 719, 1293

Konatham S., Martin-Torres J., Zorzano M.-P., 2020, Proceedings of the Royal Society A, 476, 20200148

Korzennik S., Noyes R., Brown T., Nisenson P., Horner S., 1995, ApJ, 443, L25

Kõvári Z., Weber M., 2004, PADEU, 14, 221

Kraft R. P., 1965, ApJ, 142, 681

Kragh H., 2007, Conceptions of Cosmos: From Myths to the Accelerating Universe: A History of Cosmology. OUP Oxford

Krause F., Rädler K., 1980, Mean-field magnetohydrodynamics and dynamo theory. Akademie-Verlag

Kriskovics L., Kővári Z., Vida K., Oláh K., Carroll T., Granzer T., 2019, A&A, 627, A52

Kron G., 1950, AJ, 55, 69

Kuijpers J., Frey H. U., Fletcher L., 2015, Space Sci. Rev., 188, 3

Küker M., Rüdiger G., 2007, Astron. Nachr., 328, 1050

Küker M., Rüdiger G., 2011, Astron. Nachr, 332, 933

Kunkel W. E., 1970, ApJl, 161, 503

Kupka F., Montgomery M., 2002, MNRAS, 330, L6

Lamb D. A., 2017, ApJ, 836, 10

Lammer H., Lichtenegger H., Kolb C., Ribas I., Guinan E., Abart R., Bauer S., 2003a, Icarus, 165, 9

Lammer H., Selsis F., Ribas I., Guinan E., Bauer S., Weiss W., 2003b, ApJ, 598, L121

Lamor J., 1919, Assoc. Adc. Sci. Rep, pp 159–160

Landi Degl'Innocenti E., Landi Degl'Innocenti M., 1981, Nuovo Cimento B Serie, 62, 1

Landi Degl'Innocenti E., et al., 2007, in The Future of Photometric, Spectrophotometric and Polarimetric Standardization. p. 495

Landstreet J. D., 1970, ApJ, 159, 1001

Landstreet J., 1992, Astron. Astrophys. Rev., 4, 35

Landstreet J., Mathys G., 2000, A&A, 359, 213

Lang K., 1992, Astrophysical Data: Planets and Stars. Astrophysical Data, Springer New York

Lang K., 2006, Astrophysical Formulae: Volume I & Volume II: Radiation, Gas Processes and High Energy Astrophysics/Space, Time, Matter and Cosmology. Springer Science & Business Media

Lanza A., Rodono M., Rosner R., 1998, MNRAS, 296, 893

Lawler S., et al., 2009, ApJ, 705, 89

Leboeuf J., Tajima T., Kennel C., Dawson J., 1981, Geophys. Res. Lett., 8, 257

Lehmann L., Hussain G., Jardine M., Mackay D., Vidotto A., 2019, MNRAS, 483, 5246

Leighton R. B., 1969, ApJ, 156, 1

Liebert J., Fontaine G., Young P. A., Williams K. A., Arnett D., 2013, ApJ, 769, 7

Lignières F., Petit P., Böhm T., Aurière M., 2009, A&A, 500, L41

Linsky J. L., 1980, Annu. Rev. Astron. Astrophys, 18, 439

Linsky J. L., 1989, in IAU Colloquium. pp 187–196

Linsky J., 2019, Host Stars and their Effects on Exoplanet Atmospheres: An Introductory Overview. Lecture Notes in Physics, Springer

Lopes C. F., Leão I. d. C., De Freitas D., Martins B. C., Catelan M., De Medeiros J., 2015, A&A, 583, A134

Lorentz H., 1892, La théorie électromagnétique de Maxwell et son application aux corps mouvants. Extrait des Archives néerlandaises des sciences exactes et naturelles, E.J. Brill

Luck R. E., 2016, The Astronomical Journal, 153, 21

Lyon J., Fedder J., Huba J., 1986, J. Geophys. Res. Space Phys., 91, 8057

MacGregor K., Charbonneau P., 1997, ApJ, 486, 484

Maciel W., 2014, Hydrodynamics and Stellar Winds. Springer

Maeder A., Meynet G., 1988, A&AS, 76, 411

Maggio A., Sciortino S., Vaiana G., Majer P., Bookbinder J., Golub L., Harnden Jr F., Rosner R., 1987, ApJ, 315, 687

Malagnini M., Morossi C., 1990, A&AS, 85, 1015

Maldonado J., Villaver E., Eiroa C., 2013, A & A, 554, A84

Mallik S. V., 1999, A&A, 352, 495

Marsden S. C., Mengel M. W., Donati F., Carter B. D., Semel M., Petit P., 2006, in Solar Polarization 4. p. 401

Marsden S. C., Jeffers S. V., Donati J.-F., Mengel M. W., Waite I. A., Carter B. D., 2009, in Proceedings of the IAU, 5, 130

Marsden S., et al., 2014, MNRAS, 444, 3517

Mason B. D., Wycoff G. L., Hartkopf W. I., Douglass G. G., Worley C. E., 2001, AJ, 122, 3466

Massarotti A., Latham D. W., Stefanik R. P., Fogel J., 2007, AJ, 135, 209

Mathur S., Augustson K., Brun A., Garcıa R., Metcalfe T., 2014, Proceedings of Lowell Observatory, 9, 13

Mathys G., 1989, Fundamentals of Cosmic Physics, 13, 143

Mathys G., 1995, A&A, 293, 733

Mathys G., 1999, in , Solar Polarization. Springer, pp 489–506

Matson R., Williams S., Hartkopf W., Mason B., 2020, United States Naval Observatory, Washington, DC

Matsumoto T., Kitai R., 2010, ApJL, 716, L19

Matsumoto T., Suzuki T. K., 2012, ApJ, 749, 8

Maxwell J. C., 1865, Philos. Trans. R. Soc. Lond., pp 459–512

Mayor M., Mazeh T., 1987, A&A, 171, 157

Mazeh T., Prato L., Simon M., Goldberg E., Norman D., Zucker S., 2002, ApJ, 564, 1007

McKenzie J., Axford W., Banaszkiewicz M., 1997, Geophys. Res. Lett., 24, 2877

McQuillan A., Mazeh T., Aigrain S., 2014, ApJS, 211, 24

Megessier C., 1975, A&A, 39, 263

Mengel M., et al., 2016, MNRAS, 459, 4325

Mestel L., 1968, MNRAS, 138, 359

Mestel L., Spruit H., 1987, MNRAS, 226, 57

Metcalfe T., Dziembowski W., Judge P., Snow M., 2007, MNRAS: Letters, 379, L16

Metcalfe T., Basu S., Henry T., Soderblom D., Judge P., Knölker M., Mathur S., Rempel M., 2010, APJL, 723, L213

Mewe R., 1979, Space Sci. Rev., 24, 101

Miesch M. S., Toomre J., 2009, Annu. Rev. Fluid Mech, 41, 317

Mikić Z., Linker J. A., Schnack D. D., Lionello R., Tarditi A., 1999, Phys. Plasmas, 6, 2217

Mittag M., Schmitt J., Hempelmann A., Schröder K.-P., 2019, A&A, 621, A136

Moffatt H., 1978, Magnetic Field Generation in Electrically Conducting Fluids. Cambridge Monographs on Mechanics, Cambridge University Press

Moffatt K., Dormy E., 2019, Self-Exciting Fluid Dynamos. Cambridge Texts in Applied Mathematics, Cambridge University Press

Montes D., López-Santiago J., Gálvez M., Fernández-Figueroa M., De Castro E., Cornide M., 2001, MNRAS, 328, 45

Morgan W. W., Keenan P. C., 1973, Annu. Rev. Astron. Astrophys., 11, 29

Morin J., Donati J.-F., Petit P., Delfosse X., Forveille T., Jardine M., 2010, MNRAS, 407, 2269

Moss D., Barker D. M., Brandenburg A., Tuominen I., 1995, A&A, 294, 155

Mullan D., 1971, MNRAS, 154, 467

Mullan D., 1972, ApJL, 12, 13

Neiner C., Lèbre A., 2014, in Proceedings of the Annual meeting of the French Society of Astronomy and Astrophysics. pp 505–508

Neiner C., Zahn J.-P., Landstreet J., 2009, EAS Publ. Ser., 39, 39

Neiner C., Wade G., Sikora J., 2017, MNRAS: Letters, 468, L46

Nicholson B., et al., 2016, MNRAS, 459, 1907

Nordström B., et al., 2004, A& A, 418, 989

North J., et al., 2009, MNRAS, 393, 245

Ogino T., Walker R. J., 1984, Geophys. Res. Lett., 11, 1018

Oranje B., et al., 1982, A&A, 110, 30

Oudmaijer R. D., Van der Veen W., Waters L., Trams N., Waelkens C., Engelsman E., 1992, A&AS, 96, 625

Parker E. N., 1955, ApJ, 122, 293

Parker E. N., 1958, ApJ, 128, 664

Parker E., 1960, ApJ, 132, 821

Parker E., 1975, ApJ, 198, 205

Parker E., 1979, Cosmical magnetic fields. Their origin and their activity. OUP, New York

Parker E., 1993, ApJ, 408, 707

Parker E. N., 2001, in , The century of space science. Springer, pp 225–255

Pecaut M. J., Mamajek E. E., 2013, ApJS, 208, 9

Perryman M., 2018, The Exoplanet Handbook. Cambridge University Press

Petit P., Donati J.-F., Collier Cameron A., 2002, MNRAS, 334, 374

Petit P., et al., 2010, A&A, 523, A41

Petrosyan A., et al., 2010, Space Sci. Rev., 156, 135

Pinsonneault M., DePoy D., Coffee M., 2001, ApJL, 556, L59

Piskunov N., Kochukhov O., 2002, A&A, 381, 736

Pneuman G., Kopp R. A., 1971, Sol. phys., 18, 258

Pounds K., et al., 1991, MNRAS, 253, 364

Powell K. G., Roe P. L., Linde T. J., Gombosi T. I., De Zeeuw D. L., 1999, J. Comput. Phys., 154, 284

Preston G. W., 1967a, ApJ, 150, 547

Preston G. W., 1967b, ApJ, 150, 871

Preston G. W., 1969, ApJ, 158, 251

Preston G. W., 1971, ApJ, 164, 309

Provencal J., Shipman H., Koester D., Wesemael F., Bergeron P., 2002, ApJ, 568, 324

Pyper D. M., 1969, ApJS, 18, 347

Rädler K.-H., 1980, Astron. Nachr, 301, 101

Raeder J., Walker R., Ashour-Abdalla M., 1995, Geophys. Res. Lett., 22, 349

Rains A. D., Ireland M. J., White T. R., Casagrande L., Karovicova I., 2020, MNRAS, 493, 2377

Ramírez I., Fish J., Lambert D. L., Prieto C. A., 2012, ApJ, 756, 46

Ratra B., 1992, ApJ, 391, L1

Rees M. J., 1987, QJRAS, 28, 197

Reiners A., 2007, Astron. Nachr., 328, 1034

Reiners A., Basri G., 2009, A&A, 496, 787

Reiners A., Royer F., 2004, A&A, 415, 325

Reiners A., Schmitt J. H., 2002, A&A, 384, 155

Reiners A., Schmitt J., 2003, A&A, 398, 647

Reinhold T., Gizon L., 2015, A&A, 583, A65

Reinhold T., et al., 2013, A&A, 560, A4

Rhee J. H., Song I., Zuckerman B., McElwain M., 2007, ApJ, 660, 1556

Rice J. B., 1970, A&A, 9, 189

Rice J., Wehlau W., Khokhlova V., 1989, A&A, 208, 179

Ricker G. R., et al., 2014, J. Astron. Telesc. Instrum. Syst., 1, 014003

Roberts P. H., Soward A. M., 1992, Annu. Rev. Fluid Mech., 24, 459

Robinson R., 1980, ApJ, 239, 961

Rüdiger G., Elstner D., 1994, A&A, 281, 46

Saar S., 1990, in IAU Symposium 138, The Solar Photosphere: Structure, Convection, and Magnetic Fields, Dordrecht: Kluwer. pp 427–441

Salabert D., Régulo C., Ballot J., García R., Mathur S., 2011, A&A, 530, A127

Samus N., Kazarovets E., Durlevich O., Kireeva N., Pastukhova E., 2009, VizieR Online Data Catalog, pp B–gcvs

Samus N., Kazarovets E., Durlevich O., Kireeva N., Pastukhova E., 2017, Astron. Rep., 61, 80

Santos N., Israelian G., Mayor M., 2001, A&A, 373, 1019

Sanz-Forcada J., Stelzer B., Metcalfe T., 2013, A&A, 553, L6

Sanz-Forcada J., Stelzer B., Coffaro M., Raetz S., Alvarado-Gómez J., 2019, A&A, 631, A45

Sato S., Cuntz M., Olvera C. G., Jack D., Schröder K.-P., 2014, Int. J. Astrobiology, 13, 244

Schatzman E., 1959, in Symposium - IAU , Volume 10: The Hertzsprung-Russell Diagram,. pp 129–129

Schatzman E., 1962, in Annales d'Astrophysique. p. 18

Schiff L., 1955, Quantum Mechanics. International series in pure and applied physics, McGraw-Hill

Schmitt J., Golub L., Harnden Jr F., Maxson C., Rosner R., Vaiana G., 1985, AJ, 290, 307

Schrijver C., 1987, A&A, 172, 111

Schrijver C., 1993, A&A, 269, 446

Schröder C., Schmitt J., 2007, A& A, 475, 677

Schüssler M., Baumann I., 2006, A& A, 459, 945

Schüssler M., Rempel M., 2005, A&A, 441, 337

Schwarzschild K., 1906, AKGWG, 195, 41

Schwarzschild M., 1950, ApJ, 112, 222

Seach J., Marsden S., Carter B., Neiner C., Folsom C., Mengel M., Oksala M., Buysschaert B., 2020, MNRAS, 494, 5682

Seach J., Marsden S., Carter B., Evensberget D., Folsom C., Neiner C., Mengel M., 2022a, MNRAS, 509, 5117

Seach J., Marsden S., Carter B., Neiner C., Folsom C., 2022b, MNRAS, 513, 4278

Seares F. H., 1913, ApJ, 38, 99

See V., Jardine M., Vidotto A. A., Petit P., Marsden S. C., Jeffers S. V., do Nascimento J., 2014, A&A, 570, A99

Selsis F., 2006, Ecole de Goutelas, 28, 271

Semel M., 1989, A&A, 225, 456

Semel M., Li J., 1996, Sol. Phys., 164, 417

Shapley H., Nicholson S. B., 1919, PNAS, 5, 417

Shaya E. J., Olling R. P., 2010, ApJS, 192, 2

Shibahashi H., Takata M., 1993, PASJ, 45, 617

Shnir Y. M., 2006, Magnetic monopoles. Springer Science and Business Media

Shultz M., et al., 2019, MNRAS, 490, 4154

Shurcliff W., 1962, Polarized Light: Production and Use. Harvard University Press

Sigl G., Olinto A. V., Jedamzik K., 1997, Phys. Rev. D, 55, 4582

Sikora J., Wade G., Power J., Neiner C., 2019, MNRAS, 483, 2300

Silvester J., et al., 2009, MNRAS, 398, 1505

Skiff B., 2014, General catalogue of stellar spectral classifications (Lowell Observatory, Flagstaff, 2014)

Skilling J., Bryan R., 1984, MNRAS, 211, 111

Skumanich A., 1972, ApJ, 171, 565

Sobel'man I., et al., 1972, Introduction to the Theory of Atomic Spectra. Pergamon Press

Söderhjelm S., 1999, A&A, 341, 121

Soleillet P., 1929, in Ann. Phys.. pp 23–97

Spiegel E., Weiss N., 1980, Nature, 287, 616

Steenbeck M., Krause F., Rädler K.-H., 1966, Zeitschrift für Naturforschung A, 21, 369

Stenflo J. O., 1971, in Symposium-IAU. pp 101–129

Stenflo J., 1985, in , Progress in Solar Physics. Springer, pp 189–208

Stenflo J. O., 2017, Space Sci. Rev., 210, 5

Stibbs D., 1950, MNRAS, 110, 395

Stix M., 1976, in Symposium-IAU. pp 367–388

Stix M., 1981, Sol. Phys., 74, 79

Stokes G. G., 1851, Trans. Cambridge Philos. Soc., 9, 399

Stothers R. B., Chin C.-W., 1992, ApJ, 390, L33

Strassmeier K., Rice J., 2003, A&A, 399, 315

Suess S. T., Wang A.-H., Wu S., Poletto G., McComas D., 1999, J Geophys Res Space Phys, 104, 4697

Suzuki T. K., Inutsuka S.-i., 2005, ApJ, 632, L49

Suzuki T. K., Inutsuka S.-i., 2006, J. Geophys. Res. Space Phys., 111

Takeda G., Ford E. B., Sills A., Rasio F. A., Fischer D. A., Valenti J. A., 2007, ApJS, 168, 297

Tanaka T., 1995, J. Geophys. Res. Space Phys., 100, 12057

Thompson M., Balogh A., Culhane J., Nordlund Å., Solanki S., Zahn J., 2009, The Origin and Dynamics of Solar Magnetism. Springer New York

Thomson-Paressant K., Neiner C., Zwintz K., Escorza A., 2021, MNRAS, 500, 1992

Tichonov A., John F., Arsenin V., 1977, Solutions of Ill-posed Problems. Halsted Press book, V.H. Winston & Sons

Tikhonov A., et al., 1977, Solutions of Ill-posed Problems. Halsted Press book, Winston

Tokovinin A., 2014, AJ, 147, 87

Tokovinin A., Kiyaeva O., 2015, MNRAS, 456, 2070

Torres G., Andersen J., Giménez A., 2010, Astron. Astrophys. Rev., 18, 67

Tóth G., et al., 2012, J. Comput. Phys., 231, 870

Tout C., Pringle J., 1992, MNRAS, 259, 604

Turner M. S., Widrow L. M., 1988, Physical Review D, 37, 2743

Unno W., 1956, PASJ, 8, 108

Usmanov A., 1993, Sol. phys., 146, 377

Usmanov A., Goldstein M., 2003, J. Geophys. Res. Space Phys., 108

Usmanov A. V., Goldstein M. L., Besser B. P., Fritzer J. M., 2000, J. Geophys. Res. Space Phys., 105, 12675

Vaiana G. S., Rosner R., 1978, Annu. Rev. Astron. Astrophys., 16, 393

Van Allen J. A., Ludwig G. H., Ray E. C., McIlwain C. E., 1958, J. Jet Propuls, 28, 588

Van Ballegooijen A., 1982, A&A, 106, 43

Van Belle G. T., Von Braun K., 2009, ApJ, 694, 1085

Van Leeuwen F., 2007, A&A, 474, 653

Vaughan Jr A. H., Zirin H., 1968, ApJ, 152, 123

Vaughan A. H., Preston G. W., Wilson O. C., 1978, PASP, 90, 267

Vican L., 2012, AJ, 143, 135

Vidotto A., 2014, ASTRA Proceedings, 1, 19

Vidotto A., Opher M., Jatenco-Pereira V., Gombosi T., 2009, ApJ, 703, 1734

Vidotto A., Fares R., Jardine M., Donati J.-F., Opher M., Moutou C., Catala C., Gombosi T. I., 2012, MNRAS, 423, 3285

Vidotto A., Fares R., Jardine M., Moutou C., Donati J.-F., 2015, MNRAS, 449, 4117

Vidotto A., Lehmann L., Jardine M., Pevtsov A., 2018, MNRAS, 480, 477

Vogt S. S., Penrod G. D., 1983a, in IAU Colloquium , Volume 71: Activity in Red-Dwarf Stars. pp 379–385

Vogt S. S., Penrod G. D., 1983b, PASP, 95, 565

Vogt S. S., Penrod G. D., Hatzes A. P., 1987, ApJ, 321, 496

Vögler A., Schüssler M., 2007, A&A, 465, L43

Wade G., Donati J.-F., Landstreet J., Shorlin S., 2000a, MNRAS, 313, 823

Wade G., Donati J.-F., Landstreet J., Shorlin S., 2000b, MNRAS, 313, 851

Waite I., Marsden S., Carter B., Alecian E., Brown C., Burton D., Hart R., 2011, Publ. Astron. Soc. Aust., 28, 323

Waite I., Marsden S., Carter B., Petit P., Donati J.-F., Jeffers S., Boro Saikia S., 2015, MNRAS, 449, 8

Walker M., 1954, Am. J. Phys., 22, 170

Walter F., 1983, ApJl, 274, 794

Warner B., 1976, in Symposium - IAU, Volume 73: Structure and Evolution of Close Binary Systems. pp 85–140

Watanabe K., Sato T., 1990, J. Geophys. Res. Space Phys., 95, 75

Wenger M., et al., 2000, A&AS, 143, 9

Westgate C., 1934, ApJ, 79, 357

White W. W., Siscoe G. L., Erickson G. M., Kaymaz Z., Maynard N. C., Siebert K. D., Sonnerup B. U. Ö., Weimer D. R., 1998, Geophys. Res. Lett., 25, 1605

Widrow L. M., Ryu D., Schleicher D. R., Subramanian K., Tsagas C. G., Treumann R. A., 2012, Space Sci. Rev., 166, 37

Willamo T., et al., 2021, arXiv preprint arXiv:2110.06729

Wilson O., 1963, ApJ, 138, 832

Wilson O., 1968, ApJ, 153, 221

Wilson O., 1978, ApJ, 226, 379

Wilson O., Bappu M., 1957, ApJ

Winglee R., 1994, J. Geophys. Res. Space Phys., 99, 13437

Wittenmyer R. A., Endl M., Cochran W. D., Hatzes A. P., Walker G., Yang S., Paulson D. B., 2006, AJ, 132, 177

Wolf C., Rayet G., 1867, Academie des Sciences Paris Comptes Rendus, 65, 292

Wood B. E., et al., 2015, Stellar winds in time. Springer, pp 19–35

Wu N., 2012, The Maximum Entropy Method. Springer Series in Information Sciences, Springer Berlin Heidelberg

Wu C., Walker R., Dawson J., 1981, Geophys. Res. Lett., 8, 523

Wu S., Guo W., Michels D., Burlaga L., 1999, J Geophys Res Space Phys, 104, 14789

Zarro D., 1983a, in BAAS. p. 948

Zarro D., 1983b, ApJ, 267, L61

Zarro D. M., Rodgers A., 1983, ApJS, 53, 815

Zeeman P., 1897, The London, Edinburgh, and Dublin Philosophical Magazine and Journal of Science, 43, 226

Zeldovich Y., et al., 1983, Magnetic Fields in Astrophysics. Current Topics in Environmental and Toxicological Chemistry, Gordon and Breach